A methodology for air entrainment in breaking waves and their interaction with a mono-pile

Tomaselli, Pietro Danilo

Publication date:
2016

Document Version
Publisher's PDF, also known as Version of record

A methodology for air entrainment in breaking waves and their interaction with a mono-pile

PhD Thesis

$$(EIv'')'' = q - \rho A \ddot{v}$$

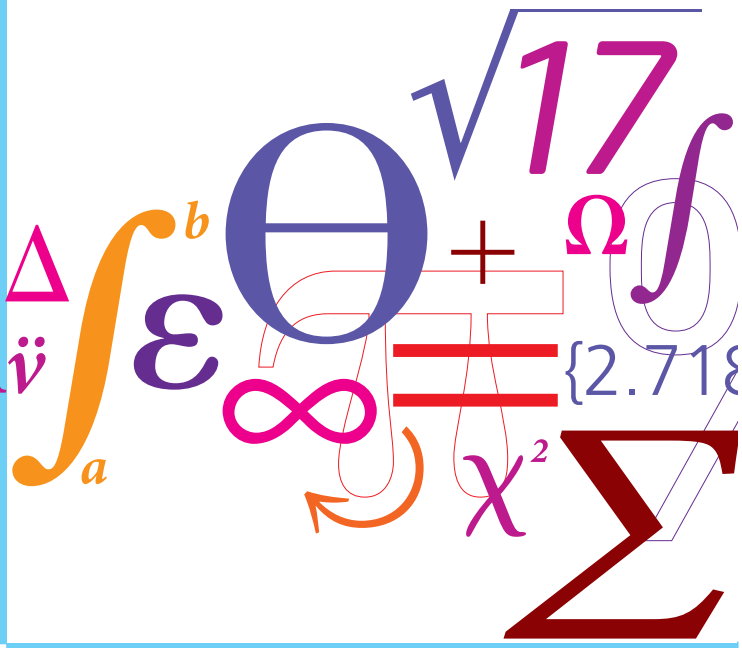

Pietro Danilo Tomaselli
August 2016

DTU Mechanical Engineering
Department of Mechanical Engineering

A methodology for air entrainment in breaking waves and their interaction with a mono-pile

by
Pietro Danilo Tomaselli

under suggestion of:
Professor Erik Damgaard Christensen (DTU), supervisor

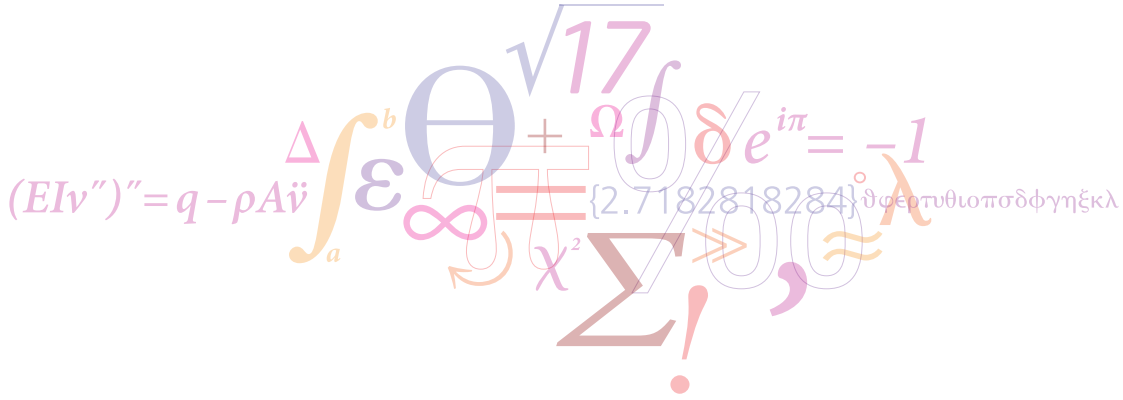

A methodology for air entrainment in breaking waves and their interaction with a mono-pile

DTU Mechanical Engineering
Section of Fluid Mechanics, Coastal and Maritime Engineering
Technical University of Denmark

Nils Koppels Allé, Bld. 403
DK-2800, Kongens Lyngby, Denmark
Phone: (+45) 45 25 19 60
Fax: (+45) 45 25 19 61
www.mek.dtu.dk

to my grandmother Michelina
for all things I learnt from her

Preface

The present thesis is submitted as a partial fulfillment of the requirements for the degree of Philosophiae Doctor (Ph.D.) at the Technical University of Denmark (DTU).

The thesis is written in the form of a monograph and it was prepared at the Section of Fluid Mechanics, Coastal and Maritime Engineering, Department of Mechanical Engineering at the Technical University of Denmark (DTU). The work was carried out from the 1st of December 2012 to the 31st of August 2016 under the supervision of Professor Erik Damgaard Christensen.

An external research stay was undertaken from April 2015 to August 2015 at the University of Delaware, Department of Civil and Environmental Engineering, Center for Applied Coastal Research, under the supervision of Professor James T. Kirby.

The Ph.D. study was funded by the Technical University of Denmark and the FP7-OCEAN-2011 project "Innovative Multi-purpose offshore platforms: planning, design and operation", MERMAID, 288710. Financial support was also received from the Otto Mønsted A/S Fond in the frame of the OMAE 2015 and OMAE 2016 conferences.

Acknowledgements

The thesis is the result of the intense work that I carried out in the past four years almost. The study has been as much challenging as thrilling, but I have always conducted it with diligence and dedication.

At first, I would like to express my deepest gratitude to my supervisor, Professor Erik Damgaard Christensen, for his unconditional trust in me, his knowledge and his guidance which have been decisive for this Ph.D. study. I am also very grateful to Ph.D. Bjarne Jensen for all times he courteously helped me.

I would like to acknowledge also the assistance of Professor James T. Kirby and his research group during my external stay at the University of Delaware. A special thanks goes to Ph.D. Morteza Derakhti for his precious suggestions.

I would like to mention also Professor Giovanni Battista Ferreri who introduced me to the Maritime Engineering field during my time as Master's student at the University of Palermo.

Copenhagen, 31st August 2016

Pietro Danilo Tomaselli

Abstract

Breaking wave-induced loads on offshore structures can be extremely severe. The air entrainment mechanism during the breaking process plays a role in the exerted forces which is still poorly understood. More knowledge needs to be gained in this regard, because a large number of constructions will be installed in the near future in intermediate water depth regions (20-40 m) where waves may break under storm conditions.

This thesis deals with the development of a numerical methodology for the reproduction of breaking waves with the related air entrainment mechanism. The methodology was optimized for the prediction of the roller in spilling breakers which is a mixture of entrained air and water that travels with the wave front with approximately the wave celerity.

The approach couples the Eulerian multiphase model for the entrained air bubbles with a volume-of-fluid method to capture the free surface. The methodology was implemented within a Computational Fluid Dynamics framework through the libraries provided by the open-source CFD package OpenFOAM. The air entrainment was obtained with a formulation which transfers mass from the air above the free surface into the bubbles in water.

The developed CFD solver was strategically validated against four experimental case studies. In the first case, a flow in a bubble column was reproduced in order to test the capability of the Eulerian multiphase model of predicting the bubble motion and the turbulence field of the water phase. In the second case, the implemented Volume-Of-Fluid method was verified in the simulation of regular spilling waves without reproducing the air entrainment. In the third and fourth case, the performance of the formulation for the air entrainment was analysed by simulating a single deep water spilling wave and regular spilling waves. These tests were repeated without entrained bubbles in order to highlight their effects on the flow.

Finally, the CFD solver was employed to investigate the impact of a laboratory spilling

wave on a vertical circular cylinder. Several impacts were reproduced for different distances of the cylinder from the breaking point. The role of the roller on the exerted forces was evaluated by performing simulations without the inclusion of entrained bubbles. Moreover, the computed in-line forces were compared with the measurements of an experiment conducted at the Technical University of Denmark.

Resumé

De laste som brydende bølgerne inducerer på offshore-konstruktioner kan være meget voldsomme. Brydende bølger spiller en vigtig rolle for de mekanismer, som giver anledning til de udøvende kræfter. Disse mekanismer er endnu ikke forstået fuldt ud. Det er nødvendigt at få mere viden indenfor området, da der i nærmeste fremtid bliver bygget et stort antal konstruktioner i områder med middeldybt vand (20-40 meters dybde), hvor bølgerne godt kan bryde og ramme disse konstruktioner under stormlignende forhold.

Dette Ph.D-projekt beskriver udviklingen af en numerisk metode til reproduktionen af luftmedrivningsprocessen ved bølgebrydningsprocessen. Denne metode blev udviklet til at forbedre beskrivelsen af den valse, der skabes i brydningens begyndelse. Valsen er en blanding af vand og luft, som rives. Blandingen af vand og luft, valsen, flyttes af bølgens forreste del med bølgens udbredelseshastighed.

Den udviklede metode koblede en flerfase "Eulerian" model, som beskriver medrivningen af luft i overfladen, med en metode til at beskrive de frie overflade i bølger baseret på "VOF" (Volume of Fluid). Metoden blev implementeret i CFD (Computational Fluid Dynamics) indenfor rammerne af open-source CFD softwaren "OpenFOAM". Luftmedrivningen blev opnået gennem en empirisk formulering, som overfører luftmasse over overfladen til vandet som luftbobler.

Den udviklede CFD-løser blev valideret mod fire eksperimentelle studier. I det første studie blev en strømning i en boblekolonne reproduceret for at teste "Eulerian" modellens evne til at håndterede forskellige faser i forbindelse med forudsigelsen af boblernes bevægelse og turbulens i vandfasen. I det andet studie blev den implementerede metode til at beskrive overfladen, VOF, (Volume of Fluid) uden medrivning af luftbobler verificeret ved simulering af regulære topbrydende bølger. I det tredje og fjerde studie analyseredes den måde, hvorpå luftmedrivningen optrådte ved at simulere en enkelt dybt vands bølgebrydning, samt flere regulære bølger. Disse tests blev ligeledes gennemført uden medrivningsmodellen (uden luftbobler i vandet), hvorved virkningen af luft-medrivningen kunne analyseres.

Sidst, men ikke mindst, blev CFD-løseren anvendt til at undersøge topbrydende bølgers påvirkning af en vertikal cylinder. Påvirkningen af cylinderen blev undersøgt for forskellige afstande mellem cylinderen og brydningspunktet. Valsen som var en blanding af luft og vand blev skubbet foran den brydende bølge. Rollen af valsen blev evalueret ved at udføre simuleringer med og uden medrivning af luft. Derudover sammenlignedes beregnede langsgående laste med målinger fra et eksperiment udført ved Danmarks Tekniske Universitet.

Papers

Part of the work performed during the Ph.D. project resulted in two conference papers which are listed hereafter. They are directly related to the main topics of this thesis and all of them have been accepted and published by the end of this project.

- Tomaselli, P. D. and Christensen, E. D. (2015). Investigation On The Use Of A Multiphase Eulerian CFD Solver To Simulate Breaking Waves. In *ASME 2015 34th International Conference on Ocean, Offshore and Arctic Engineering*. American Society of Mechanical Engineers

- Tomaselli, P. D. and Christensen, E. D. (2016). A Coupled VOF-Eulerian Multiphase CFD Model To Simulate Breaking Wave Impacts On Offshore Structures. In *ASME 2016 35th International Conference on Ocean, Offshore and Arctic Engineering*. American Society of Mechanical Engineers

Contents

List of Figures

List of Tables

Nomenclature

A_b	cross-sectional area of the bubble plume
A_b	total volume of the bubble plume
B	bubble breakage term
C	bubble coalescence term
C_D	drag coefficient
C_L	lift coefficient
C_M	inertia coefficient
C_S,C_I	coefficient dynamic Smagorinsky
C_w	wave celerity
C_{VM}	virtual mass coefficient
D	bubble degassing term
E	air bubble entrainment term
F_i	face mass flux
H_s	significant wave height
KC	Keulegan-Carpenter number
L_c	central wave length
N	number of bubble classes
P	breakage probability density function
Re	Reynolds number
S	mass transfer among phases

S_b	Schmidt number
St	Stokes number
T_c	central wave period
T_p	peak period of JONSWAP spectrum
X_b	horizontal centroid of the bubble plume
Z_b	vertical centroid of the bubble plume
Δ	cell size
α	volume fraction
α_b	total bubble phase fraction
α_b^{ave}	averaged bubble phase fraction
$\boldsymbol{D}$	deviatoric part of the rate-of-strain tensor
$\mathbf{\Gamma}^{eff}$	effective stress tensor
$\mathbf{\Gamma}^{r}$	resolved stress tensor
$\mathbf{\Gamma}^{sgs,BI}$	bubble-induced SGS stress tensor
$\mathbf{\Gamma}^{sgs,SI}$	shear-induced SGS stress tensor
$\mathbf{\Gamma}^{sgs}$	SGS stress tensor
$\mathbf{\Gamma}_I$	interfacial friction tensor
$\boldsymbol{\tau}$	instantaneous viscous stress tensor
$\dot{\mathbf{u}}$	acceleration
ϵ^{r}	resolved dissipation rate
$\epsilon^{sgs,BI}$	bubble-induced SGS stress tensor
$\epsilon^{sgs,SI}$	shear-induced SGS stress tensor
ϵ^{sgs}	SGS dissipation rate
ϵ^{tot}	total dissipation rate
η	surface elevation

γ	peak enhancement of JONSWAP spectrum
κ	interface curvature
$\mathbf{I}$	identity matrix
$\mathbf{M}_D$	drag force
$\mathbf{M}$	interfacial momentum transfer
$\mathbf{M}_L$	lift force
$\mathbf{M}_{TD}$	turbulent dispersion force
$\mathbf{M}_{VM}$	virtual mass force
$\mathbf{M}_\sigma$	surface tension force
$\mathbf{S}$	instantaneous rate-of-strain tensor
$\mathbf{S}_f$	face are vector
$\mathbf{U}$	volumetric mixture velocity
$\mathbf{U}_m$	center-of-mass velocity
$\mathbf{U}_r$	relative velocity
$\mathbf{g}$	gravity acceleration
$\mathbf{u}$	velocity
μ	dynamic viscosity
μ_{eff}	effective dynamic viscosity
ν^r	molecular kinematic viscosity
$\nu^{sgs,BI}$	bubble-induced SGS kinematic viscosity
$\nu^{sgs,SI}$	shear-induced SGS kinematic viscosity
ν^{sgs}	SGS kinematic viscosity
ρ	density
σ	surface tension
τ_0	viscous friction

τ_Δ	time scale of the flow
$\tau_{b,i}$	bubble time scale
θ	collision rate for coalescence
φ_{air}	blending function for degassing
a	coalescence frequency
a_h	Hinze scale
c_{en}	air entrainment coefficient
d	bubble diameter
d_{32}	Sauter diameter
f^{ind}	indicator function
f_p	peak frequency of JONSWAP spectrum
k^r	resolved kinetic energy
k^{sgs}	SGS turbulent kinetic energy
k^{tot}	total kinetic energy
l	width of bubble class
l_I	interfacial length scale
l_{ed}	eddy length scale
m	daughter bubble number
n	bubble number density
p	static pressure
p_d	excess pressure
r_{b}	bubble radius
s	size spectrum of entrained bubbles
v	bubble volume

1 Introduction

The design of new offshore structures is based on the accurate determination of the wave-induced loads for the verification of the overall stability and safety.

In order to find these forces, the designers have to analyse the interaction of the structure with the (irregular) waves that likely occur at the site of interest. This is not straightforward, because it involves the computation of, first, the propagation of the waves to the site of interest, and then of the wave kinematics at the time of impact. Moreover, designers need often to take into account breaking waves, making the analysis much more challenging. The wave breaking phenomenon implies that a certain amount of air entrains the water forming a mixture of these two fluids.

The present work is about *numerical* modeling of air entrainment in breaking waves. In particular, the focus is on the role that the air plays in wave loads exerted on offshore structures.
In order to make the reader fully understand the study, but in particular the motivation that drove it, a brief overview about the treated topics is given in the following. Firstly, the wave breaking phenomenon, the air entrainment process and the computation of wave loads on offshore structures are described. The current knowledge in these subjects is the result of the intense research carried out during the past years, therefore some relevant numerical and experimental studies are also presented. Secondly, the challenges in numerical simulations of air entrainment in breaking waves are described.

1.1 Background: physical processes

1.1.1 The wave breaking phenomenon

The wave breaking is a natural process during which rough and turbulent undulations arise at the sea surface. This phenomenon is visibly expressed by the sprays and the "white-caps" due to the entrained air.

In general, the breaking wave phenomenon can be described as the transformation of a predominantly laminar flow (the wave propagation) into a turbulent motion. Turbulence causes the simultaneous formation of eddies of many different length scales which through a transfer of turbulent (kinetic) energy occurs. This process is known as *Kolmogorov cascade*. The bigger eddies contain the energy, which is only partially dissipated into heat due to viscosity, because the most part is transferred to smaller scales. This transfer takes place in a range of length scales, called *inertial*, where the inertia effects are dominating and the viscosity does not play a role. The transfer ends when the size of the eddies is small enough that the viscosity becomes important and the energy is totally dissipated into heat. These smaller scales are known as *Kolmogorov microscales*. Therefore, a wave loses energy when breaking.

In shallow water areas, waves undergo shoaling when approaching the coastline. The wave height increases and the celerity decreases. As a result, the wave front becomes unstable and the wave breaking occurs. The region where the wave has broken and the foamy flow has established is called *surf zone*. The overall mechanism of breaking waves in the surf zone, i.e. shoaling, breaking and swashing, was broadly reviewed by Peregrine (1983) and Battjes (1988). The former emphasized the approach to wave breaking and the wave overturning, whereas the latter was more focused on the post-breaking mechanics. Also Christensen et al. (2002) gave a review of the studies about the wave breaking, but more focused on the vertical variation of the flow structures in the surf zone.

Wave breaking plays a role in the near-shore sediment transport which has always been a very relevant topic in the coastal engineering field. A wave can break in different ways on a sloping beach (Fig. 1.1). The breaker types have been classified as (Galvin, 1968):

- *Spilling*: a weak and small jet develops at the wave front, foam appears at the wave crest and then it spreads down along the front of the wave developing into a surface *roller*;

- *Plunging*: the wave front starts turning over and projecting forward as a tongue of water or a jet, which then falls down at the trough in front of the crest, causing a large splash;

- *Collapsing*: the lower portion of the front face collapses and the plunging breaker appears truncated;

- *Surging*: it starts as a plunging breaker at the crest of the wave, but the base of the wave surges up the beach before the crest can plunge forward.

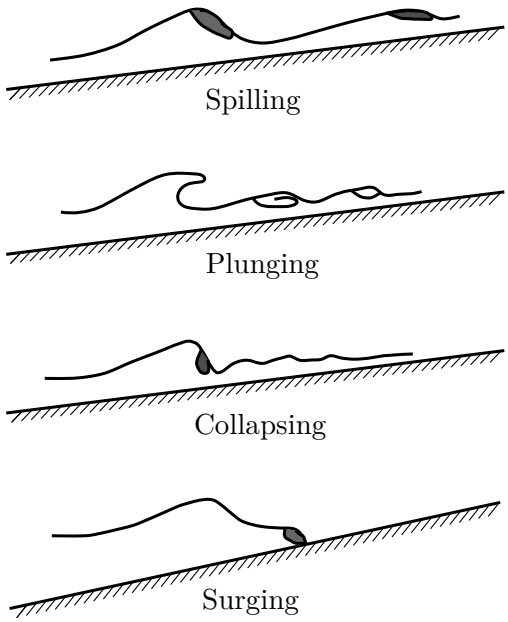

Figure 1.1: Classification of breakers (redrawn from Sorensen (1993)).

Spilling and plunging waves are characterized by different kinematics in the surf zone as shown by Ting and Kirby (1994, 1995, 1996). These authors conducted a valuable experimental investigation on plunging and spilling waves on a sloping beach. It was demonstrated that the vertical mixing of mass and momentum is stronger in plunging waves because it is carried by large-scale vortices generated by the multiple splash-ups of the wave front. In spilling waves, the mixing is instead due to the action of smaller scales originating from the surface roller. The authors reported the vertical variation of undertow and horizontal turbulent velocity, measured at different locations both upstream and downstream the breaking point, which was smaller for plunging waves than for spilling.

The mechanisms taking place after breaking are responsible for the suspension of sediments at the sea bed and their transport in the surf zone. Turbulent flow structures originate at the wave front during the breaking. These flow structures break down and exchange momentum and turbulence with the underlying flow to generate the undertow. Finally, the undertow interacts with the bed, in particular with the wave-current boundary layer. Nadaoka et al. (1988, 1989) used the LDV technique to visualize such turbulent flow structures in spilling breakers. The authors observed two-dimensional horizontal spanwise eddies around the wave crest with axis parallel to the crest line, whereas obliquely descending eddies developed behind the wave crest, in connection with the stretching of the velocity field at a direction of about 45°. Coherent flow structures were observed also by Ting (2006, 2008) in a solitary spilling

wave. A single broken wave allowed to study the evolution of the associated turbulent velocity field separately from the effects of return flow and residual turbulence. The authors found several occurrences of downburst of turbulence descending from above and diverging at the bed in their experiments.

The sediment transport is offshore under spilling waves, but onshore under plunging. This has been demonstrated by the already mentioned experiments of Ting and Kirby (1994, 1995, 1996). The authors used the correlation in a wave period between the measured mean horizontal velocities and the measured mean horizontal turbulent velocities to explain the cross-shore sediment transport in the surf zone. In spilling waves, the velocity field in a wave cycle was shown to be directed offshore predominantly: the seaward-directed velocities are larger and kept for longer time compared to the landward ones. At the same time, the turbulence level was found to be constant, meaning that the turbulence decay was larger than the wave period. Consequently, any sediment in suspension goes in the same direction as the undertow, i.e. in the offshore direction. In plunging waves, the seaward and landward-directed mean velocities had the same magnitude and for a similar period of time. On the other hand, the mean horizontal turbulent velocity was found to be much higher under the phase corresponding to the passage of the wave front. This means that the net transport of sediments has to follow the forward, i.e. onshore, movement of the wave.

Direct measurements of bed shear stress, sediment transport patterns and related bed morphology were provided by Sumer et al. (2011, 2013). In these works, the authors studied the whole plunging breaking process, shoaling, breaking, runup and rundown, in solitary and regular waves respectively.

Beside the intensive experimental research, investigations on breaking waves by the means of numerical models have been conducted. From the numerical point of view, the wave breaking process is very challenging since it is an unsteady non-linear viscous flow with a complex air-water interface and with a wide range of turbulent length scales. Nevertheless, the progress made by applied mathematics and computer architecture has allowed the exploitation of the Computational Fluid Dynamics (CFD) method: the governing Navier-Stokes (N-S) equations are discretized both in space, i.e. the domain where the flow takes place, and in time. This approach is quite powerful, because it can replicate the wave breaking process in detail without many simplifications, assumptions and approximations.

In CFD simulations of breaking waves, it is crucial the way how the turbulent eddies are reproduced, from the larger to the smaller ones. It is remarked that the action of the smaller scales is fundamental since the wave breaking is essentially a dissipative process.

Three approaches are available for handling the wide range of turbulent length

scales: Direct Numerical Simulation (DNS), Large Eddy Simulation (LES) and Reynolds-Averaged Navier-Stokes (RANS). Details are given in Ferziger and Peric (2012). Briefly, the DNS assumes that the spatial discretization, or *grid size*, is fine enough to "capture" all relevant scales. In the LES approach, scales down to the inertial subrange are resolved, whereas smaller scales are modeled. When using the RANS equations, the whole range of turbulent scales is modeled.

Therefore, the DNS approach is the simplest but the heaviest from the computational point of view. In numerical models employing this methodology, the turbulence dissipation is totally due to the *topologically* generated vorticity field as showed in Iafrati et al. (2001), Iafrati (2011) and Lubin et al. (2003). In the first two studies, the steep wave formation, the jet development, the splash-up and the air entrainment were reproduced. In particular, in Iafrati (2011) the attention was focused on the early stage of the breaking, when most of the energy is dissipated.

The LES approach has gained popularity recently since the computational cost, although high, is reduced compared with DNS. Moreover, it is conceptually simpler than RANS because a smaller part of turbulence is modeled. The great advantage of LES simulations, as well as DNS, is the opportunity of obtaining interesting three-dimensional visualizations of the developed coherent flow structures (Christensen and Deigaard, 2001, Watanabe et al., 2005, Christensen, 2006) and of the air intrusion (Lubin et al., 2006).

Numerical studies based on the RANS approach cannot provide such accurate three-dimensional information because of the inner derivation of the turbulence model. Nevertheless, Lin and Liu (1998a,b), Bradford (2000), Jacobsen et al. (2012) and Brown et al. (2016) reported numerical results for undertow and turbulence level profiles in good agreement with the experiments in Ting and Kirby (1994, 1995, 1996).

In intermediate or deep water regions, hereafter just deep water, wave breaking is not due to the variation in bed topography, rather it is the result of wave-wave, wave-current or wind-wave interactions. Also ships can make waves break when they move.

In deep water, breakers are classified as in shallow water. Waves break more often as spilling. The breaking-induced turbulent mixing enhances the exchange of heat, mass and momentum between the atmosphere and the oceans in deep water. The transfer of mass, i.e. the entrainment of air bubbles, is important for aquatic life at small scales, but it also produces scatter underwater sound and scavenge biological surfactants (Peregrine, 1983, Melville, 1996). The transfer of momentum can generate ocean currents as clearly illustrated by Rapp and Melville (1990). They used the dispersive focusing technique to generate isolated breaking wave events, both spilling and plunging. By using measurements of surface elevation and velocity in the breaking region, the authors computed the space and time integrated flux and density term

of the momentum equation. Values upstream and downstream the breaking region showed a reduction of the flux of 10% and 25% in the spilling and in the plunging case respectively. Looking at the corresponding increase in the density, they demonstrated that a fraction of the flux loss, 85% for the spilling and 60% for the plunging, was transferred into a current in the underlying water.

Experiments on deep water waves have been carried out mainly for gaining knowledge about the complicated energy budget taking place during the breaking. As already stressed, wave breaking is a turbulent, hence dissipative, process. In the already mention study of Rapp and Melville (1990), the authors tried to quantify the energy loss. By the same procedure adopted for computing the terms of the momentum equation, it was assessed that up to 40% of the total prebreaking wave energy was lost through breaking in the first four wave periods. From this time on, the decay of energy followed the inverse respect to the time ($E \propto 1/t$). After the first four wave periods, only a small fraction of the energy (2-4%) remained in the breaking region which was related to the post-breaking current.

The energy lost by a wave after breaking is not simply dissipated by the viscous scales generated by turbulence. Another factor is the energy required for the air entrainment, that is the work needed to keep the bubbles entrained against the buoyancy force. This amount of work is first transferred to bubbles as potential energy and then partially "returned" by bubbles which generate small-scale turbulence while rising. Some attempts have been made for calculating the contribution of the air entrainment to the total dissipation: Lamarre and Melville (1991) estimated up to 50%, Blenkinsopp and Chaplin (2011) up to 9% and Lim et al. (2015) 2015 up to 18%.

1.1.2 The air entrainment in breaking waves

The role of the entrained air is crucial for all mentioned processes connected to breaking. Nevertheless, the understanding of the phenomenon has been difficult because of the lack of proper laboratory instrumentation for precise measurements of air content and the high demand of computational resources for numerical simulations of air intrusion. In general, the knowledge in this topic is higher for breaking in deep water compared to shallow water depth.

Spilling and plunging breaking waves present different mechanisms driving the air entrainment (Peregrine, 1983, Battjes, 1988, Deane and Stokes, 2002, Rojas and Loewen, 2010, Kiger and Duncan, 2012).

Following Fig. 1.2 from Lim et al. (2015), the plunging breaker is discussed as follows. The wave front overturns and projects forward as a jet which falls down into the undisturbed front face of the wave (*a*). This is the main source of air entrainment,

because a tube of air (cavity) results to be entrapped beneath the jet which in turn drags some air into water. Because of the inner high pressure, the air cavity collapses into smaller bubbles. The impact of the jet induces a clockwise circulation zone and at the same time it produces a reactionary splash-up which in turn generates another clockwise vortex (*b*). The simultaneous clockwise rotation of these two coherent structures forms a shear layer which leads to further fragmentation of the bubbles coming from the collapse of the cavity. Between the backside of the splash and the upper surface of the plunging jet, a counterclockwise roller causes more air entrainment (*c*, *d*). The described occurrences produce the *primary* plume. A *secondary* plume is created in a similar manner by the mentioned splash-up which acts as the initial jet (*e*-*h*). This cycle might occur several times and other plumes might be produced. During the late stages of the breaking, a bore-like region establishes and the air entrainment occurs at its leading edge (*i*). At the same time, the first plumes outgas (*j*).

A spilling breaker is depicted in Fig. 1.2 (from Rojas and Loewen (2010)). The process starts by the appearance of a rough surface (*a*), hence the jet formation seen for the plunging case does not take place. The air entrainment mechanism is similar to what happens in the bore at the final stages of a plunging breaker. In fact, air is entrained at the leading edge of a turbulent region developing at the wave crest where the water spills down continuously (the roller, *b*). As a result, a single bubble plume grows beneath the breaker (*c*).

Entrainment and evolution of air bubbles in deep water breaking waves were described in Deane and Stokes (2002). In this work, photographic studies and measurements of the air entrainment mechanism under laboratory plunging breaking waves and in the open ocean were conducted. Although waves were plunging breakers in the laboratory, but spilling in the field, the authors recognised some similarities which allowed to draw some general conclusions about the physical process.

The life of the entrained air plume was divided into two main phases:

- the *acoustic* phase when bubbles were formed;
- the *quiescent* phase which started when active bubble formation ceased and ended when all bubbles degassed.

The attributes acoustic and quiescent come from the fact that only new created bubbles emit underwater noise. The bubble size spectrum distribution measured *at the end* of the acoustic phase is reported in Fig. 1.4. The mechanisms recognised to determine such distribution were the jet/wave-face interaction and the turbulent fragmentation of the air cavity. The former produced bubbles with radius r_b in the range $0.1 \leq r_b \leq 2$ mm and density (of distribution) proportional to the radius to the power of $\alpha = -3/2$. The latter originated bubble with radius in the range $2 \leq r_b \leq 10$

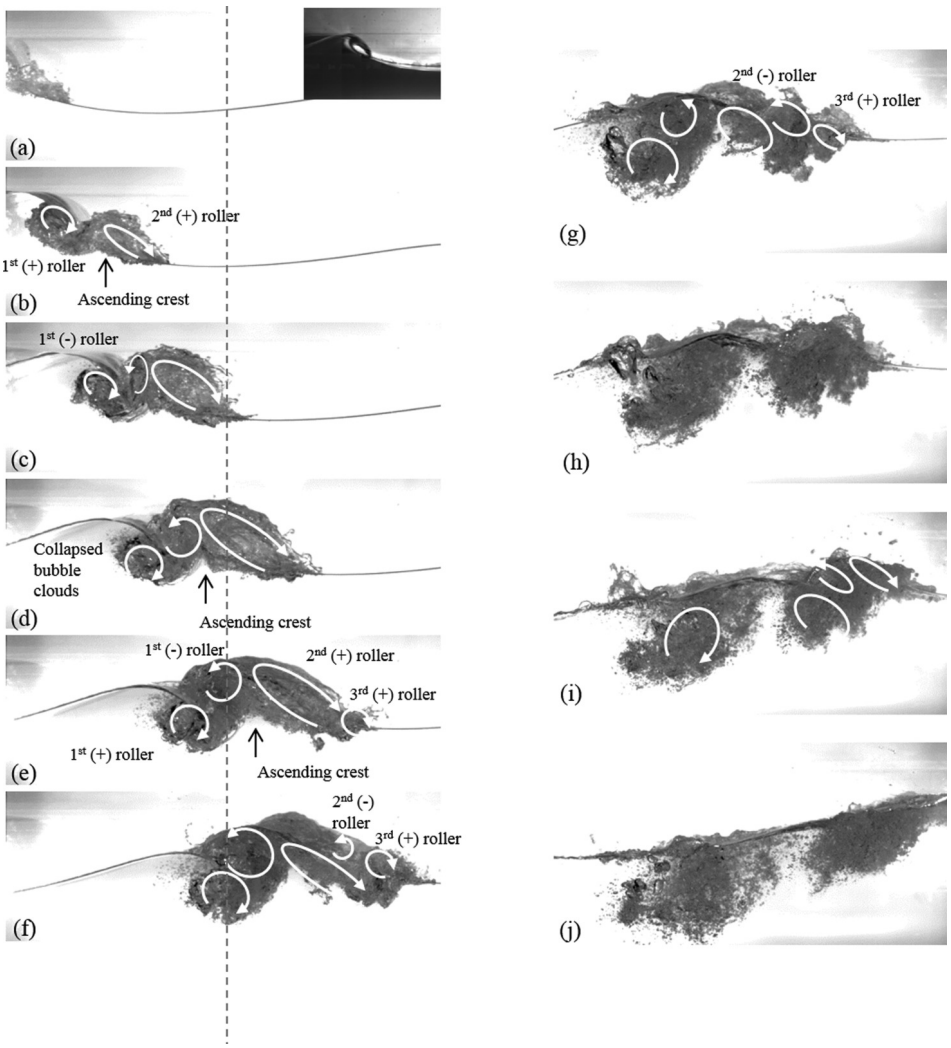

Figure 1.2: Plunging breaking process based on high-speed video images from Lim et al. (2015).

mm and density following a $\beta = -3/2$ power-law scaling. A remarkable change in slope was observed at $r_b = 1$ mm. This radius was identified as the *Hinze* scale. The evolution of the plume during the quiescent phase was found to be rapid as showed in the inset of Fig. 1.4 which depicts the distribution measured at the beginning of this phase and 1.5 s later. It was observed that both slopes increased with time because of buoyant degassing, turbulent diffusion, advection and dissolution.

The characteristics of the breaking-induced bubble plume can be analyzed through direct measurements of void fraction in laboratory waves as done in Lamarre and Melville (1991). In this fundamental study, three breakers with different energy content (two plunging and one spilling-plunging) were generated in a flat bottom flume by the dispersive focusing technique. Conductivity probes were installed in the breaking

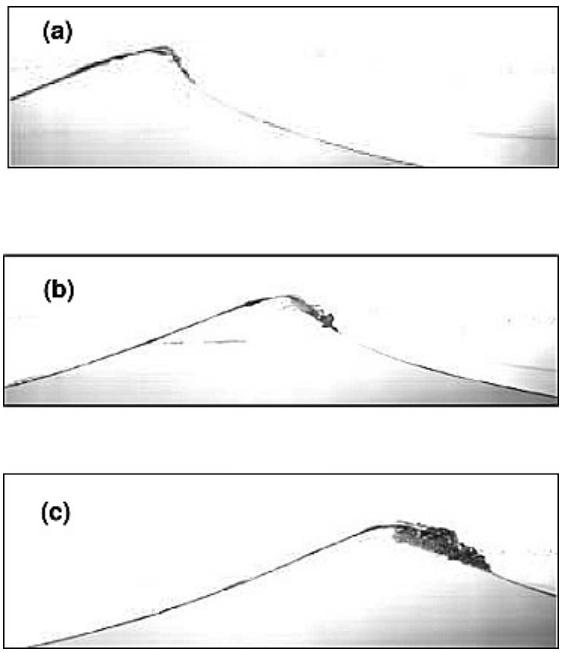

Figure 1.3: Spilling breaking process based on high-speed video images from Rojas and Loewen (2010).

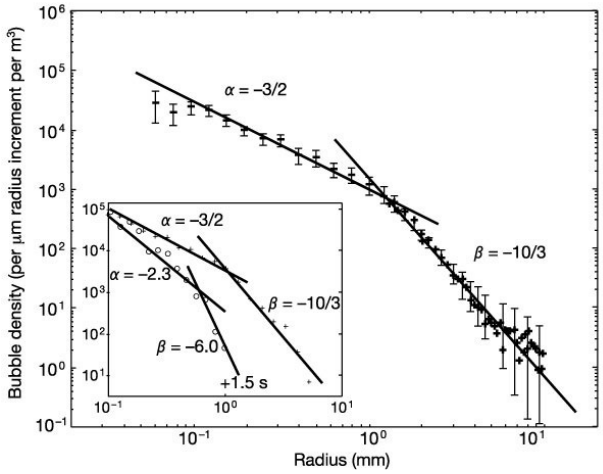

Figure 1.4: Average bubble size spectrum at the end of the acoustic phase. The vertical scale is number of bubbles per m^3 in a bin radius 1 μm wide. Inset: the bubble size distribution at the beginning of the quiescent phase (crosses) and 1.5 s into the quiescent phase (open circles). From Deane and Stokes (2002).

region in order to map the evolution with the time of the void fraction in the bubble plume. Values were found in the range 0-100% where full air was achieved both in the air cavity at the beginning of the plunging breaker and at the edge between the plume and the atmosphere. From measured maps, the authors calculated the volume per unit length of wave crest, cross-sectional area and mean void fraction (ratio of volume

to area). It was found that these integral properties evolved as a simple function of time regardless the kind of breaker. As an example, the volume rose rapidly at the beginning of the breaking, reaching the peak value around the first quarter of the wave period and then it decayed exponentially with less than 5% of the peak value remaining after one period. The mean void fraction followed $-2/3$ power-law decay. More details of this study will be given in Section 5.1. Similar findings were in Lamarre and Melville (1994) for 3D waves in a flat bottom basin and in Blenkinsopp and Chaplin (2011) who used phase detection optical probes in waves breaking in deep water after propagating over a shoal. Rojas and Loewen (2010), who provided void fraction measurements for almost the identical waves used in Lamarre and Melville (1991), observed that the spilling entrained as much air as the more energetic plunging.

The kinematics of the entrained bubble plume has been investigated by tracking in time the centroid of the void fraction distribution. Given the wave celerity C_w at the breaking location, Lamarre and Melville (1991) and Rojas and Loewen (2010) assessed that the speed of the primary plume of a plunging wave was $0.7C_w$, whereas the speed of the last plume, behind the bore, was C_w. The plume of the spilling wave, since it resembled the bore of the plunging wave, was observed to propagate with a speed of C_w as well.

In the deep water plunging breaker experimented by Lim et al. (2015), seen in Fig. 1.2, the maximum horizontal velocity during the breaking was $1.4C_w$ before the jet formation (at the vertical front), then it became $1.68C_w$ at the downward jet before the first impingement and it further increased to $2.14C_w$ at the beginning of the first splash-up.

The evolution of the entrained bubble plume in a surf zone has been less investigated. In this regard, Cox and Shin (2003) gave some insights. A spilling, a spilling-plunging and a plunging wave were generated on a flume with sloped bottom. Void fraction and horizontal velocities were measured simultaneously at different elevations at three sections in the surf zone. Peak ensemble-averaged void fractions were found in the range 15-20%. The spilling breaker showed larger values of time-averaged void fraction and turbulence intensity but in general a positive correlation between these two quantities was recognised for all breakers. Moreover, the time-averaged void fraction followed an exponential decay in each case. A broader experimental investigation was carried out by Kimmoun and Branger (2007). The authors measured dynamics and kinematics of spilling-plunging waves propagating and breaking over a $1/15$ sloping beach. In particular, they computed the complete space-time evolution of the velocity field over the whole surf zone and an exponential decay of the air content below the mean sea level was observed.
Numerical simulations of air entrainment in breaking waves by CFD models are very

demanding because the phenomenon requires extremely high space-time resolution to reconstruct the chaotic air-water interface, especially at the scales of bubble formation.

The first attempts to reproduce the breaking-induced bubbly flow by CFD models were made for predicting the distribution of bubbles around naval surface ships. The presence of bubbles can modify the total resistance and the propeller efficiency (Carrica et al., 1998, 1999, Moraga et al., 2008).

The crucial aspect in CFD models suitable for this purpose is the reproduction of the bubble injection in water rather than the plume evolution. Recently, this issue has been treated by adopting sub-grid formulations. The term "sub-grid" indicates that these formulations are designed to work in domains which are not sufficiently discretised to capture the details of the bubble formation. Therefore, the air entrainment is modeled and not resolved. Numerical models of Shi et al. (2010), Ma et al. (2011) and Derakhti and Kirby (2014) successfully adopted a sub-grid formulation for reproducing the air entrainment in deep and shallow water breaking waves.

Shi et al. (2010) simulated the quiescent phase of the plume induced by the laboratory breaking waves generated in Rapp and Melville (1990) and Lamarre and Melville (1991). The flume was discretized by a 2D grid, hence the spanwise direction was neglected. The RANS approach was employed for handling the turbulence. The sub-grid formulation for the air entrainment was built in such a way that bubbles were fed into water when the shear production at the free surface was larger than a fixed threshold. The number of injected bubbles was forced to follow the distribution given in Deane and Stokes (2002) (at the end of the acoustic phase). The velocities of bubbles were assumed to depend on their radius. The model was reasonably capable of reproducing the moments of the void fraction field defined by Lamarre and Melville (1991).

Ma et al. (2011) investigated the entrained bubble plume induced by regular waves breaking on a sloping beach. The spilling breaker in Cox and Shin (2003) was used to validate the solution. A 2D spatial discretization and the RANS approach were employed. The air entrainment was connected to the dissipation rate of the turbulent kinetic energy at the free surface, i.e. bubbles were not injected if the dissipation rate was smaller then a critical value (to be calibrated by the user). The model fairly captured the void fraction distributions observed in the experiments at three different sections in the surf zone. The plume roughly moved at the phase speed of the wave at the early stages of breaking, whereas it slightly decelerated later. The exponential decay of the total volume of entrained air was reproduced.

Derakhti and Kirby (2014) examined in depth the interaction between water and entrained bubble plume. The authors simulated some plunging and spilling waves of Rapp and Melville (1990), Lamarre and Melville (1991) and Rojas and Loewen (2010).

A 3D spatial discretization and the LES approach were employed. The air entrainment was modeled similarly to Ma et al. (2011). The model was found to predict the void fraction and the integral properties of the plume fairly accurately. The effect of bubbles on turbulence was analysed by looking at the production and dissipation term of the resolved turbulent kinetic energy (TKE) transport equation. Numerical simulations with and without inclusion of bubble motion showed that production and dissipation were reduced and enhanced respectively in the first case. As a result, it was found that bubbles damped the TKE by 20% and 50% in the plunging and in the spilling breaking wave respectively. Moreover, it was assessed that the dissipation induced by bubbles is a fraction of more than 50% of the total dissipation.

1.1.3 Wave loads on offshore structures

In intermediate or deep water depth, wave loads depend on the sea state at the location of the structure which is usually described in terms of a wave spectrum. The sea state consists of waves with different amplitudes, lengths and periods. In particular, the ratio of amplitude and length defines the steepness of a wave. Waves with very high steepness might undergo breaking, as example under storm conditions.

Waves with small/limited steepness exert on structures the *fatigue* loads. In cases when the steepness is large but not much to induce natural breaking, waves might break as a result of the impact. This occurrence generally produces larger forces but large run-ups especially.

Waves with very high steepness breaking directly on structures exert the largest loads which are referred to as *extreme*.

The fatigue loads are important for the safety and the practicability of a structure, whereas the extreme forces determine the design of the stability. For this reason, the understanding of the physics of impact due to collision of breaking waves has been very important.

The characteristics of the impact pressure, hence forces, depend closely on the relative distance between the structure and the breaking point, since the kinematics and the shape of the breaker change throughout the breaking region. This has been clearly showed by Hattori et al. (1994). Simultaneous measurements of the impact pressure on a vertical wall and plunging breaking waves revealed that the most violent impact occurred before the jet formation, when waves approached the structure with almost vertical front. Moreover, the authors observed that the air trapped between the wall and the wave front played a predominant role. When the wave front at the impact was vertical, just a small amount of air bubbles was entrapped: here the peak pressure was maximum. Conversely, when the plunging was more developed, a larger amount of air was entrapped in form of a cavity beneath the jet and the peak pressure was lower.

Essentially, some energy was spent during the fragmentation of the air cavity.

A strong sensitivity of maximum impact pressures on vertical walls to wave conditions was also highlighted by the numerical study of Bredmose et al. (2009). The authors simulated aerated violent impacts by the means of an incompressible potential-flow model coupled with a compressible treatment of the entrapped air.

Many offshore and harbour constructions are considered as cylindrical piles or composed of cylindrical members. For this reason, the rest of this section is about loads on vertical surface piercing slender cylinders. *Slender* means that the dimension (the diameter) of the cylinder is such that the incident wave field is not affected by the presence of the structure, hence the diffraction phenomenon does not take place or it is negligible.

Breaking wave-induced loads on cylinders have characteristics not much different to those on vertical flat walls. As example, Chan et al. (1995) observed in their experiments similar peak levels, post-peak oscillations and spatial and temporal distributions, for the impact pressure. Wienke and Oumeraci (2005) confirmed that the force induced by a plunging wave strongly depends on the distance between breaking location and cylinder. In their experimental investigations, the maximum force was exerted when the wave broke right in front of the cylinder and the velocity of the water mass hitting the cylinder reached the value of the wave celerity at the breaking point. Moreover, the force was shown to be proportional to the so-called "curling factor" (Goda et al., 1966), which depends on the inclination of both the cylinder and the breaker front.

The need of understanding the physics behind wave impacts on slender cylinders has been important as much as the elaboration of efficient, effective and reliable methods for calculating the induced loads. Scale model tests in laboratory are expensive and often carried out under idealized conditions. Instead, numerical models are cheaper, hence more desirable.

The force on a circular cylinder in a wave field is the result of the interaction with the flow around it. The resultant force is due to the action of pressure and friction (Fig. 1.5).

The total force F is given by (Sumer and Fredsøe, 1997):

$$\mathbf{F}(t) = \int_{-d}^{\eta(t)} \left[\int_0^{2\pi} p(z,t) \cos(\phi) \frac{D}{2} \, \mathrm{d}\phi + \int_0^{2\pi} \tau_0(z,t) \sin(\phi) \frac{D}{2} \, \mathrm{d}\phi \right] \mathrm{d}z \tag{1.1}$$

where:

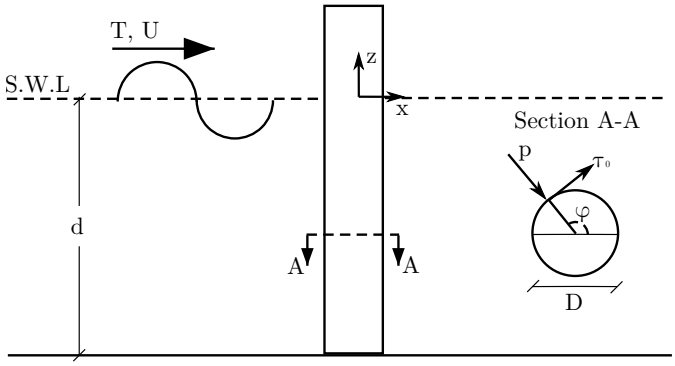

Figure 1.5: Sketch for the calculation of the total force on a cylinder in a wave field.

- t is the time;
- d is the water depth at the location of the structure;
- η is the surface elevation; ;
- p is the *static* pressure ;
- τ_0 is the viscous friction ;
- D is the diameter of the cylinder.

In practical cases, the contribution of the friction can be often neglected, being a small fraction of the total force (2-3%). The magnitude and the direction of the force are essentially the result of the pressure distribution around the cylinder. Therefore, if pressure is known, the calculation of the force is quite straightforward.

The CFD approach can be used for computing wave loads. In fact, the distribution of pressure p in the whole domain is among the outputs produced by such models. Several studies report applications of CFD models for wave loads on circular cylinders. Among the others are: Bredmose and Jacobsen (2010) and Paulsen et al. (2014b).

Nevertheless, the demand of computational time for CFD simulations of free surface flows, as waves are, is very high. On top of it, applications of this method for practical designs imply large domains wherein irregular waves propagate and hit the cylinder. In order to reduce this computational expensiveness, a CFD model can be combined with a simpler and faster solver for the wave field away from the structure. In this way, the CFD approach is applied on a smaller portion of the domain comprising the cylinder. Examples can be found in Christensen et al. (2009) and Paulsen et al. (2014a).

Among the numerical methods for wave loads (on slender cylinders), the most used

has been the application of the *Morison equation* (Morison et al., 1950):

$$F(t) = \int_{-d}^{\eta(t)} [F_D(z,t) + F_M(z,t)]\,\mathrm{d}z = \int_{-d}^{\eta(t)} \left[\frac{1}{2}\rho_\mathrm{w} C_D D u_{\mathrm{w},x}(z,t)|u_{\mathrm{w},x}(z,t)| + \rho_\mathrm{w} C_M A \dot{u}_{\mathrm{w},x}(z,t)\right]\mathrm{d}z \tag{1.2}$$

where

- ρ_w is the density of water;
- $u_{\mathrm{w},x}$ is the water horizontal velocity at the location of the cylinder;
- $\dot{u}_{\mathrm{w},x}$ is the water horizontal acceleration at the location of the cylinder;
- A is the cross sectional area of the cylinder;
- C_D and C_M are empirical coefficients.

The Morison equation gives the *in-line* component of the total force, where in-line indicates the alignment with the direction of the flow. This total force is expressed as a linear superposition of two contributions: *drag* F_D and *inertia* F_M. The former accounts for pressure exerted by the flow as it was steady. The latter expresses the extra pressure gradient due to acceleration of the flow in the immediate surroundings of the cylinder and in the outer-flow region. The relation between pressure and wave kinematics (U and $\dot{U}$) is expressed through the empirical coefficients C_D and C_M, called drag and inertia coefficient respectively.

The application of the Morison equation requires the wave kinematics and the surface elevation at the location of the cylinder. These are generally calculated by assuming that the fluid is inviscid and the flow is irrotational and incompressible. In this way, weakly or fully nonlinear potential flow solvers, which are computationally cheap, can be employed. An even more simplified methodology consists in decomposing a wave spectrum, describing the local sea state, in an enough number of components whose motion is singularly given by the linear wave theory. Surface elevation, velocity and acceleration at a given time and depth can be found by superposing the (linear) expressions of all components. This is often combined with the Wheeler stretching (Wheeler et al., 1969) that addresses the over-prediction of the linear velocity field above still water. However, incident waves are often steep and the linear assumption might lead to a high degree of inaccuracy.

Coefficients C_D and C_M are function of velocity, fluid density and diameter of the cylinder. Several laboratory experiments, where forces on circular cylinders with

different diameters and subjected to different wave fields were measured, have allowed to incorporate these dependencies into only two non-dimensional quantities:

- The Reynolds number $Re = \frac{U_m D}{\nu^r}$, where U_m the maximum horizontal velocity and ν is the kinematic viscosity of the fluid;
- The Keulegan-Carpenter number $KC = \frac{U_m T}{D}$, being T the wave period.

As is known, Re expresses the ratio of inertial to viscous forces. The KC number is the ratio of the stroke of the oscillatory wave motion around the cylinder to the diameter of the cylinder. Small values of KC indicates that the orbital motion of water particles is smaller than the diameter of the cylinder therefore separation does not occur or it occurs with formation of symmetric vortices. High values mean *vortex shedding* regime. Sumer and Fredsøe (1997) defined the range $0 < KC \ll 20-30$ as the *inertia-dominated* regime ($F_M \gg F_D$), whereas $KC > 20-30$ as *drag-dominated* regime ($F_D \gg F_M$).

It is worth to remark that the Morison equation cannot be accurate for breaking wave-induced loads. First of all, coefficients C_D and C_M have been derived for non-breaking waves. Moreover, the use of the Morison equation is often combined, as already said, with kinematics derived from potential flow solvers which do not admit reentry of water. Another reason is that velocities in the breaker are such that vortex shedding might take place, in contradiction with the hypothesis of irrotational flow. Therefore, CFD is a numerical approach suitable for calculating loads induced by breaking waves.

1.2 Background: challenges in numerical simulations of wave breaking

Numerical analyses of the wave breaking phenomenon pose arduous problems which are connected to three factors:

- it is a *two-phase* flow;
- it is a flow with a wide range of *turbulent* length and time scales;
- it is a flow with a wide range of *interfacial* length scales.

These factors are now considered individually because each of them is challenging in itself, but it should be reminded that they play at the same time.

It is a two-phase flow
A wave is a mass of water moving in a domain in a certain time interval. If the motion of the *free surface* is of interest, then it is a two-phase flow because two fluids interact: water and air. The motion of water depends on air and vice versa. This does not automatically mean that a model for two-phase flow is the only choice for wave simulations. Models in which the effect of air has been "replaced" with moving boundary conditions at the free surface have been elaborated and employed successfully ((Christensen, 2006, Derakhti and Kirby, 2014).

It is a flow with a wide range of turbulent length and time scales
At the beginning of the wave breaking, the turbulence cascade is activated. Different eddies, characterized by a wide range of length (l_{ed}) and time (t) scales, are generated. An estimation of this range can be achieved by considering a laboratory breaking wave and assuming isotropic and homogeneous turbulence: $\mathcal{O}(10^{-5}) < l_{ed}(t) < \mathcal{O}(10^{1})$ m(s). The smallest scales, i.e. Kolmogorov scales, might be even smaller during active breaking.

It is a flow with a wide range of interfacial length scales
The fact that the flow involves two fluids implies that one or more interfaces occur in between. The issue lies in the different interfacial morphologies establishing during the *complete* wave breaking process. When waves propagate, *only one* interface exists *up to* the breking point, i.e. the free surface. At the breaking point, bubbles entrain and thousands of interfaces occur in water. At the same time, the free surface is "destroyed" at early stages of breaking, but it recovers the regular shape during the evolution (the degassing) of the bubble plume. The interfacial length scale range in laboratory breaking waves can be approximated as $\mathcal{O}(10^{-4}) < l_I < \mathcal{O}(10^{1})$ m), where the lower limit is given by the bubble size distribution of Deane and Stokes (2002).

The main problem is therefore the broad range of time and length scales involved. Resolving this range requires a temporal and a spatial discretization that would increase the computational cost tremendously (DNS). For this reason, averaging procedures are generally applied. The turbulence-induced scales are handled with a turbulence model, which is *de facto* an averaging procedure.

The different interfacial scale lengths can be also treated with averaging procedures. The CFD methodologies for a generic two-phase flow depend on the expected interface morphology. In case of simulations of breaking waves, it can be asserted that:

- during wave propagation, the interface between air and water is the free surface

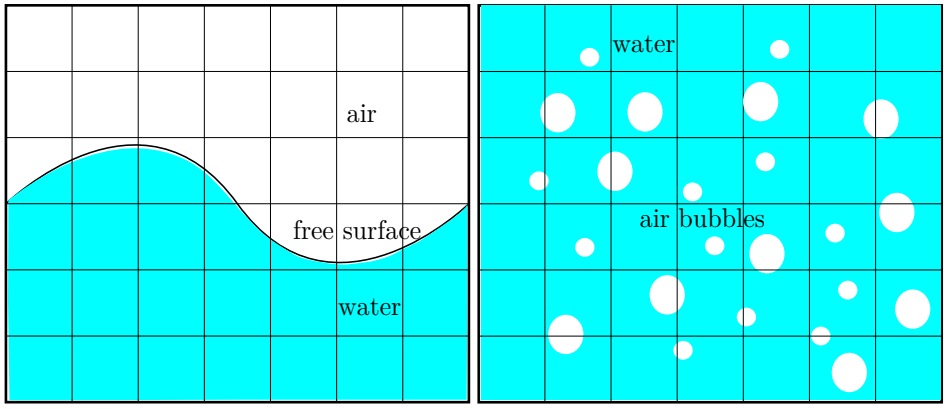

(a) Segregated up to the breaking point. **(b)** Dispersed in the breaking region.

Figure 1.6: Interfacial morphologies between air and water during the breaking process.

which is unique, well-defined and with length larger than the grid size (Fig. 1.6a). Methodologies for *segregated* flows are suitable for this kind of motion;

- during wave breaking, entrained air undergo dispersion into water. Bubbles have size generally smaller than the grid size (Fig. 1.6b) and solvers for *dispersed* flows should be employed for their motion.

Methodologies for segregated flows are reviewed in Ubbink (1997). Surface *fitting* and surface *capturing* methodologies are recognized. Among the latter, generally preferred for their robustness, the most widely used approach is the *volume fractions* in which phases on either side of the interface are marked with a scalar indicator function. In a computational cell, this scalar is between 0 and 1: either 0 or 1 indicates the presence of only one phase, whereas values in between reveal the location of the interface. The indicator function is moved throughout the domain by a convective transport equation.

The well-known Volume of Fluid (VOF) of Hirt and Nichols (1981) is a volume fractions method with a donor-acceptor formulation as a differencing scheme for the convection of the scalar indicator. This method has been so broadly employed that the acronym VOF generally indicates a method based on the volume fractions approach. This holds also in the present work.

Methodologies for dispersed flows are distinguished in Balachandar and Eaton (2010) as:

- *Dusty gas.* The dispersed particles follow the continuous phase, i.e. have the same velocity. The motion of bubbles reduces to a concentration equation;

- *Equilibrium Eulerian.* Particles have velocity different than the continuous phase, but function of the local surrounding fluid;
- *Euler-Euler.* Mass and momentum conservation equation are solved for both phases;
- *Lagrangian Point-Particle Approach.* Position, mass and momentum of all particles are tracked within a Lagrangian framework.

The present work focused on the VOF and the Euler-Euler approach. The VOF has been chosen because it can handle the folding or the rupturing of the free surface typical of wave breaking. The reasons behind the choice of the Euler-Euler method will be given in Section 3.3.2.

1.3 Motivation

The need of exploiting new energy sources, both renewable and non-renewable, will lead to the development of a large number of offshore structures in the near future.

Many of these new expected constructions will be installed in intermediate water depth regions. For instance, several Offshore Wind Farms are under development on 20-40 m water depth in the North-Sea between UK, the Netherlands, Germany and Denmark. In such areas, waves can break under storm conditions and, likely, as a spilling. The induced air entrainment is known to affect the dynamics of the breaker. Therefore, the impact of breaking waves changes compared to non-breaking and the design of these new structures has to account also for breaking wave-induced loads.

A spilling wave is not characterized by entrapment of an air pocket, rather by a mixture of entrained air bubbles and water, the roller, traveling with the wave front with approximately the wave celerity. The impact of a spilling wave on a structure is then supposed to be less violent than a plunging breaker. Therefore, spilling waves are not supposed to undermine the overall stability of an offshore structure, but it has been experienced that they can still cause severe damages. As example, external access platforms, boat-landings and railings of offshore wind turbines have been often corrupted by spilling breakers associated with large run-ups (Fig. 1.7). Nevertheless, the effects of the roller on the structural elements are still not well-known.

In order to gain more knowledge on the role of the air, the present work aimed to develop a numerical methodology for simulating waves that could account also for the entrainment process.

1.4 Thesis outline

The remainder of this thesis comprises the derivation, the validation and the application of the numerical methodology as follows:

Figure 1.7: Severe impact of the roller on an offshore wind turbine. From Nielsen et al. (2008).

- *Chapter 2* introduces the equations governing the motion of a generic two-phase system. From this set of equations, the Euler-Euler and the VOF model are derived highlighting an inner relation between these two approaches;
- *Chapter 3* explains how the relation between the Euler-Euler and the VOF method can be exploited in order to build a unique mathematical model. Needed closure terms are treated, with particular attention to the formulation adopted for the air entrainment. The implementation of the model within a CFD framework is described;
- *Chapter 4* illustrates the employment of the methodology for the analysis of two experimental case studies which were used for a preliminary validation of the numerical results. The first case is the flow in a bubble column. The second one is the propagation and the breaking of regular waves on a sloping beach. In both cases, the air entrainment phenomenon was not taken into account;
- *Chapter 5* completes the validation through other two experimental case studies which involved the simulation of the air entrainment. The first one is the breaking process of a spilling wave. The second one is the breaking-induced bubbly flow established in the surf zone of the regular spilling waves studied in Chapter 2;
- *Chapter 6* reports the numerical investigation conducted on the impact of a laboratory spilling wave against a vertical circular cylinder. The analysis is supported by measurements taken in an experiment carried out at the Technical University of Denmark. The role of the roller on the exerted force is examined;
- *Chapter 7* summarises the thesis and offers some conclusions and suggestions for future research.

2 Mathematical models for two-phase flows

Mathematical models for two-phase flows depend on the morphology of the interface between fluids. Two different morphologies are distinguished:

- segregated when the fluids are not mixed and a single well-defined interface occurs;
- dispersed when a fluid is dispersed into the other.

A breaking wave is a water-air flow where both morphologies manifest. The propagation of the wave is a segregated flow which becomes *locally* dispersed when wave breaking occurs and which regains the segregated status during the evolution of the bubble plume.
In this work, the VOF model was chosen for simulating the wave propagation, whereas the dispersion of entrained air bubbles was handled by the Euler-Euler approach. The governing equations of these two models seem different, but next section will show that *the VOF method can be derived as a simplification of the Euler-Euler approach.*

This derivation is shown because the numerical methodology developed in the present work is based on the *coupling* between the VOF and the Euler-Euler model. As it will be detailed in Chapter 3, the fact the former can be derived from the latter provided a solid ground for making the coupling realizable.

The equations governing the motion of a generic two-phase system are first introduced (*instantaneous conservation equations*). Then the Euler-Euler framework is presented (*conditional volume-averaged conservation equations*). Finally, the VOF model is derived. The exposition follows the work of Marschall et al. (2011) wherein the complete and rigorous procedure can be found. Also the work of Márquez Damián (2013) can be consulted for this subject.

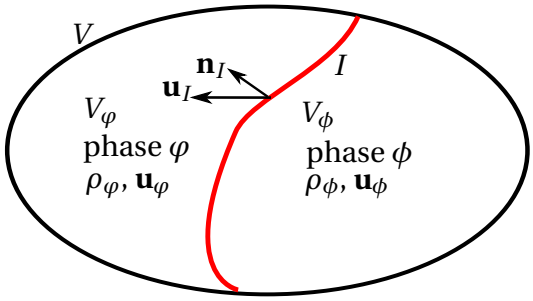

Figure 2.1: Control volume for the derivation of the instantaneous conservation equations (redrawn from Marschall et al. (2011)).

2.1 Instantaneous conservation equations

The control volume V depicted in Fig. 2.1 contains two phases, φ and ϕ, which are assumed *Newtonian* and *incompressible*. Nevertheless, the density ρ is kept in the following equations for convenience.
The volume has an arbitrary shape and it is spatially fixed within an Eulerian framework. The phases occupy portions V_φ and V_ϕ of the total volume which are separated by the interface I. In each portion, it is possible to formulate the instantaneous conservation equations for mass and momentum of the corresponding phase. As for the rest of the chapter, only equations for phase φ are reported:

$$\frac{\partial \rho_\varphi}{\partial t} + \nabla \cdot \left(\rho_\varphi \mathbf{u}_\varphi\right) = 0 \tag{2.1}$$

$$\frac{\partial \rho_\varphi \mathbf{u}_\varphi}{\partial t} + \nabla \cdot \left(\rho_\varphi \mathbf{u}_\varphi \otimes \mathbf{u}_\varphi\right) = -\nabla p_\varphi + \nabla \cdot \boldsymbol{\tau}_\varphi + \rho_\varphi \mathbf{g} \tag{2.2}$$

where:

- $\mathbf{u}_\varphi$ is the velocity;
- p_φ is the pressure;
- ρ_φ is the density;
- $\mathbf{g}$ is the gravity acceleration;
- t is the time.

The viscous stress tensor $\boldsymbol{\tau}_\varphi$ is expressed for a Newtonian fluid as a function of the deviatoric part $\boldsymbol{D}_\varphi$ of the rate-of-strain tensor $\mathbf{S}_\varphi = \frac{1}{2}\left[\nabla \otimes \mathbf{u}_\varphi + (\nabla \otimes \mathbf{u}_\varphi)^T\right]$ through the viscosity μ_φ:

$$\boldsymbol{\tau}_\varphi = 2\mu_\varphi \boldsymbol{D}_\varphi = 2\mu_\varphi \left[\mathbf{S}_\varphi - \frac{1}{3}\left(\nabla \cdot \mathbf{u}_\varphi\right)\mathbf{I}\right] \tag{2.3}$$

The system of equations is closed by discontinuity conditions at the interface I for both mass and momentum:

$$\rho_\varphi(\mathbf{u}_\varphi - \mathbf{u}_I)\cdot\mathbf{n}_I = \rho_\phi(\mathbf{u}_\phi - \mathbf{u}_I)\cdot\mathbf{n}_I \tag{2.4}$$

$$(p_\varphi\mathbf{n}_I + \boldsymbol{\tau}_\varphi\cdot\mathbf{n}_I) = (p_\phi\mathbf{n}_I + \boldsymbol{\tau}_\phi\cdot\mathbf{n}_I) + \sigma\kappa\mathbf{n}_I \tag{2.5}$$

where $\mathbf{u}_I$ is the interfacial velocity, $\mathbf{n}_I$ is the interface unit normal vector and κ is the interface curvature. In Eq. 2.4 it is assumed that interfacial mass transfer do not take place. In a water-air system, this means that there is not any condensation or evaporation.

2.2 Conditional volume-averaged conservation equations

The mathematical model represented by Eqs. 2.1-2.5 is made more suitable for building up a CFD solver by the following successive operations:

- the equations are made conditional on the presence of a particular phase by multiplying all terms by the indicator function f^{ind} defined as:

$$f_\varphi^{ind}(\mathbf{x},t) = \begin{cases} 1 & \text{if } \mathbf{x}=(x,y,z)\in\varphi \text{ at time } t, \\ 0 & \text{otherwise} \end{cases} \tag{2.6}$$

  Now the mathematical model can be applied on the whole volume V and not just on V_φ (or V_ϕ);

- the equations are volume-averaged. The solution of the instantaneous equations 2.1-2.5 would be a DNS approach where *all* interfacial scales are assumed to be reproduced. This would require a spatial discretization prohibitive in most practical cases.

Considering either mass or momentum of a biphasic system as a generic quantity $\boldsymbol{\Phi}$ being transported within a spatio-temporal domain (this is what conservation equations essentially are), the application of the two operations above yields:

$$\overline{f_\varphi^{ind}\boldsymbol{\Phi}} = \frac{1}{V}\int_V f_\varphi^{ind}\boldsymbol{\Phi}\,\mathrm{d}V = \frac{V_\varphi}{V}\frac{1}{V_\varphi}\int_{V_\varphi}\boldsymbol{\Phi}\,\mathrm{d}V = \alpha_\varphi\overline{\boldsymbol{\Phi}}^{\varphi} \tag{2.7}$$

where $\alpha_\varphi \equiv V_\varphi/V$ is the *phase volume fraction*.

When conditional volume-averaged, conservation equations 2.1-2.2 read:

$$\frac{\partial \alpha_\varphi \overline{\rho}^\varphi}{\partial t} + \nabla \cdot \left(\alpha_\varphi \overline{\rho}^\varphi \overline{\mathbf{u}}^\varphi\right) = 0 \tag{2.8}$$

$$\frac{\partial \left(\alpha_\varphi \overline{\rho}^\varphi \overline{\mathbf{u}}^\varphi\right)}{\partial t} + \nabla \cdot \left[\alpha_\varphi \overline{\rho}^\varphi \left(\overline{\mathbf{u}}^\varphi \otimes \overline{\mathbf{u}}^\varphi\right)\right] = - \nabla \cdot \left(\alpha_\varphi \overline{p}^\varphi\right) + \nabla \cdot \left(\alpha_\varphi \overline{\mathbf{\Gamma}}^\varphi\right) + \alpha_\varphi \overline{\rho}^\varphi \mathbf{g} + \mathbf{M}_\varphi \tag{2.9}$$

where $\overline{\mathbf{\Gamma}}^\varphi$ comprises the viscous and the Reynolds stress tensor and $\mathbf{M}_\varphi$ is the *interfacial momentum transfer*. Both terms stem from the conditional volume-averaging procedure which is applied on the fluctuating part of the convective term for the former and on the fluctuating part of the pressure and stress tensor at the interface for the latter.

Analogously, conditional volume averaged jump conditions at the interface become:

$$0 = 0 \tag{2.10}$$

$$\mathbf{M}_\varphi + \mathbf{M}_\phi = \mathbf{M}_\sigma \tag{2.11}$$

where $\mathbf{M}_\sigma$ is the averaged interfacial momentum source due to surface tension. It is remarked that Eq. 2.4 reduces to 0 = 0 if there is not mass transfer at the interface.

The introduction of phase indicator f produces in turn the following *interface transport equation*:

$$\frac{\partial f_\varphi}{\partial t} + \mathbf{u}_{I,\varphi} \cdot \nabla f_\varphi = 0 \tag{2.12}$$

It can be demonstrated that $\overline{f_\varphi} = \alpha_\varphi$ and that, for a biphasic system where $\overline{\mu}^\varphi \gg \overline{\mu}^\phi$, the conditional volume-averaged interface transport equation is

$$\frac{\partial \alpha_\varphi}{\partial t} + \overline{\mathbf{u}}^\varphi \cdot \nabla \alpha_\varphi = 0 \tag{2.13}$$

Bearing in mind that $\alpha_\varphi + \alpha_\phi = 1$ and defining the *volumetric mixture velocity* $\mathbf{U}$ as follows

$$\mathbf{U} = \alpha_\varphi \overline{\mathbf{u}}^\varphi + \alpha_\phi \overline{\mathbf{u}}^\phi \tag{2.14}$$

the sum of continuity equations 2.8, for incompressible phases, results in:

$$\nabla \cdot \left(\alpha_\varphi \overline{\mathbf{u}}^\varphi + \alpha_\phi \overline{\mathbf{u}}^\phi\right) = \nabla \cdot \mathbf{U} = 0 \tag{2.15}$$

It is preferable to use Eq.2.15 as the continuity equation within a CFD framework. Equation 2.8, divided by density, can govern the transport of the interface, that is

$$\frac{\partial \alpha_\varphi}{\partial t} + \nabla \cdot \left(\alpha_\varphi \overline{\mathbf{u}}^\varphi\right) = 0 \tag{2.16}$$

Therefore, the complete mathematical model, known as *Euler-Euler*, is

$$\Longrightarrow \begin{cases} \nabla \cdot \left(\alpha_\varphi \overline{\mathbf{u}}^\varphi + \alpha_\phi \overline{\mathbf{u}}^\phi\right) = 0 & (2.17) \\ \dfrac{\partial \left(\alpha_\varphi \overline{\rho}^\varphi \overline{\mathbf{u}}^\varphi\right)}{\partial t} + \nabla \cdot \left[\alpha_\varphi \overline{\rho}^\varphi \left(\overline{\mathbf{u}}^\varphi \otimes \overline{\mathbf{u}}^\varphi\right)\right] = & (2.18) \\ \qquad - \nabla \left(\alpha_\varphi \overline{p}^\varphi\right) + \nabla \cdot \left(\alpha_\varphi \overline{\boldsymbol{\Gamma}}^\varphi\right) + \alpha_\varphi \overline{\rho}^\varphi \mathbf{g} + \mathbf{M}_\varphi & \\ \dfrac{\partial \left(\alpha_\phi \overline{\rho}^\phi \overline{\mathbf{u}}^\phi\right)}{\partial t} + \nabla \cdot \left[\alpha_\phi \overline{\rho}^\phi \left(\overline{\mathbf{u}}^\phi \otimes \overline{\mathbf{u}}^\phi\right)\right] = & (2.19) \\ \qquad - \nabla \cdot \left(\alpha_\phi \overline{p}^\phi\right) + \nabla \cdot \left(\alpha_\phi \overline{\boldsymbol{\Gamma}}^\phi\right) + \alpha_\phi \overline{\rho}^\phi \mathbf{g} + \mathbf{M}_\phi & \\ \mathbf{M}_\varphi + \mathbf{M}_\phi = \mathbf{M}_\sigma & (2.20) \\ \dfrac{\partial \alpha_\varphi}{\partial t} + \nabla \cdot \left(\alpha_\varphi \overline{\mathbf{u}}^\varphi\right) = 0 & (2.21) \end{cases}$$

In order to close the system of equations, constitutive relations have to be employed for terms $\overline{\boldsymbol{\Gamma}}^\varphi$ and $\mathbf{M}_\varphi$. In general, closure models are necessary to remedy the loss of information (the fluctuations) due to the averaging procedure.

Concerning the term $\overline{\boldsymbol{\Gamma}}^\varphi$, the needed equations are provided by a turbulence model. This is a well-known subject and it will not be treated in this chapter.

The term $\mathbf{M}_\varphi$ takes into account the smaller-scale deformations of the interface which disappear when the conditional volume filter is applied.

The modeling of $\mathbf{M}_\varphi$ depends on the typology of flow strongly. If the flow is segregated, the unique interface is larger than the grid size and then it is supposed to be fully resolved. Instead, the interface of a dispersed phase has a characteristic length scale generally smaller then the grid size, therefore it is totally modeled.
Marschall et al. (2011) developed a uniform closure framework that included both kinds of flow. Conceptually, the idea was that a segregated flow could still have some not resolved interfacial length scales that could be modeled as in a dispersion. Practically, Marschall et al. (2011) provided mathematical expressions of $\mathbf{M}_\varphi$ for each category of flow.

2.3 Governing equations of the VOF model

From phases φ and ϕ, it can be created a fictitious *mixture* fluid with density and viscosity expressed by

$$\rho \equiv \alpha_\varphi \overline{\rho}^\varphi + \alpha_\phi \overline{\rho}^\phi \tag{2.22}$$

$$\mu \equiv \alpha_\varphi \overline{\mu}^\varphi + \alpha_\phi \overline{\mu}^\phi \tag{2.23}$$

Two new velocity fields are defined

$$\mathbf{U}_m \equiv \frac{\alpha_\varphi \overline{\rho}^\varphi \overline{\mathbf{u}}^\varphi + \alpha_\phi \overline{\rho}^\phi \overline{\mathbf{u}}^\phi}{\alpha_\varphi \overline{\rho}^\varphi + \alpha_\phi \overline{\rho}^\phi} \tag{2.24}$$

$$\mathbf{U}_r \equiv \overline{\mathbf{u}}^\varphi - \overline{\mathbf{u}}^\phi \tag{2.25}$$

which are the *center-of-mass velocity* and the *relative velocity* respectively. Recalling $\mathbf{U} = \alpha_\varphi \overline{\mathbf{u}}^\varphi + \alpha_\phi \overline{\mathbf{u}}^\phi$, it is possible to express the conditional volume-averaged velocity of both phases either as function of the center-of-mass velocity

$$\overline{\mathbf{u}}^\varphi = \mathbf{u}_m + \frac{\alpha_\phi \overline{\rho}^\phi}{\rho} \mathbf{u}_r \tag{2.26}$$

$$\overline{\mathbf{u}}^\phi = \mathbf{u}_m - \frac{\alpha_\varphi \overline{\rho}^\varphi}{\rho} \mathbf{u}_r \tag{2.27}$$

or as function of the relative velocity

$$\overline{\mathbf{u}}^\varphi = \mathbf{U} + (1 - \alpha_\varphi)\mathbf{U}_r \tag{2.28}$$

$$\overline{\mathbf{u}}^\phi = \mathbf{U} - (1 - \alpha_\phi)\mathbf{U}_r \tag{2.29}$$

Inserting Eq. 2.26 in Eq. 2.28, a relation for all velocities is

$$\mathbf{U}_m = \mathbf{U} + \alpha_\varphi \left(1 - \alpha_\varphi\right) \frac{\overline{\rho}^\varphi - \overline{\rho}^\phi}{\rho} \mathbf{U}_r \tag{2.30}$$

The continuity or interface transport equation 2.16 can be expressed in terms of relative velocity $\mathbf{U}_r$, through Eq. 2.26 and considering $\alpha_\phi = 1 - \alpha_\varphi$, as

$$\frac{\partial \alpha_\varphi}{\partial t} + \nabla \cdot \left(\alpha_\varphi \mathbf{U}_m\right) = -\nabla \cdot \left[\frac{\alpha_\varphi (1 - \alpha_\varphi) \overline{\rho}^\phi}{\rho} \mathbf{U}_r \right] \tag{2.31}$$

Analogously for the continuity equation of phase ϕ

$$-\frac{\partial \alpha_\varphi}{\partial t} + \nabla \cdot \left[\left(1-\alpha_\varphi\right) \mathbf{U}_m \right) = -\nabla \cdot \left[\frac{\alpha_\varphi (1-\alpha_\varphi) \overline{\rho}^\varphi}{\rho} \mathbf{U}_r \right] \tag{2.32}$$

When Eqs.2.31 and 2.32 are summed, it is obtained

$$\nabla \cdot \mathbf{U}_m = \nabla \cdot \left[\alpha_\varphi \left(1-\alpha_\varphi\right) \frac{\overline{\rho}^\varphi - \overline{\rho}^\phi}{\rho} \mathbf{U}_r \right] \tag{2.33}$$

which shows that center-of-mass velocity field of the mixture phase is not solenoidal inside the interfacial transition region.

Substituting Eq. 2.30 into the equation above leads to

$$\nabla \cdot \mathbf{U} = 0 \tag{2.34}$$

which shows instead that the volumetric mixture velocity field is solenoidal (as it was found in Eq. 2.15).

The interface transport equation 2.8 can be expressed as a function of **u** through Eq. 2.28:

$$\frac{\partial \alpha_\varphi}{\partial t} + \nabla \cdot \left(\alpha_\varphi \mathbf{U} \right) + \nabla \cdot \left[\alpha_\varphi \left(1-\alpha_\varphi\right) \mathbf{U}_r \right] = 0 \tag{2.35}$$

Adopting the common assumption that both phases share the same pressure p and summing the momentum equations 2.18 and 2.19:

$$\frac{\partial \rho \mathbf{U}_m}{\partial t} + \nabla \cdot (\rho \mathbf{U}_m \otimes \mathbf{U}_m) = -\nabla p + \nabla \cdot (\mathbf{\Gamma}_m + \mathbf{\Gamma}_I) - \nabla \cdot \left(\rho \mathbf{M}_{drift} \right) + \rho \mathbf{g} + \mathbf{M}_\sigma \tag{2.36}$$

where:

$$\mathbf{\Gamma}_I \equiv \alpha_\varphi \overline{\mu}^\varphi \left[\left(\nabla \otimes \frac{\alpha_\phi \overline{\rho}^\phi}{\rho} \mathbf{U}_r \right) + \left(\nabla \otimes \frac{\alpha_\phi \overline{\rho}^\phi}{\rho} \mathbf{U}_r \right)^T \right] - \alpha_\phi \overline{\mu}^\phi \left[\left(\nabla \otimes \frac{\alpha_\varphi \overline{\rho}^\varphi}{\rho} \mathbf{U}_r \right) + \left(\nabla \otimes \frac{\alpha_\varphi \overline{\rho}^\varphi}{\rho} \mathbf{U}_r \right)^T \right] \tag{2.37}$$

is the *interfacial friction tensor* and

$$\mathbf{M}_{drift} \equiv \frac{\alpha_\varphi \alpha_\phi \overline{\rho}^\varphi \overline{\rho}^\phi}{\rho} \mathbf{U}_r \otimes \mathbf{U}_r \tag{2.38}$$

is the *momentum drift-flux* term.

The final set of Eqs. 2.34-2.36 is the so-called *Drift-Flux* model. The difference with the Euler-Euler is that just *one* momentum equation needs to be resolved, instead of two for both phases. The missing momentum equation in the Drift-Flux model is replaced by a closure relation for $\mathbf{U}_r$.
The simplest closure is given by the *homogeneus mixture hypothesis* which implies

$$\mathbf{U}_r = 0 \tag{2.39}$$

This assumption means that a *no-slip* condition is applied to the velocity fields of the two phases, i.e. it is assumed that *the velocity fields of the two phases are equal throughout the domain.* The effects of this hypothesis are:

$$\overline{\mathbf{u}}^{\varphi} = \overline{\mathbf{u}}^{\phi} = \mathbf{U}_m = \mathbf{U} \tag{2.40}$$

$$\mathbf{\Gamma}_i = 0 \tag{2.41}$$

$$\mathbf{M}_{drift} = 0 \tag{2.42}$$

With the above relations, the Drift-Flux model (Eqs. 2.34-2.36) reduces to well known *VOF model*:

$$\Longrightarrow \begin{cases} \nabla \cdot \mathbf{U} = 0 & (2.43) \\ \dfrac{\partial \rho \mathbf{U}}{\partial t} + \nabla \cdot (\rho \mathbf{U} \otimes \mathbf{U}) = -\nabla p + \nabla \cdot \mathbf{\Gamma} - \rho \mathbf{g} + \mathbf{M}_{\sigma} & (2.44) \\ \dfrac{\partial \alpha_{\varphi}}{\partial t} + \nabla \cdot \left(\alpha_{\varphi} \mathbf{U}\right) = 0 & (2.45) \end{cases}$$

Since the VOF model is used for segregated flows where phases are *de facto* stratified, the no-slip condition is applied at the interface where the transition between phases takes place.

Now the unique framework of Marschall et al. (2011) for the closure of the equations of a generic two-phase flow (Eqs. 2.17-2.21) provides a valuable point of view to understand the application of the VOF model. In the perspective that the interfacial boundary layer of a segregated flow is *only partially* resolved within a CFD methodology, because it is however discretized and an averaging procedure is performed, the application of the VOF model inherently implies that the non-resolved interfacial scales can be neglected. Likewise, it implies that the adopted spatial discretization is fine enough for the resolved interfacial structures.

3 The numerical methodology

In general, a numerical methodology is the combination of a mathematical model and a solution method (Rusche, 2003).

The mathematical models suitable for representing the two-phase flow of a breaking wave, i.e. VOF and Euler-Euler, have been presented in Chapter 2 and consist of partial differential equations. An analytical approach cannot solve the system of equations, therefore a numerical CFD method needs to be employed.

A numerical approach provides a *discrete* solution. The discretisation is operated on the spatial domain, on the time – a breaking wave is a transient flow – and, consistently, on the model equations. This method leads to a system of algebraic relations which can be solved. The algorithm encompassing the discretisation stage and the solution of the resulting algebraic equations will be referred to as "CFD solver".
This chapter first shows the developed mathematical model extending the findings of Chapter 2. Then, the CFD solver is described.

3.1 The mathematical model

This study aimed to build a numerical methodology capable of handling the *whole* breaking process: the segregated wave propagation, the breaking with associated air entrainment and the evolution of the dispersed air bubble plume. In other words, both the VOF and the Euler-Euler model were required depending on the occurring interfacial morphology. A *coupling* of these two models was realized.

This coupling was the core of the present CFD solver and it was the main challenge throughout the development process. For this reason, it will be largely elucidated in this section, but, firstly, a necessary extension of the Euler-Euler model is introduced.

3.1.1 The Eulerian multiphase model

In the Euler-Euler model, the dispersed phase is assumed in form of spherical bubbles of the same size, i.e. the phase is *monodispersed*. Since the velocity of a bubble

depends on its size, the closure relations for the interfacial momentum transfer term $\mathbf{M}_\varphi$ ($\mathbf{M}_\phi$) can be expressed as a function of the diameter d.

Bubbles entraining water during wave breaking are not identical, but they have diameter in the range 0.2-20 mm (Deane and Stokes, 2002). The entrained air is *polydisperse*. Moreover, it has been already seen that the size distribution changes with time. This is due to the buoyancy-induced degassing but also to the fact that bubbles can interact among themselves and with the surrounding water: they can either aggregate to produce larger bubbles (*coalescence*) or break to generate smaller ones (*breakage*). A fixed bubble size model might not be suitable for predicting the correct dynamics of the entrained air bubble plume, because the interfacial interactions between dispersed and continuous phase could not be sufficiently modeled.

Since the assumption of monodispersion was quite restrictive for the needs of this study, it was chosen to model the *simultaneous* motion of bubbles of different size. For this purpose, the Euler-Euler model was extended to the Eulerian *multiphase* approach (Drew and Passman, 2006) which can handle the motion of N phases. The model equations are:

$$\Longrightarrow \begin{cases} \nabla \cdot \left(\sum_{i=1}^{N} \alpha_i \mathbf{u}_i \right) = 0 & (3.1) \\ \dfrac{\partial \left(\alpha_i \rho_i \mathbf{u}_i \right)}{\partial t} + \nabla \cdot \left[\alpha_i \rho_i \left(\mathbf{u}_i \otimes \mathbf{u}_i \right) \right] = & \\ \qquad - \nabla \left(\alpha_i p \right) + \nabla \cdot \left(\alpha_i \mathbf{\Gamma}_i \right) + \alpha_i \rho_i \mathbf{g} + \mathbf{M}_i & (3.2) \\ \sum_{i=1}^{N} \mathbf{M}_i = \mathbf{M}_\sigma & (3.3) \\ \dfrac{\partial \alpha_i}{\partial t} + \nabla \cdot \left(\alpha_i \mathbf{u}_i \right) = S_i & (3.4) \\ \sum_{i=1}^{N} S_i = 0 & (3.5) \end{cases}$$

Note that $\bar{(\cdot)}$ has been drop and the superscript indicating the phase has become a subscript.
The Eulerian multiphase model is identical to the Euler-Euler conceptually, i.e. the syestem of equations has the same form of Eqs. 2.17-2.21. Nevertheless, three differences should be noted:

- an interface transport equation is solved per each phase;
- a momentum equation is solved per each phase which implies that each phase has its own velocity field $\mathbf{u}_i$;

- the term S_i appears now on the r.h.s. of the interface transport equations: it represents the *interfacial mass transfer* (breakage and coalescence).

The fact that N coupled momentum equations have to be solved increases the computational expensiveness of the model. The multiple interface transport equations are treated in the following section.

3.1.2 The bubble population balance equation

Equation 3.4 can be seen as the so-called *bubble population balance equation* (BPBE). This is a Boltzmann's transport equation which states the conservation of the bubble number density f, i.e. the number of bubbles per unit volume of the domain. In the usual form, this equation reads:

$$\frac{\partial}{\partial t} n(\mathbf{x}, v, t) + \nabla \cdot [\mathbf{u}_i(\mathbf{x}, v, t)\, n(\mathbf{x}, v, t)] = S(\mathbf{x}, v, t) \tag{3.6}$$

where:

- $n(\mathbf{x}, v, t)$ is the bubble number density a given time t, in the spatial range d$\mathbf{x}$ about a position $\mathbf{x}$ and with volume between v and v+dv;
- $\mathbf{u}_i$ is the velocity of bubbles with volume between v and v+dv;
- S is the source/sink term.

The term S can include different mass transfer processes, but only breakage and coalescence were taken into account in this work. It was expressed as:

$$\begin{aligned} S(\mathbf{x}, v, t) = & \frac{1}{2}\int_0^v a\left(v - v', v'\right) n\left(\mathbf{x}, v - v', t\right) n\left(\mathbf{x}, v', t\right) \mathrm{d}v' \\ & - n(\mathbf{x}, v, t) \int_0^\infty a\left(v, v'\right) n\left(\mathbf{x}, v', t\right) \mathrm{d}v' \\ & + \int_v^\infty m\left(v'\right) b\left(v'\right) P\left(v, v'\right) n\left(\mathbf{x}, v', t\right) \mathrm{d}v' \\ & - b(v)\, n\left(\mathbf{x}, v', t\right) \end{aligned} \tag{3.7}$$

where:

- the first term is the birth rate of bubbles of volume v due to coalescence of bubbles of volume $v - v'$ and v with frequency a;
- the second term is the death rate of bubbles of volume v due to coalescence with other bubbles;

- the third term is the birth rate of bubbles of volume v due to breakup of bubbles whit volume larger than v with frequency b. The term m is the mean number of daughter bubbles produced by breakup of parent bubble of volume v'. The term $P(v,v')$ represents the probability density function of daughter bubbles produced upon breakup of a parent bubble with volume v';
- the fourth term is the death rate of bubbles of volume v due to breakup.

Closure formulations for terms a, P, b and m are needed. Well-established relations exist in literature and the ones employed in the present work are shown later. Here the focus is on the necessity of using a numerical approach for solving the BPBE, since analytical methods cannot be successful.

In this work, the *Method of Classes* (CM) was implemented (Kumar and Ramkrishna, 1996a,b, Ramkrishna, 2000). In this method, the continuous bubble size (diameter) range is discretized into a finite number N of classes. Each class is represented by a characteristic *pivot* with a diameter d_i or a volume v_i equivalently (bubbles are spherical). Moreover, each class has its own bubble number density n_i and velocity $\mathbf{u}_i$. Thereofre, *these classes are gaseous phases with the same density ρ and viscosity ν*.

The number density is related to the phase volume fraction α_i as follows

$$\alpha_i = n_i v_i \tag{3.8}$$

Inserting Eq. 3.8 in Eq. 3.6 and reformulating give:

$$\frac{\partial \alpha_i}{\partial t} + \nabla \cdot (\alpha_i \mathbf{u}_i) = S_i \tag{3.9}$$

which is the interface transport equation of phase i. Note that S_i now expresses Eq. 3.7 multiplied by v_i.

Therefore, it has been demonstrated that the solution of the multiple interface transport equations 3.4 inherently implies the discrete solution of the BPBE. Other procedures for solving the BPBE within a CFD algorithm can be found in (Bannari et al., 2008, Selma et al., 2010, Silva and Lage, 2011, Buffo et al., 2013).

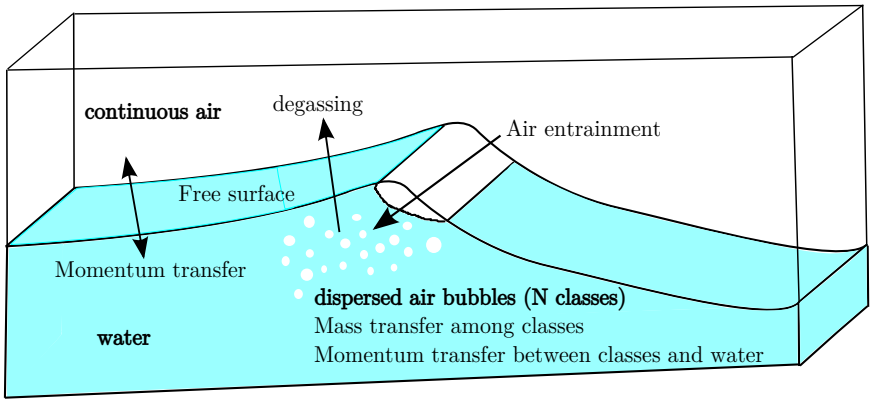

Figure 3.1: Adopted description of a breaking wave within the Eulerian multiphase model.

3.1.3 The coupling between the VOF and the Eulerian multiphase model

Why was the coupling necessary?

Although the answer to this question has been already addressed in previous chapters, it is not fully stated yet.

The basis of the developed numerical methodology was the Eulerian multiphase model and the coupling with the VOF can be considered *on top* of it. Before explaining how this coupling worked, it is beneficial to first illustrate how a breaking wave was described within the Eulerian multiphase model (Fig. 3.1).

The air above water was called *continuous* to distinguish it from the air entrained in water in the form of *dispersed* bubbles. The interface between continuous air and water was the free surface. As seen in the previous section, the dispersed bubbles were represented with N phases, or classes, each of them characterized by a diameter d_i. The classes had the same density and viscosity of the continuous air, hereafter just air. The total number of phases resolved in the model was $N+2$: water + air + N classes. All phases were incompressible and immiscible.

In the same figure, the interfacial transfers of mass and momentum among phases are also reported, that is:

- water and air exchange momentum, not mass;
- air exchanges mass with bubble classes (air entrainment and degassing);
- bubble classes exchange mass among themselves and momentum with water. Momentum exchange among bubbles due to collision was neglected.

Conceptually, just the Eulerian multiphase model would have been sufficient to simulate a breaking wave given that the momentum transfers between phases were formulated in according to the local interfacial morphology. The momentum exchanged between water and bubbles could have been modeled by the well-established relations existing in literature for dispersed phases. Instead, there would have been an issue regarding on how to formulate the transfer between water and air phase which were not dispersed, but stratified. Although some studies provide reliable solutions to this problem (Marschall et al., 2011, Štrubelj and Tiselj, 2011, Hänsch et al., 2012, Wardle and Weller, 2013), none of them directly impose that the relative velocity between water and air is zero (no-slip) which is the most appropriate condition for a segregated flow. Contrarily, the VOF model ensures that the velocity of water and air is identical at the free surface (Section 2.3). Therefore, the employment of the VOF model eliminated the uncertainty on the momentum transfer between water and air.

Note that this issue it was not just conceptual. An appropriate momentum transfer modeling was a key factor for achieving a *sharp* and *regular* simulated free surface. The sharpness of the free surface can be explained as follows. Both the VOF and the Eulerian multiphase model provide a free surface that is not reconstructed as a real geometrical entity, but it is simply represented by the transition zone in which the water void fraction α_{water} goes from the value 1 to 0. The thickness of this transition zone is the sharpness of the free surface and it must be as small as possible (in the limits of the finite volume discretisation). The term regular indicates that no instabilities must be recognised in the solution of the pressure and velocity fields which are continuous across the free surface. These instabilities usually manifest as wiggles upon the free surface.

Since the simulation of a sharp and regular free surface was an *essential* requirement for the purpose of this study, the coupling with the VOF model was believed necessary and convenient.

How does the coupling work?

The idea of coupling of a model with interface capturing capabilities, like VOF, with one based on the Eulerian methodology (Euler-Euler or multiphase) is not new. Flows with simultaneous dispersed and segregated interfaces are encountered in various fields of industry and science, therefore several studies have been conducted on this topic.

In general, two typologies of coupling can be identified:

- *dynamic* when it is implemented a criterion which distinguishes – runtime – large interfacial length scales in segregated flows from small interfacial length scales in dispersed flows in order to switch between the two coupled models (Cerne et al., 2001, Štrubelj and Tiselj, 2011);

- *static* when the interfacial morphologies are known *a priori* and phase pairs are preassigned to one of the two models (Hänsch et al., 2012, Wardle and Weller, 2013, Ojima et al., 2014).

Moreover, three different strategies for the coupling implementation can be recognised:

- the numerical methodology is provided with the governing equations of both models (Cerne et al., 2001);
- the framework is the Eulerian model and the interface capturing feature is achieved by some numerical "expedients" (Cerne et al., 2001, Hänsch et al., 2012, Wardle and Weller, 2013, Ojima et al., 2014);
- only the governing equations of the Eulerian approach are used and the closure term M_i depends on the interfacial morphologies (Marschall et al., 2011).

A dynamic coupling was not believed necessary for this study. The reason is that, although the interfacial length scales are within a quite broad range, there is a clear partition on where and when all interfacial structures occur. In fact, it was expected that:

- the segregated flow concerns the motion of water and air throughout the whole domain and the whole simulated time interval;
- the dispersed flow involves water and bubble classes. It establishes at the breaking time and it vanishes within few wave periods.

The static coupling of Ojima et al. (2014) was implemented in this study. The framework was based on the governing equations of the Eulerian multiphase model and a VOF solution for the free surface was obtained as follows. Air and water were considered as a *mixture* phase (*mixt*) with a single velocity field, that is the no-slip condition

$$\mathbf{u}_{\text{mixt}} = \mathbf{u}_{\text{w}} = \mathbf{u}_{\text{air}} \tag{3.10}$$

was imposed in the whole domain. As it has been shown in Section 2.3, it was possible to achieve a single VOF momentum equation for the mixture of these phases by summing the Eulerian momentum equations of water and air. Viscosity and density of the mixture were calculated as a weighted average of the properties of the two phases, being the volume fraction the weight

$$\rho_{\text{mixt}} = \frac{\alpha_{\text{w}}\rho_{\text{w}} + \alpha_{\text{air}}\rho_{\text{air}}}{\alpha_{\text{w}} + \alpha_{\text{air}}} \tag{3.11}$$

$$\nu_{\text{mixt}} = \frac{\alpha_{\text{w}}\nu_{\text{w}} + \alpha_{\text{air}}\nu_{\text{air}}}{\alpha_{\text{w}} + \alpha_{\text{air}}} \tag{3.12}$$

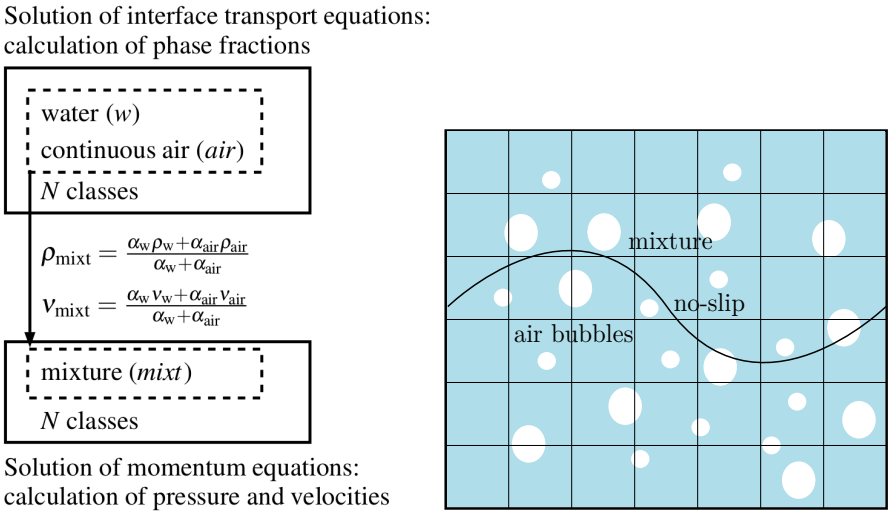

Figure 3.2: Architecture of the developed numerical methodology.

The momentum equations for water and air were *not* solved. The bubble classes were treated as dispersed in the mixture (occupying the entire domain) and not in water. Air and water were still treated separately in the calculation of phase fractions. Fig. 3.2 helps in understanding this explanation.

3.1.4 The model equations

In order to accomodate the VOF model on the Eulerian multiphase framework, Eqs. 3.1-3.5 were rewritten as follows

$$\Longrightarrow \begin{cases} \nabla \cdot \left(\sum_{i=1}^{N+2} \alpha_i \mathbf{u}_i \right) = 0 & (3.13) \\ \frac{\partial \left(\alpha_i \rho_i \mathbf{u}_i \right)}{\partial t} + \nabla \cdot \left[\alpha_i \rho_i \left(\mathbf{u}_i \otimes \mathbf{u}_i \right) \right] = & \\ \qquad \nabla \cdot \left(\alpha_i \rho_i \mathbf{\Gamma}_i^{eff} \right) - \alpha_i \nabla p_d - \alpha_i \left(\mathbf{g} \cdot \mathbf{x} \right) \nabla \rho + \alpha_i \mathbf{g} \left(\rho_i - \rho \right) + \mathbf{M}_i & (3.14) \\ \sum_{i=1}^{N+1} \mathbf{M}_i = \mathbf{M}_\sigma & (3.15) \\ \frac{\partial \alpha_i}{\partial t} + \nabla \cdot \left(\alpha_i \mathbf{u}_i \right) = S_i & (3.16) \\ \sum_{i=1}^{N+2} S_i = 0 & (3.17) \\ \mathbf{u}_w = \mathbf{u}_{air} & (3.18) \end{cases}$$

where the excess pressure $p_d = p - \rho \mathbf{g} \cdot \mathbf{x}$ has been defined with $\rho = \sum_{i=1}^{N} \alpha_i \rho_i$ and $\mathbf{x} = \mathbf{x}(x, y, z)$. It is the pressure without the contribution of the hydrostatic pressure.

Closure modelings were needed for the *effective* stress tensor $\mathbf{\Gamma}_i^{eff}$, the momentum transfer $\mathbf{M}_i$ and the mass exchange S_i among phases. The treatment of these terms is described in greater detail in the following.

Effective stress tensor $\mathbf{\Gamma}_i^{eff}$

The modeling of the turbulence in the wave breaking-induced bubbly flow poses a challenge because objective uncertainties on the turbulent behavior of water are enhanced by the random distribution of bubbles. Among the copious approaches available in literature, this work adopted the one of Derakhti and Kirby (2014). The idea was that only the turbulence of water, which was the mixture phase in the present CFD solver, was solved and in a manner that took into account the effects of the bubble motion (the formation of wakes and vortex shedding behind the bubbles as example). The stress tensor $\mathbf{\Gamma}_i^{eff}$ was named "effective" because, for the mixture phase, it included not only the dissipation induced by the (mixture) molecular viscosity, but also by the turbulence (velocity fluctuations) and the bubble motion. The effective stress tensor of the classes was due just to the molecular viscous dissipation.

The LES approach was used to handle the turbulence. A top-hat filter with a width equal to the grid-spacing Δ was used (De Villiers, 2007), consistently with the volume-averaging procedure applied to the governing equations of the model (see Chapter 2). This filter had the effect that only length-scale scales larger than Δ (Grid Scales, GS) are resolved, whereas the smaller scales (Sub-Grid Scale, SGS) were modeled. The quantities in Eqs. 3.13-3.17 have to be intended as filtered.

The effective stress tensor of the mixture could be decomposed as

$$\mathbf{\Gamma}_{\text{mixt}}^{eff} = \mathbf{\Gamma}_{\text{mixt}}^{r} + \mathbf{\Gamma}_{\text{mixt}}^{sgs} = \mathbf{\Gamma}_{\text{mixt}}^{r} + \mathbf{\Gamma}_{\text{mixt}}^{sgs,SI} + \mathbf{\Gamma}_{\text{mixt}}^{sgs,BI} \tag{3.19}$$

where:

- $\mathbf{\Gamma}_{\text{mixt}}^{r}$ is the stress tensor due to molecular kinematic viscosity (Eq. 2.3). It is function of the resolved rate-of-strain tensor $\mathbf{S}$ as follows

$$\begin{aligned} &\mathbf{\Gamma}_{\text{mixt}}^{r} = 2\nu_{\text{mixt}}^{r}\left[\mathbf{S}_{\text{mixt}} - \frac{1}{3}\left(\nabla\cdot\mathbf{u}_{\text{mixt}}\right)\mathbf{I}\right] = \\ &2\nu_{\text{mixt}}^{r}\left\{\frac{1}{2}\left[\nabla\otimes\mathbf{u}_{\text{mixt}} + \left(\nabla\otimes\mathbf{u}_{\text{mixt}}\right)^{T}\right] - \frac{1}{3}\left(\nabla\cdot\mathbf{u}_{\text{mixt}}\right)\mathbf{I}\right\} = 2\nu_{\text{mixt}}^{r}\boldsymbol{D}_{\text{mixt}} \end{aligned} \tag{3.20}$$

- $\mathbf{\Gamma}_{\text{mixt}}^{sgs,SI}$ is the shear-induced SGS stress tensor. Its anisotropic part is function of the resolved scales through the shear-induced SGS viscosity calculated by the

employed LES model:

$$\boldsymbol{\Gamma}_{\text{mixt}}^{sgs,SI,a} = -2\nu_{\text{mixt}}^{sgs,SI}\boldsymbol{D}_{\text{mixt}} \tag{3.21}$$

- $\boldsymbol{\Gamma}_{\text{mixt}}^{sgs,BI}$ is the bubble-induced SGS stress tensor. Its anisotropic part is function of the resolved scales through the bubble-induced SGS viscosity calculated as in Sato and Sekoguchi (1975):

$$\boldsymbol{\Gamma}_{\text{mixt}}^{sgs,BI,a} = -2\nu_{\text{mixt}}^{sgs,BI}\boldsymbol{D}_{\text{mixt}} = -2\left(0.6\sum_{i=1}^{N}\alpha_i d_i \|\mathbf{u}_i - \mathbf{u}_{\text{mixt}}\|\right)\boldsymbol{D}_{\text{mixt}} \tag{3.22}$$

A total SGS viscosity could be defined as a superposition of the shear and the bubble-induced viscosity:

$$\nu_{\text{mixt}}^{sgs} = \nu_{\text{mixt}}^{sgs,SI} + \nu_{\text{mixt}}^{sgs,BI} \tag{3.23}$$

and consequently

$$\boldsymbol{\Gamma}_{\text{mixt}}^{sgs,a} = \boldsymbol{\Gamma}_{\text{mixt}}^{sgs,SI,a} + \boldsymbol{\Gamma}_{\text{mixt}}^{sgs,BI,a} = -2\nu_{\text{mixt}}^{sgs}\boldsymbol{D}_{\text{mixt}} \tag{3.24}$$

It should be noted that the eddy-viscosity approximation was used in the equation above, i.e. the non-uniform component of the SGS stress tensor is locally aligned with the non-uniform part of the resolved rate-of-strain tensor. Moreover, the superposition of $\boldsymbol{\Gamma}_{\text{mixt}}^{sgs,SI,a}$ and $\boldsymbol{\Gamma}_{\text{mixt}}^{sgs,BI,a}$ lies on the consideration that bubbles have a dimension smaller than grid size (as required by the conditional volume-averaging procedure of the Eulerian approach), hence smaller than the applied LES filter.

The total SGS stress tensor is given by

$$\boldsymbol{\Gamma}_{\text{mixt}}^{sgs} = -\boldsymbol{\Gamma}_{\text{mixt}}^{sgs,a} - \frac{2}{3}k_{\text{mixt}}^{sgs}\mathbf{I} \tag{3.25}$$

since the SGS kinetic energy is defined as the trace of the SGS stress tensor. Note that k_{mixt}^{sgs} is provided by the employed LES model.

Finally, the effective stress tensor of the mixture phase was calculated as

$$\begin{aligned}\boldsymbol{\Gamma}_{\text{mixt}}^{eff} &= 2\left(\nu_{\text{mixt}}^{r} + \nu_{\text{mixt}}^{sgs}\right)\left\{\frac{1}{2}\left[\nabla\otimes\mathbf{u}_{\text{mixt}} + (\nabla\otimes\mathbf{u}_{\text{mixt}})^T\right] - \frac{1}{3}(\nabla\cdot\mathbf{u}_{\text{mixt}})\mathbf{I}\right\} - \frac{2}{3}k_{\text{mixt}}^{sgs}\mathbf{I} \\ &= 2\left(\nu_{\text{mixt}}^{eff}\right)\left\{\frac{1}{2}\left[\nabla\otimes\mathbf{u}_{\text{mixt}} + (\nabla\otimes\mathbf{u}_{\text{mixt}})^T\right] - \frac{1}{3}(\nabla\cdot\mathbf{u}_{\text{mixt}})\mathbf{I}\right\} - \frac{2}{3}k_{\text{mixt}}^{sgs}\mathbf{I}\end{aligned} \tag{3.26}$$

while the effective stress tensor of the classes was

$$\mathbf{\Gamma}_i^{eff} = 2\nu_i^r \left\{ \frac{1}{2} \left[\nabla \otimes \mathbf{u}_i + (\nabla \otimes \mathbf{u}_i)^T \right] - \frac{1}{3} (\nabla \cdot \mathbf{u}_i) \mathbf{I} \right\} \tag{3.27}$$

Similarly, the following dissipation rate terms could be formulated

$$\epsilon_{\text{mixt}}^r = 2\nu_{\text{mixt}}^r \mathbf{S}_{\text{mixt}} : \mathbf{S}_{\text{mixt}} \tag{3.28}$$
$$\epsilon_{\text{mixt}}^{sgs,SI} = 2\nu_{\text{mixt}}^{sgs,SI} \mathbf{S}_{\text{mixt}} : \mathbf{S}_{\text{mixt}} \tag{3.29}$$
$$\epsilon_{\text{mixt}}^{sgs,BI} = 2\nu_{\text{mixt}}^{sgs,BI} \mathbf{S}_{\text{mixt}} : \mathbf{S}_{\text{mixt}} \tag{3.30}$$
$$\epsilon_{\text{mixt}}^{sgs} = \epsilon_{\text{mixt}}^{sgs,SI} + \epsilon_{\text{mixt}}^{sgs,BI} \tag{3.31}$$
$$\epsilon_{\text{mixt}}^{tot} = \epsilon_{\text{mixt}}^r + \epsilon_{\text{mixt}}^{sgs,SI} + \epsilon_{\text{mixt}}^{sgs,BI} \tag{3.32}$$

The term $\epsilon_{\text{mixt}}^{tot}$ represented the dissipation rate of the resolved kinetic energy per unit mass. The term $\epsilon_{\text{mixt}}^{sgs,SI}$ represented the rate of transfer of kinetic energy per unit mass from resolved to sub-grid modeled scales.

The dynamic Smagorinsky model of Germano et al. (1991) and Lilly (1992) was employed in all simulations performed throughout this study. The underlying assumption was that the SGS scales were in equilibrium and dissipate entirely and instantaneously all the energy received from the resolved scales. The shear-induced viscosity $\nu_{\text{mixt}}^{sgs,SI}$ and the SGS kinetic energy k_{mixt}^{sgs} were determined as

$$\nu_{\text{mixt}}^{sgs,SI} = (C_S \Delta)^2 \|\mathbf{S}_{\text{mixt}}\| \tag{3.33}$$
$$k_{\text{mixt}}^{sgs} = (C_I \Delta)^2 \|\mathbf{S}_{\text{mixt}}\|^2 \tag{3.34}$$

Contrary to the constant Smagorinksy, in this model both coefficients C_S and C_I are calculated in according to the local characteristics of the flow. This feature makes the model suitable for predicting the turbulence field under breaking waves. In fact, since turbulence is limited in space and time, the sub-grid viscosity and kinetic energy can be damped near the free surface where are supposed to be reduced and in regions of the wave field where the flow is weakly or not turbulent.

The interfacial momentum transfer M_i

The momentum transfer $\mathbf{M}_i$ *between water and bubbles* was decomposed in four contributions:

- *Drag force.* Because of their relative velocity with respect to the mixture, bubbles are subject to a resisting force opposed to the direction of their movement. This

drag force was expressed as

$$\mathbf{M}_{D,i} = \frac{3}{4}\rho_{\text{mixt}}\alpha_{\text{mixt}}\alpha_i C_{D,i}\frac{\|\mathbf{u}_i - \mathbf{u}_{\text{mixt}}\|(\mathbf{u}_i - \mathbf{u}_{\text{mixt}})}{d_i} \tag{3.35}$$

The drag coefficient $C_{D,i}$ was determined either via the correlation of Schiller and Naumann (1935) which assumed spherical bubbles

$$C_{D,i} = \begin{cases} \dfrac{24\left(1+0.15Re_i^{0.687}\right)}{Re} & \text{if } Re_i = \dfrac{\|\mathbf{u}_i - \mathbf{u}_{\text{mixt}}\|d_i}{\nu^r_{\text{mixt}}} \leq 1000, \\ 0.44 & \text{if } Re_i > 1000 \end{cases} \tag{3.36}$$

or through a model which took into account bubble deformation (Ishii and Zuber, 1979, ANSYS, 2009):

$$C_{D,i} = \begin{cases} \max(C_{D,sphere}, C_{D,dist}) \\ C_{D,dist} = \min(C_{D,cap}, C_{D,ellipse}) \\ C_{D,ellipse} = \frac{2}{3}\sqrt{\frac{9.81(\rho_{\text{mixt}}-\rho_i)d_i^2}{\sigma}} \\ C_{D,cap} = \frac{8}{3} \\ C_{D,sphere} = \begin{cases} \dfrac{24\left(1+0.15Re_*^{0.687}\right)}{Re_*} & \text{if } Re_* = \dfrac{\|\mathbf{u}_i - \mathbf{u}_{\text{mixt}}\|d_i}{\mu_*} \leq 1000, \\ 0.44 & \text{if } Re_* > 1000 \end{cases} \\ \mu_* = \mu_{\text{mixt}}(1-\alpha_i)^{\frac{-2.5(\mu_i+0.4\mu_{\text{mixt}})}{\mu_i+\mu_{\text{mixt}}}} \end{cases} \tag{3.37}$$

- *Lift force.* The sheared non-uniform flow of the mixture makes bubbles undergo a component of the resisting force perpendicular to the drag force which is called lift force. It was formulated as:

$$\mathbf{M}_{L,i} = -\rho_{\text{mixt}}\alpha_{\text{mixt}}\alpha_i C_L(\mathbf{u}_i - \mathbf{u}_{\text{mixt}}) \times (\nabla \times \mathbf{u}_{\text{mixt}}) \tag{3.38}$$

  where C_L was a model constant with a value of 0.5;

- *Virtual mass force.* Bubbles with a relative acceleration with respect to the mixture experience this extra resisting force due to the fact that also the surrounding mass of mixture tends to accelerate. The virtual mass force was given by:

$$\mathbf{M}_{VM,i} = \rho_{\text{mixt}}\alpha_{\text{mixt}}\alpha_i C_{VM}\left(\frac{\mathrm{D}\mathbf{u}_i}{\mathrm{D}t} - \frac{\mathrm{D}\mathbf{u}_{\text{mixt}}}{\mathrm{D}t}\right) \tag{3.39}$$

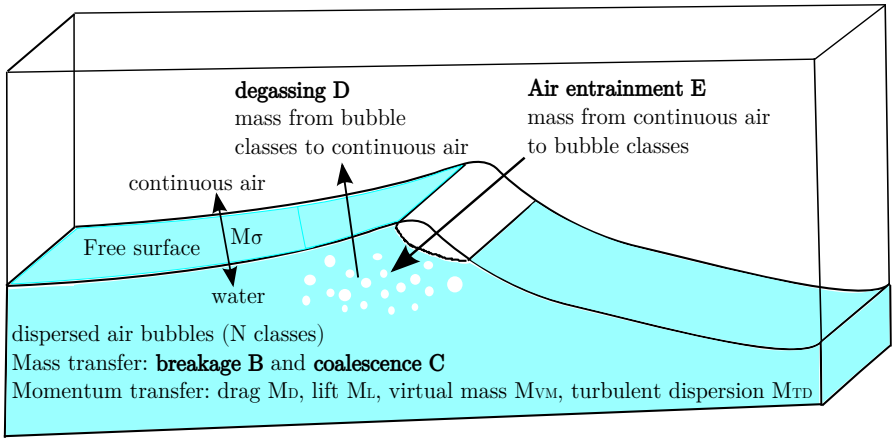

Figure 3.3: Interactions among phases in a breaking wave described within the Eulerian multiphase model.

where C_{VM} was a model constant set to 0.5;

- *Turbulent dispersion force.* The turbulent eddies of mixture phase tend to scatter bubbles as a swarm. This force was represented as

$$\mathbf{M}_{TD,i} = -\frac{3}{4} C_{D,i} \frac{\rho_{\text{mixt}}}{d_i} \frac{\nu_{\text{mixt}}^{sgs}}{S_b} \|\mathbf{u}_i - \mathbf{u}_{\text{mixt}}\| \nabla \alpha_i \tag{3.40}$$

where the Schmidt number S_b was taken equal to 0.8.

The momentum exchange *between water and air* due to surface tension was evaluated using the model of Brackbill et al. (1992):

$$\mathbf{M}_{\sigma,\text{mixt}} = \sigma \kappa \nabla \alpha \tag{3.41}$$

where κ is the interface curvature and $\sigma = 0.0728$ N/m is the surface tension. Note that this contribution was computed before the resolution of the coupled momentum equations, when water and (continuous) air are treated separately.

The interfacial mass transfer S_i

Figure 3.3 depicts the mass transfers occurring simultaneously during wave breaking. As already said in Section 3.1.2, breakage (B) and coalescence (C) were modeled as mass transfers among bubble classes. Both models were implemented within the Method of Classes which ensured that the number of bubbles was conserved. In this method, the bubble volume range, comprised between v_{min} and v_{max}, is discretized in N classes as depicted in Fig. 3.4. Each class $v_{i-1} \leq v \leq v_i$ is represented by the pivot x_i. A geometric progression was used: $x_i = 2x_{i-1}$ and $v_i = (x_{i-1} + x_i)/2$. The width of each class was $l_i = v_i - v_{i-1}$.

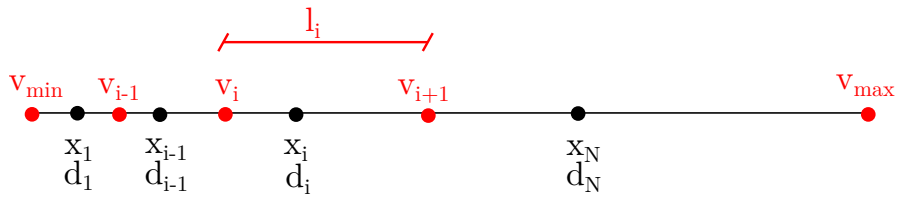

Figure 3.4: Discretisation of the bubble volume range in the Method of Classes.

Being j and k (with $x_j \geq x_k$) a couple of bubbles which collide and merge, the coalescence source and sink term were given by

$$C_i = \sum_{\forall k}^{j \geq k} \left(1 - \frac{1}{2}\delta_{j,k}\right) \left[\gamma_i \left(x_j + x_k\right) a(x_j, x_k) n_j n_k\right] - n_i \sum_{j=1}^{N} a(x_i, x_j) n_j \tag{3.42}$$

where:

- $\delta_{j,k}$ was the Kronecker delta;
- γ_i was a coefficient which (linearly) distributed a bubble produced by coalescence to the two nearest classes. It was calculated as

$$\gamma_i = \begin{cases} \dfrac{(x_j + x_k) - x_{i-1}}{x_i - x_{i-1}} & x_{i-1} \leq (x_j + x_k) \leq x_i \\ \dfrac{x_{i+1} - (x_j + x_k)}{x_{i+1} - x_i} & x_i \leq (x_j + x_k) \leq x_{i+1} \\ 0 & \text{otherwise} \end{cases} \tag{3.43}$$

- $a(x_j, x_k)$ was the coalescence frequency written as a product of collision rate $\theta_{j,k}$ and coalescence efficiency P_C as in Prince and Blanch (1990)

$$a = \begin{cases} \theta_{j,k} P_C(d_j, d_k) \\ \theta_{j,k} = 0.089 \pi n_j n_k (d_j + d_k)^2 (\epsilon_{\text{mixt}}^{sgs})^{1/3} (d_j^{2/3} + d_k^{2/3})^{1/2} \\ P_C(d_j, d_k) = \exp\left[-\dfrac{\left(\dfrac{r_{j,k}\rho_{\text{mixt}}}{16\sigma}\right)^{1/2} (\epsilon_{\text{mixt}}^{sgs})^{1/3} \ln\dfrac{h_0}{h_f}}{r_{j,k}^{2/3}} \right] \\ r_{j,k} = \left[\dfrac{1}{2}\left(\dfrac{2}{d_j} + \dfrac{2}{d_k}\right)\right]^{-1} \\ h_0 = 10^{-4}\text{m} \\ h_f = 10^{-8}\text{m} \end{cases} \tag{3.44}$$

The breakage source and sink term were expressed under the hypothesis that a mother bubble splits into two identical daughter bubbles with half of the volume:

$$B_i = \sum_j^N 2n_j b(x_j) - b(x_j)n_i \tag{3.45}$$

where $b(x_j)$ was the breakup frequency of Martìnez-Bazàn et al. (1999a,b)

$$b(x_j) = 0.25 n_j \frac{\sqrt{8.2(d_j \epsilon_{\text{mixt}}^{sgs})^{2/3} - 12\sigma/(\rho_{\text{mixt}} d_j)}}{d_j} \tag{3.46}$$

It should be noted that, in both models, the physical phenomena are driven by the turbulence field of the mixture phase through $\epsilon_{\text{mixt}}^{sgs}$.

The degassing of bubbles was modeled as in Hänsch et al. (2012) wherein it was assumed that dispersed bubbles immediately turn into (continuous) air when they reach the free surface. The transfer rate of mass from every class to air phase was expressed as

$$D_i = \frac{\varphi_{\text{air}} \rho_i \alpha_i}{a_t \Delta t} \tag{3.47}$$

where Δt was the time step of the simulation and $a_t = 50$ a constant. The term φ_{air} was a blending function detecting the continuous air field above the free surface. It was given by

$$\varphi_{\text{air}} = 0.5 \tanh[100(\alpha_{\text{air}} - 0.5)] + 0.5 \tag{3.48}$$

The air entrainment was reproduced by a sub-grid scale model which essentially was a volume source/sink term added to the continuity equations of classes and air. The model of Derakhti and Kirby (2014) was adopted wherein the authors related the air entrainment rate to the dissipation rate $\epsilon_{\text{mixt}}^{sgs,SI}$ as follows

$$E_i = \frac{c_{en}}{4\pi} \frac{\rho_{\text{mixt}}}{\sigma} \alpha_{\text{mixt}} \left(\frac{s_i l_i}{\sum_i^N (\frac{d_i}{2})^2 s_i l_i} \right) \epsilon_{\text{mixt}}^{sgs,SI} \tag{3.49}$$

where:

- c_{en} was a parameter which regulated the amount of entrained bubbles;
- s_i was the size spectrum of entrained bubbles (a_h = 1 mm is the Hinze scale)

$$s_i = \begin{cases} \left(\frac{d_i}{2}\right)^{-\frac{10}{3}} & \text{if } \left(\frac{d_i}{2}\right) > a_h \\ \left(\frac{d_i}{2}\right)^{-\frac{3}{2}} & \text{if } \left(\frac{d_i}{2}\right) \leq a_h \end{cases} \tag{3.50}$$

Bubbles were entrained *at the free surface cells* when $\epsilon_{\text{mixt}}^{sgs,SI}$ was larger than a fixed value. This threshold was needed to "switch on" the air entrainment mechanism only during the active breaking when bubbles form actually. In fact, the term s_i was consistent with the bubble size distribution observed in Deane and Stokes (2002) (see Section 1.1.2).

An important aspect is now remarked. This formulation essentially related the entrainment to the sub-grid dissipation rate which was in according with the fact the simulated bubbles were smaller than the grid size. Moreover, the formulation assumed that the entrainment was induced by turbulence activity at the free surface, which implied that the air entrainment caused by the jet impingement and successive air cavity fragmentation was in principle not reproducible in plunging breaking waves. Nevertheless, the focus of this study was on spilling waves, therefore the model was believed suitable. Both c_{en} and the threshold for $\epsilon_{\text{mixt}}^{sgs,SI}$ needed to be calibrated by comparison with experimental measurements of void fraction.

In conclusion, the term S_i representing the inter phase mass exchange was given by:

$$S_i = B_i + C_i + D_i + E_i \tag{3.51}$$

It is stressed that terms B_i and C_i were zero for water and continuous air phase.

3.2 The CFD solver

The solver was built by the means of the open-source CFD software OpenFOAM (version 2.3.1). This is essentially a package of C++ libraries which can be flexibly assembled for creating numerical solvers of continuum problems. OpenFOAM is based on the framework of the *finite volume method* (FVM) and it can support unstructured meshes for arbitrary complex geometries (Weller et al., 1998).
As any other CFD solver implemented in the OpenFOAM environment, the developed one consisted of (Rusche, 2003, Marschall et al., 2011)

- **Spatial and temporal discretisation**. The spatial domain was split in control volumes (CV, or cells). Similarly, the time domain was divided in time steps;

- **Equations discretisation**. The model equations were first integrated over each control volume. By applying the Gauss' theorem, the resulting volume integrals were translated into surface integrals which were calculated by interpolating the cell-centered values to the CV surfaces. This procedure led to a set of algebraic equations which held for each cell-centered values and were written in terms of neighboring cell values;

- **Solution of the discretized equations**. The cell-centered values were calculated by solving the coupled algebraic equations with an algorithm that ensured accuracy and correctness of results.

For the discretisation of the model equations, OpenFOAM adopts a *second-order* accurate finite volume method which is a good compromise between accuracy and computational cost. This procedure requires the employment of *differencing schemes* for interpolating the cell-centered values to the cell faces. These face values can be expressed:

- in terms of the old time-level cell values (*Euler explicit*);

- in terms of the new time-level cell values (*Euler implicit*);

- as arithmetic mean from the cell values at both the old and the new time levels (*Crank-Nicholson method*).

The theory concerning the domain and the equation discretization within the second order finite volume method is not given here as it can be found in several works (Jasak, 1996, Ubbink, 1997, Rusche, 2003, Marschall et al., 2011, Márquez Damián, 2013). Instead, the adopted discretised form of Eqs. 3.14-3.16 is reported in the following along with a brief description of the differencing schemes employed in this work.

3.2.1 Equation discretisation and differencing schemes

The illustration of the discretised Eqs. 3.14-3.16 implemented in OpenFOAM needs the following definitions:

- old is the old time step;

- new is the new time step;

- the subscript f indicates the value interpolated at the face of the cell;

- $\mathbf{S}_f$ is the outward pointing face area vector normal to the face f;

- $F_i = \alpha_{i,f}\mathbf{u}_{i,f} \cdot \mathbf{S}_f$ is the face mass flux.

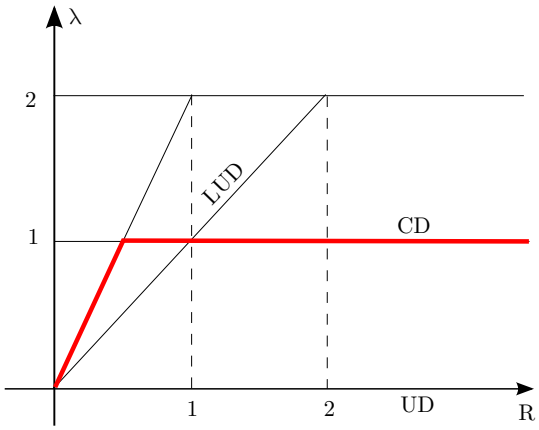

Figure 3.5: The *limitedLinear* scheme represented in the Sweby's diagram (Sweby, 1984)

.

Moreover, it is necessary to clarify the concept of high-order differencing schemes (HRS) within the *flux-limiting* scheme framework (Jasak, 1996, Márquez Damián, 2013). Flux-limiting is a switching methodology in which the discretisation practice depends on the local characteristics of the solution. In practice, the face-value of a generic quantity Φ can be calculated as the sum of the flux by the upwind scheme (UD) and a second-order antidiffusive flux from a combination of the linear (CD,Lax and Wendroff (1960)) and the linear upwind scheme (LUD, Warming and Beam (1976)):

$$\Phi_f = \Phi_{\text{UD}} + \lambda\Phi_{(\text{CD+LUD})} \tag{3.52}$$

where the limiter λ is a function of a local parameter R which can "detect" the characteristics of the flow. If the flow is such that the solution could be unbounded, hence unstable, λ is decreased. For $\lambda = 0$, the scheme is upwind solely.
The HRS are implemented in OpenFOAM as follows:

$$\Phi_f = (1-\lambda)\Phi_{\text{UD}} + \lambda\Phi_{\text{CD}} \tag{3.53}$$

The different schemes differentiate from the "shape" of the limiter that is the function $\lambda = \lambda(R)$. In the present work, the *limitedLinear* scheme gave the limiter as

$$\lambda = \max[\min(2R, 1), 0] \tag{3.54}$$

which can be depicted as in Fig. 3.5. If R is negative, λ=0 and the scheme is UD. If R is positive, λ=1 at maximum which corresponds to CD. It is known that UD is first-order accurate, unconditionally stable and diffusive, whereas CD is second-order accurate buy it does not guarantee boundedness.

Continuity equation 3.13

$$\sum_f \sum_{i=1}^{N+1} \alpha_{i,f} \mathbf{u}_{i,f} \cdot \mathbf{S}_f = \sum_f \sum_{i=1}^{N+1} F_i = 0 \tag{3.55}$$

This summation comprises the N classes and the mixture phase, because, as it will be seen further, it is calculated after the resolution of the coupled $N+1$ momentum equations.

Interface transport equation 3.16

The interface transport equation 3.16 was first rewritten in terms of $\mathbf{U}$ and $\mathbf{U}_r$ and then discretised as follows:

$$\frac{\alpha_i^{new} - \alpha_i^{old}}{\Delta t} + \frac{\sum_f \alpha_{i,f}^{old} \left(\sum_{j=1}^{N+2} F_j^{old} \right)}{V} + \frac{\sum_f \alpha_{i,f}^{old} \left(\sum_{j=1, j\neq i}^{N+2} \alpha_{j,f}^{old} \mathbf{U}_{r,f}^{old} \cdot \mathbf{S}_f \right)}{V} = S_i^{old} \tag{3.56}$$

- the Euler explicit method was applied for the time integration which is first order accurate and stable if the Courant number Co is smaller than one;
- the time-derivative term was first-order approximated;
- in the first convective term, the face-value $\alpha_{i,f}$ was obtained with the *MUSCL* HRS scheme (Van Leer, 1997);
- in the second convective term, the face-value $\alpha_{j,f}$ was given by the *interface-Compression* scheme (see Deshpande et al. (2012), Márquez Damián (2013)). For the phase pair water-air, $\mathbf{U}_{r,f}^{old}$ is zero because of the no-slip condition Eq. 3.10. Nevertheless, this second convective term is important because it has the effect of compressing the interface counteracting the numerical diffusion in the solution of the phase fraction field. Following the approach of Weller (2008), the term was recovered through the compression velocity $\mathbf{U}_{c,f}$ given by

$$\mathbf{U}_{c,f}^{old} \cdot \mathbf{S}_f = \min \left[C_\eta \left\| \frac{\left(\sum_{j=1}^{N+2} F_j^{old} \right)}{\mathbf{S}_f} \right\|, \max \left(\left\| \frac{\left(\sum_{j=1}^{N+2} F_j^{old} \right)}{\mathbf{S}_f} \right\| \right) \right] \left(\mathbf{n}_I \cdot \mathbf{S}_f \right) \tag{3.57}$$

  The direction of the compression velocity was normal to the interface because of term $\mathbf{n}_I$ which was defined in such a way that the compression velocity could vanish far from the free surface. The constant C_η was specified by the user and $C_\eta = 1$ was chosen in this work.

Momentum equation 3.14

The equation is written for a phase i of the N classes. The equation for the mixture phase is analogous, but it contains the sum of the momentum exchanges with all N classes.

$$\begin{aligned}
&\frac{\rho_i^{new}\alpha_i^{new}\mathbf{u}_i^{new}-\rho_i^{old}\alpha_i^{old}\mathbf{u}_i^{old}}{\Delta t}+\frac{\sum_f\left[\mathbf{u}_{i,f}^{new}\left(\rho_{i,f}^{old}F_i^{old}\right)\right]}{V}=\\
&\frac{\sum_f\left(\alpha_i^{new}\mu_{eff,i}^{new}\right)_f\left(\nabla\otimes\mathbf{u}_i^{new}\right)_f^{\perp}}{V}+\frac{\sum_f\left\{\alpha_i^{new}\mu_{eff,i}^{new}\left[\left(\nabla\otimes\mathbf{u}_i^{old}\right)^T\right]^{\mathrm{dev}}\right\}_f}{V}+\\
&+\mathbf{M}_{L,i}^{old}+\mathbf{M}_{TD,i}^{old}+\\
&+\left(\rho_{\mathrm{mixt}}^{new}\alpha_i^{new}\alpha_{\mathrm{mixt}}^{new}C_{VM}\frac{\mathrm{D}\mathbf{u}_{\mathrm{mixt}}^{old}}{\mathrm{D}t}+\rho_{\mathrm{mixt}}^{new}\alpha_i^{new}\alpha_{\mathrm{mixt}}^{new}C_{VM}\frac{\mathrm{D}\mathbf{u}_i^{new}}{\mathrm{D}t}\right)
\end{aligned}\tag{3.58}$$

- the Euler implicit method was applied to the convective term. The scheme is first order accurate and unconditionally stable. The face-value $\mathbf{u}_{i,f}$ was obtained with the *limitedLinear* scheme;
- the effective stress tensor was handled semimplicitly. The term was split in two contributions: one was treated with the Euler implicit (first term on the r.h.s.) and the other explicitly (second term on the r.h.s). The face value $\alpha_i^{new}\mu_{eff,i}$ was expressed with the CD scheme. For the surface normal gradient of $\mathbf{u}_i$, the CD scheme was applied with an explicit correction for non-orthogonal meshes;
- the lift and the turbulent dispersion force were explicit (Rusche, 2003);
- the virtual mass force was split into two parts (Rusche, 2003): one was explicit (fifth term on the r.h.s.) and the other was implicit (sixth term on the r.h.s);
- the time-derivative term was first-order approximated;
- the drag force and the terms involving gravity acceleration and pressure do not appear here because they were treated differently (see Section 3.2.2);
- It should be noted that Eq. 3.14 becomes singular when the phase fraction α_i approaches zero. To overcome this issue, the *phase-intensive* form of Rusche (2003) is generally implemented. In this work, the treatment in Wardle and Weller (2013) was instead adopted. In practice, if the void fraction of a phase was smaller than a user-specified limit value (generally 1e-03), a "residual drag" was still calculated as a function of this void fraction threshold and of an user-specified "residual slip" (generally 1e-03 m s^{-1}). The artificious "residual drag"

did not affect the results and stabilized the phase momentum coupling. It is stressed that the residual value of the void fraction was not taken into account in the resolution of the continuity equations.

It should be noted that both Eq. 3.56 and Eq. 3.58 are systems where every row represents one algebraic equation for each cell of the domain.

3.2.2 The solution procedure

The most important steps of the solution procedure are illustrated in Fig. 3.6 .

- **domain discretisation**. It is realized by a mesh tool provided in the OpenFOAM package;
- **input files reading**. Files with initial values and boundary conditions for α_i and $\mathbf{u}_i$ are needed for all N+2 phases as well as for p^d, $\nu_{\text{mixt}}^{sgs,SI}$ and k_{mixt}^{sgs}. Moreover, an other single input file is read with a list of properties of each phase: diameter, density, viscosity, drag, lift, virtual mass, turbulence dispersion force formulation, "residual" void fraction and "residual" velocity;
- **mixture phase creation**. The mixture phase is created (Eqs. 3.10-3.12);
- **turbulence field updating**. Based on the calculated $\mathbf{u}_{\text{mixt}}$, ν_{mixt}^{sgs} and k_{mixt}^{sgs} are updated (Eqs. 3.33- 3.34). Moreover, the total dissipation rate $\epsilon_{\text{mixt}}^{tot}$ is determined (Eq. 3.32) since it is needed for expressing the source term of Eq. 3.56;
- **interface transport equations resolution**. The MULES algorithm solves Eq. 3.56. The void fractions of all N+2 phases are computed ensuring that $\sum_i^{N+2} \alpha_i = 0$. Details about how this algorithm works for a two-phase system can be found in Márquez Damián (2013). The extension of MULES for multiphase flows followed the work of Wardle and Weller (2013);
- **mixture phase updating**. Density and viscosity of the mixture phase are updated in according to the new values of α_{w} and α_{air} (Eqs. 3.11-3.12);
- **momentum equations resolution**. The PISO algorithm (Issa, 1986) solves the pressure-velocity coupling under the crucial assumption that it is much stronger than the non-linear coupling in the convection term. This hypothesis was definitely reasonable in this study as the resolution of Eq. 3.56 required very small time steps, hence the non-linearity could be assumed to vary slowly. PISO is a segregated approach which means that the equations are solved sequentially and not simultaneously. Details of the different steps can be found in (Jasak, 1996, Marschall et al., 2011, Márquez Damián, 2013). It is stressed that the drag

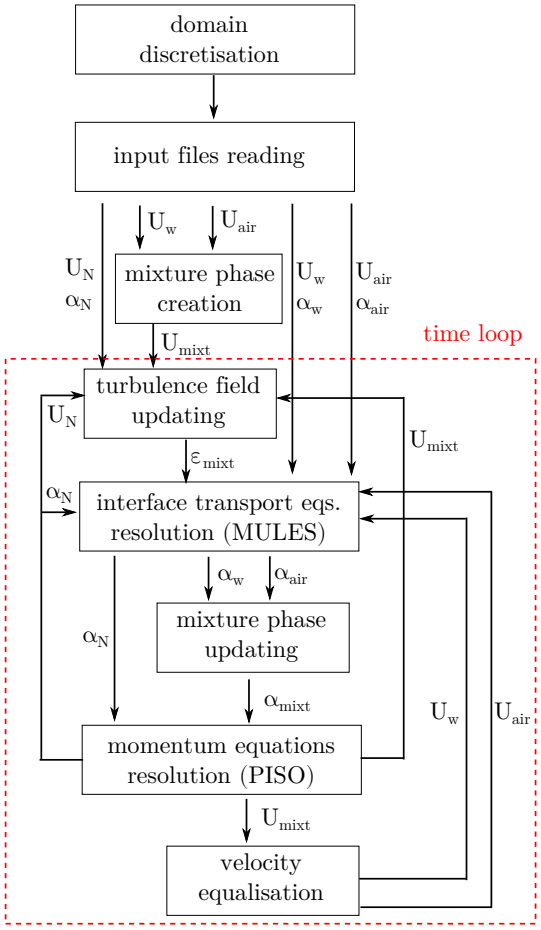

Figure 3.6: Flow chart of the developed CFD solver.

force and the gravity terms, that were excluded in the discretisation of Eq. 3.58, are reintroduced as fluxes during the PISO iterations (*in the spirit of Rhie-Chow* Rhie and Chow (1983)). At the end of this step, pressure p^d, velocities of classes $\mathbf{u}_i$ and velocity of mixture $\mathbf{u}_{\text{mixt}}$ are known;

- **velocity equalisation** The no-slip condition Eq. 3.10 is applied again for determining $\mathbf{u}_{\text{w}}$ and $\mathbf{u}_{\text{air}}$ that are needed by MULES in the new time iteration, whereas the new value of $\mathbf{u}_{\text{mixt}}$ is used in the turbulence field updating step.

The CFD solver could be configured to work without taking into account the motion of bubble classes. This modality could be realized by "switching off" the air entrainment formulation either using $c_{en} = 0$ or applying a very large threshold for $\epsilon_{\text{mixt}}^{sgs,SI}$ in Eq. 3.49. As another option, it was also possible to exclude bubbles from the simulation at the input step.

3.3 Some remarks about the numerical methodology

Now that all elements of the methodology have been given, it is possible to expatiate upon some important questions which arose during the development process.

3.3.1 Issues in the implemented VOF model

Either under the configuration without classes or with classes but far from the breaking region, the sum of the bubble void fractions is zero. In such cases, the CFD solver gave substantially *the same results* of the VOF solver `interFoam`, already implemented in OpenFOAM (version 2.3.1). In other words, the VOF solution of the developed CFD solver is *as accurate as* the state of the art in the OpenFOAM environment. Nevertheless, this had also a negative implication. In fact, although `interFoam` has been widely used in both research and industry, it is well known that it suffers from some large unphysical (*spurious*) velocities at the free surface in the air phase. The developed CFD solver suffered from the same issue. This section not only shows the effects of the spurious velocities, but it wants also to stress that they were "inherited" from `interFoam` whose VOF approach was adopted in the present study.

In order to show these spurious velocities, the following test case was set-up. A 2D domain 1.5 m high by 1.5 m wide in the vertical x-z plane was discretised with a uniform mesh of cell size 0.01 m and it was filled with water up to z = 0.6 m. Air and water phase were considered inviscid and the surface tension was neglected. The case was hydrostatic because no external forces were applied, except the gravity. A simulation was performed both with `interFoam` and the present CFD solver (no bubbles). Figure 3.7 depicts the void fraction and the magnitude of the velocity after 10 seconds respectively. Although the free surface was horizontal and stable, it is clearly recognisable that the hydrostatic conditions did not hold as a velocity field developed, especially in the air phase. Moreover, it can be noted the both models gave almost identical results.

Vukčević (2016) explained the origin of the spurious velocities as follows. For the simulated test case, momentum equation 3.14 can be rewritten as

$$\frac{\partial(\rho\mathbf{u})}{\partial t} = -\nabla p_d - (\mathbf{g}\cdot\mathbf{x})\nabla\rho \tag{3.59}$$

The r.h.s. of the equation above can be seen as a jump condition at the interface for the dynamic pressure. Since `interFoam` as well as the present CFD solver are segregated solvers, a natural imbalance between gradient of dynamic pressure and gradient of density is produced (at the free surface). In fact, pressure and density

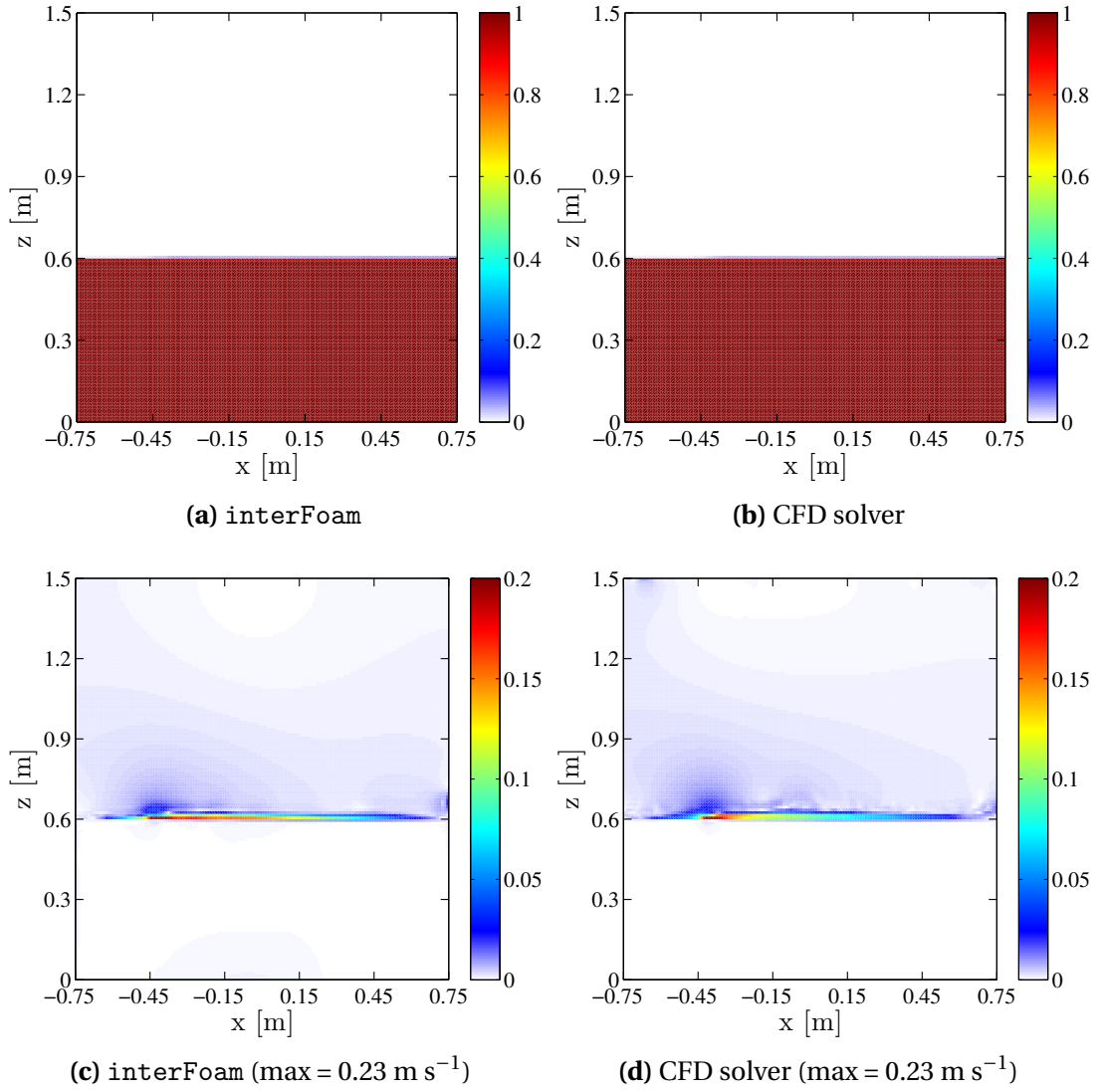

(a) `interFoam` **(b)** CFD solver

(c) `interFoam` (max = 0.23 m s^{-1}) **(d)** CFD solver (max = 0.23 m s^{-1})

Figure 3.7: Void fraction (top) and magnitude of velocity (bottom) at t = 10 s.

are not resolved simultaneously. Therefore, the prediction of the velocity from the momentum equation, that is before the resolution of the pressure, is affected by this inconsistency. This implies

$$\frac{\partial(\rho\mathbf{u})}{\partial t} \neq 0 \tag{3.60}$$

which means that a velocity field develops in time and especially in the air phase because it is lighter than water ($\mathbf{u}$ is given by the r.h.s. of Eq. 3.59 divided by density).

Furthermore, the inconsistency in Eq. 3.59 is increased if the density and the dynamic pressure gradient are determined with ordinary discretisation schemes that

cannot take into account the discontinuity at the free surface. In the simulated case, neither `interFoam` nor the developed CFD solver were provided with such schemes.

As reported in Vukčević (2016), the spurious velocities are different than the so-called *parasitic currents* which constitute another issue of originating from the numerical representation of the surface tension effect `interFoam` (Deshpande et al., 2012, Scardovelli and Zaleski, 1999). The parasitic currents were not important in this study. It is reminded that action of the surface tension was not modeled for bubbles since their interfaces were not reconstructed, whereas it was taken into account at the free surface where the curvature is very small though (Eq. 3.41).

On the other hand, the existence of spurious velocities was a concern because they develop right at the free surface where the air entrainment takes place. Furthermore, simulations by the means of `interFoam` have shown that waves can break prematurely (Jacobsen et al., 2012) or even nonphysically, that is when the breaking process is not supposed to happen (Amini Afshar, 2010). The spurious velocities may be among the causes of both occurrences because they affect the kinematics of the wave front.

An example of distorted wave propagation is now presented. The case had the following properties:

- Domain: a 2D wave flume 18 m long and 1.2 m high with flat bottom;
- Discretisation: uniform mesh of cell size 0.01 m;
- Wave: Stokes 5^{th} order with $H = 0.01$ m and $T = 0.767$ s;
- Initial conditions: still water (depth $d = 1$ m).

The surface elevation η along the flume at $t = 14$ s is displayed in Fig. 3.8. The comparison with the analytical solution is quite good until $x = 7$ m, thereafter an unphysical shoaling-like process is visible. The breaking point is located at around $x = 9.5$ m. Figure 3.9 depicts the profiles of the horizontal velocity at $x = 9$ m under a crest at $t = 8.35$ s and the successive trough.
The comparison with the analytical profile is good up to the wave top where spurious velocities manifested as a sort of *overshooting*. Similar observations are in Wroniszewski et al. (2014) where the role of the compression velocity in Eq. 3.57 was also investigated.

As shown in Vukčević (2016), the spurious velocities can be eliminated by solving the pressure-density coupling inside the pressure equation and by employing discretisation schemes corrected for handling the discontinuity at the free surface.

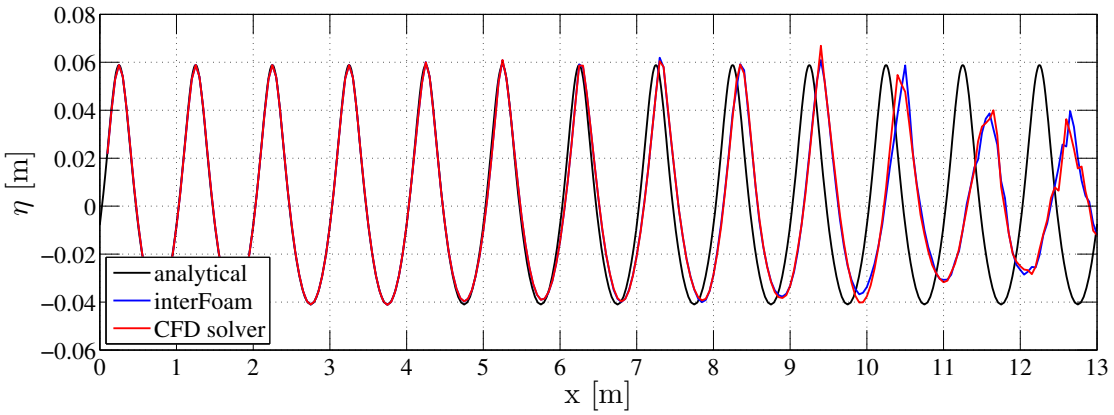

Figure 3.8: Surface elevation at $0 \leq x \leq 13$ m and at $t = 14$ s.

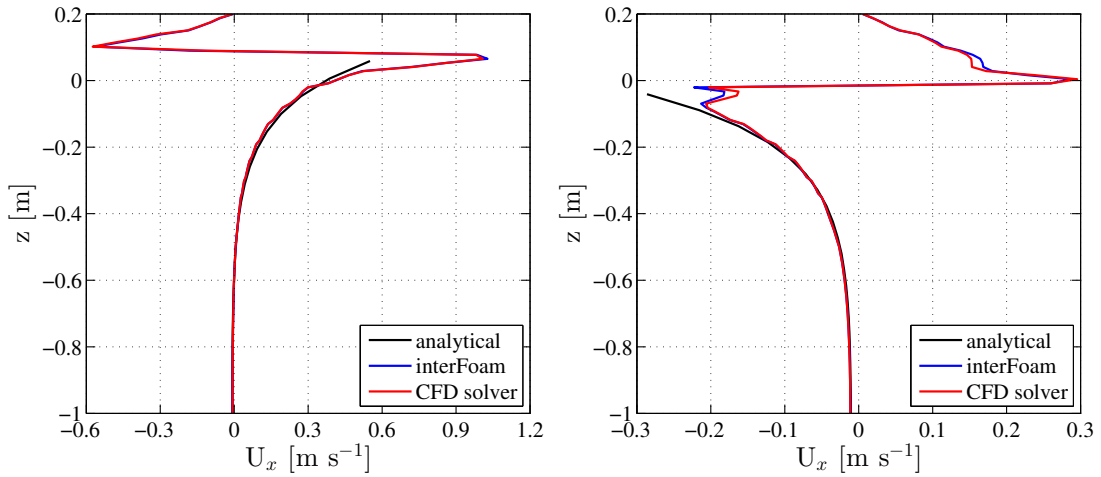

(a) Under the wave crest

(b) Under the wave trough

Figure 3.9: Horizontal velocity profiles along the depth of the flume at $x = 9$m.

The research of a method for eliminating the problem was beyond the scope of the present study. Nevertheless, some precautions were used in the numerical settings of simulations in order to mitigate the effects.

3.3.2 Why the Eulerian multiphase model?

The necessity of taking into account the polydispersion of the entrained air excluded the Euler-Euler model. The use of the Eulerian multiphase approach was neither the only option nor the cheapest computationally. The drawback of the Eulerian multiphase is the large number of coupled continuity and momentum equations to be solved. It will be seen in the next chapters that a number of classes up to 14 was used, corresponding to 16 continuity equations (considering also water and contin-

uous air) and 15 momentum equations (classes and mixture phase). Therefore, the computational cost of the developed solver was high.
As reported in Section 1.2, different methodologies for dispersed flows were available. Excluding the Lagrangian Point-Particle and the DNS approach which would have been more expensive in this study, the Dusty Gas and the Equilibrium Eulerian could have been an option. Both are computationally cheaper than the Eulerian multiphase because some assumptions are made for the bubble velocities. In particular, the Dusty Gas assumes that bubbles have the same velocity and equal to the water velocity. This assumption can be done when bubbles are really small and do not affect the water flow. For bigger bubbles, the Equilibrium Eulerian models the bubble velocities through some expressions function of the bubble size and the velocity of water. An example of application for air entrainment in waves can be found in Shi et al. (2010). The advantage of both models lies on the fact that momentum equations for bubbles are not solved.

From the theoretical point of view, the suitability of the mentioned models for the purpose of this study could be assessed through the procedure in Balachandar and Eaton (2010) as follows. To parametrize the behaviour of a single bubble dispersed in water, the authors used the *Stokes number St* which is the ratio of the characteristic bubble timescale $\tau_{b,i}$ to a characteristic timescale of the flow τ_Δ. The larger St, the less bubbles follow the flow of water. Balachandar and Eaton (2010) expressed St as

$$St_i = \frac{\tau_{b,i}}{\tau_\Delta} = \left[\frac{2\left(\frac{\rho_{air}}{\rho_w}\right)+1}{36}\right]\left(\frac{1}{1+0.15Re_i^{0.687}}\right)\left(\frac{d_i}{\Delta}\right)^2\left(\frac{\Delta}{\eta_k}\right)^{4/3} \tag{3.61}$$

where η_k is the Kolmogorov microscale.

For a case representative of the numerical simulations performed in this study, the range of suitability of each model could be expressed as in Fig. 3.10. It is stressed that the lower St limit of each range indicates the point at which the application of the model is not convenient anymore, but still allowed. Therefore, the Equilibrium Eulerian model could have been chosen for predicting the motion of the smaller classes with good accuracy, but at the same time it could not have been suitable for the bigger ones. The Eulerian multiphase model could be capable of handling the motion of all classes.

The number of classes used in the performed simulation could have been reduced by the employment of a more efficient method for handling the bubble population balance equation than the method of classes. As example, given the same width of the

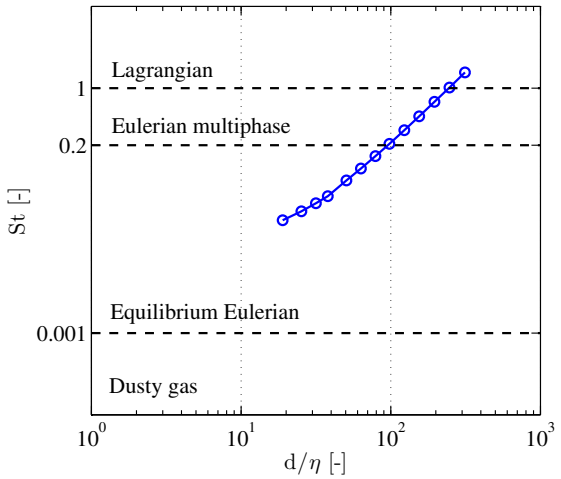

Figure 3.10: Stokes number versus nondimensional particle size. The range of applicability of each model is comprised between the dashed horizontal lines.

bubble size range, the Direct Quadrature Method of Moments (DQMOM) (Marchisio and Fox, 2005) requires less classes to describe the evolution of the size distribution, given the same width (Bannari et al., 2008, Selma et al., 2010). Nevertheless, the implementation of this method was left for future improvements of the solver.

3.3.3 Was the already existing `multiphaseEulerFoam` suitable for this study?

OpenFOAM (version 2.3.1) was provided with the hybrid VOF-Eulerian CFD solver called `multiphaseEulerFoam` of Wardle and Weller (2013). This model could flexibly predict the flow of multiple phases with interfaces both dispersed and segregated within the Eulerian multiphase approach. The (static) coupling consisted of an optional numerical compression of any interface, between a pair of phases, that was expected to be segregated.

The suitability of the coupling implemented in `multiphaseEulerFoam` was evaluated at the beginning of the development process (Tomaselli and Christensen, 2015). A bubble column flow (as in Section 4.1) and a solitary breaking wave were performed. In the former case, the model correctly handled the free surface and the bubble motion. Instead, the latter case showed some issues regarding the representation of the free surface. Although it was almost as sharp as the one obtainable with the *pure* VOF solver implemented in OpenFOAM, the wave profile exhibited some unphysical undulations at the crest.

In the author's opinion, these instabilities originated from the modeling of the

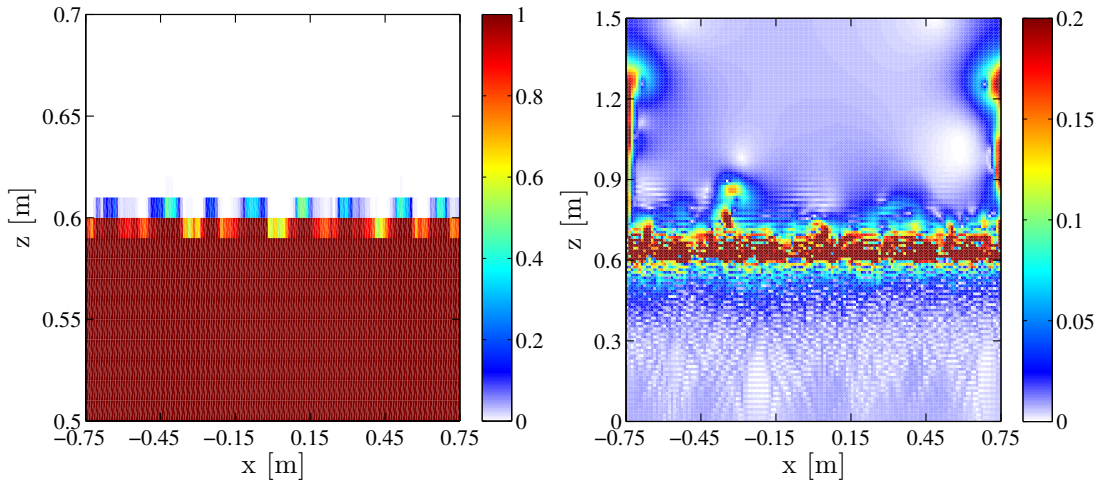

(a) Void fraction **(b)** Magnitude of velocity (max = 2.35 m s^{-1})

Figure 3.11: Results at t = 10 s of the simulation performed by `multiphaseEulerFoam`.

momentum exchange between water and continuous air at the free surface and especially of the drag force contribution. In fact, `multiphaseEulerFoam` treated *all* N+2 phases as dispersed. Numerically, this implicated that momentum transfers (drag, lift, virtual mass, turbulent dispersion) among all phases had to be modeled, *also* between water and continuous air (contrarily to the actual CFD solver). In order to obtain a VOF-type solution for the motion of the free surface, the optional numerical compression was applied for the water-continuous air pair. The undulations were caused by the fact that `multiphaseEulerFoam` was not provided with any models for drag force between stratified phases as in Marschall et al. (2011), but it used the formulation of Schiller-Naumann (Eq. 3.36) which is actually valid for dispersed bubbles.

For the sake of completeness, the hydrostatic case presented in Section 3.3.1 was performed also by `multiphaseEulerFoam`. Results are reported in Fig. 3.11. The comparison with Figs. 3.7b-3.7d clearly reveals that the direct imposition of the no-slip condition was crucial for the stability of the free surface. In particular, the undulations at the free surface mentioned above are visible.

In conclusion, the coupling of `multiphaseEulerFoam` was not believed applicable for the objectives of the present study where a sharp and stable free surface was essential. However, its Eulerian multiphase framework was largely used for developing the CFD solver in object.

3.3.4 Why was the air assumed incompressible?

The compressibility of the air phases was neglected because of the following reasons:

- the present model was optimized for spilling wave impacts on slender monopiles, therefore air pockets were not supposed to be entrapped between the wave front and the surface of the structure;
- numerical simulations were conducted at a laboratory scale, therefore impact pressures were expected close to the atmospheric value;
- although the speed of sound in the roller is supposed to be reduced compared to the value both in pure water and in pure air, velocities at a laboratory scale are such that the Mach number results smaller than 0.3 which is the limit of validity of the incompressible flow assumption.

4 Validation: part I

The validation process of the CFD solver needed to cover many aspects because of the coupling of two different models. Firstly, the two approaches were tested separately and results are reported in this chapter. Note that this *does not* mean that the Eulerian multiphase and the VOF model were not coupled, rather that the CFD solver was employed in case studies that "stressed" one approach more than the other.

In this first part, the validation involved two experimental cases: a bubble column flow and the breaking of regular waves. In the former, the focus was on the capability of the Eulerian multiphase framework of predicting the bubble motion and the turbulence field of the water phase. The latter was simulated in order to test the VOF algorithm.

An important remark is that all simulations of this chapter were performed with the air entrainment formulation "switched off" as explained in Section 3.2.2.

4.1 A bubble column flow

Bubble column reactors are widely used in chemical, petrochemical and biochemical processes and a huge research has been carried out on CFD simulations of bubble column flows (Bannari et al., 2008, Selma et al., 2010, Ojima et al., 2014). In the context of the present study, this case was chosen not only to test the implementation of the Eulerian multiphase framework, but also for performing a sensitivity analysis of the adopted closure terms (Section 3.1.4).

The bubble column flow experimentally investigated by Deen et al. (2000) was modeled. The column had a square cross-section of 0.15×0.15 m^2 and a height of 1 m, filled with water up to 0.45 m (Fig. 4.1). Air was fed into the column via a diffuser plate placed at the bottom. The set of experimental data used for this validation consisted of:

- instantaneous axial water velocity measured at the horizontal centerline of the

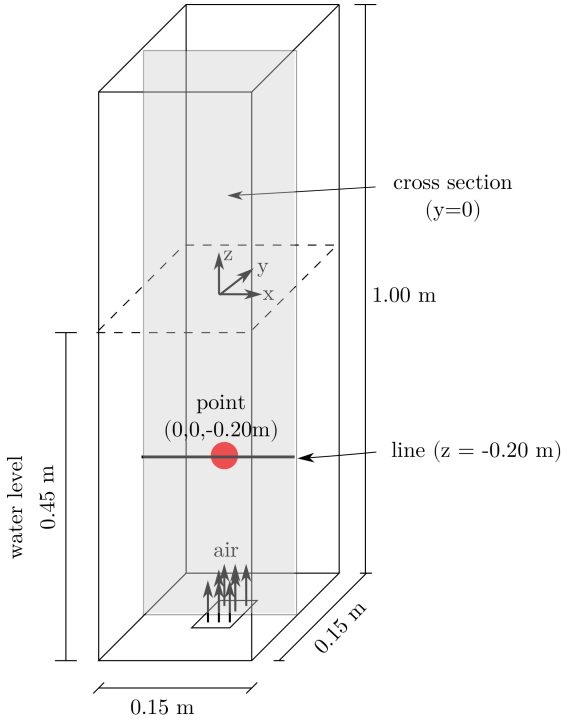

Figure 4.1: Experimental setup in Deen et al. (2001).

column at a height of 0.25 m from the bottom;

- horizontal distribution of the mean axial water velocity at a height of 0.25 m from the bottom;
- horizontal distribution of axial and radial turbulence quantities (r.m.s. velocities) at a height of 0.25 m from the bottom;
- horizontal distribution of the Sauter mean diameter at a height of 0.25 m from the bottom (from Hansen (2009));

The case was set-up as follows:

- Mesh. Uniform 3D hexahedral mesh with 22550 cells of size 0.01 m;
- Number of phases. Water (w), air (air) and N=11 classes (b) with $0.001 \leq d_i \leq 0.01$ m;
- Boundary conditions. The diffuser plate at the bottom (inlet) was modeled by a central area of 0.03×0.03 m^2 from which only one dispersed bubble class with diameter $d = 0.004$ m was introduced from the bottom with $\alpha = 1$ and $u_z = 0.12$ m s^{-1}. This diameter was observed to be the mean bubble size, then it could

represent the hydrodynamical behavior of the whole bubble population (Deen et al., 2001). At the rest of the inlet, phase fractions and velocities were equal to zero for all phases. At the top (outlet), the atmospheric value was assigned to pressure and a backflow was allowed only for air (with velocity normal to the boundary). The other conditions are listed in Table 4.1.

- Drag force formulation. The Ishii-Zuber formulation (Eq. 3.37) was employed;
- Time range simulation. Simulation started at $t = 0$ s and ended at $t = 620$ s.

	$\mathbf{u}_{\text{mixt}}$	$\mathbf{u}_{\text{b},i}$	α_{w}	α_{air}	$\alpha_{\text{b},i}$	p_d	$\nu_{\text{mixt}}^{sgs,SI}$	k_{mixt}^{sgs}
inlet	D.	D.	D.	D.	D.	N.	D.	D.
walls	no-slip	no-slip	N.	N.	N.	N.	N.	N.
outlet	N./D.	N./D.	N./D.	N./D.	N./D.	D.	N.	N.

Table 4.1: Boundary conditions employed in the numerical simulations of the experiments in Deen et al. (2001). *N.* = Neumann (gradient equal to zero). *D.* = Dirichlet (fixed value). *N./D.* = Neumann for outflow and Dirichlet for inflow.

The choice of the grid needs to be expatiated. The derivation of the Eulerian multiphase model assumes that the control volume size comprises all interfacial scales. This constraint has to be obeyed also in the numerical applications of the model. The spatial filter, hence the cell size, should be in the inertial subrange of the turbulence spectrum in the LES approach. In order to meet both requirements, it was assigned the same value to the uniform cell size and to the upper limit of the bubble size range. However, Milelli (2002) suggested that the cell size must be at least 50% larger than the largest diameter in order to increase the accuracy of the LES computation.

Results presented in the rest of this section were averaged in time ($\bar{.}$), unless they are reported as instantaneous. The averaging operation started at $t = 30$ s in order to exclude the initialization of the flow.

The variation with the time of the axial water velocity is depicted in Fig. 4.2a. The turbulent character of the flow was captured consistently to Fig. 2 of Deen et al. (2001). Figure 4.2b shows the simulated and experimental axial water mean velocity. The agreement was very good. As expected, numerical values were more symmetric with respect to the axial line because, as noted in Deen et al. (2000), the sample period in the experiments was too short to obtain steady time averaged data. Moreover, it can

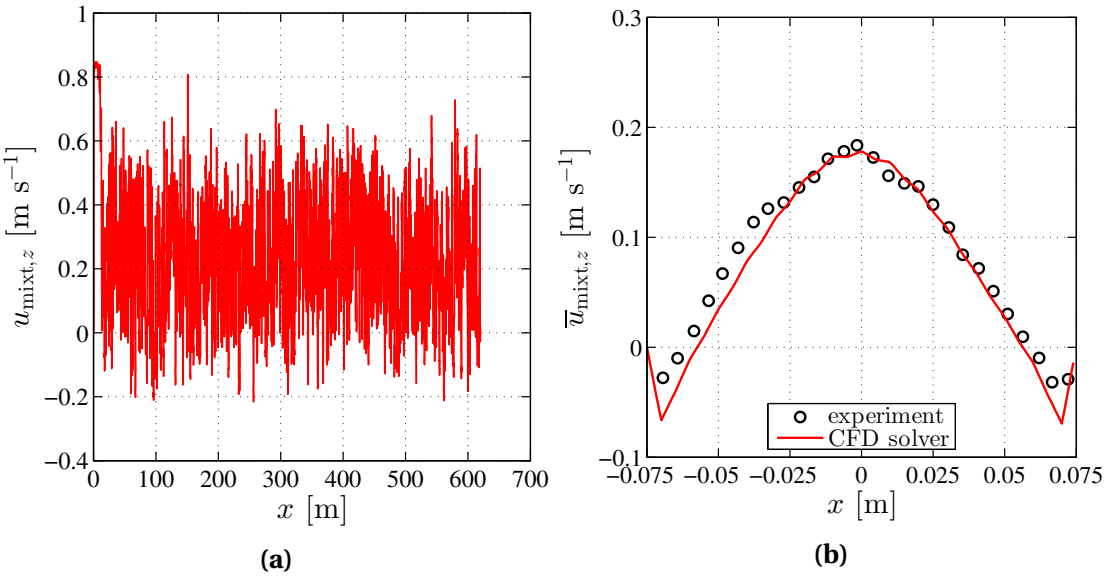

(a) **(b)**

Figure 4.2: Axial water velocity. (**a**) Instantaneous at (0.0, 0.0, -0.20) m. (**b**) Mean horizontal profile at z = -0.20 m.

be noted that the downflow of water alongside the plume was correctly reproduced.

The model was found to be reliable in predicting the turbulence levels. In Figure 4.3, the simulated and experimental mean turbulence levels and mean resolved turbulent kinetic energy ($\overline{k}^r_{\mathrm{mixt}}$) are reported. The r.m.s velocities were determined directly form the resolved velocity field. As in Deen et al. (2001), the TKE was calculated as $\overline{k}^r_{\mathrm{mixt}} = 0.5(\overline{u'^2}_{\mathrm{w},z} + 2\overline{u'^2}_{\mathrm{w},x})$.

The agreement for the r.m.s. velocities as well as for the TKE is good and the expected radial symmetry is recognisable. It is apparent from these figures that the grid size, hence the spatial filter of the LES model, was adequate to solve not only the mean flow, but also a large part of the turbulence scales. The sub-grid scale contribution to the total TKE was very small (not shown).

In this section and for the rest of the present work α_{b} indicates the (total) bubble phase fraction:

$$\alpha_{\mathrm{b}} = \sum_{1}^{N} \alpha_i \tag{4.1}$$

The horizontal distribution at z = -0.20 m of the simulated mean bubble phase fraction $\overline{\alpha}_{\mathrm{b}}$ is depicted in Fig. 4.4a. The study of Deen et al. (2000) did not report any measurements of α_{b}. The calculated values were consistent with the results of Bannari et al. (2008) and Selma et al. (2010) wherein similar bubble column flows were investigated. The distribution of the total bubble phase fraction along a horizontal centerline at a

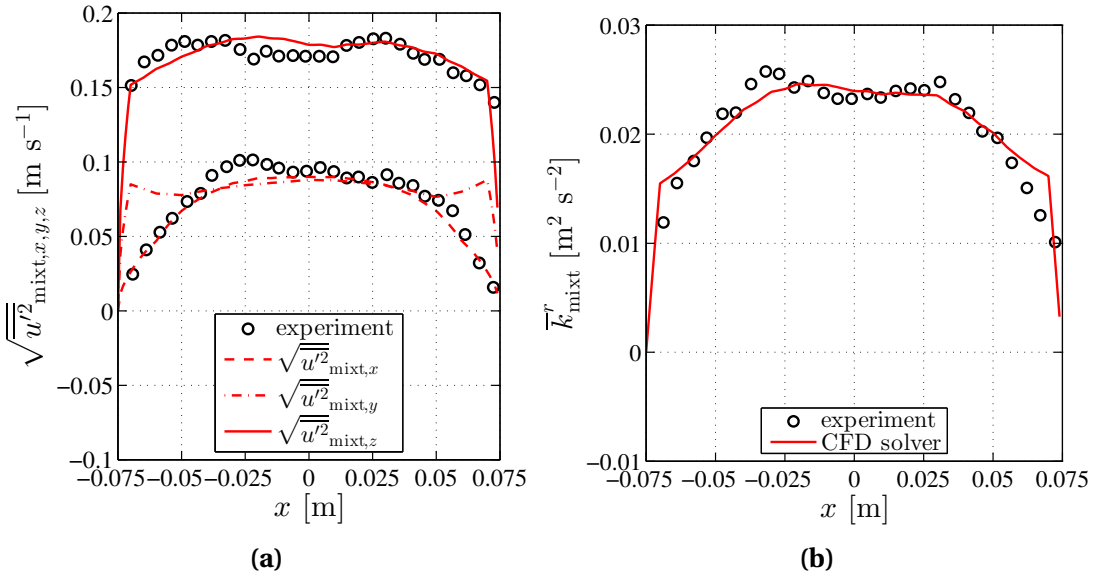

Figure 4.3: Turbulence quantities along the horizontal centerline at z = -0.20 m. (**a**) Mean turbulence levels. (**b**) Mean TKE.

certain elevation is commonly referred to as *gas hold-up*.

The bubble size distribution is commonly expressed through the *Sauter diameter* d_{32} which is given by

$$d_{32} = \frac{\sum_1^N \alpha_i}{\sum_i^N (\alpha_i / d_i)} \tag{4.2}$$

Figure 4.4b displays the distribution of the Sauter diameter at z = -0.20 m. The experimental values are from Hansen (2009). It is apparent that the overall comparison is good, but the prediction is worse at x = -0.060 m. The reason could be that the time-averaged values of the experimental measurements were not steady yet. However, the CFD solver reasonably predicted the fact that bigger bubbles moved in the middle of the column, whereas smaller ones approached the walls on average. As observed in Selma et al. (2010), bubbles tended to aggregated in the column center because coalescence dominated, while breakage was predominant close to the sides.

Figure 4.5 displays the instantaneous bubble phase fraction and Sauter diameter field at t = 620 s on the axial plane. It is possible to appreciate that:

- the meandering of the bubble plume observed in the experiments was captured. Bubbles were periodically pushed laterally by the lift force acting in the direction perpendicular to their rising velocity and, as a consequence, they drastically decelerated;

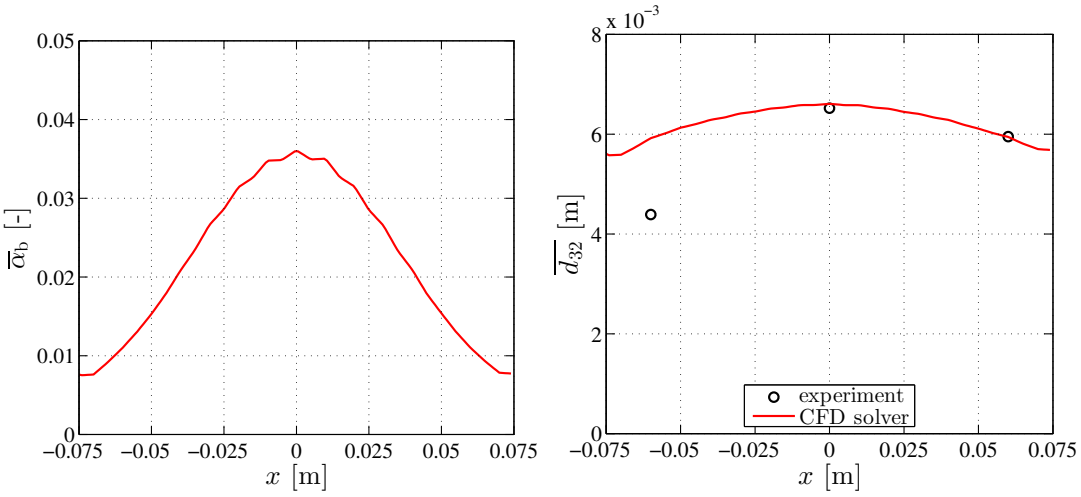

(a) **(b)**

Figure 4.4: Bubble distribution profile at z = -0.20 m. (**a**) Mean gas hold-up. (**b**) Mean Sauter diameter.

- the bubble motion produced large-scale eddies in water phase;
- the degassing formulation (Eq. 3.47) was effective as bubbles disappeared almost instantaneously as they reached the free surface (z = 0.0 m);
- the coupled VOF, which still worked in this simulation, guaranteed a stable free surface with limited spurious velocities. For consistency with the degassing model, it was assigned the diameter of the N^{th} class to the air above the free surface.

Figure 4.5b indicates that the Sauter diameter was mainly in the range $0.006 < d_{32} < 0.007$ m. It is important to note that this does not mean that the most part of bubbles had size in that range (at t = 620 s). The Sauter diameter is obtained with an average weighted with the void fraction of classes, hence is based on the volume and not on the number of bubbles.

The distribution of the mean number of bubbles is given in Fig. 4.6.

In agreement with the observations of Deen et al. (2000, 2001), the largest part of the bubble population had size of 0.004. Nevertheless, it is clear that the classes with diameter smaller than 0.004 m were not involved actually. This was due to the simplified breakage model (a bubble could split only into two bubbles with the same volume) combined to the fact that only bubbles with a diameter of 0.004 m were imposed as a boundary condition at the bottom. As investigated in Buwa and Ranade (2002), the representation of the diffuser plate at the bottom as well as the bubble

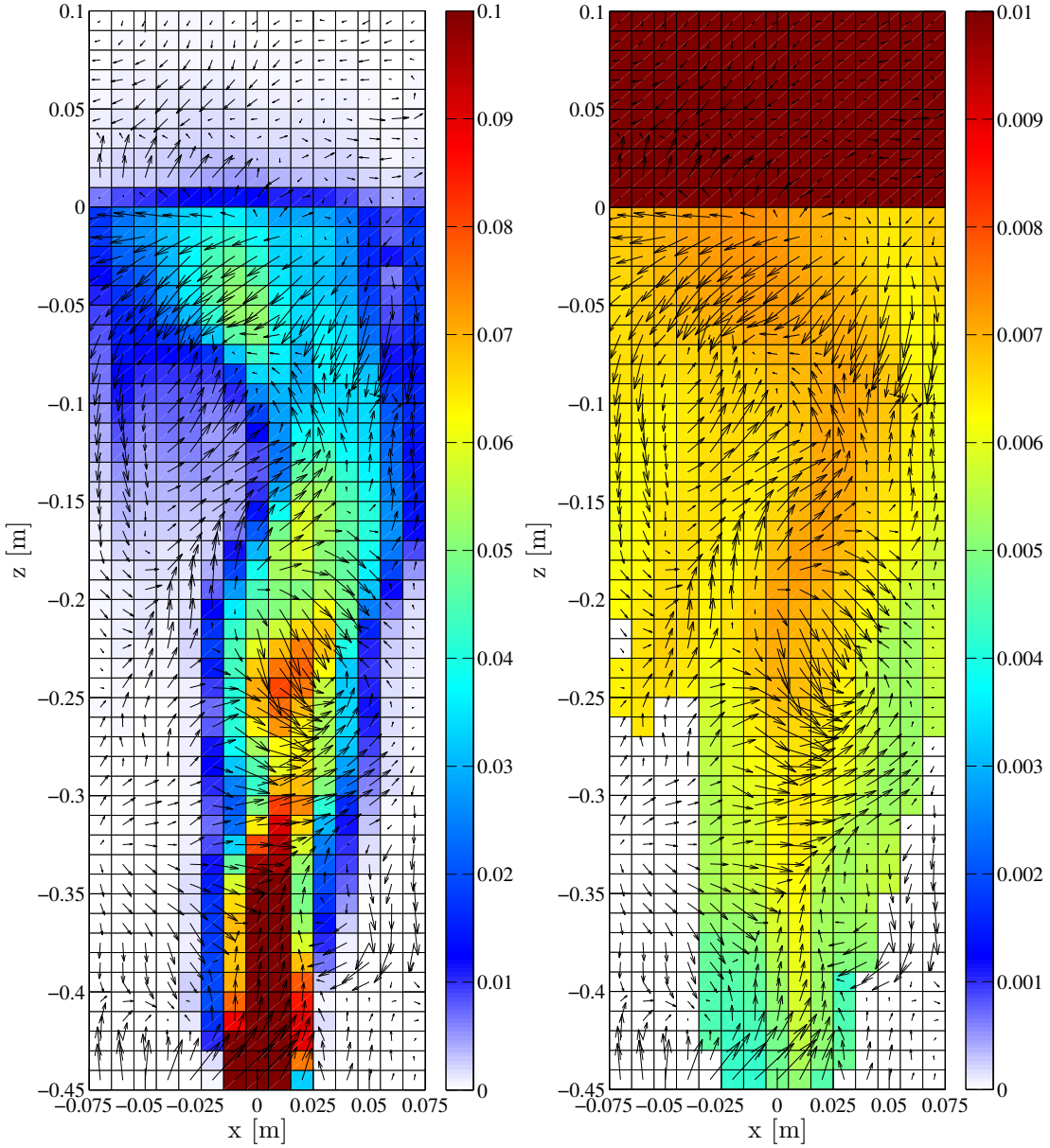

(a) **(b)**

Figure 4.5: Instantaneous flow at $t = 620$ s on the axial plane. Black arrows indicate the velocity field of the mixture. (**a**) Bubble phase fraction α_b. (**b**) Sauter diameter d_{32}.

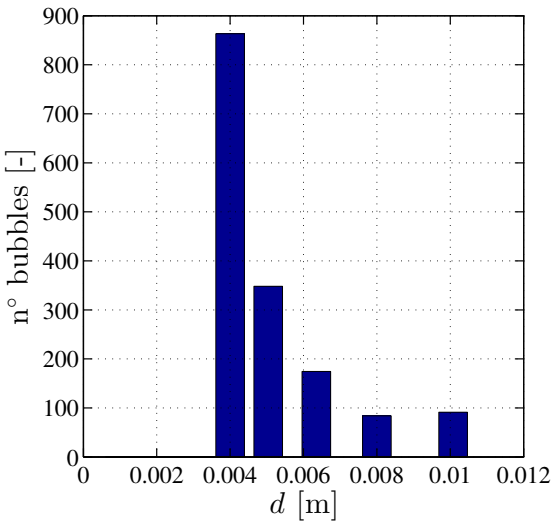

Figure 4.6: Mean number of dispersed bubbles for each class.

population fed into the column are two factors that play a role in this regard.

The simulation described above was used as reference case (R) for a sensitivity analysis which involved the following aspects: number of classes, drag formulation, turbulence model and bubble-induced contribution term (Eq. 3.22). The performed tests are listed in Table 4.2.

Test	N	d [m]	Drag	LES Smagorinsky model	BIT model
R	11	0.001-0.01	Ishii-Zuber	dynamic	yes
A	1	0.001	Ishii-Zuber	dynamic	yes
B	1	0.004	Ishii-Zuber	dynamic	yes
C	1	0.01	Ishii-Zuber	dynamic	yes
D	1	0.004	Ishii-Zuber	constant	yes
E	1	0.004	Ishii-Zuber	dynamic	no
F	11	0.001-0.01	Schiller-Naumann	dynamic	yes

Table 4.2: Test matrix for the sensitivity analysis on number of classes N, diameter d, drag formulation, BIT model and LES turbulence model.

Cases A, B and C were run with a single class. The diameters used in A and C were the minimum and the maximum of the range used in the reference case respectively, whereas the diameter in B could be considered as representative of the whole bubble population (Deen et al., 2001). The objective was to estimate how much the results improved by taking into account a (discrete) range of bubble size, rather than

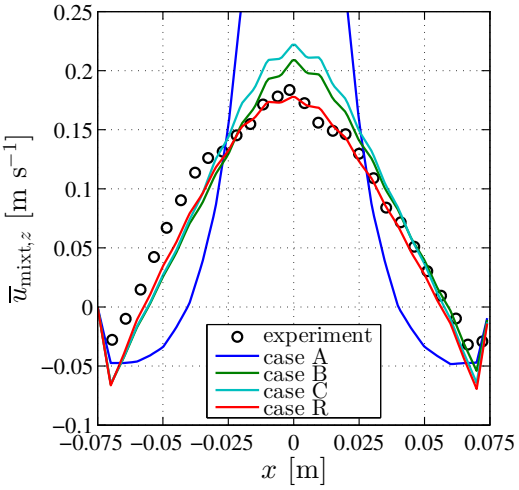

(a) mean axial water velocity (max value of case A ≈ 1 m s^{-1})

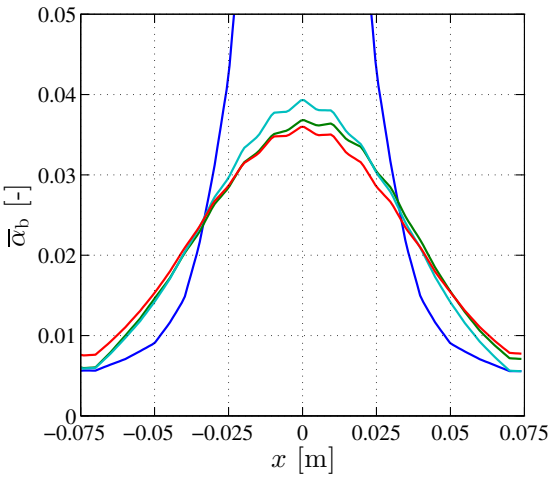

(b) mean gas hold-up

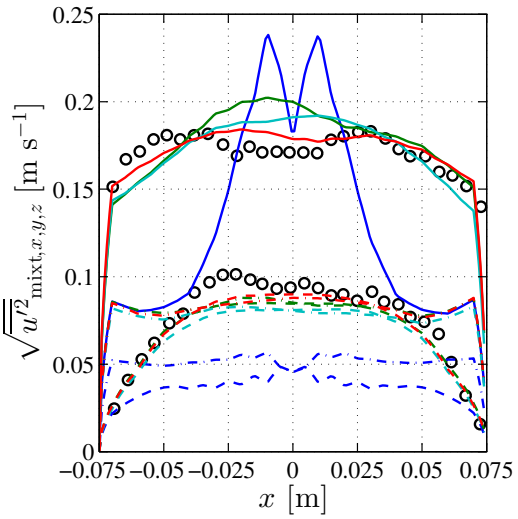

(c) turbulence levels: x (– – –), y (–·–·–), z (——)

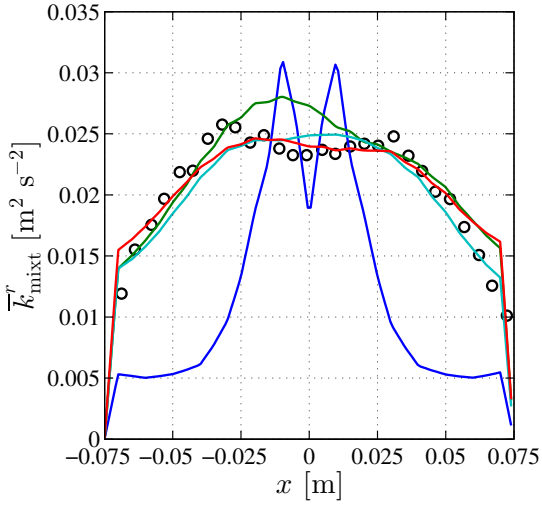

(d) resolved mean water TKE

Figure 4.7: Comparison of results of cases A, B, C and R. Profiles along the horizontal centerline at z = -0.20 m.

a monodisperse population. The comparison for the mean axial water velocity, the gas hold-up, the turbulence levels and the TKE is shown in Fig. 4.7. The predictions were wrong in case A. Because of their small size, the velocity of bubbles relative to mixture phase was really modest. Therefore, an equilibrium condition established in the flow such that bubbles simply followed the water motion. In particular, the action of the lift force was so reduced that the plume did not meander. As a consequence, all profiles in Fig. 4.7 for case A present a large central peak.
Results of cases B and C fairly matched the experiments, but as expected the agree-

ment was less good compared to the reference case. In particular, the mean and r.m.s. axial water velocity were overestimated in both cases. The distribution of the gas hold-up is almost the same.

It can be objected that case R with 11 classes did not produce results much better than A and B where a single class was employed. This is true especially when considering that case R ran for 30 hours approximately, whereas cases A and B needed only 10 hours (both on 16 cores of an HPC cluster). Nevertheless, three aspects have to be considered:

- it was adopted a simplified breaking formulation that "penalized" some of the classes (cf. Fig. 4.6);
- the bubble size distribution is quite narrow in bubble columns (Chen et al., 2005) and the assumption of a single bubble size is generally justified;
- the bubble size distribution was known *a priori*, allowing to use reasonable values for the diameter (cases B and C).

Still in the configuration with a single bubble class (d = 0.004 m), the employment of a constant Smagorinsky model was tested in case D. The importance of applying the LES Smagorinsky model with a dynamic determination of C_S is clear from Fig. 4.8. The constant Smagorinsky, where C_S had a fixed value of 0.2, increased the effective viscosity $\nu_{\text{mixt}}^{sgs,SI}$ and damped the bubble plume dynamics. Similarly to case A, the simulated mean axial water velocity is steeper and exhibits a large central peak. Since the plume meandering was substantially suppressed, turbulence levels were limited, the radial ones particularly. Instead, the clear reduction of $\sqrt{\overline{u'^2}}_z$ was mainly due to the fact the constant Smagorinsky model did not damp $\nu_{\text{mixt}}^{sgs,SI}$ as approaching the walls which is instead an important feature of the dynamic version. Similar findings are in Dhotre et al. (2008), Zhang et al. (2006).
The same figure displays the results of case E where the bubble-induced turbulence term was *not* taken into account. From the comparison with case R, it is apparent that the this term played a role at the center of the column where the flow was more turbulent. Therefore, the predicted mean axial water velocity, the turbulence levels and the TKE increased around x = 0 in case E.

Finally, the role played by the drag force formulation was verified. The other contributions to the momentum exchange between bubbles and mixture phase, i.e. lift, virtual mass and turbulent dispersion force, were not treated in this analysis. The reason is that the drag force was essential in the developed CFD solver for the numerical stability of the PISO algorithm in cells with no bubbles (see Section 3.2.1).

The Schiller-Naumann drag model (Eq. 3.36) was used in case E. The number

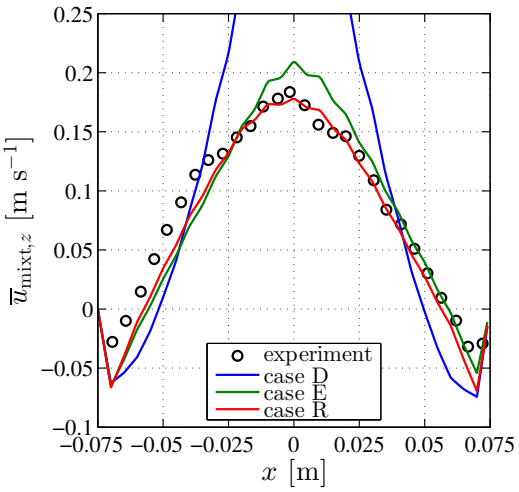

(a) mean axial water velocity (max value case D ≈ 0.4 m s^{-1})

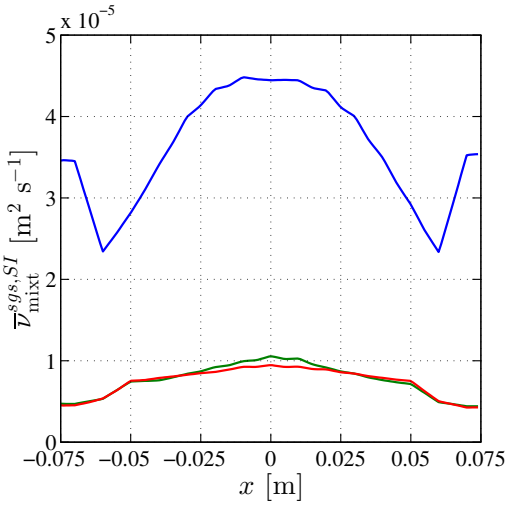

(b) mean shear-induced sgs kinematic viscosity

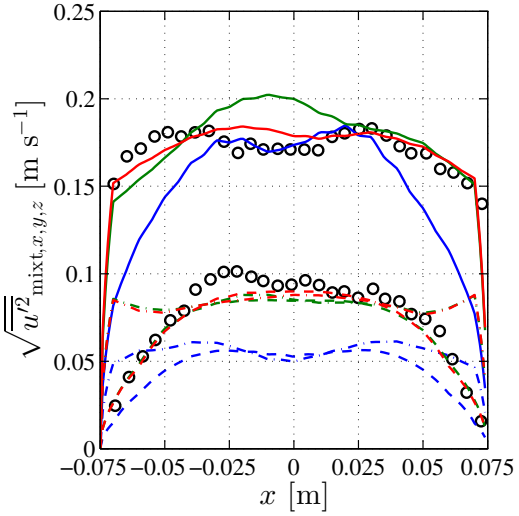

(c) turbulence levels: x (– – –), y (–·–·–), z (——)

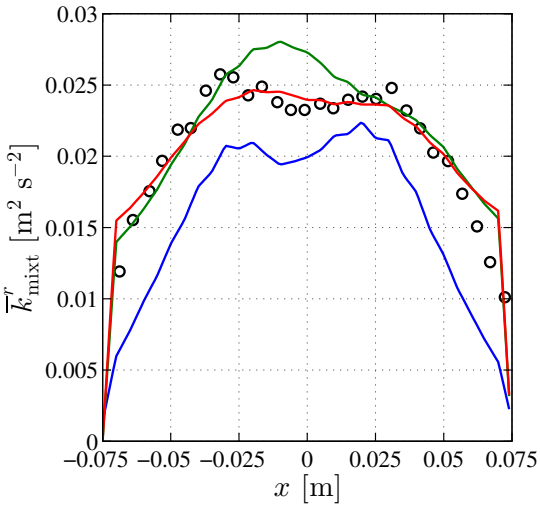

(d) mean resolved water TKE

Figure 4.8: Comparison of results of cases D, E and R. Profiles along the horizontal centerline at z = -0.20 m.

of classes was 11 since the drag exerted on a bubble is function of the diameter. The comparison in Fig. 4.9 reveals slight differences in the prediction of the mean axial water velocity. As a major finding, a large underestimation of the turbulence quantities in case E was recognised. In fact, the implementation of the Schiller-Naumann model was not provided with any corrections for distorted bubbles that instead were assumed as rigid spheres. The Ishii-Zuber model applied such corrections in case R. As a result, the drag coefficient C_D was generally smaller in case E compared to case R,

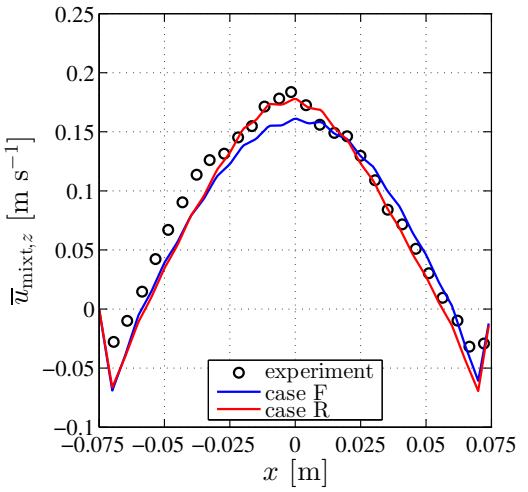

(a) mean axial water velocity

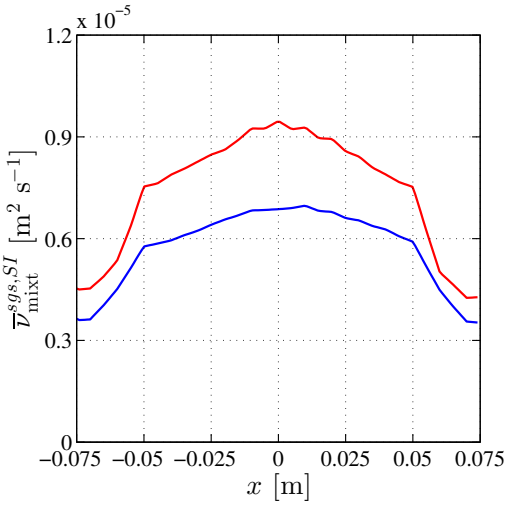

(b) mean shear-induced sgs kinematic viscosity

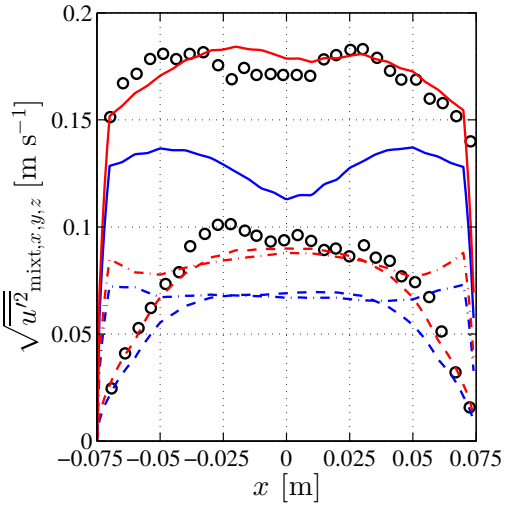

(c) turbulence levels: x (– – –), y (–·–·–), z (——)

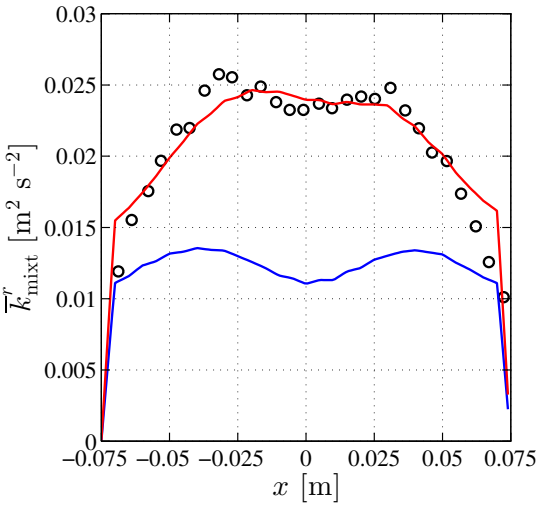

(d) mean resolved water TKE

Figure 4.9: Comparison of results of cases F and R. Profiles along the horizontal centerline at z = -0.20 m.

hence the momentum exchange diminished.

In conclusion, this case study has mainly shown that the implemented Eulerian multiphase model could successfully reproduce the dynamics of a bubble population. Particular emphasis has been given to the prediction of the water turbulence field which was induced by the motion of bubbles. The liquid-bubble interaction was a crucial aspect in the simulations of breaking waves presented in Chapter 5.

4.2 Regular spilling waves without entrained bubbles

The capability of the coupled VOF method was tested against the laboratory breaking waves of Ting and Kirby (1994, 1996). The experimental investigation was carried out in a flume 40 m long by 0.60 m wide by 1.00 m high filled with water to a depth of h = 0.40 m. Cnoidal regular waves, produced by a piston-type generator, propagated over a flat bottom and broke in the form of a spilling breaker on a constant sloping beach (1:35). The wave height H was 0.125 m in the constant-depth region and the period T was 2.0 s.
Given that ($\langle\cdot\rangle$) and ($\overline{\cdot}$) represent phase averaging and time averaging respectively, the experimental data used for the validation consisted of:

- maximum phase averaged surface elevation ($\langle\eta\rangle_{\max}$), minimum phase averaged surface elevation ($\langle\eta\rangle_{\min}$) and phase- and time- averaged surface elevation ($\overline{\langle\eta\rangle}$) along the flume;
- phase- and time- averaged streamwise water velocity $\overline{\langle u\rangle}$ measured at different depths at the locations listed in Table 4.3;
- time-averaged water turbulent kinetic energy $\overline{k}$ computed at different depths at the locations listed in Table 4.3.

The case was set-up as follows:

- Mesh. The computational domain, sketched in Fig. 4.10, was 22.65 m long by 0.30 m wide and the height of the domain was variable from 0.60 m at the left boundary (inlet) to 0.21 m at the right one (outlet). The vertical dimensions of the left and right boundary were chosen such that their difference was not large in order to reach a good compromise, in the sloping part, between aspect ratio, non-orthogonality and skewness of cells. The mesh consisted of 1444000 hexaedral cells with a cell size of 0.015 m in the flat part of the domain;
- Number of phases. The simulation was performed under the no-bubbles configuration, therefore only water (w) and air phase were used;
- Boundary conditions. Waves were generated by the means of the utility described in Jacobsen et al. (2012) which employs the relaxation method for wave generation and absorption. A relaxation zone of 4 m (from the inlet) was used for generating the wave. In this portion of the domain, the utility imposed conditions for α_{w}, α_{air} and $\mathbf{u}_{\mathrm{mixt}}$ variable with the time according to the stream function theory. The absorption zone at the outlet was not employed. At the top, the atmospheric value was assigned to pressure and a backflow was allowed

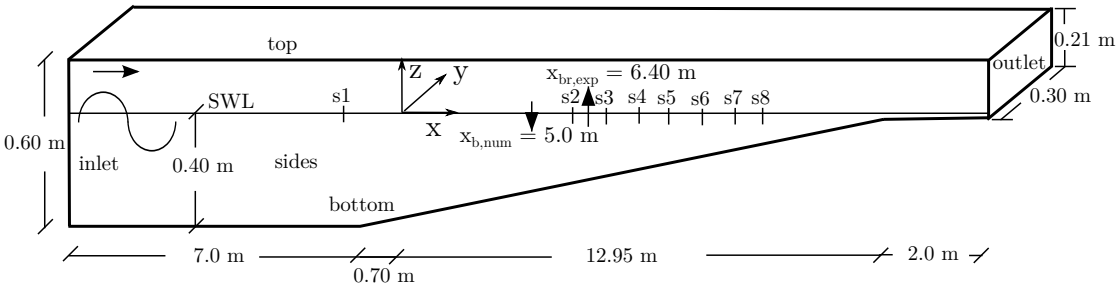

Figure 4.10: Domain adopted for the numerical simulation of the experiment in Ting and Kirby (1994, 1996). Not to scale.

section	s1	s2	s3	s4	s5	s6	s7	s8
x [m]	-1.265	5.945	6.665	7.275	7.885	8.495	9.110	9.725
d_{sw} [m]	0.4	0.208	0.185	0.169	0.152	0.137	0.119	0.097
h [m]	0.4	0.212	0.192	0.175	0.161	0.148	0.133	0.112

Table 4.3: Locations of measurements with corresponding local still water depths d_{sw} and local phase- and time-averaged wave heights h in the experiment of Ting and Kirby (1994, 1996)

only for air (with velocity normal to the boundary). The other conditions are given in Table 4.4;

- Drag force formulation. Since entrained bubbles were not taken into account, the formulation for the drag force was not necessary;
- Time range simulation. The simulation was performed for 50 wave periods and it took 48 hours on 32 cores of an HPC cluster.

boundary	$\mathbf{u}_{\text{mixt}}$	α_{w}	α_{air}	p_d	$\nu^{sgs,SI}_{\text{mixt}}$	k^{sgs}_{mixt}
inlet	D.	D.	D.	N.	D.	D.
outlet	N.	N.	N.	N.	N.	N.
bottom	no-slip	N.	N.	N.	N.	N.
top	N./D.	N./D.	N./D.	D.	N.	N.
sides	slip	N.	N.	N.	N.	N.

Table 4.4: Boundary conditions employed in the numerical simulation of the experiments in Ting and Kirby (1994, 1996). *N.* = Neumann (gradient equal to zero). *D.* = Dirichlet (fixed value). *N./D.* = Neumann for outflow and Dirichlet for inflow.

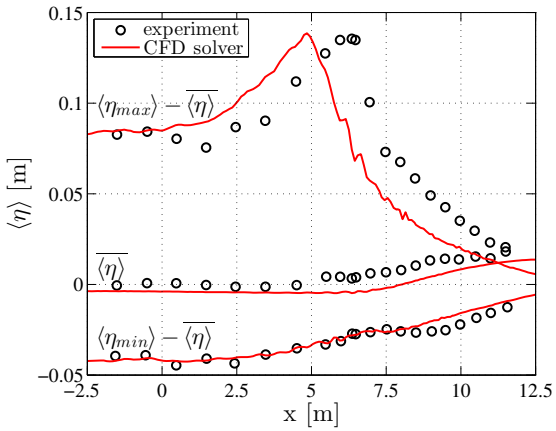

Figure 4.11: Comparison of predicted mean, max and min phase-averaged surface elevation η against experimental data along the x-axis of the domain.

The same set-up was employed for a simulation *with* bubbles in Section 5.2. The present case was considered as a comparison term to investigate the effects of the air entrainment, hence the same mesh had to be adopted. A standard grid sensitivity analysis was not performed since the minimum cell size was constrained by the maximum bubble diameter, as seen in the bubble column case. On the other hand, a larger average cell size was not chosen, because the mesh was judged already coarse ($\approx$ 8 cells per wave height in the constant-depth region).
Before illustrating the comparison between experimental and numerical results, the concept of spanwise averaging is elucidated. In Ting and Kirby (1994, 1996), phase- and time-averaging operation were applied on the instantaneous measurements taken along the centerline of the wave tank (x-direction in Fig. 4.10). The present numerical results were instead first averaged in the longshore direction (spanwise, y-axis in Fig. 4.10) and then phase- and time-averaged. The average along the y-axis was possible because uniform numerical conditions held in the longshore direction. In the perspective of the Reynolds decomposition of a quantity, the spanwise averaged value could be interpreted as an organized motion and the deviation from the average as the turbulent fluctuation (Christensen and Deigaard, 2001). This procedure was advantageous because it allowed to obtain reliable turbulent fluctuations within a limited number of simulated wave periods.

All results presented in the rest of this section were averaged along the y-direction ($\widetilde{\cdot}$) and phase-averaged over the last 30 wave periods.

Figure 4.11 displays the comparison of $\langle\eta\rangle_{\max}$, $\langle\eta\rangle_{\min}$ and $\overline{\langle\eta\rangle}$ along the flume.

It is apparent that the breaking was premature. The numerical breaking point was recognised at $x_{br,exp} \approx$ 5m, whereas the experimental one was at $x_{br,sim}$ = 6.40 m. Nev-

ertheless, the post-breaking decay of $\langle\eta\rangle_{\max}$ followed the experiments. The premature breaking was partially due to the spurious velocities (see Section 3.3.1). Another explanation is the coarse mesh resolution together with the fact that the aspect ratio of cells in the surf zone could not be equal to one. In fact, Jacobsen et al. (2012) performed numerical simulations of the same case by the means of the equivalent solver `interFoam` (see Section 3.3.1) and observed that the performance of the VOF algorithm worsened when the aspect ratio of cells was larger than one. These reasons were responsible also for the simulated wave setup which occurred further along the flume than was in the experiments. However, the CFD solver still predicted the increase of the mean water level that balanced the decrease of momentum after breaking.

The vertical profiles of $\overline{\langle\widetilde{u}\rangle}_{\text{mixt},x}$ at the locations of Table 4.3 are shown in Fig. 4.12. It should be noted that normalized depths are used. Results revealed that $\overline{\langle\widetilde{u}\rangle}_{\text{mixt},x}$ was generally overestimated. Nevertheless, the overall agreement is good. In particular, the CFD solver predicted the offshore-directed undertow current which balanced the mass of water transported onshore in the upper part of the wave during the breaking process. As reported in Ting and Kirby (1994, 1996), the undertow decreased towards the bottom outside the surf zone (s1, s2), whereas it increased near the bottom inside the surf zone (s3-s8). Furthermore, the gradient of the profiles ($\partial\overline{\langle\widetilde{u}\rangle}_{\text{mixt},x}/\partial z$) is consistent with the experimental one in the bulk of the water column, hence the prediction of the momentum mixing was good at intermediate depths (Christensen, 2006). The worse results near the bottom could be due to the applied no-slip condition combined with a poor mesh resolution. The spurious velocities played a role in the sharp increase of $\overline{\langle\widetilde{u}\rangle}_{\text{mixt},x}$ near the free surface.

The resolved turbulent kinetic energy was calculated as

$$\widetilde{k}^{r}_{\text{mixt}} = \frac{1}{2}\left(\left\langle\widetilde{u'^2}\right\rangle_{\text{mixt},x} + \left\langle\widetilde{u'^2}\right\rangle_{\text{mixt},y} + \left\langle\widetilde{u'^2}\right\rangle_{\text{mixt},z}\right) \tag{4.3}$$

The total TKE is found adding the sub-grid scale contribution:

$$\widetilde{k}^{tot}_{\text{mixt}} = \widetilde{k}^{r}_{\text{mixt}} + \widetilde{k}^{sgs}_{\text{mixt}} \tag{4.4}$$

Figure 4.13 shows the vertical profiles of the square root of time-averaged total TKE at the different locations. In Ting and Kirby (1994, 1996), the TKE was computed from section s4. A good agreement was achieved in the comparison. Numerical results followed the common assumption that, in a spilling breaking wave, turbulence is generated beneath the surface roller which propagates towards the shoreline and then it is slowly spread downward by convection and diffusion. In fact, the TKE was larger near the free surface and decreased towards the bottom.

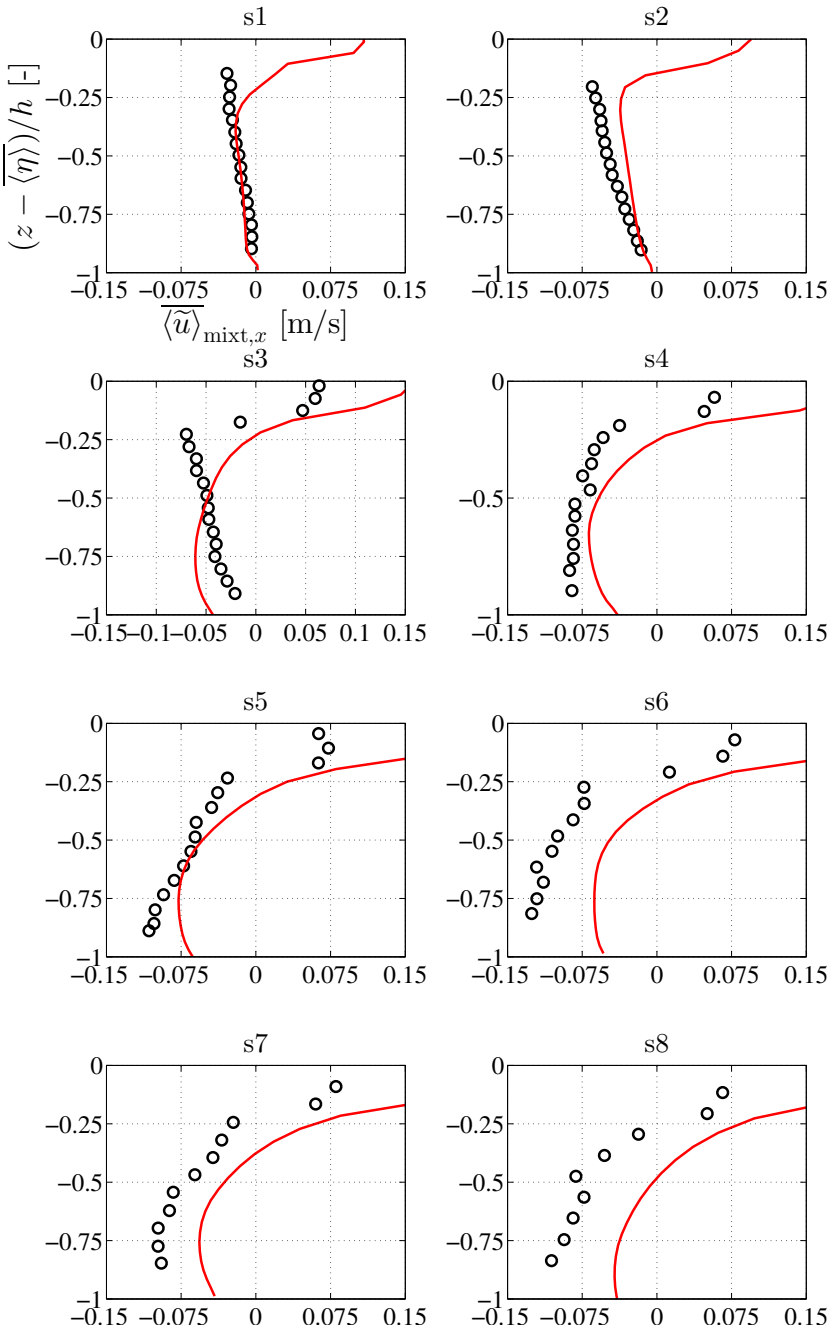

Figure 4.12: Comparison of numerical and experimental vertical profiles of phase- and time-averaged streamwise velocity $\overline{\langle\widetilde{u}\rangle}_{\mathrm{mixt},x}$ at different locations. Circles: experiments. Solid line: present CFD solver

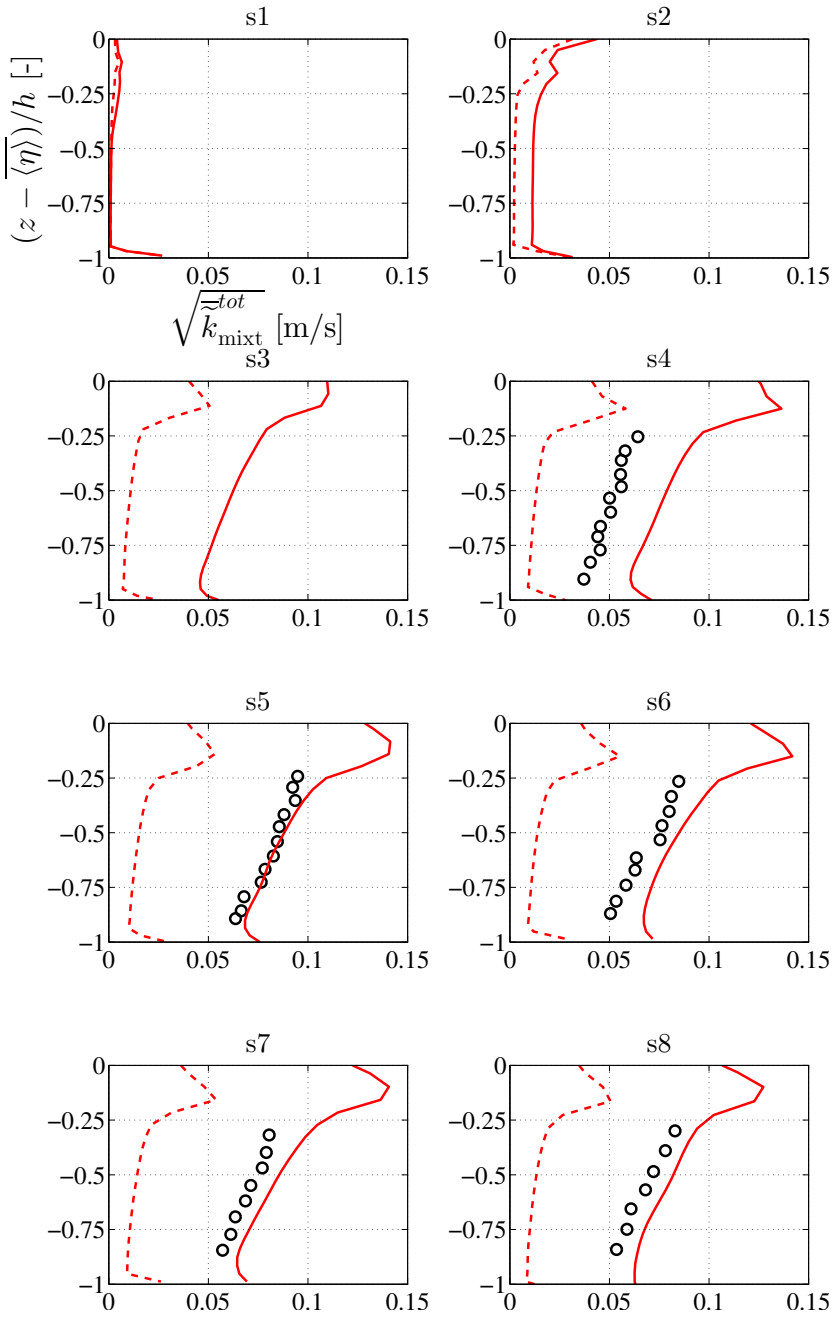

Figure 4.13: Comparison of experimental and numerical time-averaged TKE at different locations. Circles: experiment. Solid line: $\widetilde{\overline{k}}^{tot}_{\mathrm{mixt}}$. Dashed line: $\widetilde{\overline{k}}^{sgs}_{\mathrm{mixt}}$.

The fact that the simulated flow was almost laminar in section s2, which was located almost 1 m downstream the numerical breaking point, suggested that the initialization of the simulated breaking process was delayed. Also in a spilling wave, the incipient breaking process depends on the motion of the wave front which was not reconstructed accurately enough in the numerical simulation. For this reason, the present comparisons were still made at the locations reported in Ting and Kirby (1994, 1996), instead of at locations with the same distance relative to the breaking point.

In conclusion, this case study has shown that the VOF algorithm of the developed CFD solver was capable of handling the motion of a breaking wave, although some issues were identified (premature breaking, large velocities at the free surface and overestimation of TKE). Nevertheless, it is reminded that the same problems would have been found if the same numerical simulation was performed by `interFoam`. The purpose of the present case study was not to show any improvements in this regard.

5 Validation: part II

This chapter presents the investigation performed on the adopted air entrainment formulation. Two different laboratory spilling breakers were simulated, i.e a single deep water wave and the regular waves breaking on a sloping beach illustrated in Chapter 4. Unlike the first part of the validation, these two case studies also tested the reliability of the coupling in simulations where the role of the VOF model and the Eulerian multiphase approach was of the same importance.

5.1 A single deep water spilling wave

The study of Lamarre and Melville (1991) provided a quantitative study on the air entrainment occurring in laboratory breaking waves as described in Section 1.1.2.

The experimental facility was a flume 25 m long by 0.70 m wide filled to a depth of 0.60 m. In each repetition of the experiment, a single breaker was generated by focusing a dispersive wave packet of N_{lc} linear components with amplitude a_i, frequency f_i, phase Φ_i and wave number k_i. The wave packet was parametrized by the global steepness $G = ak_c$, the central frequency f_c and the band $\Delta f = f_{N_{lc}} - f_1$ over which frequencies f_i were uniformly spaced.

The focusing was operated on the crests of all components which were synchronized at point $x_{br,th}$ and at time $t_{br,th}$. In other words, it was prescribed a theoretical breaking by focusing the energy of all components at point $x_{br,th}$ and at time $t_{br,th}$. By the superposition of all linear components, the analytical surface elevation at the wave paddle was given by:

$$\eta(0,t) = \sum_{i=1}^{N_{lc}} a_i \cos\left[2\pi f_i \left(t - t_{br,th}\right) + k_{w,i} x_{br,th}\right] \tag{5.1}$$

Frequencies f_i and the wave numbers k_i were determined as follows:

1. N_{lc}, $G = ak_c$, f_c and $\Delta f / f_c$ were chosen;

2. $f_1 = f_c - \frac{1}{2}(\Delta f)$ and $f_i = f_{i-1} + \frac{\Delta f}{N_{lc}-1}$ for i = 2,3,4...N_{lc};
3. k_c calculated from the dispersion relation $\left(2\pi f_c\right)^2 = k_c \tanh\left(k_c d\right)$;
4. a_i defined as a/N_{lc} therefore $a_i = G/(N_{lc}k_c)$.
5. k_i computed from dispersion relations $\left(2\pi f_i\right)^2 = k_i \tanh\left(k_i d\right)$

In the experiments, Δf = 0.88 Hz and f_c = 0.88 Hz were chosen. Three values were used for G, i.e. 0.54, 0.45 and 0.38, which produced a plunging, a less energetic plunging and a spilling breaker respectively. The experiment consisted of generating these waves and mapping the entrained air bubble plume by the means of electrical probes. Only the spilling wave was simulated in the present study.

The experimental data used for this validation consisted of:

- The cross-sectional area A_b of the bubble plume

$$A_\mathrm{b} = \int_{A_\mathrm{b}} \mathrm{d}A_\mathrm{b} \tag{5.2}$$

- The total volume V_b of the bubble plume

$$V_\mathrm{b} = l_y \int_{A_b} \alpha_\mathrm{b}\, \mathrm{d}A_\mathrm{b} \tag{5.3}$$

  where l_y is width of the flume;

- The averaged bubble phase fraction α_b^{ave}

$$\alpha_\mathrm{b}^{ave} = \frac{V_\mathrm{b}}{A_\mathrm{b}} \tag{5.4}$$

- The horizontal and vertical centroid of the plume

$$X_\mathrm{b} = \frac{\int_{A_\mathrm{b}} \alpha_\mathrm{b} x\, \mathrm{d}A_\mathrm{b}}{V_\mathrm{b}} \tag{5.5}$$

$$Z_\mathrm{b} = \frac{\int_{A_\mathrm{b}} \alpha_\mathrm{b} z\, \mathrm{d}A_\mathrm{b}}{V_\mathrm{b}} \tag{5.6}$$

The bubble phase fraction probes used in Lamarre and Melville (1991) were insensitive to values lower than 0.003. The same threshold was applied to the numerical results. The spanwise averaged bubble phase fraction $\widetilde{\alpha}_\mathrm{b}$ was used in the formulas above.

The case was set-up as follows:

- Mesh. The computational domain was 18.0 m long by 0.70 m wide by 1.00 m height. The still water depth was at 0.60 m. The mesh was uniform and comprised 5160960 hexaedral cells of size 0.0125 m;

- Number of phases. Three simulations were performed: no-bubbles, N = 7 (0.0025 m $\leq$ d$_i$ $\leq$ 0.01 m) and N = 14 (0.0005 m $\leq$ d$_i$ $\leq$ 0.01 m). The simulations were performed without taking into account the bubble coalescence because the first tests showed that the adopted modeling (Eq. 3.44) was time-consuming for large domains. Shi et al. (2010) obtained good results for the same case neglecting the bubble coalescence transfer;

- Boundary conditions. Waves were generated by the means of the utility described in Jacobsen et al. (2012) which employs the relaxation method for wave generation and absorption. A relaxation zone of 4 m (from the inlet) was used for generating the wave. In this portion of the domain, the utility imposed conditions for α_{w}, α_{air} and $\mathbf{u}_{\text{mixt}}$ variable with the time according to Eq. 5.1. An absorption zone of 4 m was used at the end of the domain. At the top, the atmospheric value was assigned to pressure and a backflow was allowed only for air (with velocity normal to the boundary). The other conditions are given in Table 5.1;

- Drag force formulation. Schiller-Neumann (Eq. 3.36);

- Air entrainment parameters. c_{en} = 20 and $\epsilon_{\text{mixt}}^{sgs,SI}$ = 0.1 m^2 s^{-3} as threshold (Eq. 3.49);

- Time range simulation. The flow was simulated for 25 s and it took 24 hours for the case without bubbles, 27 hours with 7 classes and 50 hours with 14 classes on 40 cores of an HPC cluster.

	$\mathbf{u}_{\text{mixt}}$	$\mathbf{u}_{\text{b},i}$	α_{w}	α_{air}	$\alpha_{\text{b},i}$	p_d	$\nu_{\text{mixt}}^{sgs,SI}$	k_{mixt}^{sgs}
inlet	D.	N.	D.	D.	N.	N.	D.	D.
outlet	N.	N.	N.	N.	N.	N.	N.	N.
bottom	slip	slip	N.	N.	N.	N.	N.	N.
top	N./D.	N./D.	N./D.	N./D.	N./D.	D.	N.	N.
sides	slip	slip	N.	N.	N.	N.	N.	N.

Table 5.1: Boundary conditions employed in the numerical simulations of the experiments in Lamarre and Melville (1991). *N.* = Neumann (gradient equal to zero). *D.* = Dirichlet (fixed value). *N./D.* = Neumann for outflow and Dirichlet for inflow.

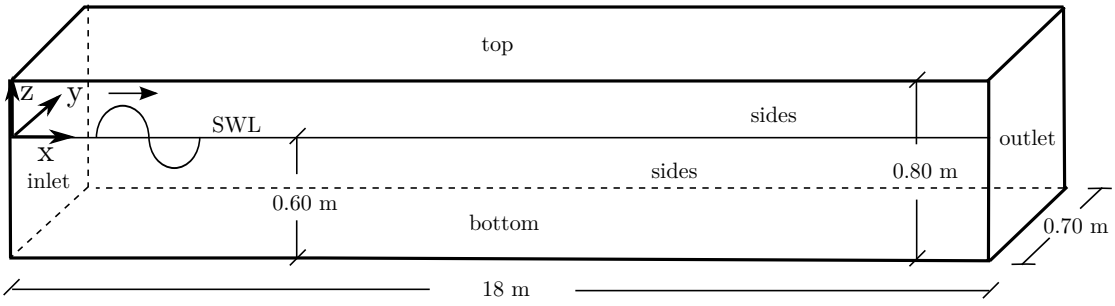

Figure 5.1: Domain adopted for the numerical simulation of the experiment in Lamarre and Melville (1991). Not to scale.

Following results are reported in non-dimensional time and space expressed as in Lamarre and Melville (1991)

$$x^* = \frac{x - x_{br,sim}}{L_c} \tag{5.7}$$

$$t^* = \frac{t - t_{br,sim}}{T_c} \tag{5.8}$$

where $x_{br,sim}$ and $t_{br,sim}$ are the location and the time of the simulated breaking and $L_c = 2\pi/k_c$ and $T_c = 1/f_c$ are the central wave length and central period of the wave packet respectively. The exact definition of breaking in a laboratory spilling wave is ambiguous. In fact, the wave front evolves gradually from the non-broken status and there is not a specific reference as the forward-projected jet hitting the undisturbed free surface in plunging waves. In this case study, the breaking was defined as occurring when a bulge was observed at the wave front, therefore slightly later (0.2 s) than the time of the maximum (not broken) surface elevation. This choice was consistent with Rapp and Melville (1990) wherein the observed breaking point was defined as the starting of significant air entrainment.

The development and the evolution with the time of the simulated bubble plume within the first wave period in the case with 7 classes is shown in Fig. 5.2. The wave broke as spilling, but the breaker was close to become plunging. Therefore, an interfacial structure resembling a small forward-projected jet was recognised, but the spatial resolution was not fine enough for the VOF algorithm to reconstruct it accurately. It will be shown that this occurrence affected the prediction of the amount of entrained bubbles. The initial bulge/cavity can be observed at $t^* = 0.03$, then the CFD solver reproduced the development of a single bubble plume as it should have been for a spilling wave (see Section 1.1.2). At $t^* = 0.5$, the expected bore front established and air entrainment at the toe of this front became the main source of dispersed bubbles. The plume advanced with the bore region with a thickness of ≈

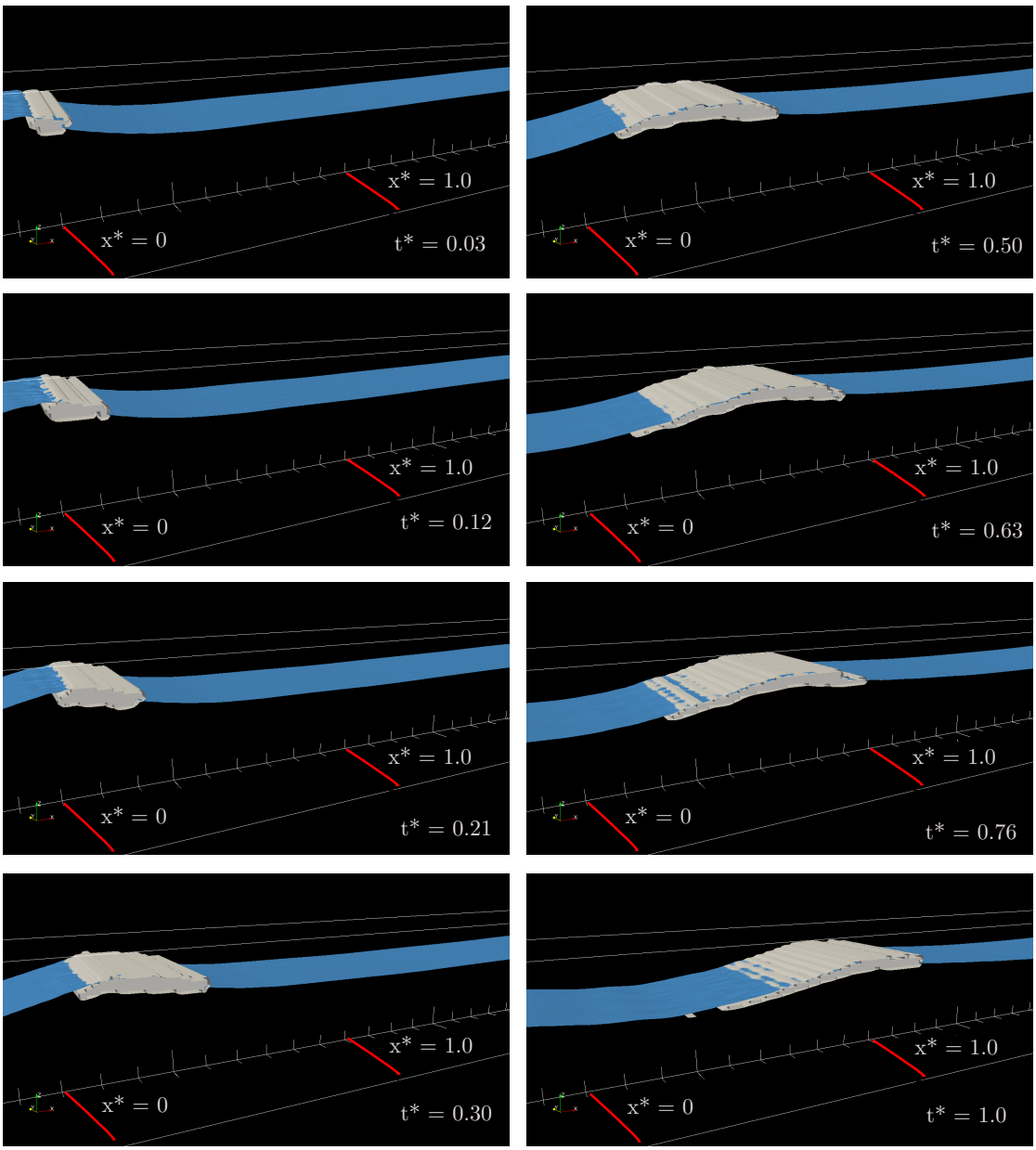

Figure 5.2: Breaking process in the case with 7 classes. The bubble plume is bounded by the isosurface $\alpha_b = 0.0001$ [-].

5 cm and a length of 1.50 m in according to the observations of Rojas and Loewen (2010) who investigated the same wave experimentally.

The following remark is necessary before describing the results. The free surface was simulated by the means of a VOF approach, therefore it was not reconstructed, but arbitrarily defined as the isosurface $\alpha_{mixt} = 0.5$. As said in Section 3.1.4, the adopted air entrainment formulation of Derakhti and Kirby (2014) (Eq. 3.49) was derived under the

assumption that the source of entrainment was a turbulent-dependent mechanism as the one occurring in *pure* spilling waves. Since the breaker of the present case was almost plunging, it was *unavoidable* that a certain amount of (continuous) air entrained the water in the breaking region where the free surface could not be sharp anymore. As a result, this entrained air was "dispersed" in the same manner as in a simulation performed by a standard VOF solver. Instead, the CFD solver, through the air entrainment formulation Eq. 3.49, should have "transferred" the phase fraction of this entrained continuous air (α_{air}) into the dispersed bubble phase fraction (α_{b}). Nevertheless, this exchange could not be neither instantaneous nor complete to not undermine the numerical stability of the CFD solver. Consequently, the bubble phase fraction was generally underestimated, but the variation with time was captured.

Figure 5.3 depicts the evolution of the spanwise averaged bubble phase fraction with the time over the first wave period after breaking in the case with 7 classes.

The small entrapped air cavity can be recognised at $t^* = 0.03$ with a maximum bubble phase fraction of ≈ 0.30. At $t^* = 0.12$, the roller was larger and the bubble phase fraction was still around 0.30 which was in agreement with the numerical simulations of Derakhti and Kirby (2014), but smaller compared to the measurements of (Rojas and Loewen (2010), Fig. 17b) where $\widetilde{\alpha}_{\text{b}} \approx 0.50$ was measured. The difference was attributed to $\widetilde{\alpha}_{\text{air}}$. Then the wave front became unstable and rough as water spilt down the face of the wave until $t^* = 0.50$. During these stages, the maximum of $\widetilde{\alpha}_{\text{b}}$, which was still ≈ 0.30, was closer to the experiments of (Rojas and Loewen (2010), Fig. 18b), because the bubbles not captured at the beginning already escaped in the experiments. At $t^* = 0.5$, the bore region established and $\widetilde{\alpha}_{\text{b}}$ decreased with the time until $t^* = 1.0$. The development of a "tail" of bubbles could be also recognised. During these stages, the entrainment mainly occurred at the leading edge of the bore front.

The integral properties of the bubble plume reported in Lamarre and Melville (1991) are compared in Fig. 5.4 for cases with 7 and 14 classes. In the experiments, measurements started at $t^* = 0.25$.

Both the experimental and the simulated volume V^{b} and area A^{b} are normalized through the maximum volume per unit length of crest measured in the experiments which was 0.0025 $\text{m}^3\ \text{m}^{-1}$. Concerning the volume (Fig. 5.4a), the experiments revealed a sharp increase at $0 \leq t^* \leq 0.25$ when the maximum value was reached and then a rapid decrease with only 5% of the initially entrained air remaining after a wave period. The evolution of the volume was essentially driven by the motion of bubbles with a radius larger than 1 mm (Hinze scale). The rising at $0 \leq t^* \leq 0.25$ was due to such bigger bubbles originated in the bulge/cavity (see Section 1.1.2). The rapid decrease was caused by the fast degassing of the same bubbles, because they have larger rise velocity compared to smaller bubbles. The CFD solver reproduced a time-variation

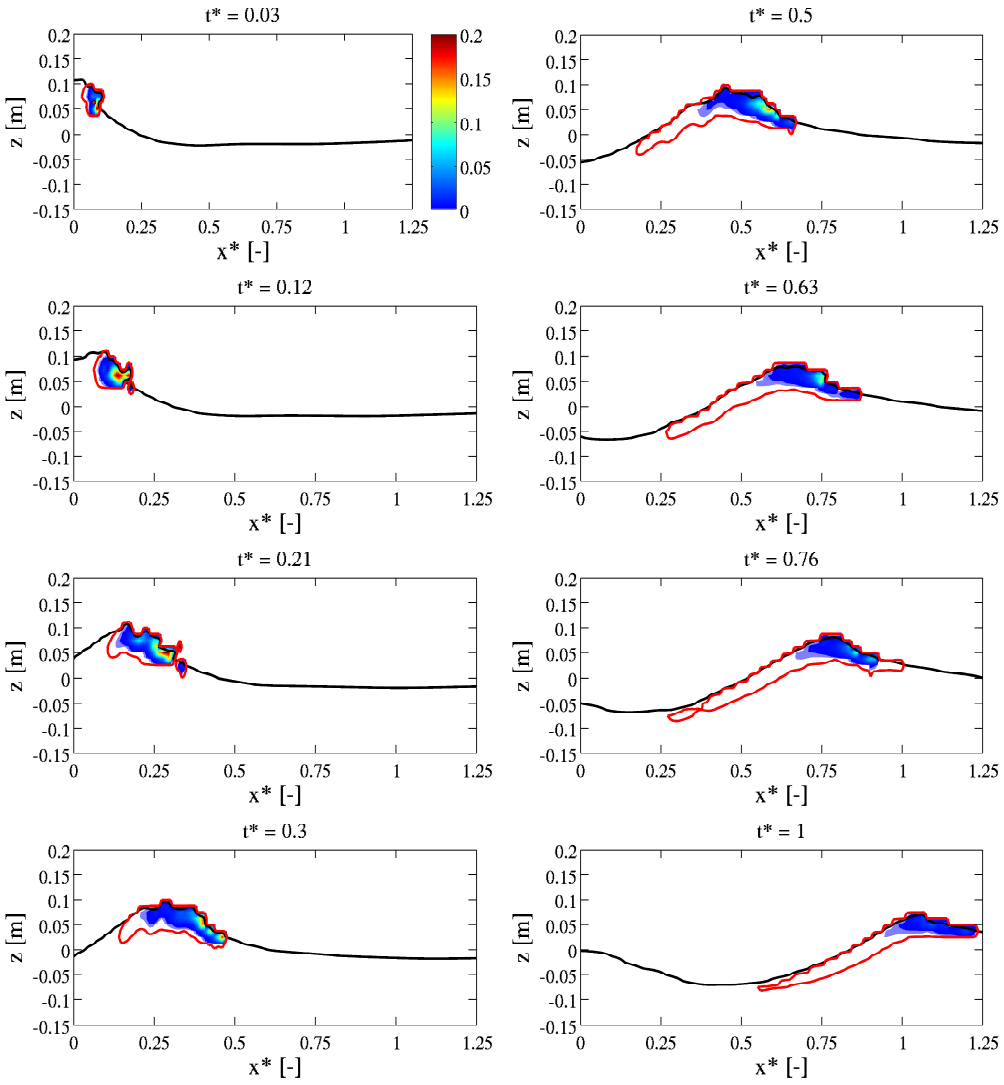

Figure 5.3: Variation with the time of the spanwise averaged volume fraction of the entrained bubbles $\widetilde{\alpha}_b$ in the case with 7 classes. The red contour line is for $\widetilde{\alpha}_b = 0.0001$ [-]. The black contour line is the free surface.

of the volume in agreement with the experiments, but the maximum value was only $\approx 30\%$ of the experimental one. A similar underestimation was found in Derakhti and Kirby (2014). As already explained, the reason lied on the difficulty of the CFD solver in handling the initial entraining which was not purely induced by a turbulent-dependent mechanism. In fact, the agreement improved from $t^* \approx 0.35$ when the bore induced-entrainment began. Still concerning the volume of the plume, cases with 7 and 14 classes did not show remarkable differences, since both reproduced the motion of bubbles with a radius larger than 1 mm which are the ones that played a role.

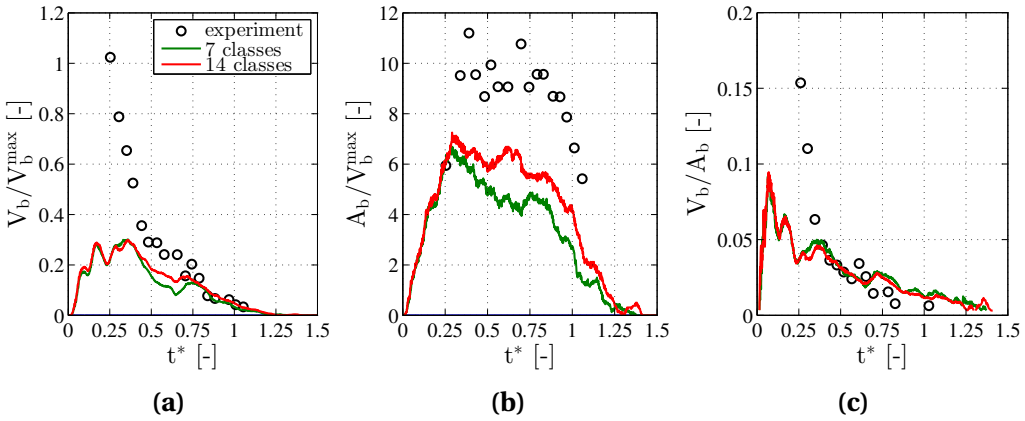

Figure 5.4: Experimental and simulated integral properties of the bubble plume. (**a**) Normalized total volume of entrained air per unit length of crest. (**b**) Normalized cross-sectional area of the bubble plume. (**c**) Averaged bubble phase fraction.

In the experiments, the cross-sectional area was found to not vary much with the time in the interval $0.25 \leq t^* \leq 1$ as it was mainly dependent on bubbles with a radius smaller than 1 mm which outgassed slowly and stayed in water for longer time (Fig. 5.4b). A decrease was observed after the first wave period. The CFD solver gave the same time-variation, but smaller values were again found. As explained in Derakhti and Kirby (2014), discrepancies in this comparison were expected since A_b significantly depended on the minimum bubble phase fraction considered for the calculation (0.003). In fact, Lamarre and Melville (1991) reported that the area of the plume did not reach its asymptotic value for the chosen threshold. Furthermore, it is important to note that the case with 14 classes showed slightly better results because the motion of bubbles with a radius smaller than 1 mm was also taken into account.

In the experiments, the averaged bubble phase fraction reached the value of 0.15. The comparison in Fig. 5.4c confirmed the expected underestimation until $t^* \approx 0.35$ in the numerical results.

The horizontal and vertical centroid are compared in Fig. 5.5. The CFD solver consistently predicted that the plume moved at the phase speed of the wave (Fig. 5.5a) and almost horizontally (Fig. 5.5b). Nevertheless, the simulated plume did not slow down at $t^* \approx 0.75$ as in the experiments as well as the vertical centroid was slightly overestimated. These discrepancies were related to the threshold applied to the bubble phase fraction as explained above.

Figure 5.6 depicts the time-variation of the bubble population in the case with 14 classes. In particular, the evolution of the normalized bubble number density is shown

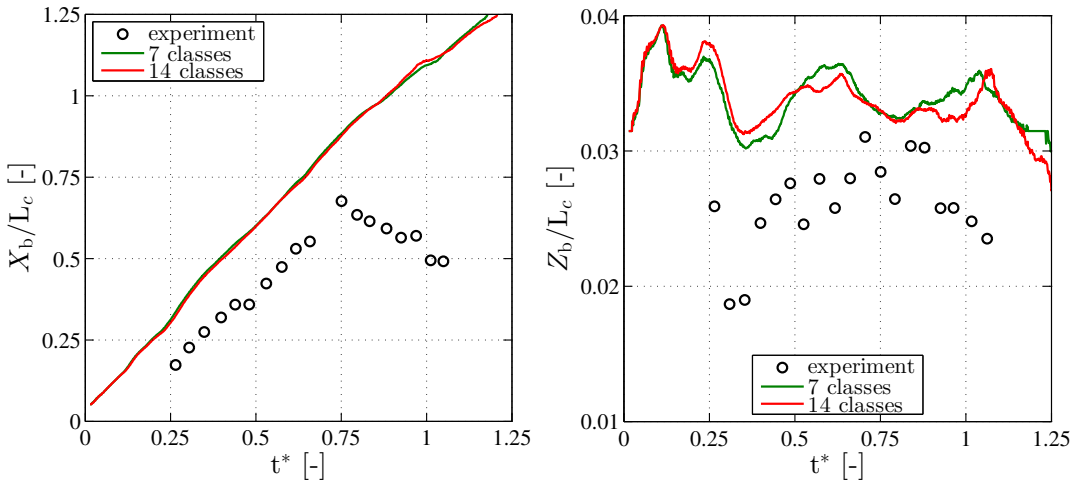

(a) Horizontal **(b)** Vertical

Figure 5.5: Comparison of the experimental and simulated centroids of the bubble plume.

in Fig. 5.6a. Larger bubbles with relatively higher rise velocity tended to escape the water quickly, therefore their density reached the maximum at the first stages of the breaking when the entrainment was more intense. As example, the density of bubbles with a radius of 2.5 and 5 mm rapidly reached the maximum value at $t^* = 0.20$ and at the end of the first wave period was already reduced by 80%. The entrainment of bubbles with smaller size occurred since the beginning of the breaking, but, because of their longer retention time in water, their density reached the maximum value later and approximately when the bore motion started. As example, the density of bubbles with a radius of 0.25 and 0.4 mm was maximum at $0.50 \leq t^* \leq 0.75$ and then decreased gradually, being reduced only by 50% at $t^* = 1.5$. The density of the Hinze scale, i.e. radius equal to 1 mm, reached the maximum value at $t^* = 0.45$ and the rate of the outgassing was as much as the one of the bigger bubbles.

The simulated bubble size spectrum is displayed in Fig. 5.6b for $t^* = 0.20$ and $t^* = 0.75$. The two slopes reported on the plot, based on the results of Deane and Stokes (2002) (see Section 1.1.2, Fig. 1.4), characterized the initial distribution of bubbles bigger and smaller than the Hinze scale (Eq. 3.50). It can be recognised that these slopes changed with the time. This was due to buoyant degassing and bubble breakage. Nevertheless, the variation of the slope was not the same for small and big bubbles, because of the differences explained above. The spectrum of bubbles with a radius larger than 1 mm steepened more and faster than that of smaller bubbles (with a radius less than 1 mm). At $t^* = 0.20$, the spectrum slope was still $-3/2$ at the smaller radii, whereas it already increased at $1 \leq r_b \leq 5$ mm since the larger bubbles escaped earlier. At $t^* = 0.75$, the spectrum slope at $r_b \leq 1$ mm increased as well.

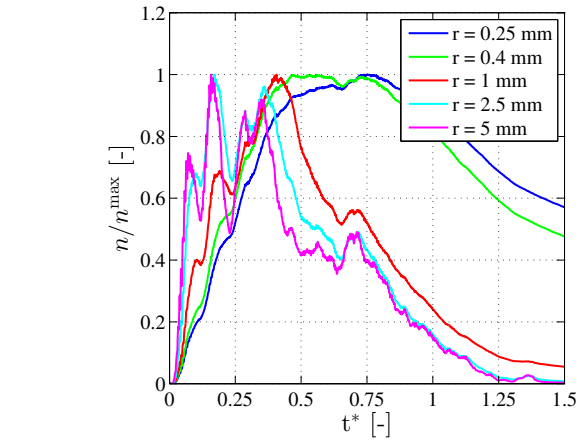

(a)

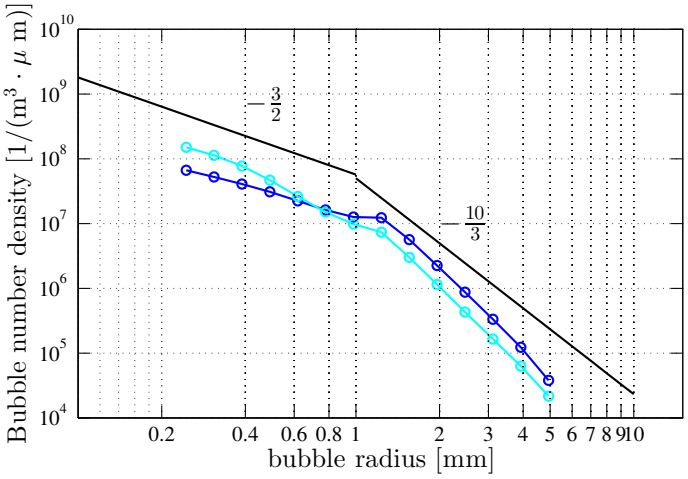

(b)

Figure 5.6: Case with 14 classes. (**a**) Evolution of the normalized bubble number density for different bubble diameters. (**b**) Bubble size spectrum at $t^* = 0.20$ (blue line) and at $t^* = 0.75$ (ciano line).

Beside the validation against the available measurements in Lamarre and Melville (1991), an investigation of the influence of the entrained air on the turbulence was performed as in Derakhti and Kirby (2014). As discussed in Section 1.1.2, the dispersed bubbles play a role in the dissipation occurring during breaking. Part of the wave potential energy is spent to keep the air entrained against the buoyancy force. This energy is partially returned to water when bubbles rise up creating small turbulent scales which in turn enhance the viscous dissipation into heat (at the Kolmogorov microscales).

In the developed numerical methodology, the assumption was that bubbles were smaller than the grid size which was equivalent to the spatial filter applied by the LES turbulence model. Therefore, the turbulent scales associated with the motion of

bubbles were in the inertial subrange where the energy was transferred to the smaller scales and then dissipated. This process was modeled by the bubble-induced dissipation term $\epsilon_{\text{mixt}}^{sgs,BI}$ (Eq. 3.30).

The following analysis quantified the increase of the dissipation in the simulation with bubbles compared to the case without. Furthermore, the same investigation was done on the resolved turbulent kinetic energy, which was expected to be reduced because of the enhanced dissipation.

Figure 5.7 depicts the time-variation of the spanwise averaged total sgs dissipation rate $\widetilde{\epsilon}_{\text{mixt}}^{sgs} = \widetilde{\epsilon}_{\text{mixt}}^{sgs,SI} + \widetilde{\epsilon}_{\text{mixt}}^{sgs,BI}$ with bubbles (7 classes) and without. Comparing the two cases, the sub-grid dissipation rate was enhanced at $0 \leq t^* \leq 0.5$ when the bubble phase fraction was greater. At $0.5 \leq t^* \leq 1$, $\widetilde{\epsilon}_{\text{mixt}}^{sgs}$ decreased and similar values were found with and without bubbles meaning that the contribution of $\widetilde{\epsilon}_{\text{mixt}}^{sgs,BI}$ was smaller. The noticeable sub-grid dissipation rate followed the development of the bubble plume (red contour line) and it was collocated in regions with higher vorticity as demonstrated in Fig. 5.8.

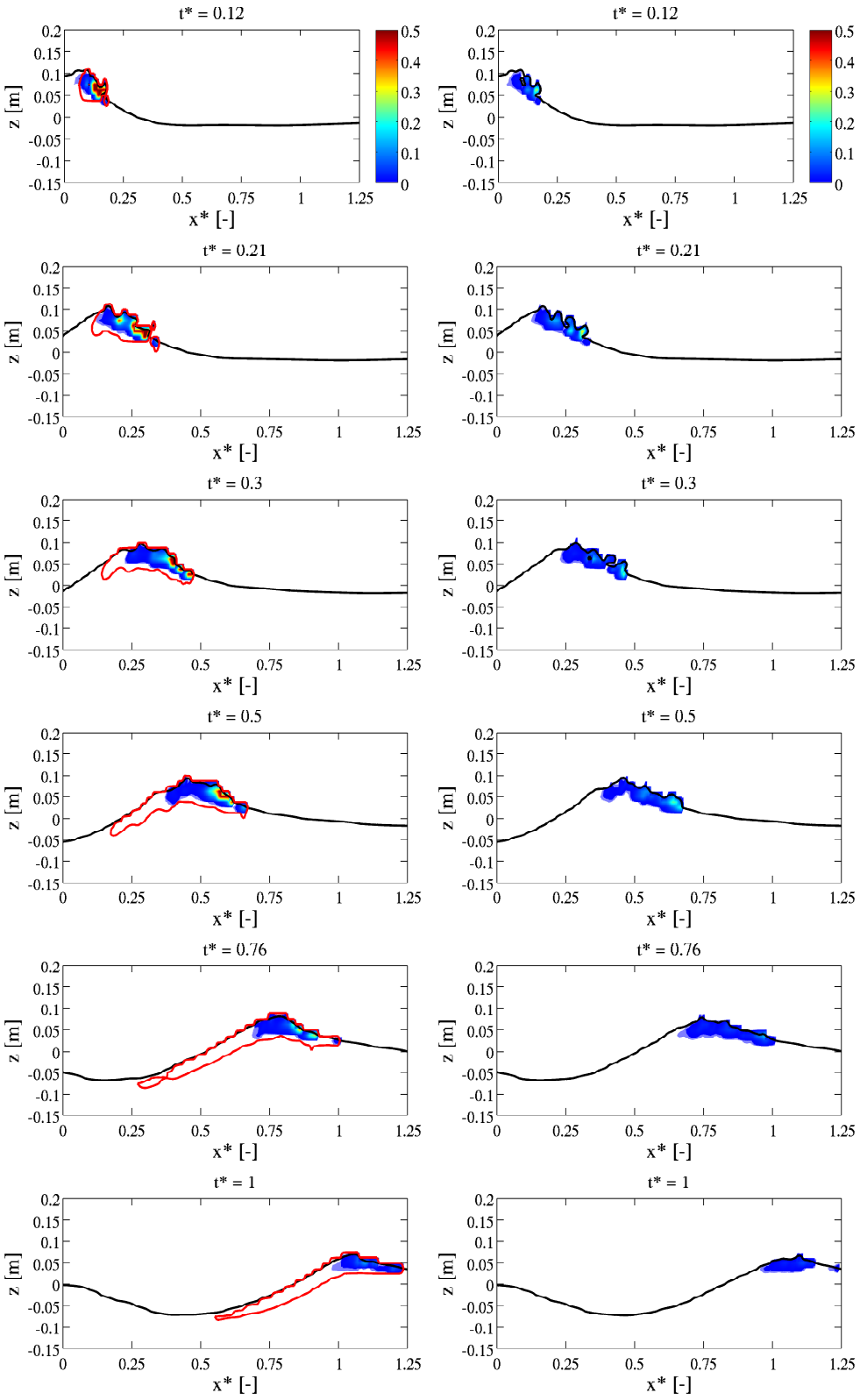

Figure 5.7: Variation with the time of the spanwise averaged sgs dissipation rate $\widetilde{\epsilon}^{sgs}_{\text{mixt}}$ [m^4 s^{-3}] with bubbles (7 classes, left side) and without (right side). The red contour line is for $\widetilde{\alpha}_{\text{b}}$ = 0.0001 [-]. The black contour line is the free surface.

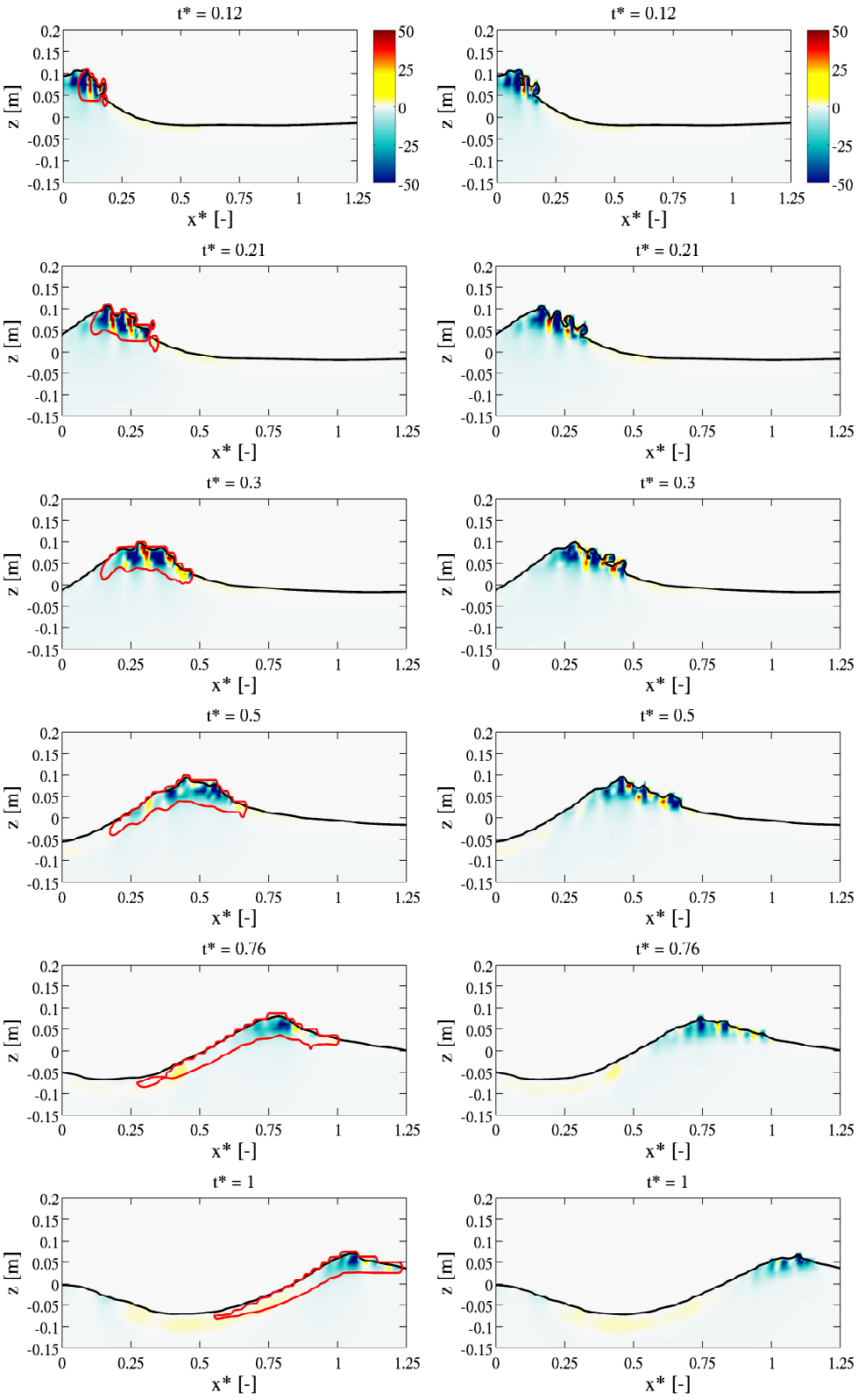

Figure 5.8: Variation with the time of the spanwise averaged vorticity $\widetilde{Q}^r_{\text{mixt}}$ [s^{-2}] with bubbles (7 classes, left side) and without (right side). The red contour line is for $\widetilde{\alpha}_b = 0.0001$ [-]. The black contour line is the free surface.

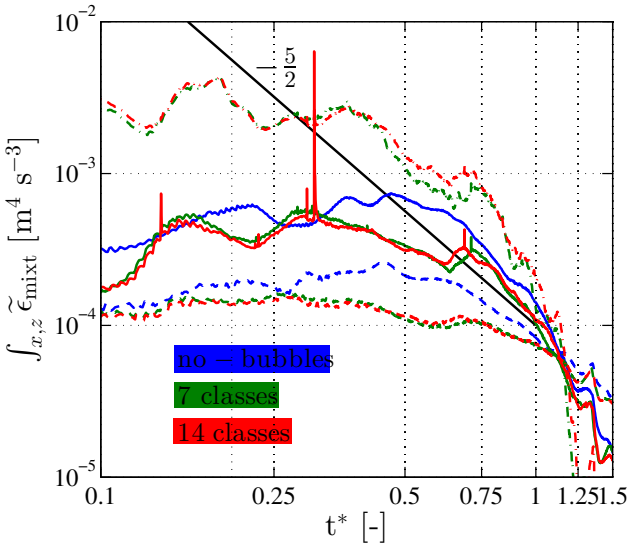

Figure 5.9: Viscous $\widetilde{\epsilon}^{r}_{\mathrm{mixt}}$ (– – –), shear-induced $\widetilde{\epsilon}^{sgs,SI}_{\mathrm{mixt}}$ (——) and bubble-induced $\widetilde{\epsilon}^{sgs,BI}_{\mathrm{mixt}}$ (–·–·–) dissipation rate per unit length of crest integrated in space over the breaking region with bubbles (7 and 14 classes) and without.

The different contributions to the total spanwise averaged dissipation rate, i.e. viscous, shear-induced and bubble-induced, were integrated in space over two wave lengths downstream the breaking point and the results are plotted in Fig. 5.9. The two cases with bubbles provided similar values for each contribution, therefore the smaller bubbles played a minor role in the dissipation process and they did not affect the water turbulence field. A spike can be spotted at $t^* \approx 0.30$ in the results of the case with 14 classes, likely due to some numerical instabilities.

In the simulations with and without bubbles, the viscous dissipation rate $\widetilde{\epsilon}^{r}_{\mathrm{mixt}}$ (per unit length of crest) was the smallest contribution during the first wave period, since the Kolmogorov microscale was much smaller than the grid size (the Reynolds number was high). In $0 \leq t^* \leq 1$, the simulations with bubbles generally showed reduced values of viscous and shear-induced dissipation rate, meaning that the resolved rate-of-strain tensor was limited by the entrained air. The bubble-induced dissipation rate was predominant, being comparable with the other two contributions form $t^* \approx 1$. At the end of the first wave period, the decay of the three dissipation rates started to follow the -5/2 slope reported by Rapp and Melville (1990) and Drazen and Melville (2009).

An estimation of the total dissipation per unit length of crest occurred in the three cases was obtained by integrating the total dissipation rate over the time. Looking at Fig. 5.10, the following observations can be made:

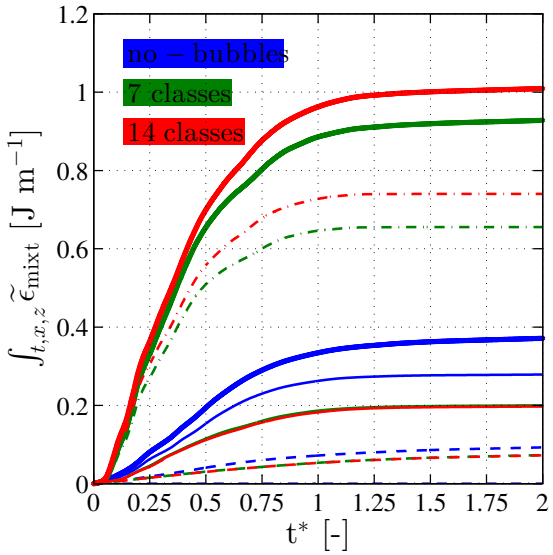

Figure 5.10: Viscous $\widetilde{\epsilon}^{r}_{\text{mixt}}$ (– – –), shear-induced $\widetilde{\epsilon}^{sgs,SI}_{\text{mixt}}$ (——), bubble-induced $\widetilde{\epsilon}^{sgs,BI}_{mixt}$ (–·–·–) and total $\widetilde{\epsilon}^{tot}_{\text{mixt}}$ (▬▬) dissipation per unit length of crest with (7 and 14 classes) and without bubbles.

- almost the whole dissipation occurred within the first wave period after breaking in each case;
- the total dissipation in the simulations with bubbles was 250% larger compared to the no-bubbles case;
- the bubble-induced dissipation accounted for approximately 70% of the total dissipation;
- the (resolved) viscous dissipation was relatively small.

These findings were consistent with the work of Derakhti and Kirby (2014), although the total dissipation in the present study was much smaller (1 J m^{-1} < 2.6 J m^{-1}). The reason could be a different implementation of the LES dynamic Smagorinsky turbulence model, adopted in both studies, because the largest discrepancy lied on the shear-induced dissipation. However, both the present study and Derakhti and Kirby (2014) underpredicted the total dissipation found in the experiments which was estimated as 4.3 J m^{-1}.

The same typology of analysis was performed on the resolved turbulent kinetic energy. The time-variation of the spanwise averaged resolved TKE is depicted in Fig. 5.11 for the case with 7 classes.

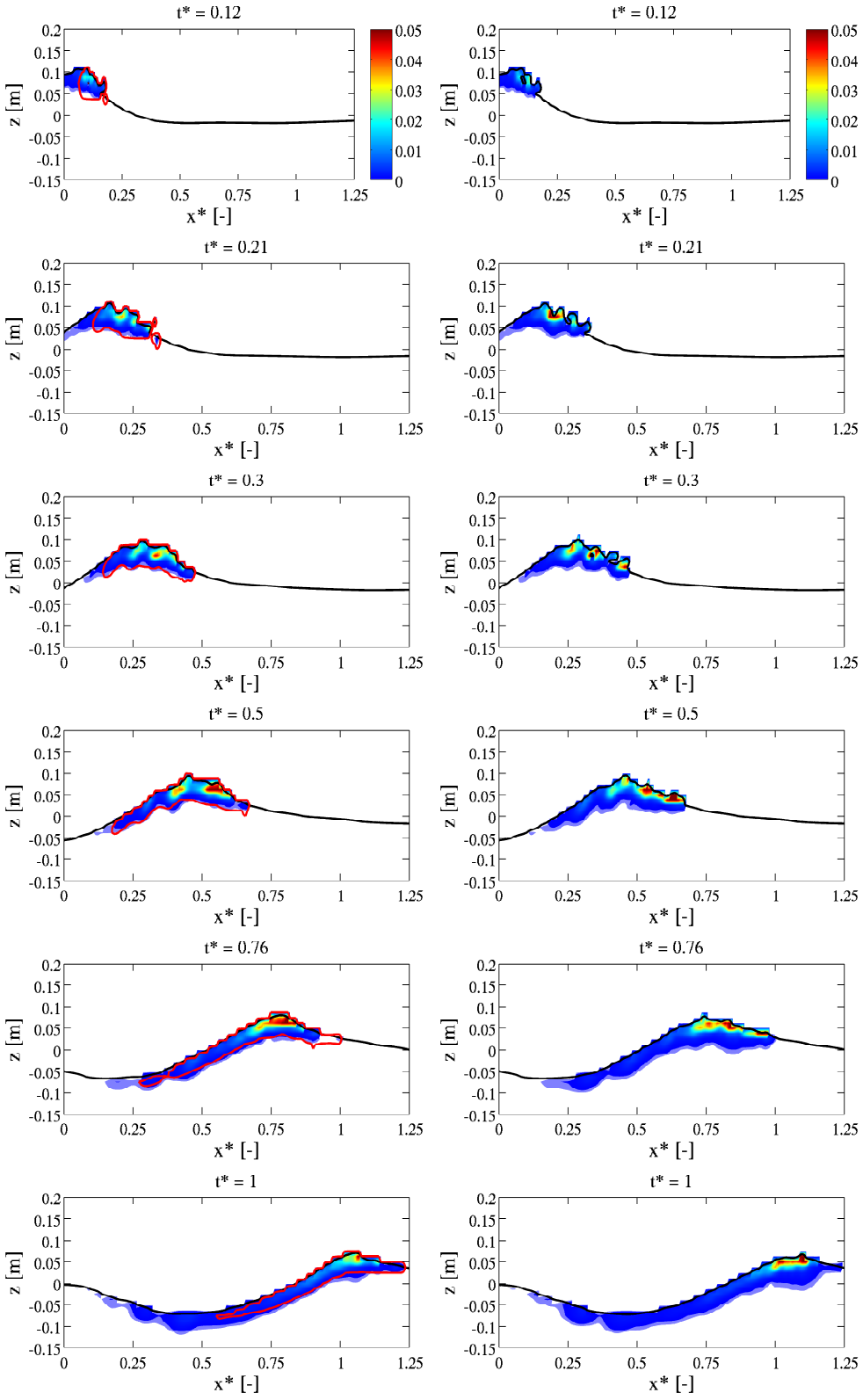

Figure 5.11: Variation with the time of the spanwise averaged resolved TKE $\widetilde{k}^{r}_{\text{mixt}}$ [m^2 s^{-2}] with bubbles (7 classes, left side) and without (right side). The red contour line is for $\widetilde{\alpha}_{\text{b}} = 0.0001$ [-]. The black contour line is the free surface.

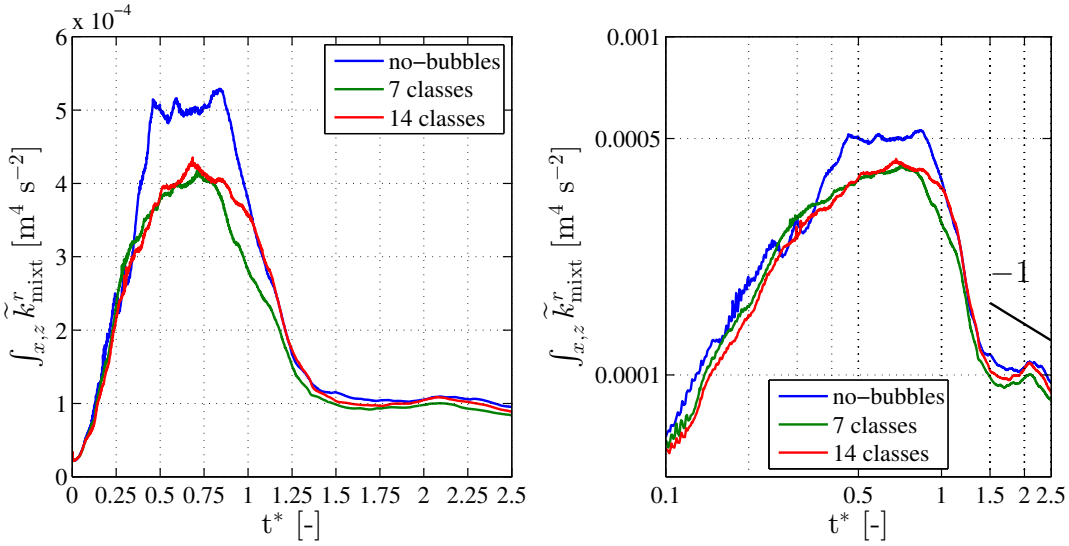

Figure 5.12: Time-variation of the spanwise averaged resolved TKE integrated in space over two wave lengths after breaking. (**a**) Linear scale axes. (**b**) Logarithmic scale axes.

A TKE cloud originated at the wave front at the beginning of the breaking process and it developed with the time like the bubble plume in Fig. 5.3. In particular, similarities were apparent on the tail beneath the wave front. This was not unexpected since it is known that smaller bubbles, which formed the tail, are transported by the occurring coherent turbulent structures. Furthermore, it can be recognised that the TKE cloud did not penetrate the whole water column. The mixed layer depth was $0.4H_{br,sim}$ approximately, where $H_{br,sim}$ is the wave height at the breaking point.

The spanwise averaged resolved TKE was integrated in space over two wave lengths for the three cases as shown in Fig. 5.12. The resolved TKE per unit length of crest was damped by approximately 20% when bubbles were included, with both 7 and 14 classes. In fact, the damping started at $t^* \approx 0.25$. At $0 \leq t^* \leq 0.25$ the results are comparable since the dispersed bubbles not only enhanced the dissipation but also the production of turbulence as explained in Derakhti and Kirby (2014). The same results plotted in logarithmic scale axes in Fig. 5.12b revealed that the decay of the turbulent kinetic energy followed the inverse respect to the time as observed in Rapp and Melville (1990) and Drazen and Melville (2009).

5.2 Regular spilling waves with entrained bubbles

The case study illustrated in Section 4.2 was analysed again, but with the inclusion of dispersed bubbles.

Cox and Shin (2003) investigated the same spilling regular waves of Ting and Kirby (1994, 1996) and measured the void fraction and the streamwise water velocity in the surf zone at three (horizontal) distances (sb1, sb2, ab3) from the breaking point and at different depths. These measurements were used to validate the predicted bubble phase fraction distribution. Table 5.2 reports the three sections and the depths at which the comparisons were made. Some of the experimental data were taken from Ma et al. (2011) wherein a numerical study similar to the present one was carried out.

	sb1 (+0.74 m)	sb2 (+0.87 m)	sb3 (+1.10 m)
depth1 [m]	+0.025	+0.025	+0.025
depth2 [m]	+0.015	+0.015	+0.015
depth3 [m]	0.0	+0.005	-0.015
depth4 [m]	-	-0.005	-
depth5 [m]	-	-0.015	-

Table 5.2: Sections and corresponding depths at which the predicted bubble phase fraction was compared with the experimental measurements of Cox and Shin (2003).

The case was set-up as follows:

- Mesh. The computational domain was the same adopted for the simulation without bubbles and it is sketched in Fig. 4.10;
- Number of phases. The simulation was performed with $N = 5$ (0.0025 m $\leq$ $d_i \leq$ 0.0062 m). The exclusion of classes with diameters 0.008 m and 0.01 m, compared to the case of the single spilling wave with 7 classes, was necessary in order to not employ a large grid size in the surf zone. Bubble coalescence was not taken into account;
- Boundary conditions. Waves were generated by the means of the utility described in Jacobsen et al. (2012) which employs the relaxation method for wave generation and absorption. A relaxation zone of 4 m (from the inlet) was used for generating the wave. In this portion of the domain, the utility imposed conditions for α_w, α_{air} and $\mathbf{u}_{mixt}$ variable with the time according to the stream function theory. The absorption zone at the outlet was not employed. At the top,

the atmospheric value was assigned to pressure and a backflow was allowed only for air (with velocity normal to the boundary). The other conditions are given in Table 5.3;

- Drag force formulation. Schiller-Neumann;
- Air entrainment parameters. c_{en} = 10 and $\epsilon_{\text{mixt}}^{sgs,SI}$ = 0.05 m^2 s^{-3} as threshold (Eq. 3.49);
- Time range simulation. The simulation was performed for 50 wave periods and it took 332 hours on 32 cores of an HPC cluster (almost seven times longer than the no-bubbles simulation).

	$\mathbf{u}_{\text{mixt}}$	$\mathbf{u}_{\text{b},i}$	α_{w}	α_{air}	$\alpha_{\text{b},i}$	p_d	$\nu_{\text{mixt}}^{sgs,SI}$	k_{mixt}^{sgs}
inlet	D.	N.	D.	D.	N.	N.	D.	D.
outlet	N.	N.	N.	N.	N.	N.	N.	N.
bottom	no-slip	slip	N.	N.	N.	N.	N.	N.
top	N./D.	N./D.	N./D.	N./D.	N./D.	D.	N.	N.
sides	slip	slip	N.	N.	N.	N.	N.	N.

Table 5.3: Boundary conditions employed in the numerical simulations of the experiments in Cox and Shin (2003). *N.* = Neumann (gradient equal to zero). *D.* = Dirichlet (fixed value). *N./D.* = Neumann for outflow and Dirichlet for inflow.

The development and the evolution with the time of the instantaneous bubble plume during a wave period is shown in Fig. 5.13.

At t^* = 0, the wave front broke at around x = 5.0 m and the roller started to form at the crest. At the same time, one or more bubble plumes were already evolving some meters downstream the breaking point. They were both induced by the previous main wave and caused by some other small breakers occurring in the surf zone. During the rest of the period, the water spilt down the face of the wave and a bore formed gradually. The new generated plume interacted with the remainder of the previous one. At t^* = 1, the same breaker was recognised at around x = 5.0 m, but the already developed plume in the surf zone had a different shape compared to t^* = 0.

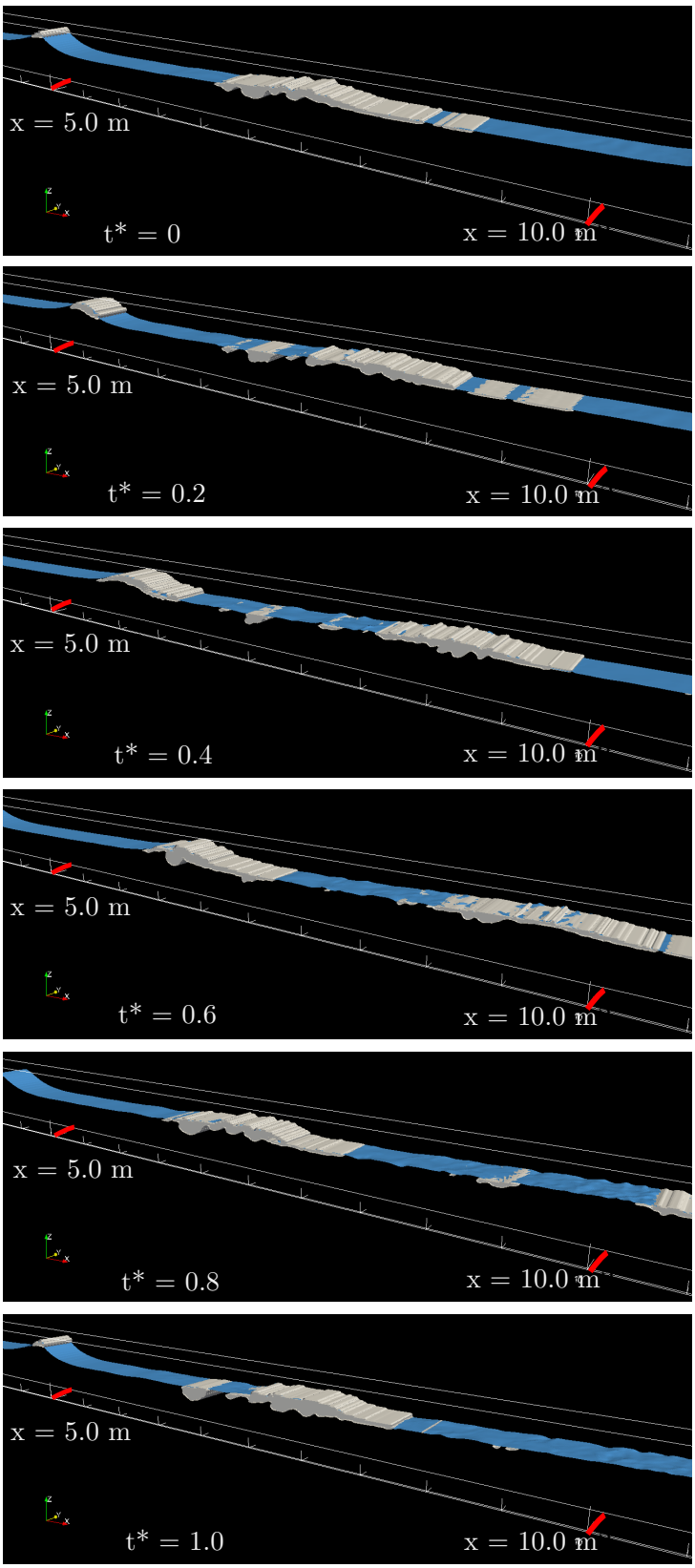

Figure 5.13: Evolution with the time of the breaking-induced bubbly flow in the surf zone. The bubble plume is bounded by the isosurface α_b = 0.0001 [-].

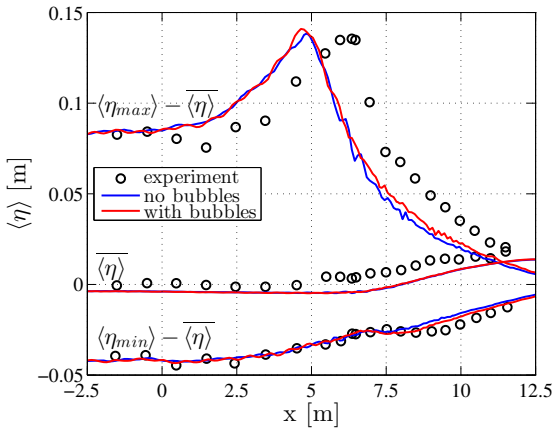

Figure 5.14: Comparison of predicted mean, max and min phase-averaged surface elevation η against experimental data along the x-axis of the domain with and without bubbles.

The same plots of Section 4.2 are shown now. All results were averaged along the y-direction ($\widetilde{\cdot}$) and phase-averaged ($\langle\cdot\rangle$) over the last 30 wave periods in order to be compared with the case without bubbles consistently.

Figure 5.14 displays the minimum, the mean and the maximum surface elevation along the flume. The vertical profiles of $\overline{\langle\widetilde{u}\rangle}_{\text{mixt},x}$ at the locations of Table 4.3 are displayed in Fig. 5.15. As expected, both comparisons did not show particular changes in the case with bubbles.

Figure 5.16 shows the vertical profiles of the square root of time-averaged total turbulent kinetic energy at the different locations of Table 4.3. Although results were similar, it can be appreciated the general tendency of the total TKE to be limited by the presence of dispersed bubbles as it was seen for the single spilling wave of Section 5.1. In particular, the reduction was more intense at the top of the water column because the bubble plume was mainly located near the free surface. Therefore, the TKE was limited at its source that is beneath the bore propagating towards the shoreline. The damping was recognised over the entire water column at sections s7 and s8. This was due not only to the smaller TKE diffused from the bore, but also to a deeper penetration of the bubble plume as represented in Fig. 5.17. The red, the green and the yellow isosurfaces comprise bubbles with a diameter of 0.0025 m, 0.004 m and 0.0063 m respectively at a certain time instant after breaking. The smaller bubbles, transported by some descending eddies, penetrated more the water column. In fact, Ting and Kirby (1994, 1996) observed that dispersed bubbles reached the bottom in the inner surf zone and not in proximity to the breaking point.

The comparison of the cases with and without bubbles could suggest that the role

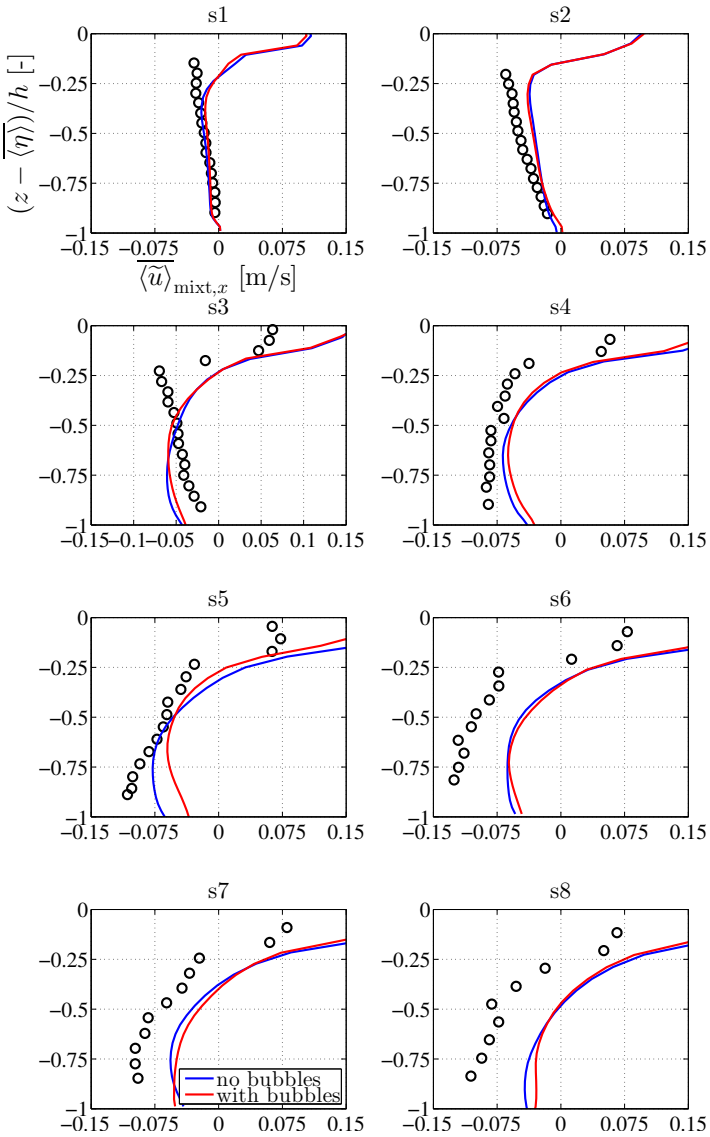

Figure 5.15: Comparison of numerical and experimental vertical profiles of phase- and time-averaged streamwise velocity $\overline{\langle\widetilde{u}\rangle}_{\mathrm{mixt},x}$ at different locations with and without bubbles. Circles: experiments. Solid line: present CFD solver.

of the dispersed air was not crucial, in particular in the estimation of the turbulent kinetic energy. Nevertheless, it should be reminded that the exclusion of bubbles *did not imply that the air entrainment was not taken into account.* In fact, the developed numerical procedure was such that, even in a simulation without bubbles, some continuous air above the free surface entrained the water during breaking as a solution of the VOF algorithm. This air could not be properly treated as dispersed, but it *still* formed a roller-like mixture traveling with the wave front. Therefore, the development of turbulence was similar in both cases, with a slight overestimation without bubbles

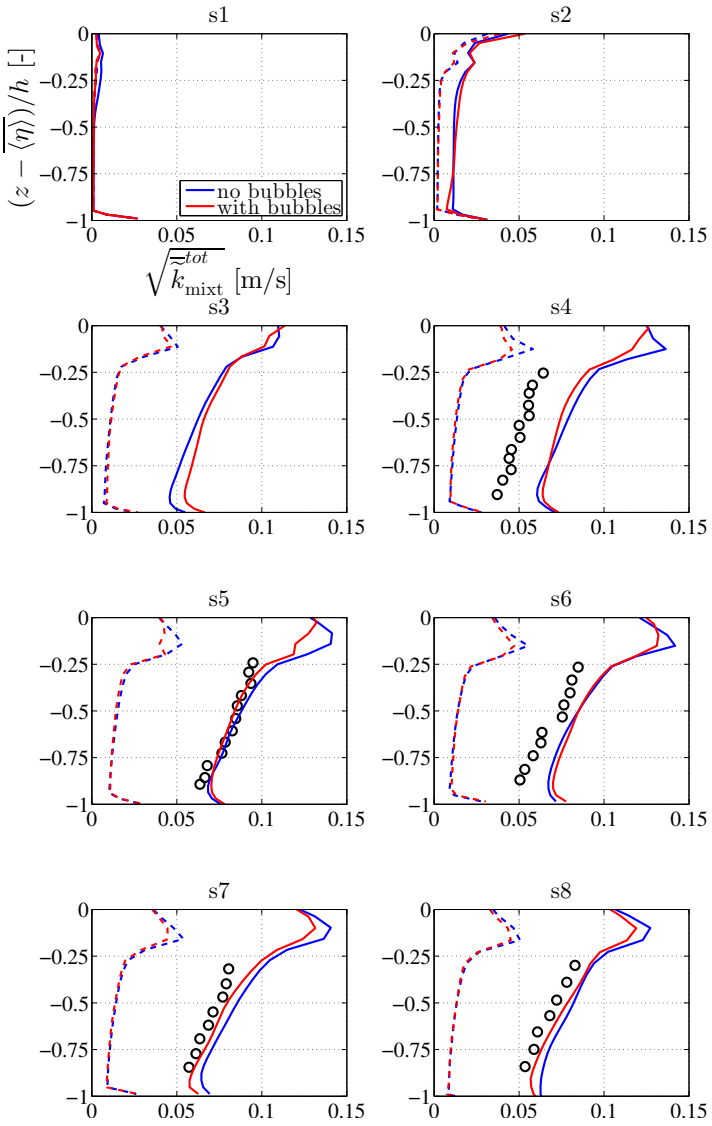

Figure 5.16: Comparison of experimental and numerical time-averaged TKE at different locations. Circles: experiment. Solid line: $\overline{\tilde{k}}^{tot}_{\mathrm{mixt}}$. Dashed line: $\overline{\tilde{k}}^{sgs}_{\mathrm{mixt}}$.

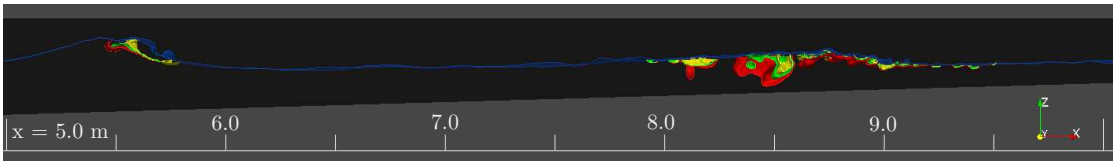

Figure 5.17: Isosurfaces for $\alpha_{\mathrm{b},i}$ = 0.0001 [-] of bubbles with a different diameter at a certain time step after breaking. Red: 0.0025 m. Green: 0.004 m. Yellow: 0.0063 m.

because of the missing extra dissipation rate term. Furthermore, it can be assumed that the different density between the upper and the lower part of the water column

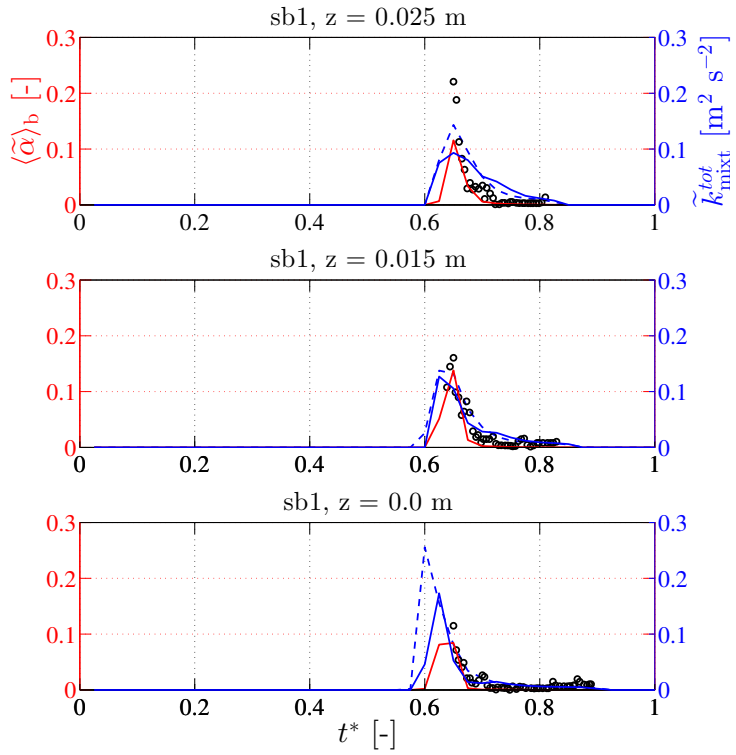

Figure 5.18: Section sb1. Left y-axis: experimental (circles) and simulated phase-averaged bubble phase fraction $\langle\widetilde{\alpha}\rangle_b$. Right y-axis: simulated total TKE $\widetilde{k}^{tot}_{mixt}$ with (——) and without bubbles (– – –).

led to a weak penetration of the TKE over the depth in the surf zone. The simulation without bubbles *still* reproduced such difference, since the VOF algorithm calculated the density of the mixture from the phase fraction of water and continuous air (Eq. 3.11) which were somehow mixed in the surf zone.

The case with bubbles allowed an investigation on the correlation between bubble phase fraction and TKE in the surf zone.

Figures 5.18-5.20 depict the comparison between simulated and experimental bubble phase fraction at the three sections and corresponding depths listed in table 5.2. These figures suggest that:

- the CFD solver captured the sharp increase and the exponential decay of $\langle\widetilde{\alpha}\rangle_b$ at a given location as well as the decrease of the peak with the depth;
- values of $\langle\widetilde{\alpha}\rangle_b$ were underestimated in particular near the wave crest. Nevertheless, section sb3 showed a larger underestimation (-50%) compared to sb1 and sb2 which could not be due only to the explained deficiencies of the approach. A reason could be that the sampling frequency adopted to output the

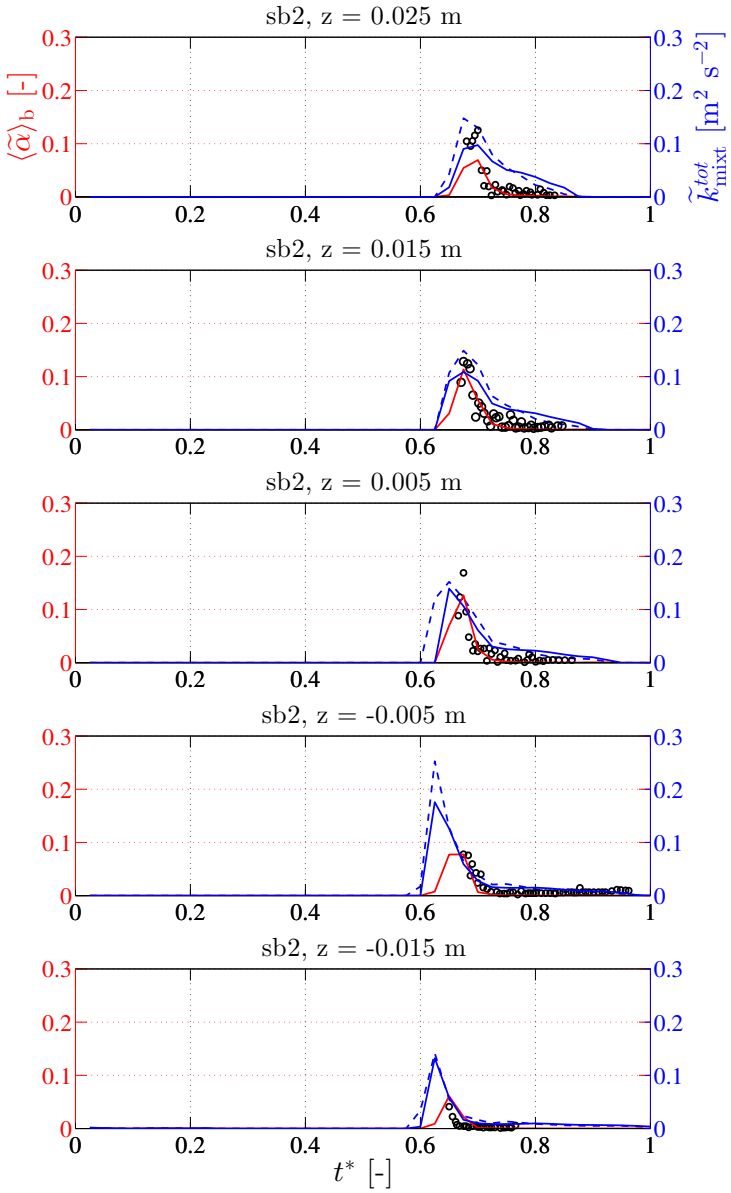

Figure 5.19: Section sb2. Left y-axis: experimental (circles) and simulated phase-averaged bubble phase fraction $\langle\widetilde{\alpha}\rangle_b$. Right y-axis: simulated total TKE $\widetilde{k}^{tot}_{mixt}$ with (——) and without bubbles (– – –).

instantaneous $\widetilde{\alpha}_b$ was not adequate and this likely led to miss the peak of the distribution;

- it is apparent that bubble phase fraction and TKE were correlated;
- the TKE was generally reduced in the case with bubbles as it was found in Section 5.1.

A further investigation was carried out on the correlation between bubble phase

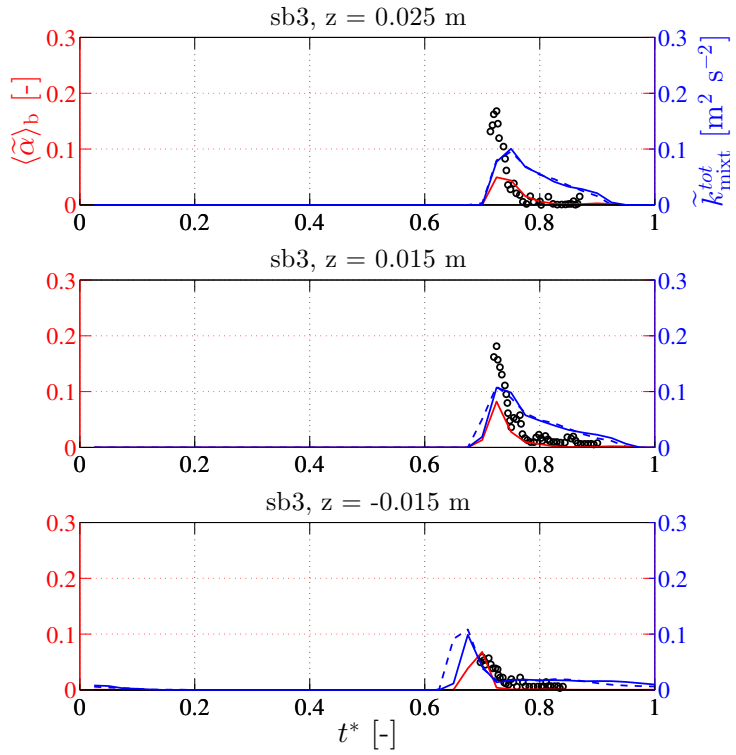

Figure 5.20: Section sb3. Left y-axis: experimental (circles) and simulated phase-averaged bubble phase fraction $\langle\widetilde{\alpha}\rangle_b$. Right y-axis: simulated total TKE $\widetilde{k}^{tot}_{mixt}$ with (——) and without bubbles (– – –).

fraction and turbulence following Cox and Shin (2003). For consistency with the rest of the present study, the total TKE was employed as a measure of the turbulence intensity, whereas Cox and Shin (2003) used the streamwise turbulent velocity $\left\langle \widetilde{u'^2} \right\rangle_{mixt,x}$ since only the streamwise water velocity was measured. Ma et al. (2011) demonstrated that these two quantities are comparable in this case.

Both $\langle\widetilde{\alpha}\rangle_b$ and $\widetilde{k}^{tot}_{mixt}$ were time-averaged over the "wet" period at sections sb1, sb2, sb3 and at all depths above the mean trough level. Results are plotted in Figs. 5.21-5.22.

The experimental values of Cox and Shin (2003) indicate that:

- the bubble phase fraction and the streamwise turbulent velocity increased with increasing the horizontal position from the breaking point;
- the bubble phase fraction decreased with depth;
- the bubble phase fraction reached the maximum just above the mean trough level and it decreased towards the mean crest.

The predicted values of $\overline{\langle\widetilde{\alpha}\rangle}_b$ actually showed a maximum above the mean trough level and decreased with depth. The increase with the distance from the breaking point was

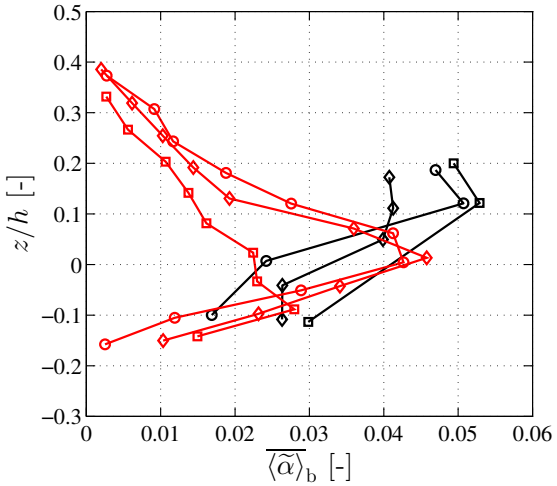

Figure 5.21: Vertical variation above the mean trough level of the phase- and time-averaged bubble phase fraction $\overline{\langle\widetilde{\alpha}\rangle}_{\mathrm{b}}$ at sections sb1 (circles), sb2 (diamonds) and sb3 (squares). Red line: present CFD solver. Black line: experiment.

not recognised especially at sections sb3 where values were largely underestimated as discussed above. The simulated TKE was in fair agreement with the experimental one, but overestimated in all sections likely because of the spurious velocities. Furthermore, a reduction of TKE could be recognised at sb1 and sb2 in the case with bubbles.

Values of averaged bubble phase fraction and averaged TKE in Figs. 5.21-5.22 are plotted together in Fig. 5.23. As in the experiments of Cox and Shin (2003), a positive linear correlation was recognised at sb1 and sb2 up to the maximum of the bubble phase fraction, whereas at sb3 the large underestimation of $\langle\widetilde{\alpha}\rangle_{\mathrm{b}}$ affected the results. The same correlation was found by Lim et al. (2015) in a laboratory plunging breaker. In conclusion, the case studies illustrated in this chapter have shown that:

- the developed coupling between the Eulerian multiphase and the VOF model was stable;
- the implemented air entrainment formulation of Derakhti and Kirby (2014) was reliable;
- the main effect of the dispersed bubbles was to reduce the turbulent kinetic energy. This damping, although apparent, was not found large when compared to the results of a standard VOF algorithm which took into account the air phase, hence the variation of density in the water column after breaking.

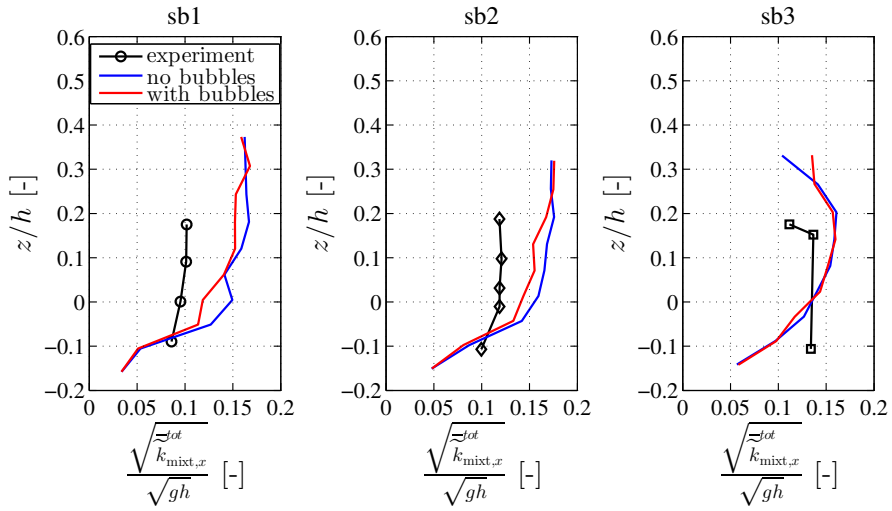

Figure 5.22: Vertical variation above the mean trough level of the non-dimensional time-averaged turbulent kinetic energy at sections sb1, sb2 and sb3.

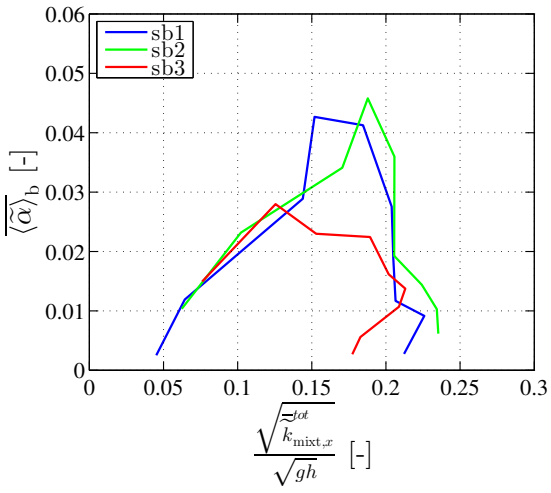

Figure 5.23: Case with bubbles. Correlation between simulated phase- and time-averaged bubble phase fraction and simulated non-dimensional time-averaged turbulent kinetic energy.

6 Application: breaking wave impact on a cylinder

The developed CFD solver was employed for reproducing the impact of a spilling breaking wave on a vertical circular cylinder which was chosen as representative of a real mono-pile offshore structure.

The numerical analysis was conducted at a laboratory scale, since experimental measurements of the force exerted on the same cylinder by the same wave were available. The experiment was carried out at the Technical University of Denmark, but before the development of the CFD solver and not by the authors of the present study.

As in the experimental tests, the relative distance between the breaking point and the location of the cylinder was varied in the numerical simulations which were performed with and without the inclusion of dispersed bubbles. This procedure was followed in order to:

- understand how the in-line force exerted on the cylinder changed within the breaking region. In this regard, the experiment already gave a clarification;
- verify whether a proper modeling of the air entrainment changed the computed value of the in-line force compared to a standard VOF method which already takes into account the mixture of air and water after breaking.

The following sections cover the experiment, the numerical reproduction of the laboratory waves and of the impact.

6.1 The experiment

6.1.1 Experimental setup

The experiment took place at the Technical University of Denmark but it was not conducted by the authors of the present study.
The investigation was carried out in a flume 28 m long by 0.60 m wide by 0.80 m high

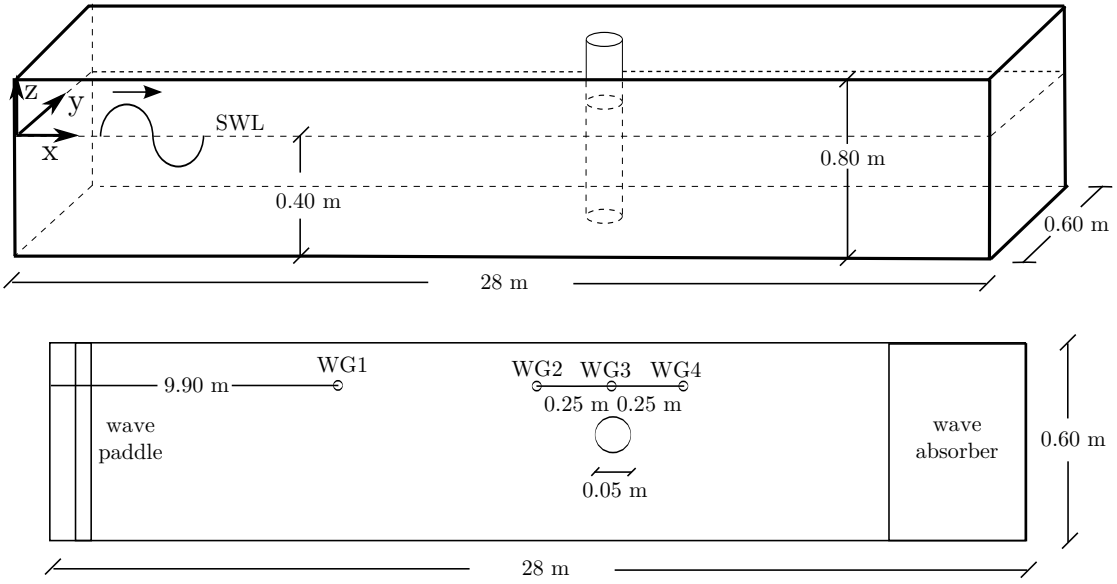

Figure 6.1: Sketch of the laboratory wave flume where the experiment was conducted. Top: 3D view. Bottom: view from above.

filled with water to a depth of h_{sw} = 0.40 and with a flat bottom. At the inlet, waves were produced by a piston-type wave generator provided with Active Wave Absorption Control System (AWACS) developed by DHI Water & Environment in order to avoid spurious reflection from the wavemaker. A system to absorb waves was installed at the end of the flume.

Figure 6.1 depicts the experimental setup. The cylinder was made of aluminum and has a diameter D = 0.05 m. It was equipped with two force transducers which measured the force at the bottom and at top. The total force was defined as the sum of these two contributions. A rail along the centerline of the bottom of the flume (x-axis) allowed to place the cylinder at different locations. The surface elevation was measured by the means of wave gauges (WG) at four stations: WG1 at 9.90 m from the inlet of the flume, and WG2, WG3, WG4 at -0.25 m, +0.0, +0.25m from the cylinder respectively. The experimental setup can be appreciated also in photographs taken during the experiment (Fig. 6.2).

Several tests were performed. A test consisted of generating waves from still water conditions and simultaneously measuring both the surface elevation at the four gauges and the forces on the cylinder (bottom and top). The generated waves produced a single spilling breaker at a certain time and location. For each test, 14 repetitions of this procedure were carried out.

Figure 6.2: Arrangement of cylinder and wave gauges WG1, WG2, WG3 and WG4 in the experiment.

The generated waves were the same in each test, but the cylinder was placed at a different location with respect to the fixed wave breaking point. Wave gauges WG2, WG3 and WG4 were moved as well, whereas WG1 was kept at 9.90 m from the inlet in each test. The scope was to measure how the exerted forces varied inside the breaking region, where the bubble plume, hence the roller, evolved both in space and time as it has been seen in Chapter 5.

The locations at which the cylinder was mounted in terms of distance (in meters) relative to the breaking point (X) were: -0.50, -0.10, -0.05, +0.0, +0.05, +0.10, +0.15, +0.20, +0.25, +0.30, +0.35, +0.40, +0.45, +0.50, +0.55, +0.60, +0.65, +0.70, +1.0 and +1.5.

6.1.2 The experimental spilling breaker

A spilling breaker was obtained by the means of a dispersive focusing technique similar to the one described in Section 5.1. The wave packet was derived from a

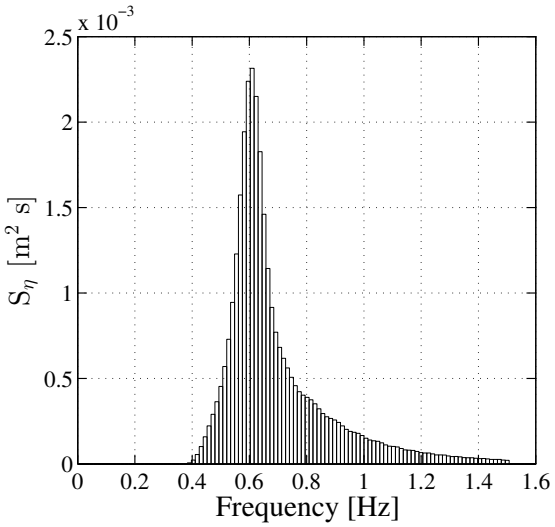

Figure 6.3: JONSWAP spectrum employed to derive the linear components of the wave packet for the wave generation in the experiment.

parameterized JONSWAP spectrum given by

$$S_\eta = \left[\frac{0.0624}{0.230+0.0336\gamma-\frac{0.185}{1.9+\gamma}}\right] H_s^2 f_p^4 f^{-5} \gamma^\beta \exp\left[-\frac{5}{4}\left(\frac{f_p}{f}\right)^4\right] \tag{6.1}$$

where

$$\beta = \exp\left[-\frac{(f-f_p)^2}{2\sigma^2 f_p^2}\right] \qquad \text{with } \sigma = \begin{cases} 0.07 & \text{if } f \le f_p, \\ 0.09 & \text{if } f > f_p \end{cases}$$

The values of the peak enhancement γ, the significant wave height H_s and the peak frequency $f_p = 1/T_p$ were chosen in order to obtain a spectrum representative of a scaled scenario in the North Sea at deep/intermediate water depth. The values are reported in the table below.

peak enhancement γ [-]	significant wave height H_s [m]	peak period T_p [s]
3.3	0.084	1.7

Table 6.1: Parameters of the employed JONSWAP spectrum.

The resulting JONSWAP spectrum was discretized in $N_{lc} = 80$ linear components as depicted in Fig. 6.3.

Each component was expressed as

$$\eta_i = A_i \left[\cos\left(\omega_i t\right) - k_i x + \Phi_i\right] \tag{6.2}$$

and had a frequency $f_i = 2\pi/\omega_i$ (middle of each bar) and an amplitude $A_i = \sqrt{2S_{\eta,i}\Delta f}$ with $\Delta f = f_{i+1} - f_i$. The wave length $L_i = 2\pi/k_i$ was calculated as suggested in (Veritas, 2000).

$$L_i = T_i\sqrt{(g h_{sw})}\sqrt{\frac{1+\sum_{j=1}^{4}\alpha_j\overline{\omega}^j}{1+\omega\left(1+\sum_{j=1}^{4}\alpha_j\overline{\omega}^j\right)}} \qquad \text{with} \begin{cases} \alpha_1 = 0.666 \\ \alpha_2 = 0.445 \\ \alpha_3 = -0.105 \\ \alpha_4 = 0.272 \end{cases} \tag{6.3}$$

Phases Φ_i were determined by synchronizing the downcrossing point of each component at $x_{br,th}$ = 13.5 m and $t_{br,th}$ = 0 s . It was verified that the synchronization of the downcrossing points, instead of the crests, focused the energy in a way that the breaker could be a spilling.

The superposition of all components gave the surface elevation at the wave paddle η_p

$$\eta_p = \sum_{i=1}^{80}\eta_i = A_i\left[\cos\left(\omega_i t\right) - k_i x_p + \Phi_i\right] \tag{6.4}$$

which was transformed into the paddle horizontal displacement through the Biésel transfer functions.

6.1.3 The results of the experiment

In order to better understand the following comparisons with the numerical results, an example of the outputs given by a single repetition of a test is shown in this section. The case is for the cylinder placed right at the breaking point (X = 0 m) which was observed at $x_{br,exp}$ = 11.20 m. The photographic sequence of the impact and of the development of the bubble plume is reported in Fig. 6.4.

The time-variation of surface elevation at the four wave gauges is displayed in Fig. 6.5a. Recalling that WG2, WG3 and WG4 were in each test at -0.25 m, +0.0 m and +0.25 m from the cylinder respectively, in this test WG2 was at x = 10.95 m, WG3 at x = 11.20 m and WG4 at x = 11.45 m, whereas WG1 was at x = 9.90 m as in all tests.

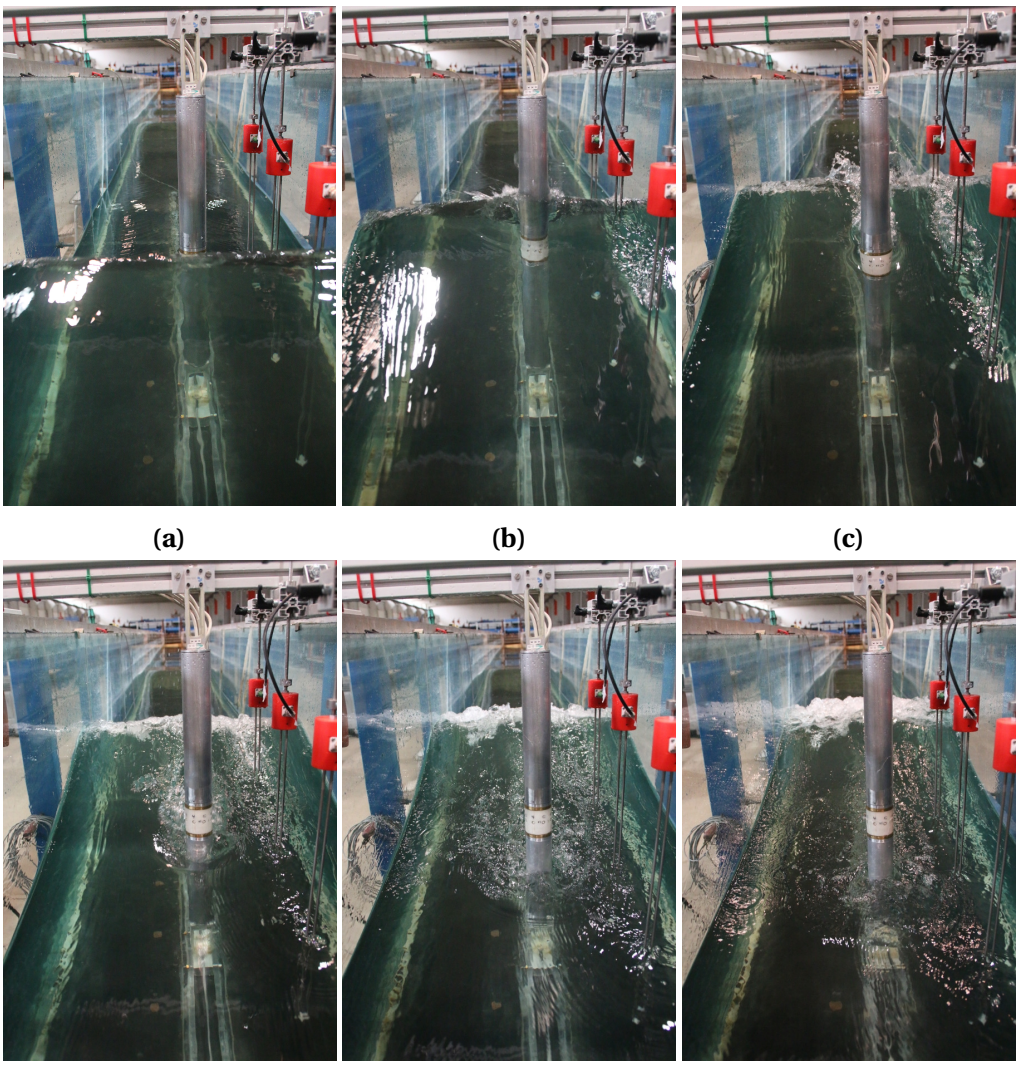

Figure 6.4: Photographic sequence of the impact and of the development of the bubble plume for the case $X = 0$.

A wave train propagated along the flume with different wave heights. Because of the focusing, the height of the highest wave at a given point x of the flume increased with increasing x. At a certain location, the height of the highest wave was too large compared to the depth (the bottom was flat) and this wave broke. As already said, the wave breaking was observed to start at $x = 11.20$ m when the height $H_{br,exp}$ became 0.22 m approximately. The period of the breaking wave $T_{br,exp}$ was estimated to be 1.80 s.

The surface elevation at WG3 and the total force on the cylinder are plotted together in Figs. 6.5b. As expected, the maximum force occurred before the maximum surface

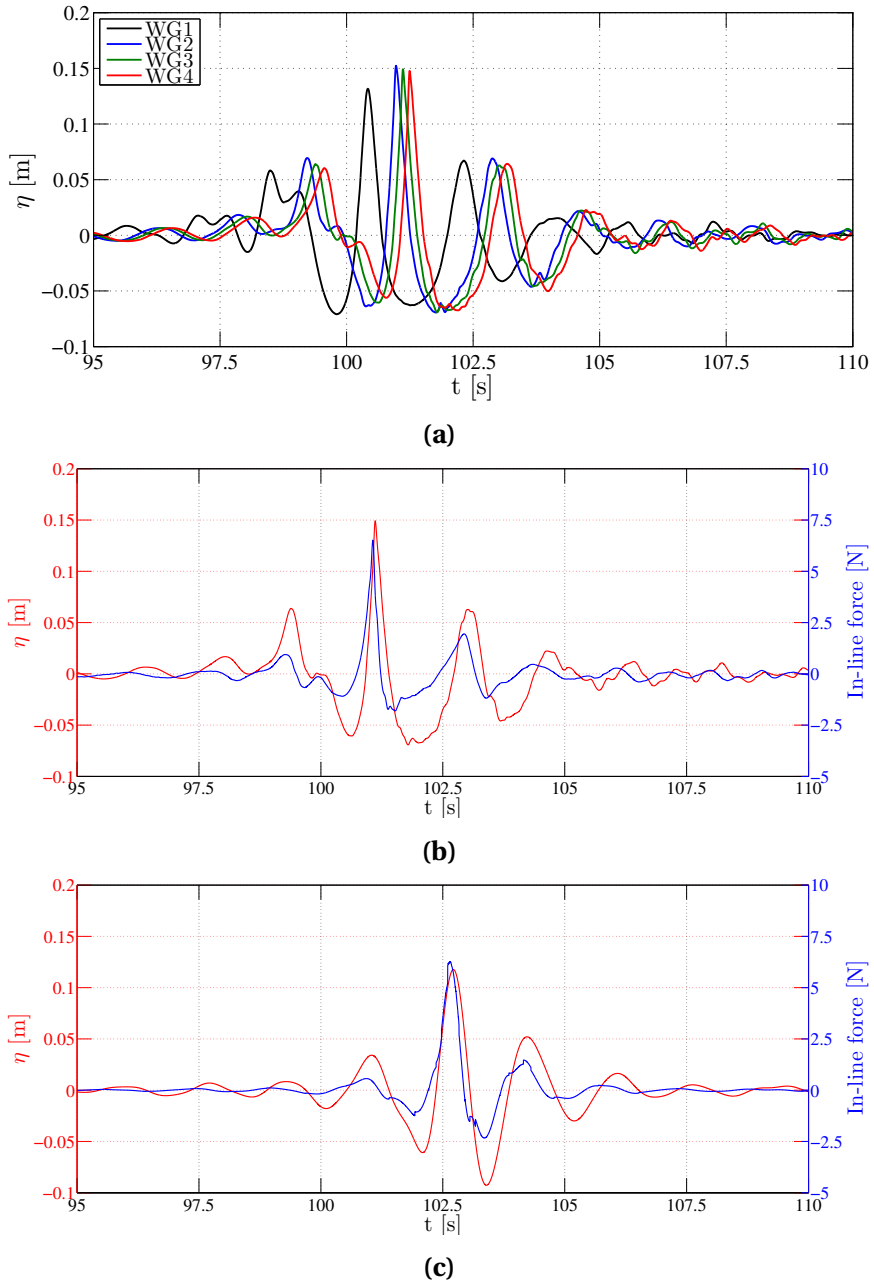

Figure 6.5: Case $X = 0$ m. (**a**) Time-variation of the experimental surface elevation η at the four wave gauges installed along the flume. (**b**) Time-variation of the experimental surface elevation η at WG3 and the simultaneous total in-line force exerted on the cylinder. (**c**) Time-variation of the analytical surface elevation η at WG3 based on the linear wave theory and the simultaneous total in-line force exerted on the cylinder given by the Morison equation.

elevation. Figure 6.5c displays the same time series based on the application of the linear wave theory and the Morison equation. The nonlinear effects in the experiments are evident from the comparison of the figures.

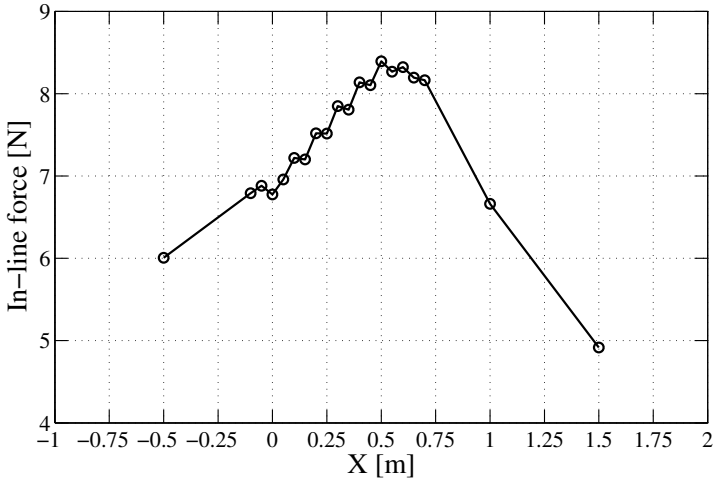

Figure 6.6: The maximum value of the experimental total in-line force exerted on the cylinder placed at different locations X.

Figure 6.6 shows the maximum values of the experimental total in-line force measured at the different distances X, mainly within the breaking region. It can clearly appreciated that the maximum of total in-line force increased after the breaking and then decreased, reaching a maximum 0.50 m downstream the breaking point approximately. Therefore, *the maximum instantaneous force did not occur when the cylinder was at the breaking point.*

6.2 The numerical reproduction of the laboratory waves

Before the simulation of the impacts with and without dispersed bubbles by the developed CFD solver, it was necessary to find the proper set-up in order to achieve an accurate numerical reproduction of the laboratory waves. In particular, two aspects were investigated through several tests:

- a proper input wave signal, i.e. the boundary conditions at the inlet of the numerical flume, in order to obtain the experimental spilling breaker;
- a good prediction of the wave breaking that is the motion of the roller and of the breaking-induced bubble plume.

The final set-up was the following:

- Mesh. These tests were performed by employing a computational domain without the cylinder as depicted in Fig. 6.7. The domain was 25.0 m long by 0.60 m wide by 0.6 m height. The still water depth was at 0.40 m. The mesh was uniform and comprised 4608000 hexaedral cells of size 0.0125 m;

- Number of phases. Three simulations were performed: no-bubbles, N = 7 (0.0025 m $\leq$ d$_i$ $\leq$ 0.01 m) and N = 14 (0.0005 m $\leq$ d$_i$ $\leq$ 0.01 m). The simulations were performed without taking into account the bubble coalescence. The case without bubbles was used for testing the wave input signal;

- Boundary conditions. Waves were generated by the means of the utility described in Jacobsen et al. (2012) which employs the relaxation method for wave generation and absorption. A relaxation zone of 4 m (from the inlet) was used for generating the wave. In this portion of the domain, the utility imposed conditions for α_{w}, α_{air} and $\mathbf{u}_{\mathrm{mixt}}$ variable with the time as it will be shown later. An absorption zone of 4 m was used at the end of the domain. At the top, the atmospheric value was assigned to pressure and a backflow was allowed only for air (with velocity normal to the boundary). The other conditions are given in Table 6.2;

- Drag force formulation. Schiller-Neumann (Eq. 3.36);

- Air entrainment parameters. c_{en} = 10 and $\epsilon^{sgs,SI}_{\mathrm{mixt}}$ = 0.01 m^2 s^{-3} as threshold (Eq. 3.49);

- Time range simulation. The flow was simulated from 0 to 35 s and it took 21 hours for the case without bubbles, 40 hours with 7 classes and 55 hours with 14 classes on 40 cores of an HPC cluster;

	$\mathbf{u}_{\mathrm{mixt}}$	$\mathbf{u}_{\mathrm{b},i}$	α_{w}	α_{air}	$\alpha_{\mathrm{b},i}$	p_d	$\nu^{sgs,SI}_{\mathrm{mixt}}$	k^{sgs}_{mixt}
inlet	D.	N.	D.	D.	N.	N.	D.	D.
outlet	N.	N.	N.	N.	N.	N.	N.	N.
bottom	slip	slip	N.	N.	N.	N.	N.	N.
top	N./D.	N./D.	N./D.	N./D.	N./D.	D.	N.	N.
sides	slip	slip	N.	N.	N.	N.	N.	N.

Table 6.2: Boundary conditions employed in the numerical simulations of the experiment without cylinder. $N.$ = Neumann (gradient equal to zero). $D.$ = Dirichlet (fixed value). $N./D.$ = Neumann for outflow and Dirichlet for inflow.

6.2.1 The input wave signal

The input wave signal was the set of boundary conditions to be prescribed at the inlet of the domain for both α_{w}, α_{air} and $\mathbf{u}_{\mathrm{mixt}}$ in order to generate the wave train. The case

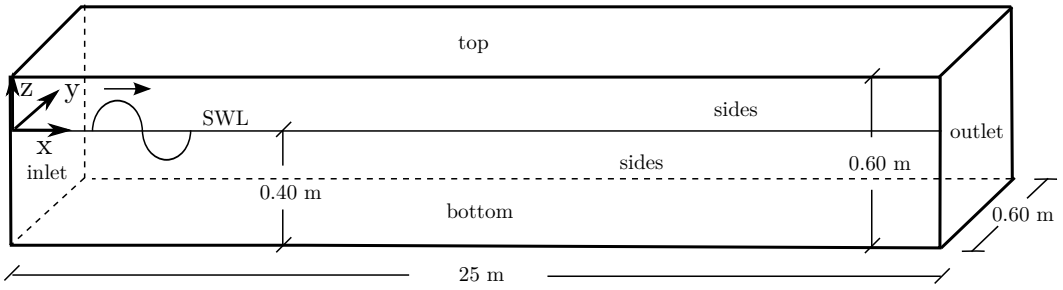

Figure 6.7: Domain adopted for the numerical simulation of the experiment. Not to scale.

without bubbles was used to test the signal. The experimental measurements for the case $X = 0$ m (Section 6.1.3) were employed to assess the accuracy of the numerical reproduction of the generated waves.

The first tests concerned the direct application of Eq. 6.4 and the corresponding relations for $u_{\text{mixt},x}$ and $u_{\text{mixt},z}$ based on the linear wave theory, but they did not produce satisfying results. The comparison with the experimental surface elevation at the four wave gauges revealed that the simulated wave train evolved differently (not reported here).

For a better accuracy, it was decided to reconstruct the input signal from the experimental measurements. Practically, the reconstruction consisted of deriving the linear components to be superposed (Eq. 6.4) not from the JONSWAP spectrum as in Section 6.1.2, but through the application of a Fourier transform algorithm on the experimental time series. In particular, the Fourier transform was applied on both the measured displacement of the wave paddle and the measured surface elevation at WG1. The results are displayed in Fig. 6.8 and it can observed that:

- the shape of the spectrum of the actual paddle displacement is slightly different than the one derived from the prescribed JONSWAP spectrum in Fig. 6.3. In fact, the input signal from Eq. 6.4 was further tailored at the laboratory;
- the spectrum of the experimental wave train evolved between the inlet and WG1 which was 9.90 m farther downstream. In particular, new components with frequencies around 0.2 Hz and 1 Hz arose. The former suggest that standing waves with a long period likely established. The latter indicate the nonlinearities of the generated waves.

The linear components provided by the Fourier transform algorithm were superposed to obtain the input wave signal. As an example, a portion of the reconstructed surface elevation at the paddle, derived from the measured paddle displacement (Fig. 6.8a), is shown in Fig. 6.9.

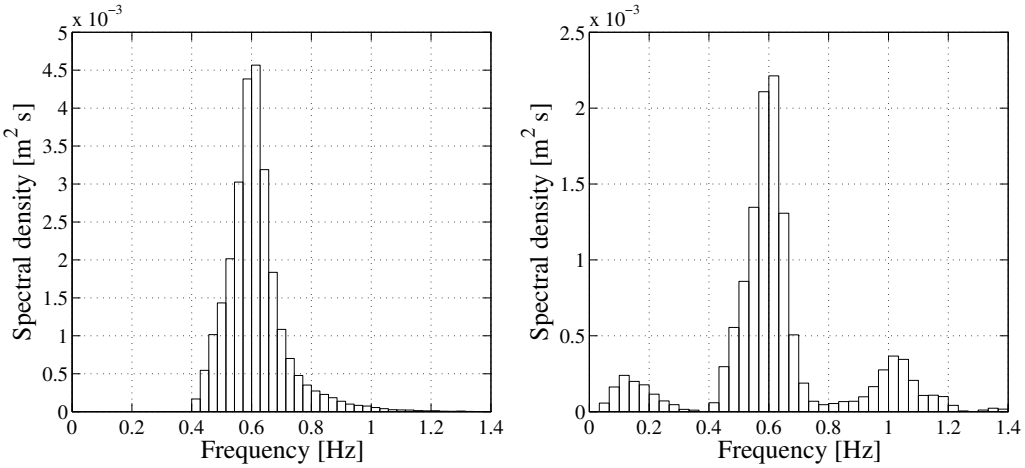

(a) Paddle **(b)** WG1

Figure 6.8: Case $X = 0$ m. Variance spectrum of the experimental paddle horizontal displacement (**a**) and of the experimental surface elevation at WG1 (**b**).

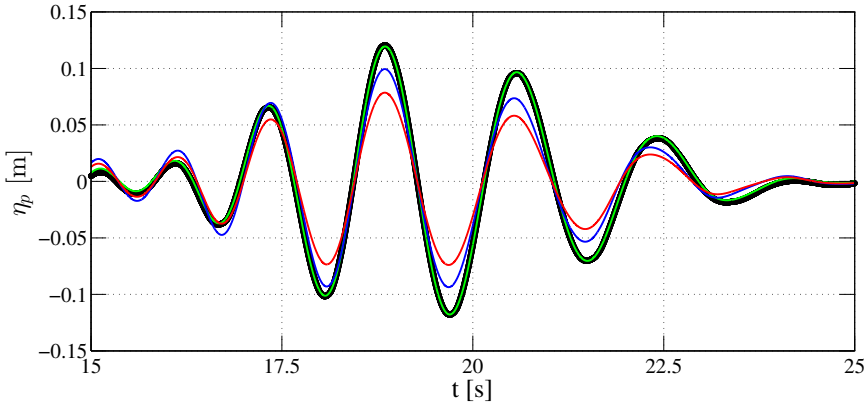

Figure 6.9: Reconstruction of surface elevation at the paddle from the experimental paddle displacement. Thick black line: experimental paddle displacement. Green line: reconstructed paddle displacement. Blue line: reconstructed surface elevation at the paddle. Red line: reconstructed surface elevation at the paddle after the application of the amplification factor.

The thick black line is the paddle displacement signal which overlaps the green line representing the reconstructed signal. The blue line is the surface elevation at the paddle found by applying the Bièsel transfer function. The meaning of the red line will be explained later. Furthermore, the time series for $u_{\mathrm{mixt},x}$ and $u_{\mathrm{mixt},z}$ were calculated consistently.

The numerical simulations carried out with both reconstructed input wave signals were not successful. A large wave formed right after the inlet boundary and broke prematurely in the generation zone (within 4 m from the inlet). This occurrence was

attributed to the chosen wave generation method. In fact, the prescription of the time-variation of both the water phase fraction and the velocities at the inlet was an approximation since the actual movement of the paddle was not replicated. Moreover, the piston-type wavemaker generated some turbulent motions around the paddle which were not taken into account, especially near the gap between the paddle and the sides of the flume.

In order to remedy the premature breaking, the input wave signal was multiplied by an amplification factor A_f. The best results were obtained for A_f = 0.80. This sort of adjustment, although arbitrary, is also employed in laboratory experiments when the amount of energy in a wavepacket is too high and waves break at the paddle. The reduced input signal is represented with a red line in Fig. 6.9.

The reconstruction from the two experimental signals, paddle displacement and surface elevation at WG1, are compared in Figs. 6.10-6.11. From this figures, it is apparent that the employment of the paddle displacement signal gave much better results, hence it was used throughout the rest of this analysis.

Looking at Fig. 6.10, it can be appreciated that the CFD solver fairly reproduced the surface elevation at each wave gauge. The highest waves of the train suffered from some discrepancies at the crests and at the troughs. The former were attributed to the mesh resolution which was not relatively high (17 cells for the height of the highest wave). The latter were likely caused by the linear theory adopted for the wave generation procedure which neglected nonlinear interactions among the components.

The wave breaking was observed to start at $x_{br,sim}$ = 12.65 m and $t_{br,sim}$ = 27.35 s when the wave height $H_{br,sim}$ was 0.207 cm approximately. This breaking point is intended to be the time instant at which the surface elevation reached the maximum value and the wave front broke. The period of the breaking wave $T_{br,sim}$ was calculated to be 1.80 s.

6.2.2 The wave breaking

For the present investigation on the role of the roller in a wave breaking-induced impact against a cylinder, an accurate simulation of the air entrainment phenomenon was necessary.

The calibration of the air entrainment formulation, that is the choice of the value for c_{en} and of the threshold for $\epsilon_{\text{mixt}}^{sgs,SI}$, was achieved through the same analysis presented in Section 5.1 for the experimental spilling breaker of Lamarre and Melville (1991).

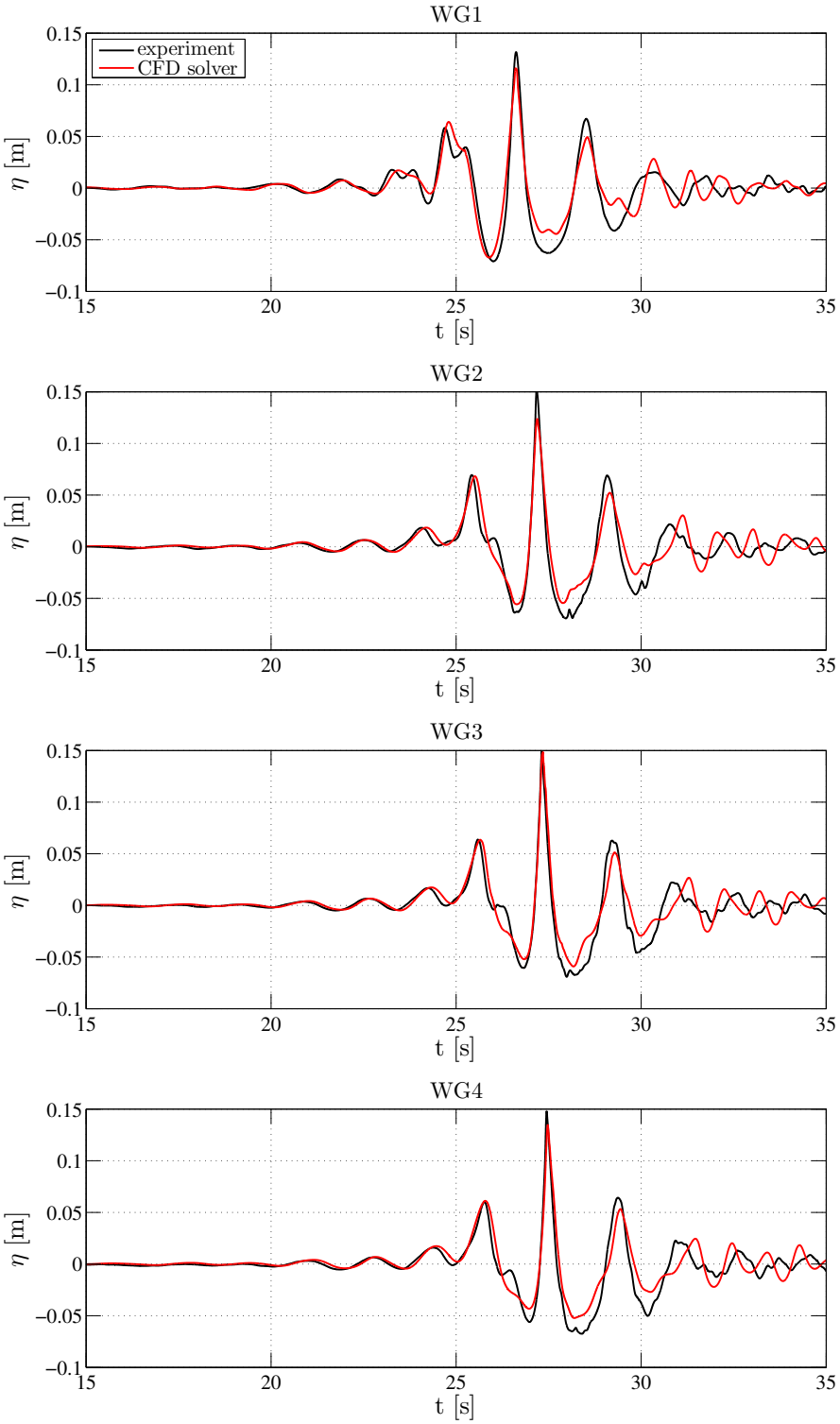

Figure 6.10: Time-variation of the experimental and simulated surface elevation at WG1, WG2, WG3 and WG4 for the case where the input wave signal was reconstructed from the experimental paddle displacement.

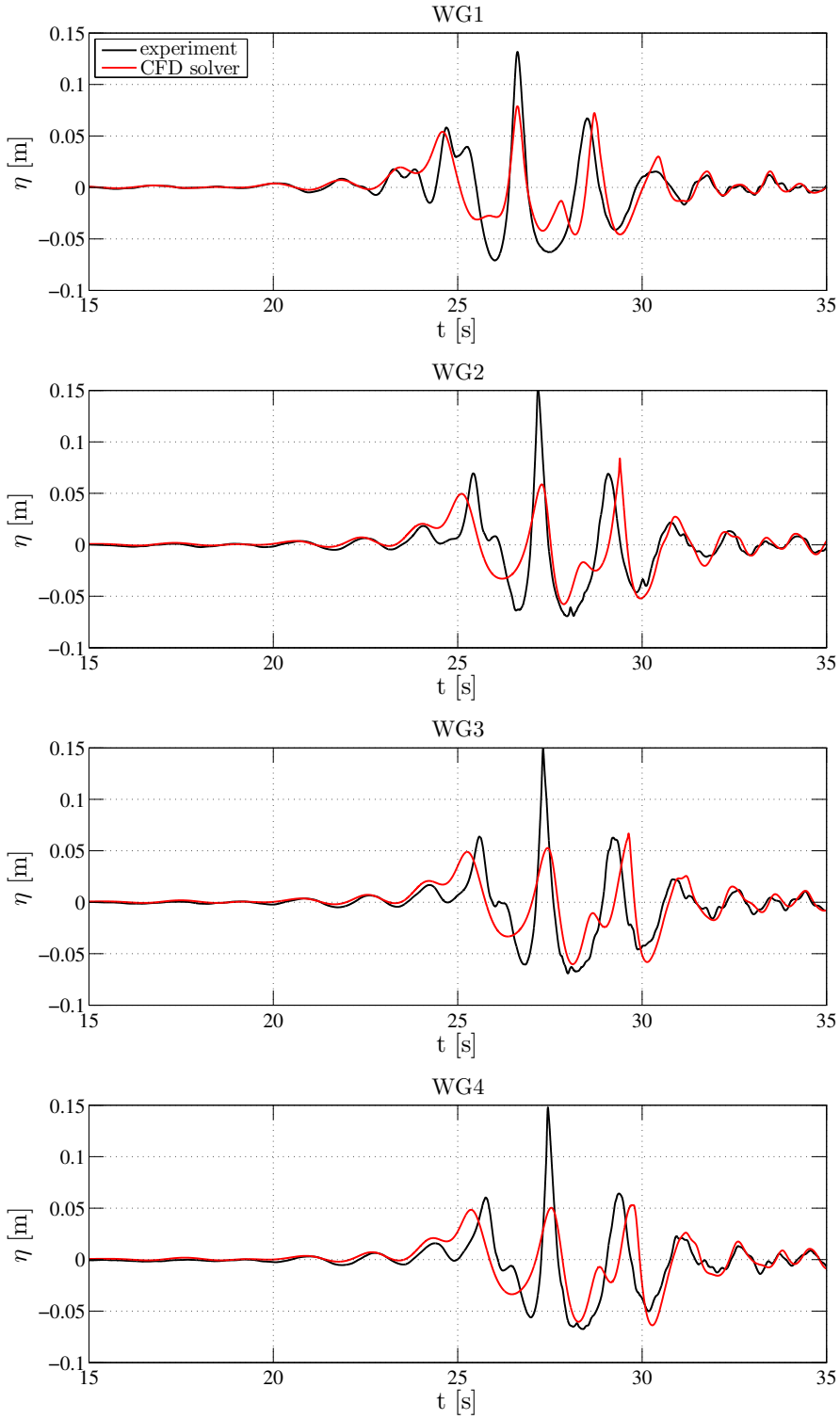

Figure 6.11: Time-variation of the experimental and simulated surface elevation at WG1, WG2, WG3 and WG4 for the case where the input wave signal was reconstructed from the experimental surface elevation at WG1.

In the present case, the best results were obtained by choosing $c_{en} = 10$ and $\epsilon_{\text{mixt}}^{sgs,SI} = 0.01\ \text{m}^2\text{s}^{-3}$.

The numerical air entrainment became noteworthy at $x_{en,sim} = 13.25$ and $t_{en,sim} = 27.6$ s, therefore 0.60 m downstream the point $x_{br,sim}$ when the bulge of air and water formed. As discussed in Section 5.1, this occurrence was defined as the breaking.

The breaking point ($x_{en,sim}$, $t_{en,sim}$) and the corresponding wave length $L_{en,sim}$ and period $T_{en,sim} = 1.80$ s were used to express the non-dimensional space x^* and time t^* (Eqs. 5.8).

Figure 6.12 shows the time-variation of the spanwise averaged ($\tilde{.}$) bubble phase fraction with the time over the first wave period after breaking in the case with 7 classes. It can be recognised that the evolution of the bubble plume was similar to the one depicted in Fig. 5.3. For this reason, the measurements of Lamarre and Melville (1991) were used to validate the calibration also in the present case. The same comparisons introduced in Section 5.1 are given in the following. Since the two breakers were comparable, the obtained results can be expatiated analogously.

The integral properties of the bubble plume are plotted in Fig. 6.13. The apparent differences between Fig. 5.4a and Fig. 6.13a come from the fact that, in the present case, the total volume V_{b} was normalized through the maximum value 0.0015 $\text{m}^3\ \text{m}^{-1}$ instead of 0.0025 $\text{m}^3\ \text{m}^{-1}$, which was the maximum volume measured in Lamarre and Melville (1991). The maximum volume predicted in the present spilling breaker was higher then the one in the simulation in Section 5.1 (0.0008 $\text{m}^3\ \text{m}^{-1}$). The visualization of the videos recorded during the experiment as well as of the animations of the numerical simulations suggested that the present spilling breaker was not close to become plunging, therefore it was believed less energetic than the one in Lamarre and Melville (1991). Nevertheless, since the air entrainment was more dependent on a turbulent mechanism, the CFD solver was more effective in transferring the mass from the continuous air into dispersed bubbles as discussed in Section 5.1 and the total volume of the plume per unit length of crest was higher. From the comparison of Fig. 6.13b and Fig. 5.4b, it can be appreciated the sensitivity of the cross-sectional area to the kind of breaker. The averaged bubble phase fraction was underestimated as already explained in previous chapters.

The horizontal and vertical centroid are compared in Fig. 6.14 and again the CFD solver predicted that the plume moved horizontally at the phase speed of the wave. The time-variation of the bubble number density is shown in Fig. 6.15a. The bubble size spectrum at two different time instants is depicted in Fig. 6.15b.

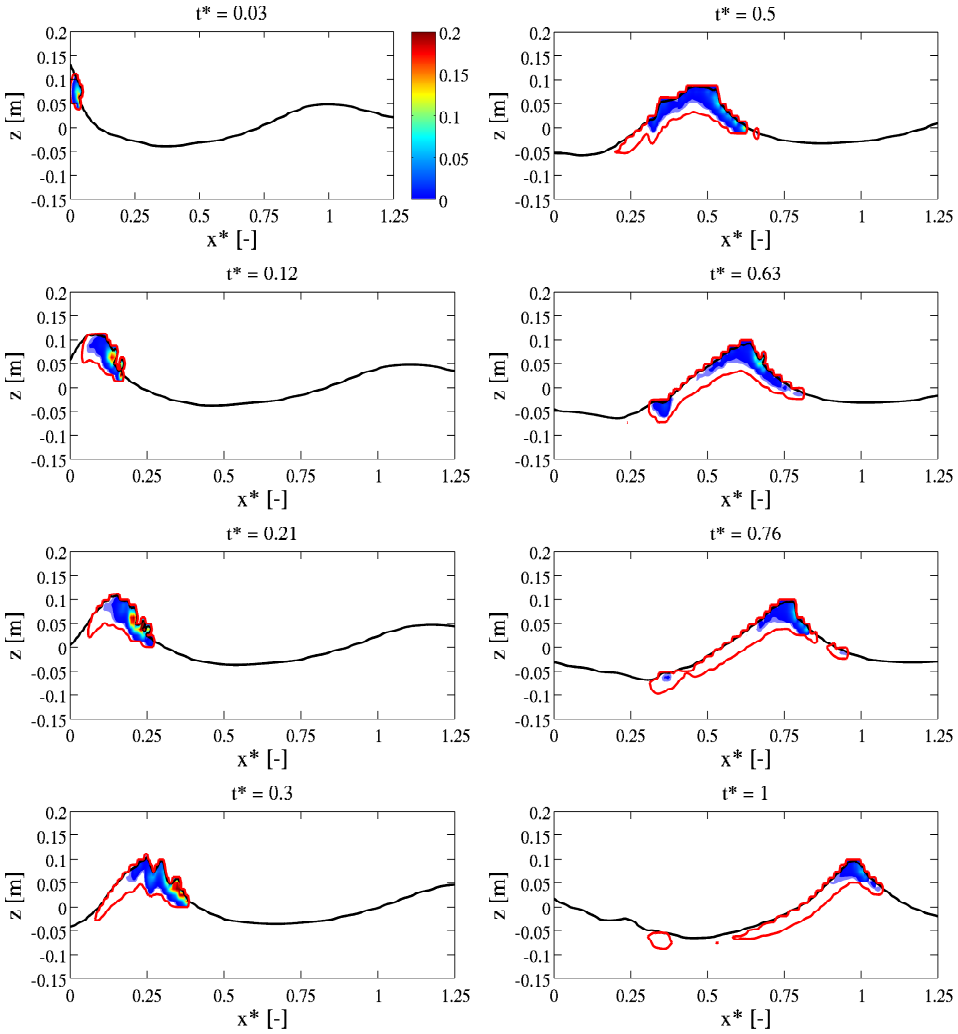

Figure 6.12: Variation with the time of the spanwise averaged volume fraction of the entrained bubbles $\widetilde{\alpha}_b$ in the case with 7 classes. The red contour line is for $\widetilde{\alpha}_b = 0.0001$ [-]. The black contour line is the free surface.

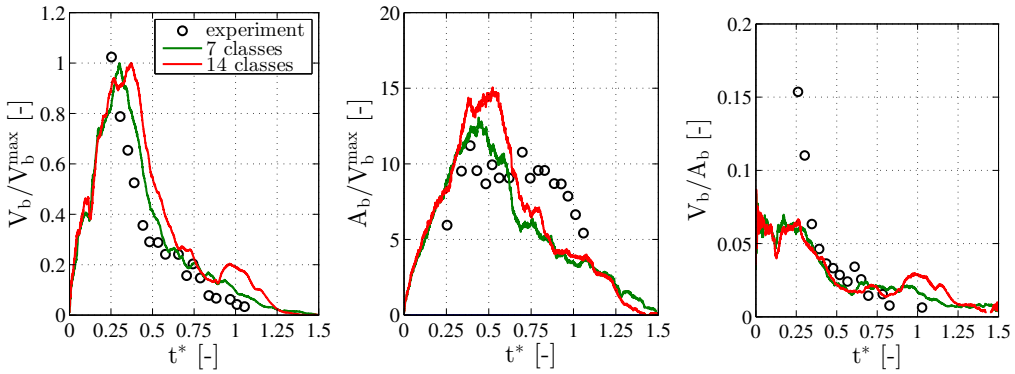

Figure 6.13: Experimental and simulated integral properties of the bubble plume. (**a**) Normalized total volume of entrained air per unit length of crest. (**b**) Normalized cross-sectional area of the bubble plume. (**c**) Averaged bubble phase fraction.

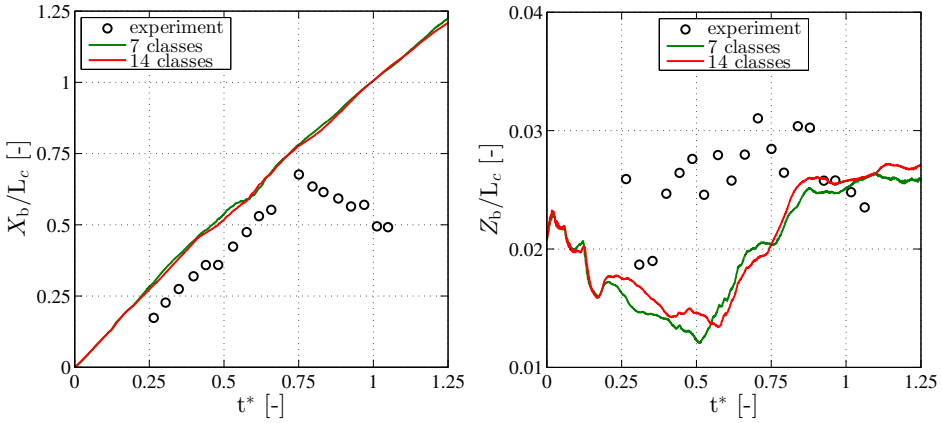

Figure 6.14: Comparison of the experimental and simulated centroids of the bubble plume.

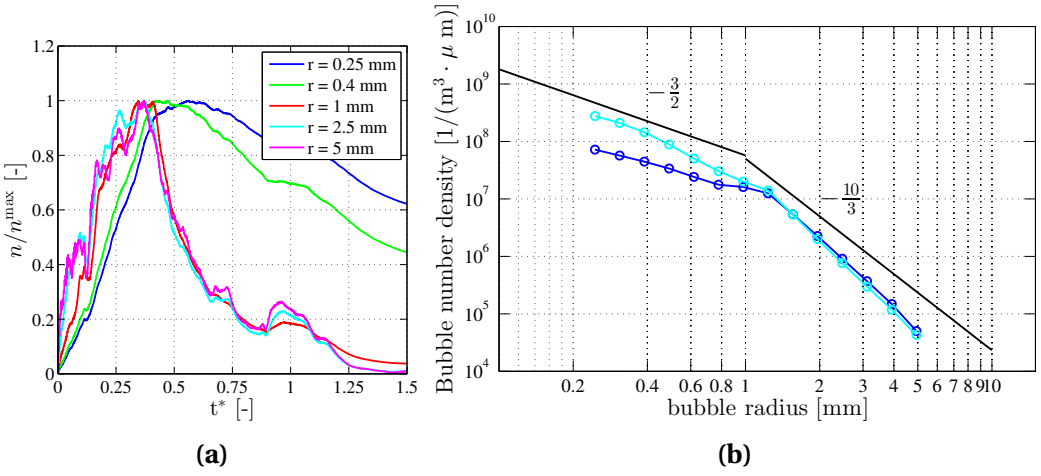

Figure 6.15: Case with 14 classes. (**a**) Evolution of the normalized bubble number density for different bubble diameters. (**b**) Bubble size spectrum at $t^* = 0.20$ (blue line) and at $t^* = 0.75$ (ciano line).

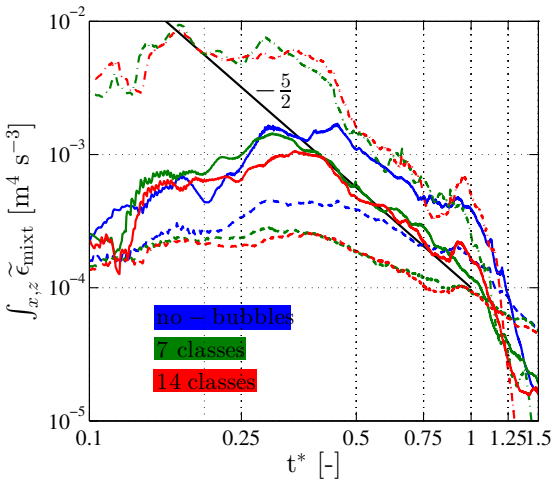

Figure 6.16: Viscous $\widetilde{\epsilon}^{r}_{\mathrm{mixt}}$ (– – –), shear-induced $\widetilde{\epsilon}^{sgs,SI}_{\mathrm{mixt}}$ (——) and bubble-induced $\widetilde{\epsilon}^{sgs,BI}_{\mathrm{mixt}}$ (–·–·–) dissipation rate per unit length of crest integrated in space over the breaking region with (7 and 14 classes) and without bubbles.

The investigation of the influence of the entrained air on the turbulence showed the same results of Section 5.1, i.e. the resolved turbulent kinetic energy field was damped because the motion of the dispersed bubbles enhanced the sub-grid dissipation rate. Nevertheless, this damping was found to be larger for the present spilling breaker. In fact, the integration of the different contributions of the spanwise averaged sgs dissipation rate over two wave lengths (Fig. 6.16) and especially the successive integration over the time (Fig. 6.17) revealed that the bubble-induced dissipation was enhanced compared to the breaker in Section 5.1. In particular, Figure 6.17 suggests that:

- almost the whole dissipation was concentrated within the first wave period after breaking;
- the total dissipation in the simulations with bubbles was 300% larger compared to the no-bubbles case;
- the bubble-induced dissipation accounted for approximately 70% of the total dissipation;
- the (resolved) viscous dissipation was relatively small.

The time-variation of the spanwise averaged total sgs dissipation rate is depicted in Fig. 6.18. The same considerations done on Fig. 5.7 can be repeated.

The increased damping of the resolved turbulent kinetic energy is not visible in Fig. 6.19 where the time-variation of the spanwise averaged resolved TKE is illustrated (for

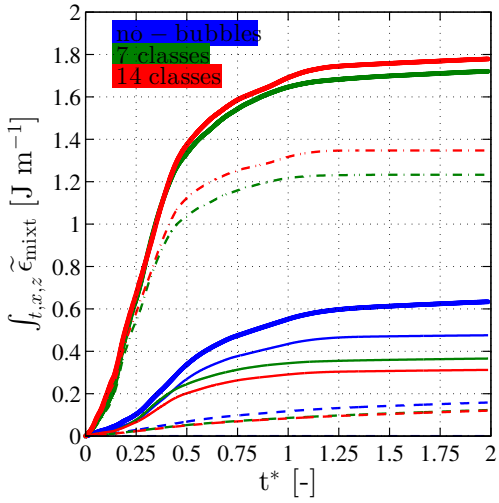

Figure 6.17: Viscous $\widetilde{\epsilon}^{r}_{\text{mixt}}$ (– – –), shear-induced $\widetilde{\epsilon}^{sgs,SI}_{\text{mixt}}$ (——), bubble-induced $\widetilde{\epsilon}^{sgs,BI}_{mixt}$ (–·–·–) and total $\widetilde{\epsilon}^{tot}_{\text{mixt}}$ (▬▬) dissipation per unit length of crest with (7 and 14 classes) and without bubbles.

the case with 7 classes), but becomes clear in Fig. 6.20 where the spanwise averaged resolved TKE is integrated in space over two wave lengths. Concerning the present breaker, the adopted number of classes produced a difference. In the case with 14 classes, the TKE was damped by approximately 50%, whereas by approximately 35% with 7 classes. For the breaker of Section 5.1, the reduction was by 20%. Also Derakhti and Kirby (2014) found that the damping was larger in a "pure" spilling breaker than in a plunging or spilling/plunging.

The performed analysis on the simulated wave breaking led to the following conclusions:

- the calibration of the air entrainment formulation was believed appropriate since both the motion of the roller and the evolution of the bubble plume was in agreement with the experimental measurements of Lamarre and Melville (1991) where comparable breaking waves were investigated. This setup was used for the simulations of the wave impact on the cylinder;
- the prediction of the bubble entrainment by the CFD solver was really sensitive to the kind of breaker. As expected, it was found that the closer the breaker to be a spilling, the smaller the influence of the coupled VOF algorithm on the total amount of entrained air. As a consequence, more entrained air was treated as dispersed;
- since the volume of the dispersed bubbles was larger, the damping of TKE consistently increased.

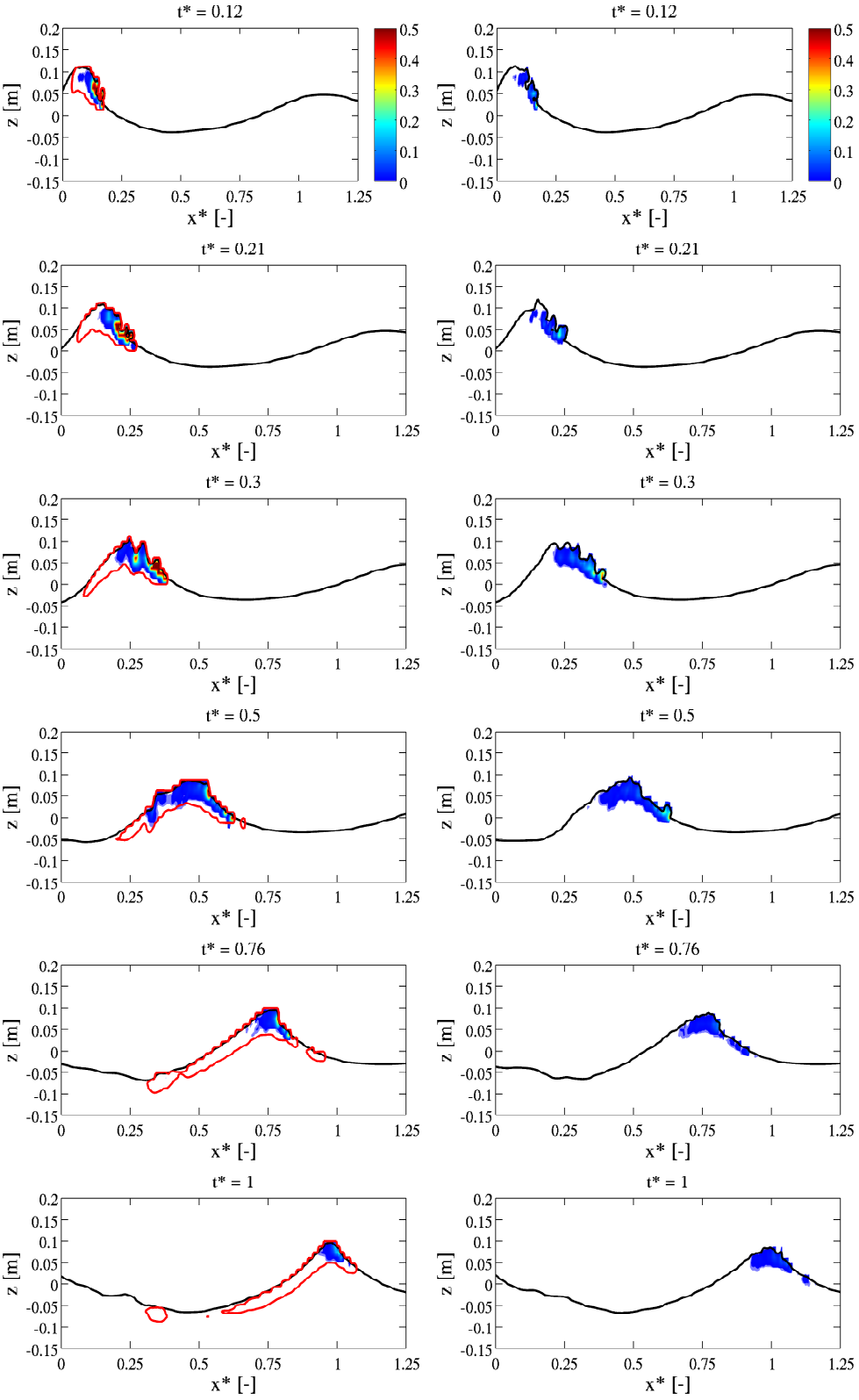

Figure 6.18: Variation with the time of the spanwise averaged sgs dissipation rate $\widetilde{\epsilon}^{sgs}_{\text{mixt}}$ [m^4 s^{-3}] with (7 classes, left side) and without bubbles (right side). The red contour line is for $\widetilde{\alpha}_{\text{b}}$ = 0.0001 [-]. The black contour line is the free surface.

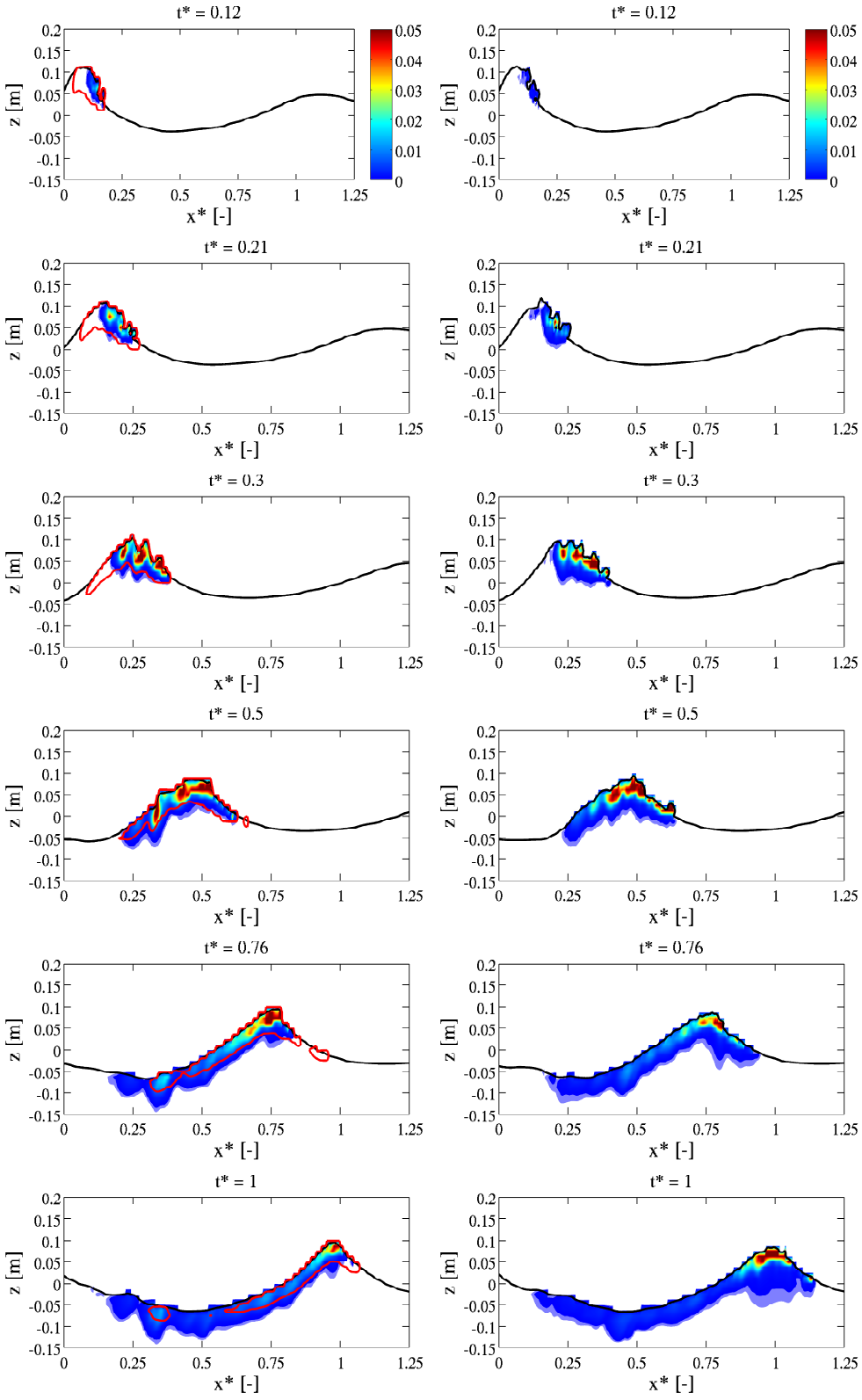

Figure 6.19: Variation with the time of the spanwise averaged resolved TKE $\widetilde{k}^r_{\text{mixt}}$ [m^2 s^{-2}] with bubbles (7 classes, left side) and without (right side). The red contour line is for $\widetilde{\alpha}_b = 0.0001$ [-]. The black contour line is the free surface.

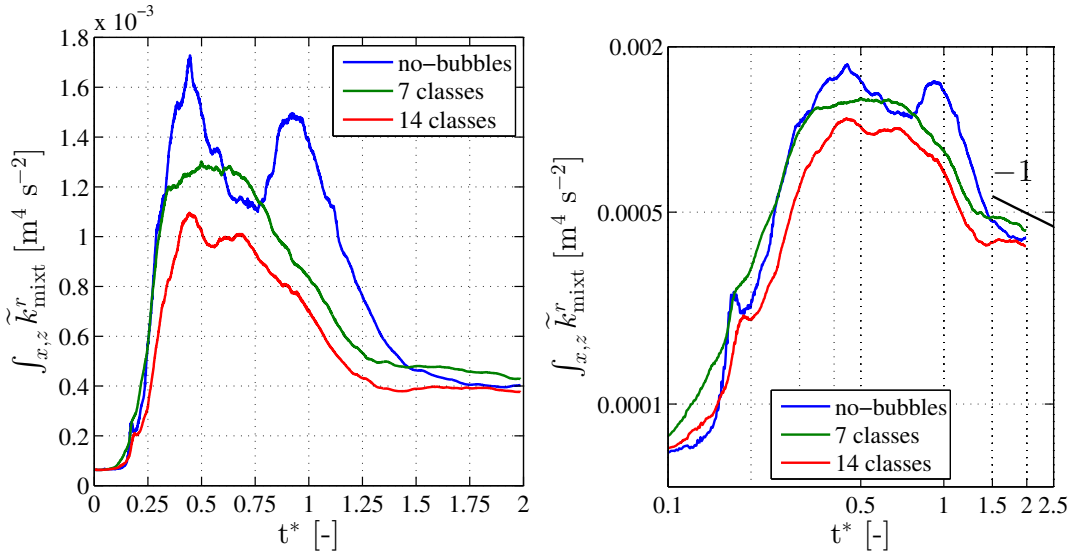

(a) **(b)**

Figure 6.20: Time-variation of the spanwise averaged resolved TKE integrated in space over two wave lengths after breaking. (**a**) Linear scale axes. (**b**) Logarithmic scale axes.

6.3 The numerical reproduction of the impact

The setup described in the previous sections was used for reproducing the impact of the spilling breaker against the cylinder. In fact, a series of simulation was executed and in each of them the distance X of the cylinder relative to the breaking point was changed as in the experiment. At each X, the simulation was performed without and with the inclusion of dispersed bubbles. In both cases, the total in-line force on the cylinder was computed and then compared in order to understand the role of the entrained bubbles in the impact.

6.3.1 A remark on the breaking point

Three breaking points have been defined so far and are reported in Table 6.3

		simulations	
	experiment	broken wave front	significant air entrainment
	(br, exp)	(br, sim)	(en, sim)
x [m]	11.20	12.65	13.25
t [s]	not available	27.35	27.60

Table 6.3: The three breaking points involved in the present analysis.

The fact that $x_{br,sim}$ ($t_{br,sim}$) did not match with the experimental breaking point was expected, but it did not concern, since this investigation was based on the relative distance X between the cylinder and the breaking point, therefore a comparison could be done on the same X.

On the other hand, the shift in the numerical simulations between the beginning of the breaking at $x_{br,sim}$ ($t_{br,sim}$) and the formation of the bulge at $x_{en,sim}$ ($t_{en,sim}$) implied that the numerical entrainment started at x = 13.25 m (0.60 m downstream the breaking point), hence no differences between the impact without and with bubbles could be recognised before this point. In fact, the simulations with bubbles were not even performed for X < 0.60 m.

The importance of this remark becomes apparent looking again at Fig. 6.6 which shows the maximum values of the experimental total in-line force at different $X = x_{cyl,exp} - x_{br,exp}$. The role of the roller could not be investigated exactly where the maximum exerted force increased that is in the range 0 m ≤ X ≤ 0.60 m. The experimental videos of the impacts in this range showed that the entrainment of air was relatively small, hence it could be hypothesized the bubbles played a minor role in the observed increase of the force. However, this hypothesis needs to be verified with further research.

6.3.2 A remark on the computation of the in-line force

The computation of the in-line force on the cylinder was not straightforward. The issue concerned the definition of the free surface in order to determine the wet portion of the cylinder, hence the zone (the cells) where pressure and tangential stress had to be integrated (see Section 1.1.3).

As already said, the free surface was arbitrarily defined at α_{mixt} = 0.5 and this limit is commonly applied to the integration of pressure and friction around a cylinder. It was decided to not apply such limit in this study. The pressure and the tangential stress were summed over all boundary faces of the cylinder in order to compute the total in-line force. The reason was that the employment of a limit such as α_{mixt} = 0.5 could "cut" some of the cells situated in the roller region where the analysis was actually focused. Moreover, the definition of a free surface in the breaking region could be disputable.

The cylinder was divided in a discrete number of subelements as in Fig. 6.21. The integration of pressure and tangential stress was performed *separately* on each subelement. The two resulting discrete forces, one due to pressure $F^i_{x,p}$ and the other to friction $F^i_{x,\tau}$, were believed applied on the center of each subelement. Both the total force due to pressure and the one due to friction were the sum of all discrete contri-

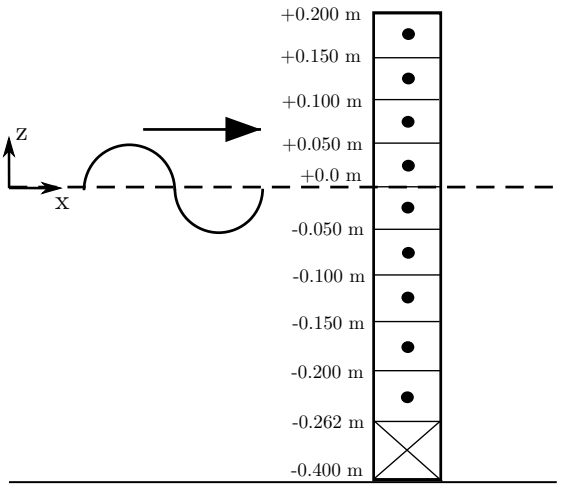

Figure 6.21: Discretisation adopted for the calculation of the in-line force exerted on the cylinder in the numerical simulations.

butions. The total in-line force was defined as $F = \sum_i F^i_{x,p} + \sum_i F^i_{x,\tau}$. The subelement between z = -0.400 m and z = -0.262 m was not taken into account as it represented the force transducer at the bottom.

This remark made on the computation of the in-line force implies another important consideration. The threshold on α_{mixt} has generally the effect of "cutting" potential numerical inaccuracies in some cells right above the free surface. This is particularly true when an OpenFOAM-based solver is employed, because of the already mentioned spurious velocities (see Section 3.3.1). Since the VOF algorithm of the developed CFD solver suffered from these inaccuracies (see Section 4.2), which could be mitigated by the dispersed bubbles only partially (see Section 5.2), the adopted strategy for computing the force allowed to not ignore the problem arbitrarily, rather to "visualize" and discuss it. Therefore, the pressure and the tangential stress could be integrated also over the boundary faces of cells where spurious velocities produced not feasible results, especially in the breaking region.

6.3.3 The results of the numerical simulations

The computational domain used for the simulation of the spilling breaker (Fig. 6.7) was modified to accomodate the cylinder. The outer dimensions were the same, but the mesh could not be regular anymore since in proximity to the cylinder was as in Fig. 6.22. Forty cells were used in the first layer around the cylinder with dimension 0.004 m × 0.015 m × 0.0125 m. The constraint on the minimum volume of a cell, which must have contained at least one bubble of the class with the largest diameter, did not allow a higher resolution.

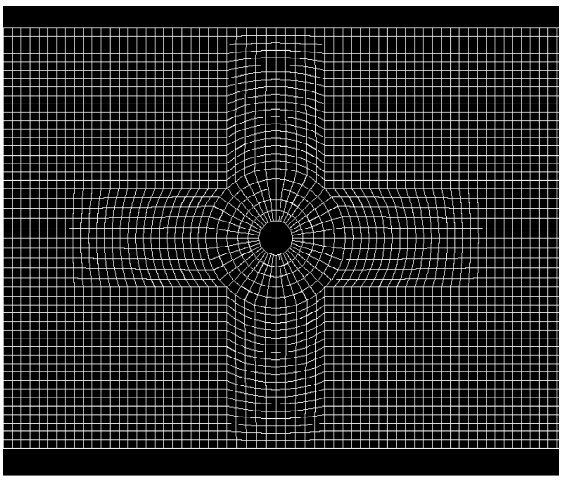

Figure 6.22: Mesh around the cylinder. Plane x-y.

The adopted boundary conditions are repeated in the table below for the domain with the cylinder.

	$\mathbf{u}_{\text{mixt}}$	$\mathbf{u}_{\text{b},i}$	α_{w}	α_{air}	$\alpha_{\text{b},i}$	p_d	$\nu_{\text{mixt}}^{sgs,SI}$	k_{mixt}^{sgs}
inlet	D.	N.	D.	D.	N.	N.	D.	D.
outlet	N.	N.	N.	N.	N.	N.	N.	N.
bottom	slip	slip	N.	N.	N.	N.	N.	N.
top	N./D.	N./D.	N./D.	N./D.	N./D.	D.	N.	N.
sides	slip	slip	N.	N.	N.	N.	N.	N.
cylinder	no-slip	slip	N.	N.	N.	N.	N.	N.

Table 6.4: Boundary conditions employed in the numerical simulations of the experiment with cylinder. $N.$ = Neumann (gradient equal to zero). $D.$ = Dirichlet (fixed value). $N./D.$ = Neumann for outflow and Dirichlet for inflow.

Since a large number of computationally demanding simulations had to be performed, it was decided to employ only seven classes ($N = 7$, 0.0025 m $\leq d_i \leq$ 0.01 m). Section 6.2.2 has shown some slight dissimilarities between simulations with 7 and 14 classes, but it cannot be excluded that they were relevant for this investigation. In practice, bubbles with a radius smaller than the Hinze scales were neglected. Although the impact of the roller was the main focus and the "excluded" small bubbles would have been concentrated in the tail of the plume, it will be seen later that the enhanced dissipation and the damped TKE might have played a role in the value of the total force predicted with bubbles. The employment of 14 (or more) classes was left for future analyses.

In order to better understand the following figures, it is stressed that the locations of the cylinder are expressed through two quantities:

$$X = x_{cyl,exp} - x_{br,exp} = x_{cyl,sim} - x_{br,sim} \tag{6.5}$$

$$x^*_{cyl,sim} = \frac{x_{cyl,sim} - x_{en,sim}}{L_{en,sim}} \tag{6.6}$$

The location X was used for comparing the experimental and numerical results. The non-dimensionalisation in $x^*_{cyl,sim}$ was already applied for the analysis on the development of the bubble plume, therefore it could be useful for relating the position of the cylinder, hence the force exerted, to the status of the roller. Furthermore, the non-dimensional time was expressed as

$$t^* = \frac{t - t_{en,sim}}{T_{en,sim}} \tag{6.7}$$

The time-variation of the total force computed in the case X = 0 m ($x^*_{cyl,sim} \approx$ -0.18) is shown in Fig. 6.23. In particular, the contributions from pressure and from friction are depicted. It is reminded that simulations with bubbles were not run for cases X < 0.60 m. The agreement between experimental and numerical results was fair in Fig. 6.23a. It was estimated that the Reynolds number Re and the Keulegan-Carpenter number KC were $\approx 1.5 \cdot 10^5$ and ≈ 70 respectively at the wave crest. Therefore the contribution from friction was negligible and the force was essentially due to the action of pressure around the cylinder.

The remarkable overestimation of the peak force (+20 %) could be explained with the discussion made in Section 6.3.2, but it was also believed that the resolution of mesh played a role as well, especially concerning the reconstruction of the boundary layer around the cylinder. The values of Re and KC indicated that separation occurred and the vortex shedding regime established, hence the proper localisation of the separation points became relevant. The adopted mesh likely did not allow the CFD solver to reproduce the correct pressure around the cylinder, especially at the top of the water column where the major contributions to the total force were exerted (Fig. 6.23b). It is reminded that the employment of a finer mesh around the cylinder was a not practicable solution, given the mentioned limitation on the cell size.

The numerical simulations were performed as above at X = -0.50 m and X = +0.0 m only without bubbles and from X = +0.60 m to X = +2.00 m, with an interval of 0.10 m, both without and with bubbles. For each simulation, i.e. at each X, the total in-line force was computed and the value of the peak force was registered.

Figure 6.24 shows the experimental and simulated maximum values of the total in-line force at the different locations of the cylinder expressed through the distance

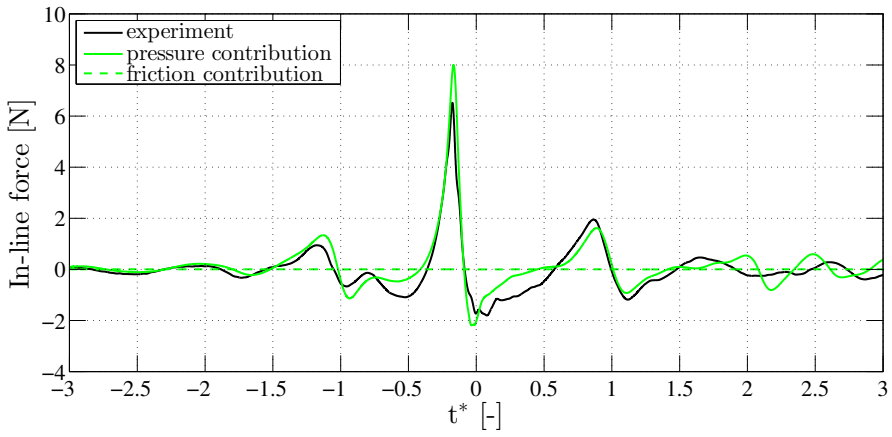

(a)

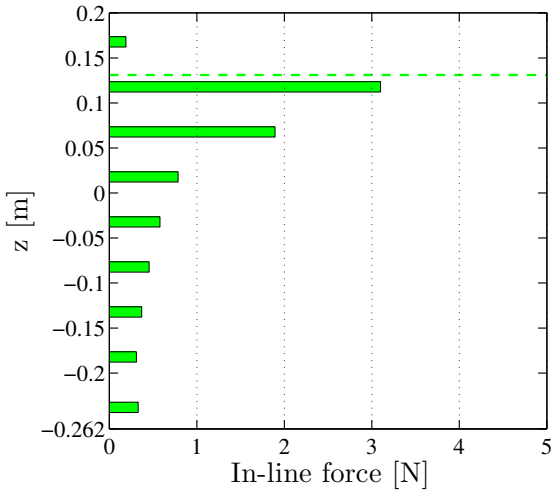

(b)

Figure 6.23: Experimental and predicted total in-line force exerted on the cylinder in the case X = +0.0 m without entrained bubbles. (**a**) Time-variation. (**b**) Distribution along the cylinder at the instant when the total force reached its maximum. The dashed line is the elevation of the free surface at the same time and in proximity to the cylinder.

x^*. The following observations can be made:

- the trend of the experimental variation was captured by the CFD solver. The maximum peak force was found at around $x^* = 0$ (X = +0.60 m) in agreement with the experiment;
- an overestimation of the predicted force was obtained at each x^* both without and with bubbles, especially at around $x^* = 0$;
- the forces computed in cases with bubbles was larger at each x^*. The difference was small up to $x^* \approx 0.35$ and became more relevant for larger values of x^*;

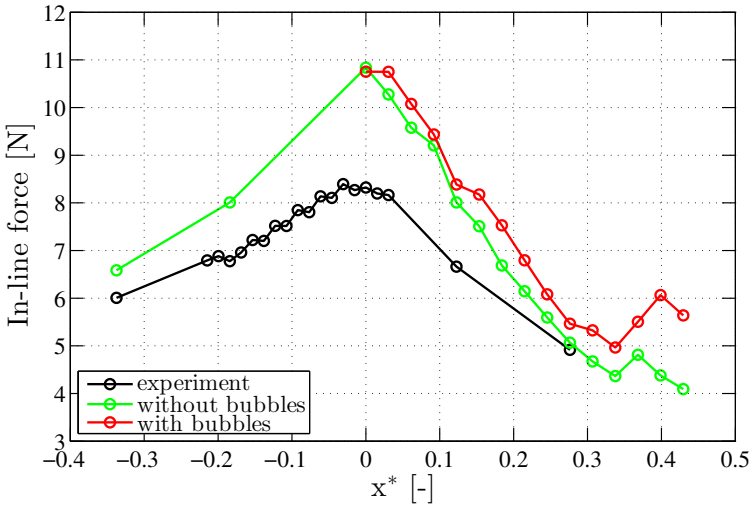

Figure 6.24: Variation of the maximum total in-line force exerted on the cylinder placed at different locations x^*.

- few experimental tests were conducted in the range $x^* > 0$, where instead the cases with bubbles could be performed.

The overestimation of the force compared to the experiment was also the result of the strategy adopted for its computation. The mesh resolution was another factor that played a role surely. However, this aspect was not further examined. The main scope of this analysis was to test whether the simulation of the air entrainment could change the computed force compared to a standard VOF method and how these potential changes could be related with the evolution of the roller and the bubble plume. In this perspective and at a status of this investigation that could be considered preliminary, the experimental measurements were used more to qualitatively compare the variation of the force with changing the distance X from the breaking point, rather than as a reference to be matched at each value of X.

The comparison between experimental and numerical results both without and with inclusion of dispersed bubbles is shown for $x^* \approx 0.03$ (X = +0.70 m), $x^* \approx 0.12$ (X = +1.00 m) and $x^* \approx 0.27$ (X = +1.50 m) in Figs. 6.25-6.27.

In each case the reproduction of both the surface elevation and the force was in fair agreement with the experimental results. The peak of the predicted forces occurred slightly after than in the experiment (Figs. 6.25c-6.26c-6.27c). The dissimilarities between the predicted forces were very small. The maximum value in the simulation with bubbles is larger in each case. In fact, the maximum force was larger in the case $x^* \approx 0.12$ because of an isolated spike at $t^* \approx 0.16$. It was verified that this outlier value

was produced by a local numerical instability above the free surface and it was not excluded from the integration of pressure and friction as discussed in Section 6.3.2. Nevertheless, this issue occurred only in this case among all simulations.

Small undulations with high frequency are apparent at the peak of the force in the simulation with bubbles in the first two cases, whereas the variation is smoother in the third one. These small oscillations were attributed to the bubble entrainment which was more chaotic at the beginning of the breaking. Conversely, undulations of the force appeared in the simulation without bubbles in the case $x^* \approx 0.27$ (X = +1.50 m). Probably, this was caused by a missing proper reproduction of the roller which was instead already established at the time of the impact in the simulation with air entrainment.

The difference in the magnitude of the force was expected to be originated at the top of the water column that is the region where the roller evolved. This is confirmed in Figs. 6.25d-6.26d-6.27d which show the distribution of the force along the cylinder. From these figures, it can be seen that the forces exerted at the top of the wave were the larger contributions to the total force, hence the role of the roller is in general potentially relevant. Moreover, the discrete forces exerted in the roller region were larger in the simulation with bubbles than in the one without. In particular, it was observed that the relative difference at each location x^* increased with increasing x^*. This was related to the fact that the size of the roller became larger (in the simulation where the air entrainment was simulated).

Since the bubble plume traveled with the wave celerity ($t^* \propto x^*$, Fig. 6.14a), the cylinder was impacted, in each of the three cases above, within the range in which the volume of the simulated bubble plume increased sharply to the maximum value and the roller grew quickly (Fig. 6.13a). Therefore, the fact that the forces at the top of the water column varied largely with the time did not surprise. Nevertheless, the difference the forces predicted without and with bubbles was found really small, whereas it became remarkable at $x^* > 0.3$ (Fig. 6.24), hence after the plume reached its maximum volume. This aspect was investigated by analysing the case $x^* \approx 0.43$ below.

Figures 6.28a-6.28b display that dissimilarities between the simulation without and the one with bubbles occurred only during the passage of the plume. From Fig. 6.28c, it can be appreciated that the peak of the force in the simulation with bubbles was delayed and more intense (+45%). This peak did not manifest as a consequence of some numerical instabilities as in Fig. 6.26c, rather as a steep but continuous increase. Figure 6.28d highlights that the larger contributions to the total force were exerted in the region of the roller where the differences between the two forces originated.

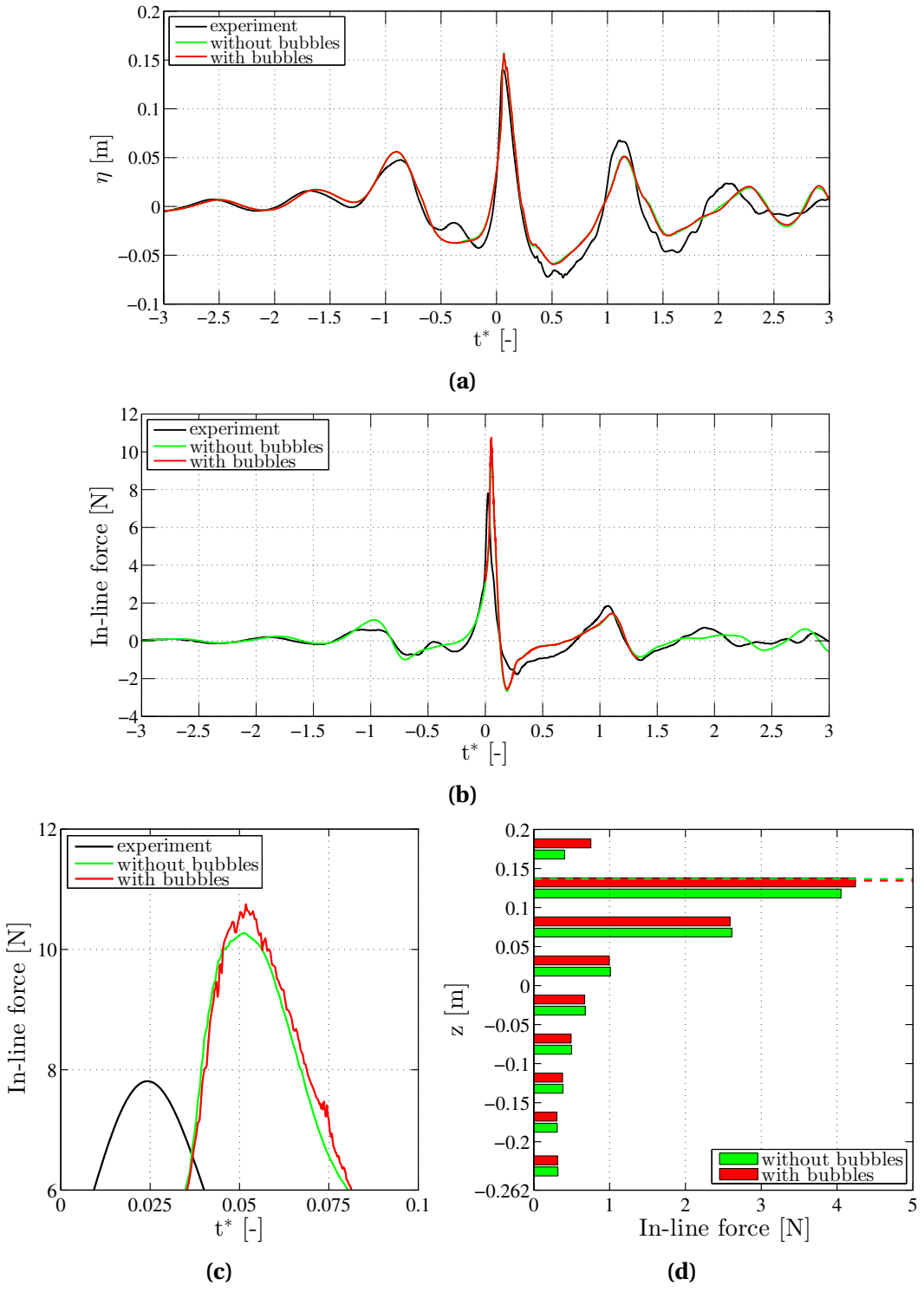

Figure 6.25: Case $x^* \approx 0.03$ ($X = +0.70$ m). Experimental and numerical results both without and with entrained bubbles. (**a**) Time-variation of the surface elevation in proximity to the cylinder. (**b**) Time-variation of the total in-line force on the cylinder. (**c**) Close-up around the time instant when the peaks occurred. (**d**) Distribution along the cylinder of the total in-line predicted forces at the instants of their maximums. The dashed line is the elevation of the free surface at the same time and in proximity to the cylinder.

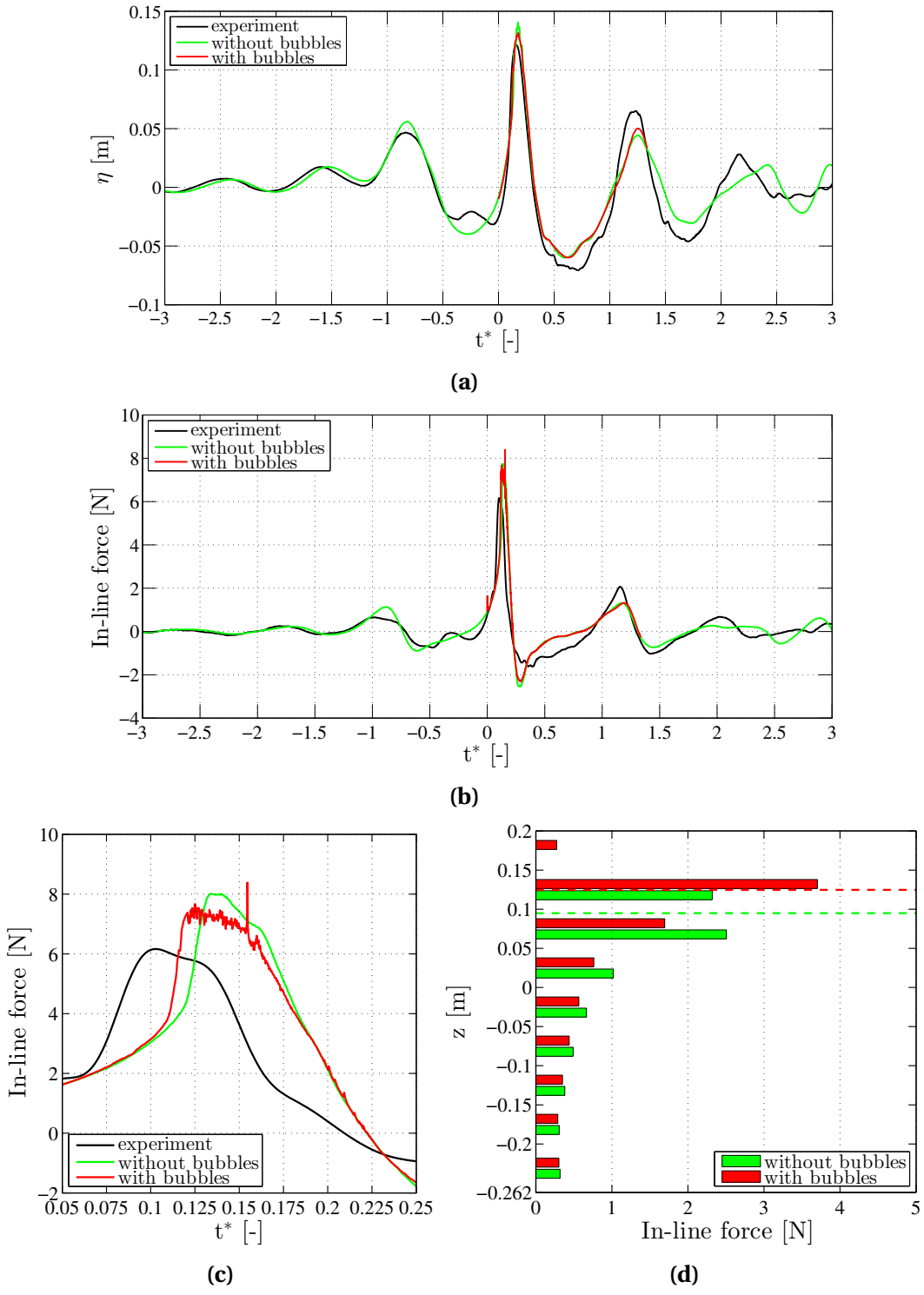

Figure 6.26: Case $x^* \approx 0.12$ ($X = +1.00$ m). Experimental and numerical results both without and with entrained bubbles. (**a**) Time-variation of the surface elevation in proximity to the cylinder. (**b**) Time-variation of the total in-line force on the cylinder. (**c**) Close-up around the time instant when the peaks occurred. (**d**) Distribution along the cylinder of the total in-line predicted forces at the instants of their maximums. The dashed line is the elevation of the free surface at the same time and in proximity to the cylinder.

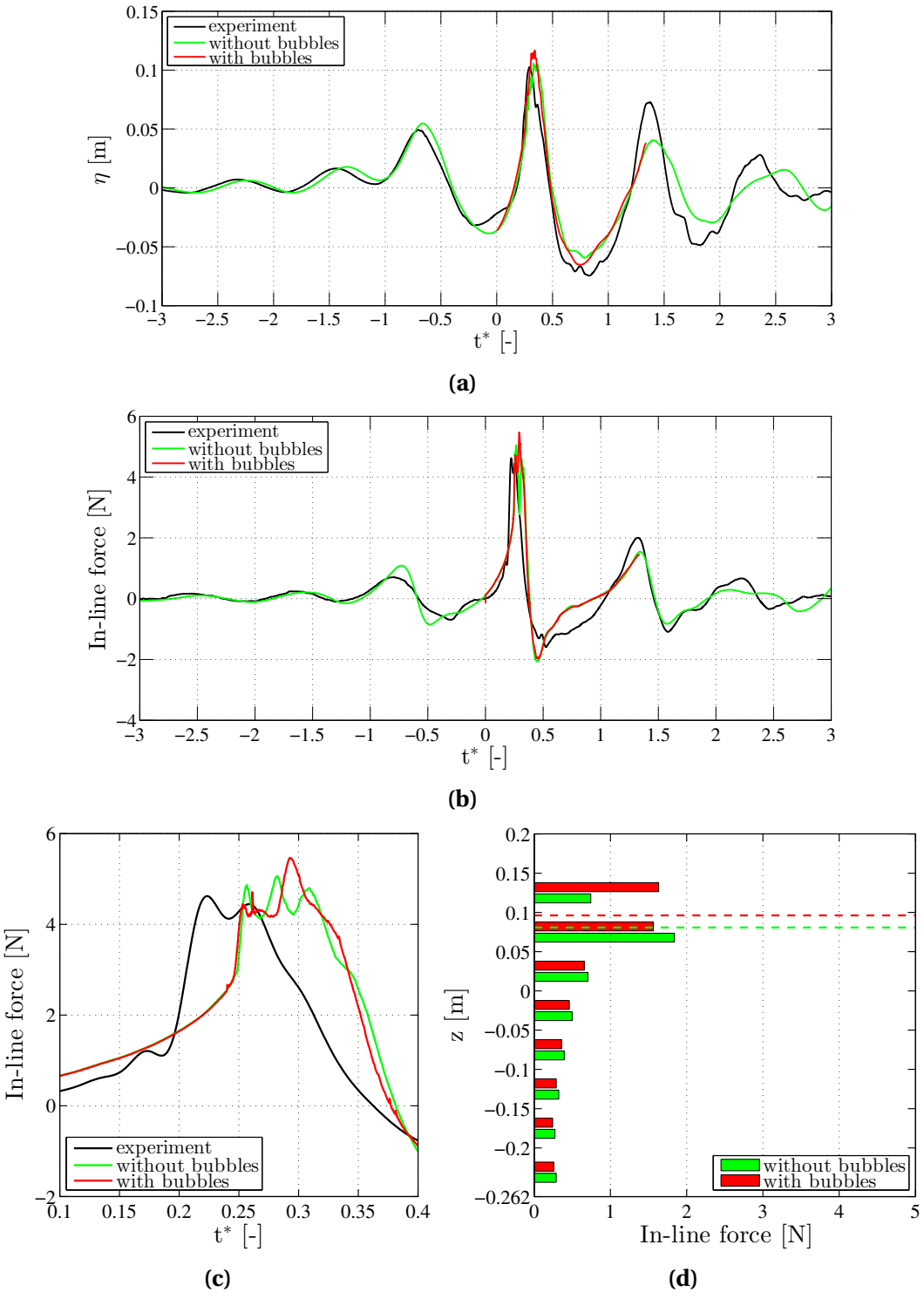

Figure 6.27: Case $x^* \approx 0.27$ ($X = +1.50$ m). Experimental and numerical results both without and with entrained bubbles. (**a**) Time-variation of the surface elevation in proximity to the cylinder. (**b**) Time-variation of the total in-line force on the cylinder. (**c**) Close-up around the time instant when the peaks occurred. (**d**) Distribution along the cylinder of the total in-line predicted forces at the instants of their maximums. The dashed line is the elevation of the free surface at the same time and in proximity to the cylinder.

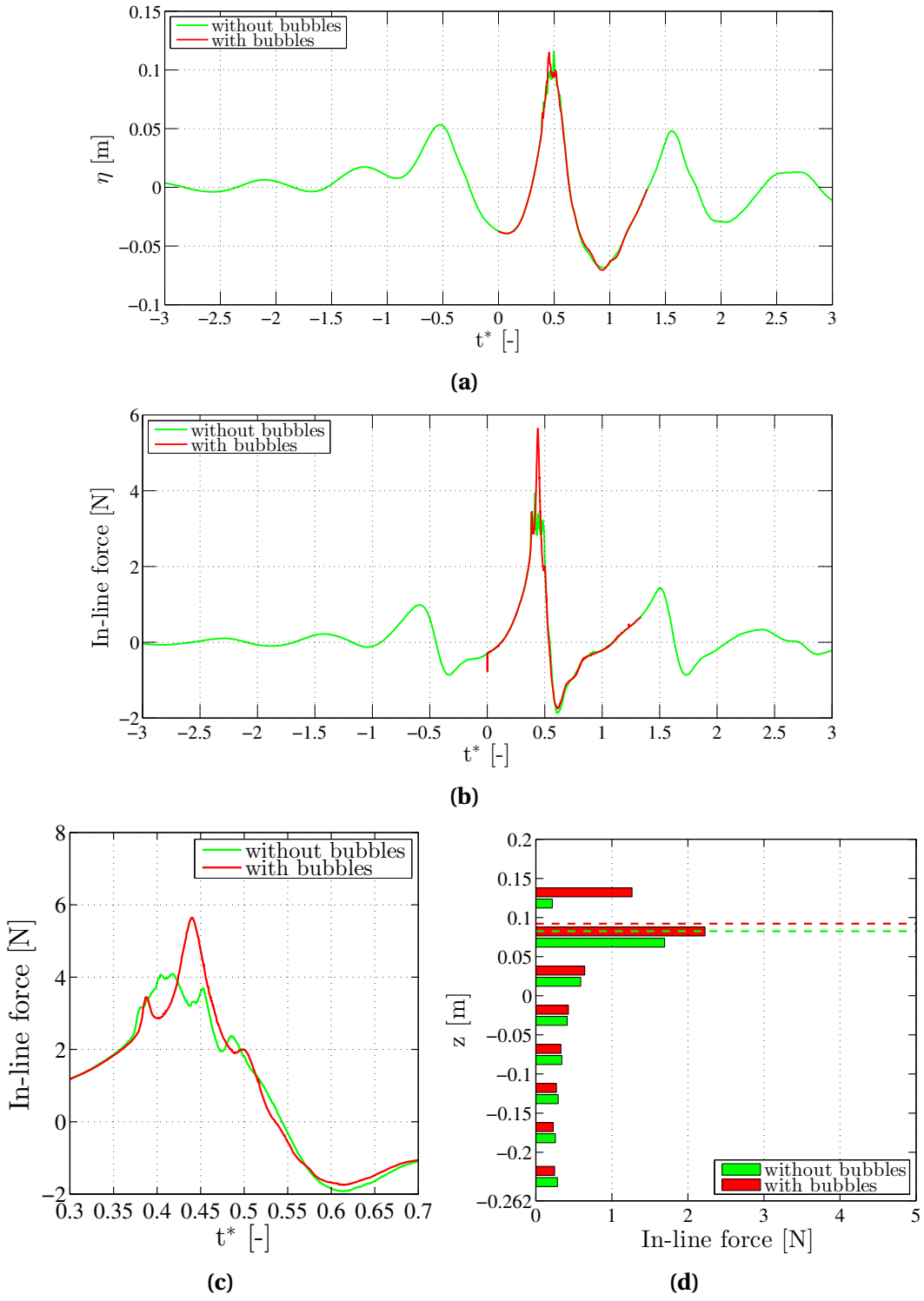

Figure 6.28: Case $x^* \approx 0.43$ ($X = +2.00$ m). Experimental and numerical results both without and with entrained bubbles. (**a**) Time-variation of the surface elevation in proximity to the cylinder. (**b**) Time-variation of the total in-line force on the cylinder. (**c**) Close-up around the time instant when the peaks occurred. (**d**) Distribution along the cylinder of the total in-line predicted forces at the instants of their maximums. The dashed line is the elevation of the free surface at the same time and in proximity to the cylinder.

Figure 6.29 illustrates the time interval in which the bubble plume passed through the cylinder in the simulation with air entrainment. The *simultaneous* distribution of pressure on the cylinder in both simulations is shown in Figs. 6.30-6.33. It is stressed that the *excess* pressure is reported, i.e. the actual pressure minus the hydrostatic contribution.

From Fig. 6.28c, it is apparent that the differences between the forces began at around $t^* = 0.40$ when the roller reached the cylinder (cf. Fig. 6.29). Before this time instant, the distributions of pressure, hence the total in-line forces, were almost identical as at $t^* = 0.37$ (Fig. 6.30).

The maximum value of the force predicted without bubbles occurred at $t^* \approx 0.40$. The distribution of pressure at this time presented some localized high values right below the free surface at $\alpha_{\text{mixt}} = 0.5$. At the same time, the force in the simulation with bubbles was smaller.

The results at time $t^* = 0.43$ of Fig. 6.31 allowed a comparison of the characteristics of the impact when the force was maximum in both simulations. In fact, the peak of the force predicted without air entrainment occurred at $t^* = 0.41$, whereas it happened at $t^* = 0.44$ in the simulation with bubbles. The distribution of pressure was not available at these two time instants, but it could be assumed that the differences were negligible. Figure 6.29 reveals that the cylinder was surrounded by the plume at time $t^* = 0.43$, being the front of the roller already downstream. The thickness of the plume was estimated to be 0.07 m approximately. The pressure on the cylinder was distributed differently than in the simulation without bubbles. The higher values were spread over a wide area, instead of being concentrated locally. As a result, the peak force was larger. This could have been the effect of the roller which enhanced the mixture of air and water and leveled out the pressure distribution.

At time $t^* = 0.47$, the disparity between the forces reduced (+24% with bubbles). The distribution of pressure was still more uniform in the simulation with air entrainment. The cylinder was in the middle of the plume with a thickness around 0.07 m.

At times $t^* = 0.50$, the two predicted pressure distributions reappeared again similar.

At times $t^* = 0.53$, 0.56 and 0.60 the force reduced in both simulations progressively and became negative. At $t^* = 0.60$, almost the entire plume was downstream the cylinder.

This analysis on case $x^* \approx 0.43$ allowed to highlight an interesting finding. The roller and the wave front arrived at the cylinder simultaneously, but the peak force did not occur at this moment, but later when the cylinder was already "within" the plume. Therefore, it could be argued that the effects of the roller on the force were not directly connected to its impact. Instead, the different time-variation of the force might have

been caused by the changes on the flow induced by the bubbles as described in Section 6.2.2. This hypothesis could be supported by the observation that the impact of the roller did not produce larger differences even when its size was at the maximum. In fact, Fig. 6.24 has shown that the effect of the air entrainment on the force became important at distances x^* reached when the volume of the bubble plume, that is the size of the roller to some extent, was already decaying ($t^* \geq 0.30$). The dissipation and the damping of TKE were already relatively large at the same time according to Figs. 6.17-6.20, whereas they were smaller when the volume of the bubble plume was maximum. Therefore, the numerical effect of the bubble motion on the force became more remarkable as the roller traveled farther for a period of time sufficiently long to induce changes on the flow.

Recalling the objectives of this investigation given at the beginning of the chapter, it can be concluded that:

- the force exerted by an experimental spilling wave on a vertical circular cylinder was not maximum when the cylinder was located at the breaking point, but downstream (0.50 m precisely);
- numerical simulations showed that the total in-line force changed when the air entrainment and the motion of the roller were simulated compared to a prediction without bubbles that is the one provided by a standard VOF method;

Concerning the last point, it was observed that:

- the force changed only in the interval when the plume passed through the cylinder;
- the differences increased with increasing the distance of the cylinder from the breaking point;
- the peak of the force was delayed;
- the force was generally larger.

Physical argumentations which related the variation of the measured force in the breaking region to the evolution of the roller were not given. Further research, supported with a more suitable set of laboratory measurements, is needed for this scope.

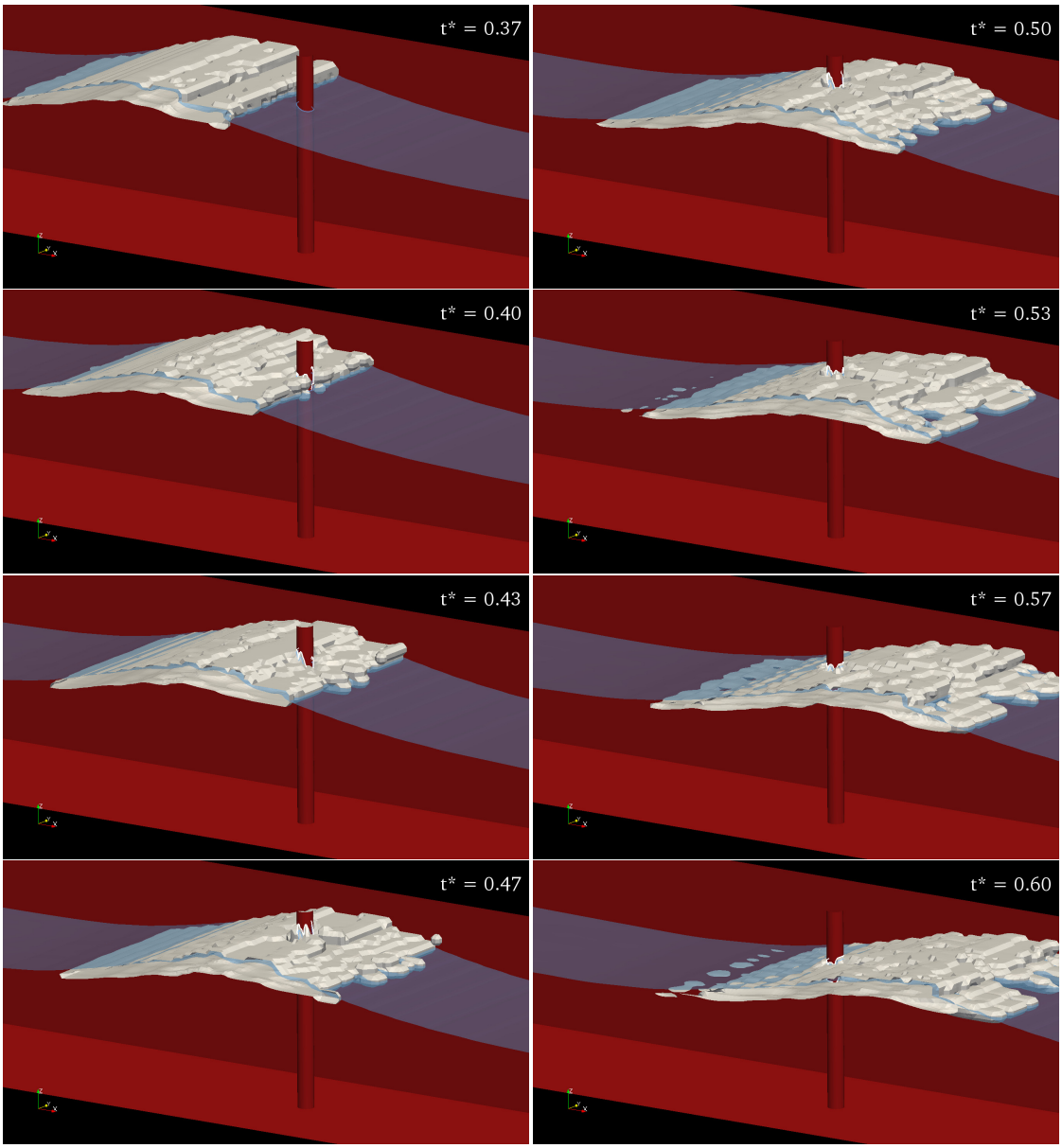

Figure 6.29: Case $x^* \approx 0.43$ ($X = +2.00$ m). Evolution of the breaking-induced roller with the time. The bubble plume is bounded by the isosurface $\alpha_b = 0.0001$ [-].

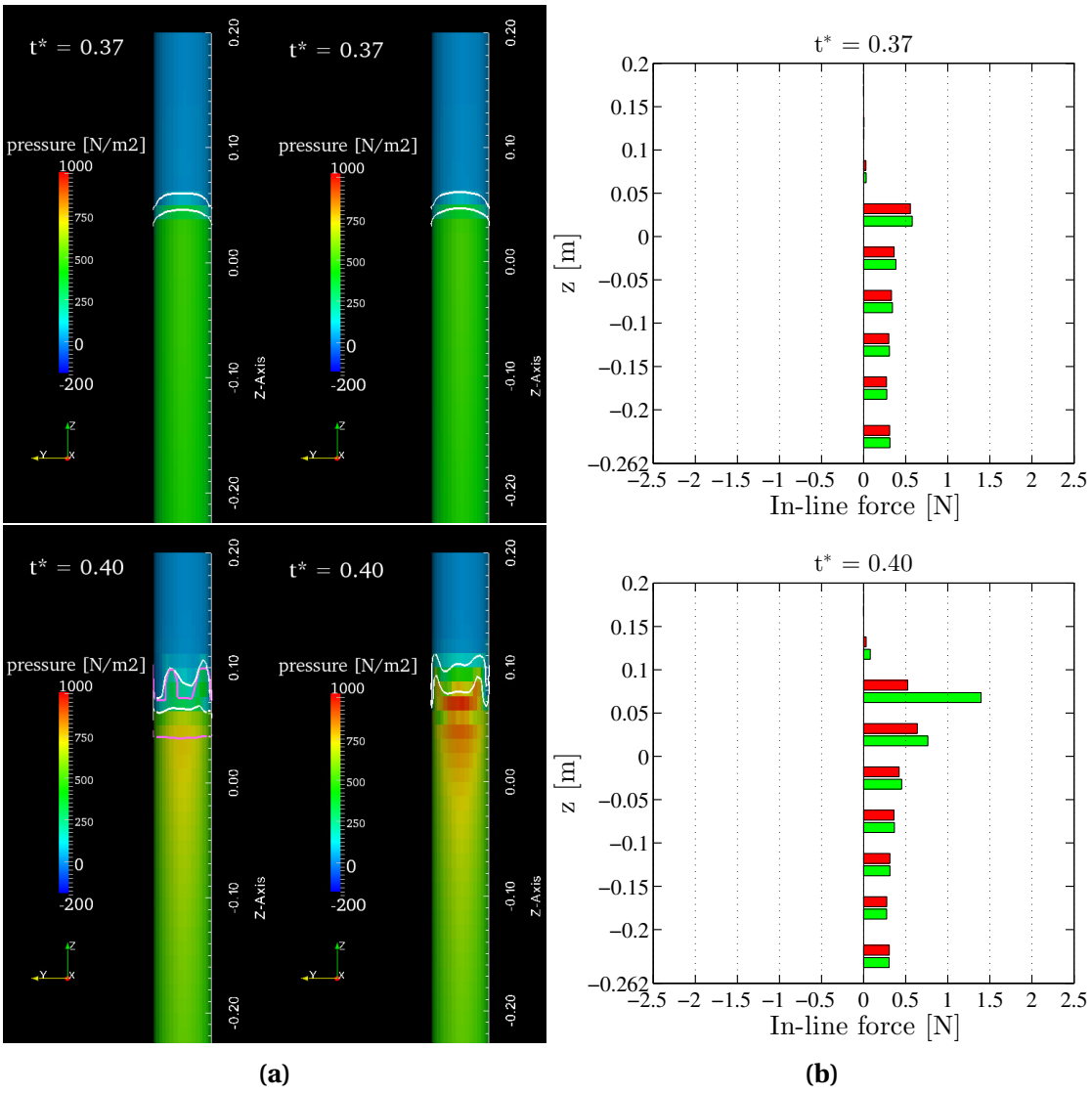

Figure 6.30: Case $x^* \approx 0.43$ ($X = +2.00$ m), $t^* = 0.37$ and $t^* = 0.40$. (**a**) Distribution of pressure on the upper portion of the cylinder in the simulation with bubbles (left column) and without (right column). White lines indicate the free surface for $\alpha_{\text{mixt}} = 0.5$ (lower line) and $\alpha_{\text{mixt}} = 0.1$ (upper line). Magenta lines mark the bubble plume defined as $\alpha_{\text{b}} = 0.0001$ [-]. (**b**) Distribution along the cylinder of the total in-line force predicted with bubbles (red) and without (green).

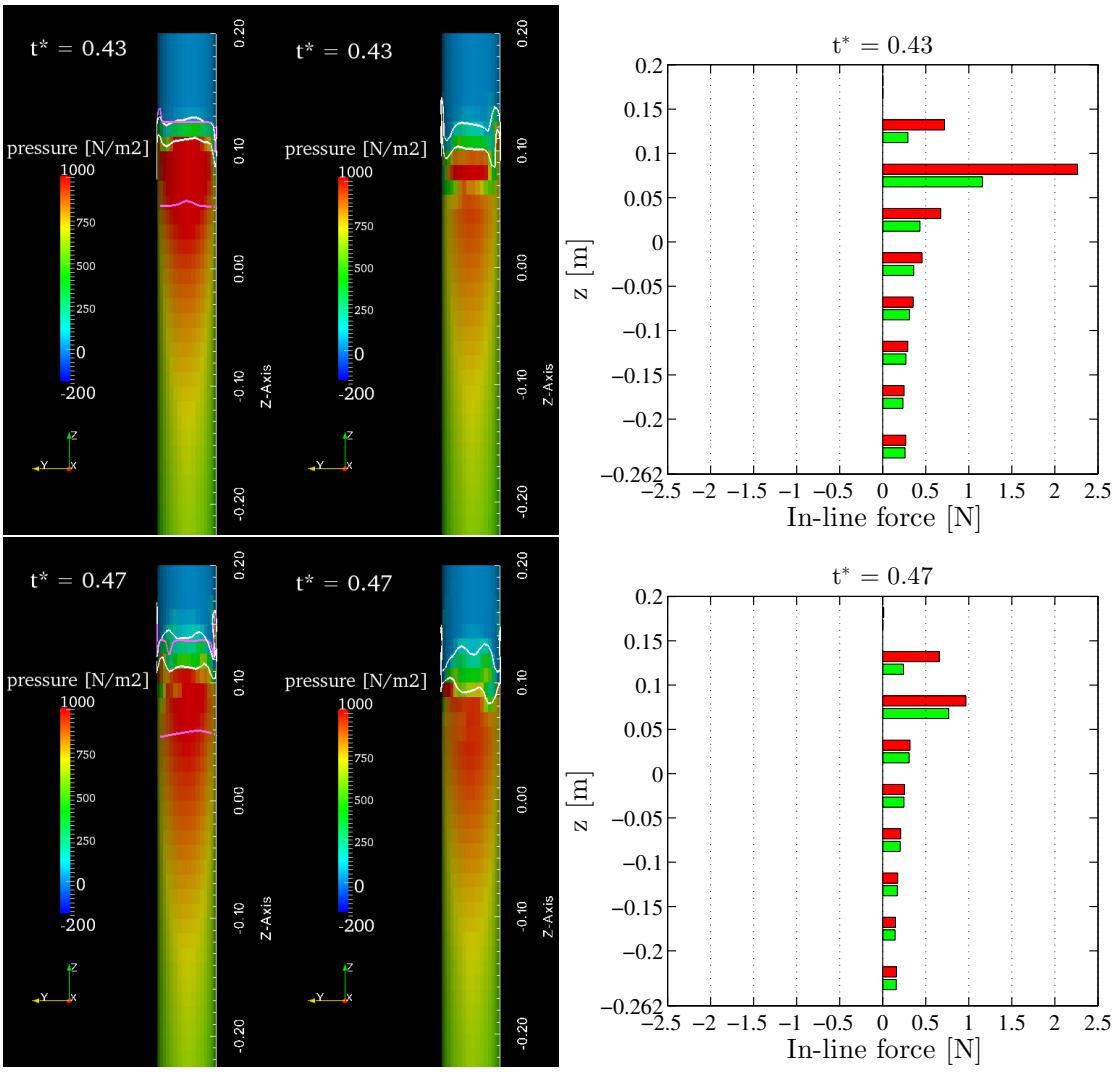

(a) **(b)**

Figure 6.31: Case $x^* \approx 0.43$ ($X = +2.00$ m), $t^* = 0.43$ and $t^* = 0.47$. (**a**) Distribution of pressure on the upper portion of the cylinder in the simulation with bubbles (left column) and without (right column). White lines indicate the free surface for $\alpha_{\text{mixt}} = 0.5$ (lower line) and $\alpha_{\text{mixt}} = 0.1$ (upper line). Magenta lines mark the bubble plume defined as $\alpha_{\text{b}} = 0.0001$ [-]. (**b**) Distribution along the cylinder of the total in-line force predicted with bubbles (red) and without (green).

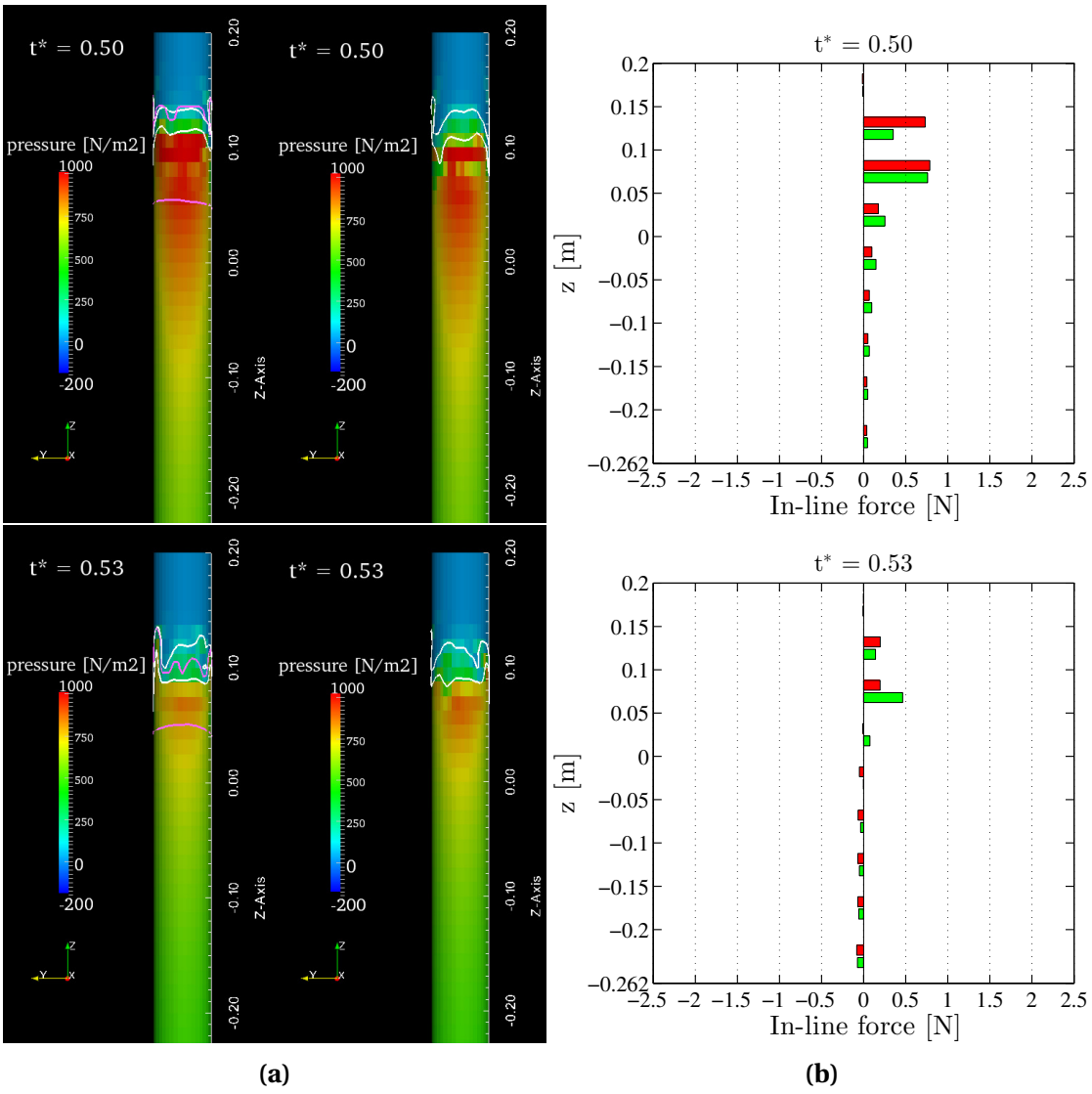

(a) **(b)**

Figure 6.32: Case $x^* \approx 0.43$ (X = +2.00 m), $t^* = 0.50$ and $t^* = 0.53$. (**a**) Distribution of pressure on the upper portion of the cylinder in the simulation with bubbles (left column) and without (right column). White lines indicate the free surface for $\alpha_{\text{mixt}} = 0.5$ (lower line) and $\alpha_{\text{mixt}} = 0.1$ (upper line). Magenta lines mark the bubble plume defined as $\alpha_{\text{b}} = 0.0001$ [-]. (**b**) Distribution along the cylinder of the total in-line force predicted with bubbles (red) and without (green).

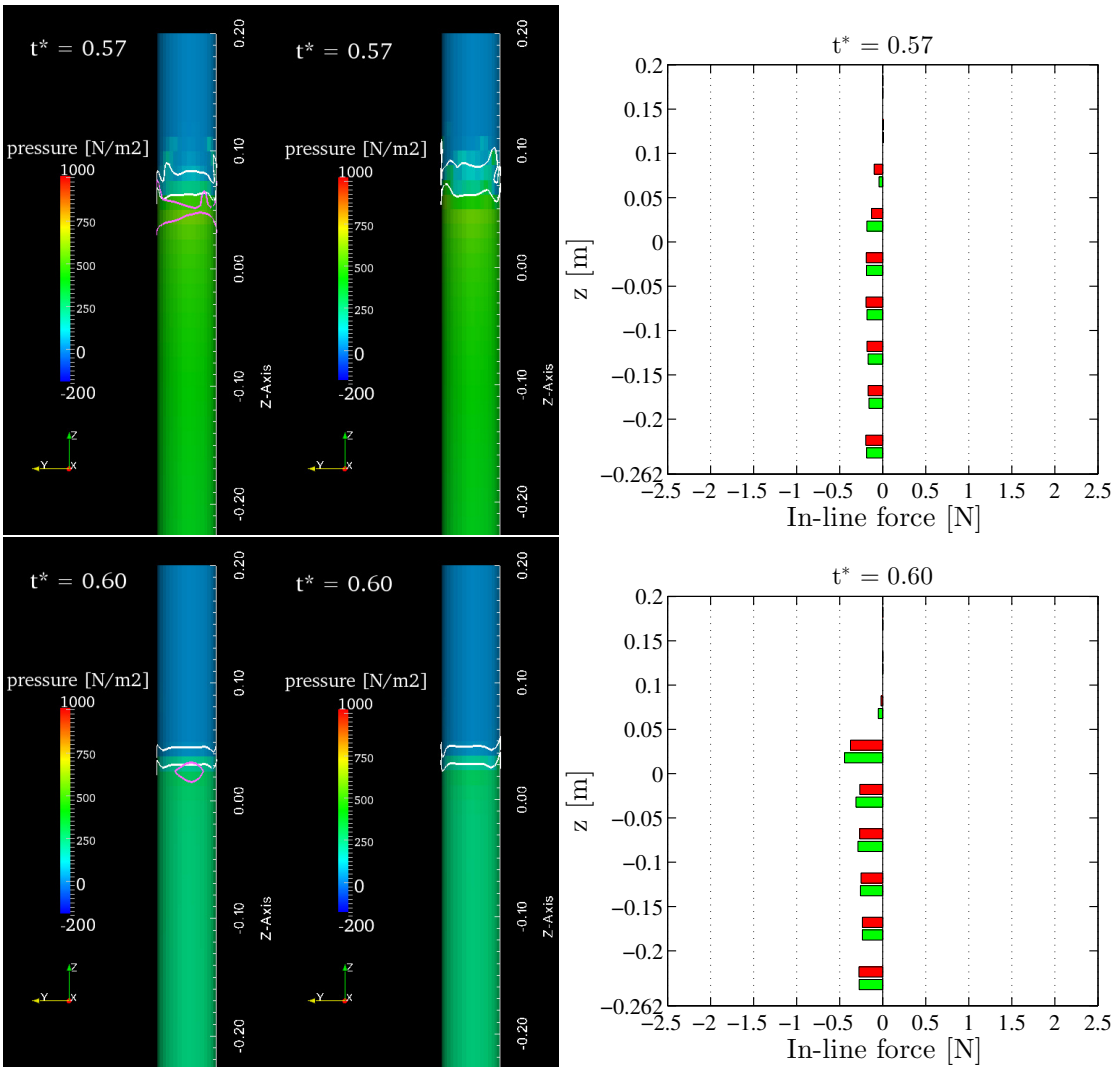

(a) **(b)**

Figure 6.33: Case $x^* \approx 0.43$ ($X = +2.00$ m), $t^* = 0.57$ and $t^* = 0.60$. (**a**) Distribution of pressure on the upper portion of the cylinder in the simulation with bubbles (left column) and without (right column). White lines indicate the free surface for $\alpha_{\text{mixt}} = 0.5$ (lower line) and $\alpha_{\text{mixt}} = 0.1$ (upper line). Magenta lines mark the bubble plume defined as $\alpha_{\text{b}} = 0.0001$ [-]. (**b**) Distribution along the cylinder of the total in-line force predicted with bubbles (red) and without (green).

7 Summary and future work

In impacts of breaking waves on offshore structures it is still not well-known how the air entrainment phenomenon affects the exerted loads. In particular, the interaction between the roller characterizing the entrainment in spilling waves and a mono-pile structure is still poorly understood. With the aim to gain some knowledge on this topic, a numerical methodology capable of handling the whole wave breaking process, i.e. generation, propagation and air bubble entrainment, was developed during a Ph.D. study and presented in this thesis.

The numerical methodology consisted of a mathematical model suitable for the problem in object and its implementation within a Computational Fluid Dynamics (CFD) framework in order to obtain a numerical solution. The final result of the development process was a CFD solver.

A breaking wave was treated as the flow of a two-phase system composed of air and water. The mathematical model was based on the application of the Navier-Stokes equations for such two-phase flow combined with a LES turbulence approach.

In general, the way how the Navier-Stokes equations are handled within a two-phase system depends on the morphology of the interface between fluids, i.e. segregated or dispersed. The CFD solvers commonly employed for breaking waves are derived under the assumption that the flow is segregated, hence that the length scale of the interface between air and water is larger than the scale adopted for the spatial discretisation. This assumption is usually valid up to the breaking point. Once the wave breaks, air entrains into water undergoing a dispersion in the form of bubbles which are likely much smaller than the adopted grid size. Nevertheless, CFD solvers for segregated flows, based on the Volume-Of-Fluid (VOF) approach as example, are broadly employed for numerical reproductions of breaking waves because the focus is generally on the overall motion of the free surface.

The scope of the present study required a mathematical model that could treat both the motion of the free surface and the breaking-induced bubbly flow. In prin-

ciple, a CFD solver for segregated flow could have been suitable, given the adopted mesh so fine that the interface of bubbles could be reconstructed. Since experimental observations have shown that the smaller entrained bubbles have a radius of 0.1 mm, the employment of a VOF solver was believed impracticable.

In order to handle the whole breaking process in reasonable spatial discretisations, it was elaborated a mathematical model which coupled the Eulerian multiphase approach for the entrained dispersed bubbles with a VOF algorithm to capture the free surface.

The coupling was developed by describing a breaking wave as follows. The air above the free surface was called continuous to distinguish it from the air dispersed in water in the form of bubbles. The dispersed air was split in different classes, each of them representing bubbles with the same diameter. Each class was treated as dispersed in the mixture of water and continuous air which was considered as a single phase only in the solution of the momentum equations in order to accommodate the VOF approach. Therefore, the continuity equations were solved for each class, for water and for continuous air, whereas the momentum equations were solved for each class and the mixture.

Formulations for mass and momentum transfers among phases were implemented. The air entrainment was formulated as the mass transferred from continuous air to each class. Following Derakhti and Kirby (2014), this transfer took place at the free surface cells where the shear-induced sgs turbulence energy dissipation rate was higher than an user-specified threshold. The escaping of bubbles through the free surface was modeled as mass moving from each class to continuous air. Other mass exchanges concerned breakage and coalescence among bubbles. Momentum equations accounted for drag, lift, virtual mass and turbulent dispersion force as inter-phase momentum transfer.

The CFD solver was built by the means of the libraries provided by the open-source CFD package OpenFOAM. The governing equations were discretised on collocated grids using the finite volume method. The pressure-velocity coupling was handled by the PISO algorithm.

The CFD solver turned out to be a complex assembly of different elements. At the beginning, the solver underwent a long and heavy testing in order to assess the stability and the numerical accuracy of each component. This stage of the development process has not been reported in this thesis but it was crucial. The effects induced by bubbles were not expected large, hence it was avoided that they could be mistaken for some numerical inaccuracies.

The CFD solver was validated through the simulation of four experimental case stud-

ies. The numerical results were compared with the measurements in each case.

In the first two cases, the air entrainment formulation was not used. The strategy was to test the reliability of the Eulerian multiphase model and of the VOF algorithm separately but operating under the coupled configuration.

The first case was about the flow in a bubble column. The comparison with the experimental measurements showed that the solver could reproduce the dynamic of a bubble population and especially the induced turbulence field in water.

The second case was on regular waves breaking as spilling on a sloping beach. The agreement with the experimental results was fair, but the main aspect was that the VOF algorithm was found as accurate as the one implemented in OpenFOAM and it did not suffer from any instabilities because of the coupling with the other model.

The third case tested the air entrainment modeling in a single deep water spilling wave. The comparison with experimental observations and measurements revealed a reasonable performance of the CFD solver. The prediction of the maximum volume of the bubble plume as well as the averaged bubble phase fraction was found underestimated. Since the experimental wave was close to be a plunging, such discrepancies were expected. The air entrainment formulation was derived in Ma et al. (2011) and Derakhti and Kirby (2014) under the hypothesis the mechanism depends on the turbulence intensity at the free surface solely, hence it produces the best results when the breaker is purely spilling. Nevertheless, this was not as issue as the focus of this study was on spilling waves.

The simulation of the same case repeated without bubbles allowed to identify the effect on whole flow when the entrainment of air was taken into account. The main findings were that the total sub-grid dissipation rate was enhanced and, consequently, the turbulent kinetic energy of the resolved scales was reduced.

The fourth case was the simulation of the same regular spilling waves of the second case, but with the prediction of the bubbly flow in the surf zone. The solver correctly repeated the entrainment as many times as the number of simulated waves. The inclusion of bubbles slightly improved the results obtained in the second case, especially concerning the turbulent kinetic energy. Nevertheless, these difference were not found large, because, even if the formation of bubbles was not taken into account, the air above the free surface still underwent a sort of dispersion in water.

Finally the CFD solver was ready to be employed for an investigation on the impact of a spilling wave against a circular cylinder at a laboratory scale. Both in the experiments and in the numerical simulations, the cylinder was located at different distances from the breaking point, upstream and downstream. At each distance, two simulations

were performed, one without and the other with bubbles. It was showed that the CFD solver overestimated the force at each X. Nevertheless, the in-line force was calculated as the integration of pressure and friction over all boundary cells of the cylinder, without neglecting some potential numerical inaccuracies that could happen exactly above the free surface. A definition of a free surface – *de facto* a threshold on the number of cells where the integration is performed – could have even led to the opposite result, that is to un underestimation of the computed force compared to the experimental results. However, the predictions with and without bubbles, in agreement with measurements, clearly showed that the maximum value of the total in-line force was exerted when the cylinder was at around 0.50 m from the breaking point.

It was found that the peak of the total in-line force predicted with bubbles was delayed and generally larger especially for the farther locations of the cylinder from the breaking point. Furthermore, the distribution of pressure on the cylinder was more uniform when the passage of the roller was reproduced. It was argued that these effects were not directly related to the impact of the roller on the cylinder, rather to the changes that the reproduction of the air entrainment induced on the flow in the breaking region.

Physical argumentations for the variation of the measured force in the breaking region in connection with the evolution of the roller were not given. Nevertheless, this point was beyond the objectives of the present research. The main scope was the development of a methodology that could support further investigations on this problem and especially the assessment that a standard VOF solver might not be sufficient to carry out such investigations. In fact, the differences in the predictions of the force with and without bubbles demonstrated that the simulation of the air entrainment played a role.

Future works should focus on either further applications of the current CFD solver or changing the mathematical model in order to produce more simplified approaches. A deeper investigation on the characteristics of the flow around the cylinder in the case of the laboratory spilling wave impact is suggested. A major analysis should be conducted on the degree of reconstruction of the boundary layer with the corresponding set of appropriate boundary conditions. Since the resolution of the mesh around the cylinder is limited by the size of bubbles, the opportunity of excluding the classes with a larger size could be evaluated. The employment of a turbulence approach provided with a wall function could be worthy, but it should be verified whether it would conflict with the current stability of the air entrainment modeling. Above all, any further numerical analysis on this case should be supported by many more experimental measurements. The force should be measured at farther distances

from the breaking point. Moreover, measurements of pressure around the cylinder at the elevations invested by the roller would be extremely useful.

The current version of the developed CFD solver does not appear suitable for practical engineering applications since it is still computationally demanding. The main factor is that the larger the number of phases, the longer the simulation given the discretised domain. Beside some possible code optimization, two main paths are suggested in order to improve the performances:

- the implementation of the Direct Quadrature Method of Moments (DQMOM) for handling the solution of the bubble population balance equation with a reduced number of classes;
- the production of simplified approaches on the basis of successive approximations. In fact, the developed methodology is very general, but it could be tailored for some specific applications of the CFD solver. As example, in the resolution of the momentum equations, the bubble classes with the smaller size could be grouped into a single phase which has the same velocity of the mixture (partial Equilibrium Eulerian approach). An alternative would be to group all classes into a single phase with its own velocity field determined on the basis of the Sauter diameter. A very practical engineering tool could be given by the development of a formulation for the sgs turbulent energy dissipation rate that takes somehow into account the enhancement induced by the air entrainment without the need of simulating the motion of bubbles.

Bibliography

Amini Afshar, M. (2010). Numerical wave generation in open foam®. Master's thesis, Chalmers University of Technology.

ANSYS, I. (2009). Cfx-solver theory guide.

Balachandar, S. and Eaton, J. K. (2010). Turbulent dispersed multiphase flow. *Annual Review of Fluid Mechanics*, 42:111–133.

Bannari, R., Kerdouss, F., Selma, B., Bannari, A., and Proulx, P. (2008). Three-dimensional mathematical modeling of dispersed two-phase flow using class method of population balance in bubble columns. *Computers & Chemical Engineering*, 32(12):3224–3237.

Battjes, J. (1988). Surf-zone dynamics. *Annual Review of Fluid Mechanics*, 20(1):257–291.

Blenkinsopp, C. and Chaplin, J. (2011). Void fraction measurements and scale effects in breaking waves in freshwater and seawater. *Coastal Engineering*, 58(5):417–428.

Brackbill, J., Kothe, D. B., and Zemach, C. (1992). A continuum method for modeling surface tension. *Journal of computational physics*, 100(2):335–354.

Bradford, S. F. (2000). Numerical simulation of surf zone dynamics. *Journal of Waterway, Port, Coastal, and Ocean Engineering*, 126(1):1–13.

Bredmose, H. and Jacobsen, N. G. (2010). Breaking wave impacts on offshore wind turbine foundations: focused wave groups and cfd. In *ASME 2010 29th International Conference on Ocean, Offshore and Arctic Engineering*, pages 397–404. American Society of Mechanical Engineers.

Bredmose, H., Peregrine, D., and Bullock, G. (2009). Violent breaking wave impacts. Part 2: modelling the effect of air. *Journal of Fluid Mechanics*, 641:389–430.

Brown, S., Greaves, D., Magar, V., and Conley, D. (2016). Evaluation of turbulence closure models under spilling and plunging breakers in the surf zone. *Coastal Engineering*, 114:177–193.

Buffo, A., Vanni, M., Marchisio, D., and Fox, R. O. (2013). Multivariate quadrature-based moments methods for turbulent polydisperse gas–liquid systems. *International Journal of Multiphase Flow*, 50:41–57.

Buwa, V. V. and Ranade, V. V. (2002). Dynamics of gas–liquid flow in a rectangular bubble column: experiments and single/multi-group cfd simulations. *Chemical Engineering Science*, 57(22):4715–4736.

Carrica, P., Bonetto, F., Drew, D., and Lahey, R. (1998). The interaction of background ocean air bubbles with a surface ship. *International journal for numerical methods in fluids*, 28(4):571–600.

Carrica, P., Drew, D., Bonetto, F., and Lahey, R. (1999). A polydisperse model for bubbly two-phase flow around a surface ship. *International journal of multiphase flow*, 25(2):257–305.

Cerne, G., Petelin, S., and Tiselj, I. (2001). Coupling of the interface tracking and the two-fluid models for the simulation of incompressible two-phase flow. *Journal of computational physics*, 171(2):776–804.

Chan, E.-S., Cheong, H.-F., and Tan, B.-C. (1995). Laboratory study of plunging wave impacts on vertical cylinders. *Coastal Engineering*, 25(1):87–107.

Chen, P., Sanyal, J., and Duduković, M. (2005). Numerical simulation of bubble columns flows: effect of different breakup and coalescence closures. *Chemical Engineering Science*, 60(4):1085–1101.

Christensen, E. D. (2006). Large eddy simulation of spilling and plunging breakers. *Coastal Engineering*, 53(5):463–485.

Christensen, E. D., Bredmose, H., and Hansen, E. A. (2009). Transfer of boussinesq waves to a navier-stokes solver: Application to wave loads on an offshore wind turbine foundation. In *ASME 2009 28th International Conference on Ocean, Offshore and Arctic Engineering*, pages 917–926. American Society of Mechanical Engineers.

Christensen, E. D. and Deigaard, R. (2001). Large eddy simulation of breaking waves. *Coastal engineering*, 42(1):53–86.

Christensen, E. D., Walstra, D.-J., and Emerat, N. (2002). Vertical variation of the flow across the surf zone. *Coastal Engineering*, 45(3):169–198.

Cox, D. T. and Shin, S. (2003). Laboratory measurements of void fraction and turbulence in the bore region of surf zone waves. *Journal of engineering mechanics*, 129(10):1197–1205.

De Villiers, E. (2007). *The potential of large eddy simulation for the modelling of wall bounded flows*. PhD thesis, Imperial College, University of London.

Deane, G. B. and Stokes, M. D. (2002). Scale dependence of bubble creation mechanisms in breaking waves. *Nature*, 418(6900):839–844.

Deen, N. G., Hjertager, B. H., and Solberg, T. (2000). Comparison of piv and lda measurement methods applied to the gas-liquid flow in a bubble column. In *10th international symposium on applications of laser techniques to fluid mechanics*.

Deen, N. G., Solberg, T., and Hjertager, B. H. (2001). Large eddy simulation of the gas–liquid flow in a square cross-sectioned bubble column. *Chemical Engineering Science*, 56(21):6341–6349.

Derakhti, M. and Kirby, J. T. (2014). Bubble entrainment and liquid–bubble interaction under unsteady breaking waves. *Journal of Fluid Mechanics*, 761:464–506.

Deshpande, S. S., Anumolu, L., and Trujillo, M. F. (2012). Evaluating the performance of the two-phase flow solver interfoam. *Computational science & discovery*, 5(1):014016.

Dhotre, M., Niceno, B., and Smith, B. (2008). Large eddy simulation of a bubble column using dynamic sub-grid scale model. *Chemical Engineering Journal*, 136(2):337–348.

Drazen, D. A. and Melville, W. K. (2009). Turbulence and mixing in unsteady breaking surface waves. *Journal of Fluid Mechanics*, 628:85–119.

Drew, D. A. and Passman, S. L. (2006). *Theory of multicomponent fluids*, volume 135. Springer Science & Business Media.

Ferziger, J. H. and Peric, M. (2012). *Computational methods for fluid dynamics*. Springer Science & Business Media.

Galvin, C. J. (1968). Breaker type classification on three laboratory beaches. *Journal of Geophysical Research*, 73(12):3651–3659.

Germano, M., Piomelli, U., Moin, P., and Cabot, W. H. (1991). A dynamic subgrid-scale eddy viscosity model. *Physics of Fluids A: Fluid Dynamics (1989-1993)*, 3(7):1760–1765.

Goda, Y., Haranaka, S., and Kitahata, M. (1966). Study on impulsive breaking wave forces on piles. *Report Port and Harbour Technical Research Institute*, 6(5):1–30.

Hänsch, S., Lucas, D., Krepper, E., and Höhne, T. (2012). A multi-field two-fluid concept for transitions between different scales of interfacial structures. *International Journal of Multiphase Flow*, 47:171–182.

Hansen, R. (2009). *Computational and experimental study of bubble size in bubble columns*. PhD thesis, Esbjerg Institute of Technology, Aalborg University.

Hattori, M., Arami, A., and Yui, T. (1994). Wave impact pressure on vertical walls under breaking waves of various types. *Coastal Engineering*, 22(1):79–114.

Hirt, C. W. and Nichols, B. D. (1981). Volume of fluid (vof) method for the dynamics of free boundaries. *Journal of computational physics*, 39(1):201–225.

Iafrati, A. (2011). Energy dissipation mechanisms in wave breaking processes: Spilling and highly aerated plunging breaking events. *Journal of Geophysical Research: Oceans*, 116(C7).

Iafrati, A., Di Mascio, A., and Campana, E. (2001). A level set technique applied to unsteady free surface flows. *International Journal for Numerical Methods in Fluids*, 35(3):281–297.

Ishii, M. and Zuber, N. (1979). Drag coefficient and relative velocity in bubbly, droplet or particulate flows. *AIChE Journal*, 25(5):843–855.

Issa, R. I. (1986). Solution of the implicitly discretised fluid flow equations by operator-splitting. *Journal of computational physics*, 62(1):40–65.

Jacobsen, N. G., Fuhrman, D. R., and Fredsøe, J. (2012). A wave generation toolbox for the open-source cfd library: Openfoam®. *International Journal for Numerical Methods in Fluids*, 70(9):1073–1088.

Jasak, H. (1996). *Error Analysis and Estimation for the Finite Volume Method with Applications to Fluid Flows, 1996*. PhD thesis, Imperial College, University of London.

Kiger, K. T. and Duncan, J. H. (2012). Air-entrainment mechanisms in plunging jets and breaking waves. *Annual Review of Fluid Mechanics*, 44:563–596.

Kimmoun, O. and Branger, H. (2007). A particle image velocimetry investigation on laboratory surf-zone breaking waves over a sloping beach. *Journal of Fluid Mechanics*, 588:353–397.

Kumar, S. and Ramkrishna, D. (1996a). On the solution of population balance equations by discretization - I. A fixed pivot technique. *Chemical Engineering Science*, 51(8):1311–1332.

Kumar, S. and Ramkrishna, D. (1996b). On the solution of population balance equations by discretization - II. A moving pivot technique. *Chemical Engineering Science*, 51(8):1333–1342.

Lamarre, E. and Melville, W. (1991). Air entrainment and dissipation in breaking waves. *Nature*, 351(6326):469–472.

Lamarre, E. and Melville, W. (1994). Void-fraction measurements and sound-speed fields in bubble plumes generated by breaking waves. *The Journal of the Acoustical Society of America*, 95(3):1317–1328.

Lax, P. and Wendroff, B. (1960). Systems of conservation laws. *Communications on Pure and Applied mathematics*, 13(2):217–237.

Lilly, D. K. (1992). A proposed modification of the germano subgrid-scale closure method. *Physics of Fluids A: Fluid Dynamics (1989-1993)*, 4(3):633–635.

Lim, H.-J., Chang, K.-A., Huang, Z.-C., and Na, B. (2015). Experimental study on plunging breaking waves in deep water. *Journal of Geophysical Research: Oceans*, 120(3):2007–2049.

Lin, P. and Liu, P. L.-F. (1998a). A numerical study of breaking waves in the surf zone. *Journal of fluid mechanics*, 359(1):239–264.

Lin, P. and Liu, P. L.-F. (1998b). Turbulence transport, vorticity dynamics, and solute mixing under plunging breaking waves in surf zone. *Journal of Geophysical Research: Oceans*, 103(C8):15677–15694.

Lubin, P., Vincent, S., Abadie, S., and Caltagirone, J.-P. (2006). Three-dimensional large eddy simulation of air entrainment under plunging breaking waves. *Coastal engineering*, 53(8):631–655.

Lubin, P., Vincent, S., Caltagirone, J.-P., and Abadie, S. (2003). Fully three-dimensional direct numerical simulation of a plunging breaker. *Comptes Rendus Mecanique*, 331(7):495–501.

Ma, G., Shi, F., and Kirby, J. T. (2011). A polydisperse two-fluid model for surf zone bubble simulation. *Journal of Geophysical Research: Oceans*, 116(C5).

Marchisio, D. L. and Fox, R. O. (2005). Solution of population balance equations using the direct quadrature method of moments. *Journal of Aerosol Science*, 36(1):43–73.

Márquez Damián, S. (2013). *An extended mixture model for the simultaneous treatment of short and long scale interfaces*. PhD thesis, Universidad Nacional del Litoral, Argentina.

Marschall, H. et al. (2011). *Towards the Numerical Simulation of Multi-Scale Two-Phase Flows*. PhD thesis, Technische Universität München.

Martìnez-Bazàn, C., Montanes, J., and Lasheras, J. C. (1999a). On the breakup of an air bubble injected into a fully developed turbulent flow. Part 1. Breakup frequency. *Journal of Fluid Mechanics*, 401:157–182.

Martìnez-Bazàn, C., Montanes, J., and Lasheras, J. C. (1999b). On the breakup of an air bubble injected into a fully developed turbulent flow. Part 2. Size pdf of the resulting daughter bubbles. *Journal of Fluid Mechanics*, 401:183–207.

Melville, W. (1996). The role of surface-wave breaking in air-sea interaction. *Annual review of fluid mechanics*, 28(1):279–321.

Milelli, M. (2002). *A numerical analysis of confined turbulent bubble plumes*. PhD thesis, Swiss Federal Insitute of Technology, Zurich.

Moraga, F., Carrica, P., Drew, D., and Lahey, R. (2008). A sub-grid air entrainment model for breaking bow waves and naval surface ships. *Computers & Fluids*, 37(3):281–298.

Morison, J., Johnson, J., Schaaf, S., et al. (1950). The force exerted by surface waves on piles. *Journal of Petroleum Technology*, 2(05):149–154.

Nadaoka, K., Hino, M., and Koyano, Y. (1989). Structure of the turbulent flow field under breaking waves in the surf zone. *Journal of Fluid Mechanics*, 204:359–387.

Nadaoka, K., Ueno, S., and Igarashi, T. (1988). Field observation of three-dimensional large-scale eddies and sediment suspension in the surf zone. *Coastal Engineering in Japan*, 31(2):277–287.

Nielsen, A. W., Mortensen, S. B., Jacobsen, V., and Christensen, E. D. (2008). Numerical modelling of wave run-up on a wind turbine foundation. In *ASME 2008 27th International Conference on Offshore Mechanics and Arctic Engineering*, pages 597–603. American Society of Mechanical Engineers.

Ojima, S., Hayashi, K., Hosokawa, S., and Tomiyama, A. (2014). Distributions of void fraction and liquid velocity in air–water bubble column. *International Journal of Multiphase Flow*, 67:111–121.

Paulsen, B. T., Bredmose, H., and Bingham, H. B. (2014a). An efficient domain decomposition strategy for wave loads on surface piercing circular cylinders. *Coastal Engineering*, 86:57–76.

Paulsen, B. T., Bredmose, H., Bingham, H. B., and Jacobsen, N. G. (2014b). Forcing of a bottom-mounted circular cylinder by steep regular water waves at finite depth. *Journal of Fluid Mechanics*, 755:1–34.

Peregrine, D. H. (1983). Breaking waves on beaches. *Annual Review of Fluid Mechanics*, 15(1):149–178.

Prince, M. J. and Blanch, H. W. (1990). Bubble coalescence and break-up in air-sparged bubble columns. *Journal of Fluid Mechanics*, 36(10):1485–1499.

Ramkrishna, D. (2000). *Population balances: Theory and applications to particulate systems in engineering*. Academic press.

Rapp, R. J. and Melville, W. (1990). Laboratory measurements of deep-water breaking waves. *Philosophical Transactions of the Royal Society of London A: Mathematical, Physical and Engineering Sciences*, 331(1622):735–800.

Rhie, C. and Chow, W. (1983). Numerical study of the turbulent flow past an airfoil with trailing edge separation. *AIAA journal*, 21(11):1525–1532.

Rojas, G. and Loewen, M. (2010). Void fraction measurements beneath plunging and spilling breaking waves. *Journal of Geophysical Research: Oceans*, 115(C8).

Rusche, H. (2003). *Computational fluid dynamics of dispersed two-phase flows at high phase fractions*. PhD thesis, Imperial College, University of London.

Sato, Y. and Sekoguchi, K. (1975). Liquid velocity distribution in two-phase bubble flow. *International Journal of Multiphase Flow*, 2(1):79–95.

Scardovelli, R. and Zaleski, S. (1999). Direct numerical simulation of free-surface and interfacial flow. *Annual review of fluid mechanics*, 31(1):567–603.

Schiller, L. and Naumann, Z. (1935). A drag coefficient correlation. *Vdi Zeitung*, 77(318):51.

Selma, B., Bannari, R., and Proulx, P. (2010). Simulation of bubbly flows: Comparison between direct quadrature method of moments (dqmom) and method of classes (cm). *Chemical Engineering Science*, 65(6):1925–1941.

Shi, F., Kirby, J. T., and Ma, G. (2010). Modeling quiescent phase transport of air bubbles induced by breaking waves. *Ocean Modelling*, 35(1):105–117.

Silva, L. and Lage, P. (2011). Development and implementation of a polydispersed multiphase flow model in openfoam. *Computers & Chemical Engineering*, 35(12):2653–2666.

Sorensen, R. M. (1993). *Basic wave mechanics: for coastal and ocean engineers*. John Wiley & Sons.

Štrubelj, L. and Tiselj, I. (2011). Two-fluid model with interface sharpening. *International journal for numerical methods in engineering*, 85(5):575–590.

Sumer, B. M. and Fredsøe, J. (1997). *Hydrodynamics around cylindrical structures*, volume 12. World Scientific.

Sumer, B. M., Guner, H., Hansen, N. M., Fuhrman, D. R., and Fredsøe, J. (2013). Laboratory observations of flow and sediment transport induced by plunging regular waves. *Journal of Geophysical Research: Oceans*, 118(11):6161–6182.

Sumer, B. M., Sen, M. B., Karagali, I., Ceren, B., Fredsøe, J., Sottile, M., Zilioli, L., and Fuhrman, D. R. (2011). Flow and sediment transport induced by a plunging solitary wave. *Journal of Geophysical Research: Oceans*, 116(C1).

Sweby, P. K. (1984). High resolution schemes using flux limiters for hyperbolic conservation laws. *SIAM journal on numerical analysis*, 21(5):995–1011.

Ting, F. C. (2006). Large-scale turbulence under a solitary wave. *Coastal Engineering*, 53(5):441–462.

Ting, F. C. (2008). Large-scale turbulence under a solitary wave: Part 2: Forms and evolution of coherent structures. *Coastal Engineering*, 55(6):522–536.

Ting, F. C. and Kirby, J. T. (1994). Observation of undertow and turbulence in a laboratory surf zone. *Coastal Engineering*, 24(1):51–80.

Ting, F. C. and Kirby, J. T. (1995). Dynamics of surf-zone turbulence in a strong plunging breaker. *Coastal Engineering*, 24(3):177–204.

Ting, F. C. and Kirby, J. T. (1996). Dynamics of surf-zone turbulence in a spilling breaker. *Coastal Engineering*, 27(3):131–160.

Tomaselli, P. D. and Christensen, E. D. (2015). Investigation On The Use Of A Multiphase Eulerian CFD Solver To Simulate Breaking Waves. In *ASME 2015 34th International Conference on Ocean, Offshore and Arctic Engineering*. American Society of Mechanical Engineers.

Tomaselli, P. D. and Christensen, E. D. (2016). A Coupled VOF-Eulerian Multiphase CFD Model To Simulate Breaking Wave Impacts On Offshore Structures. In *ASME 2016 35th International Conference on Ocean, Offshore and Arctic Engineering*. American Society of Mechanical Engineers.

Ubbink, O. (1997). *Numerical prediction of two fluid systems with sharp interfaces*. PhD thesis, Imperial College, University of London.

Van Leer, B. (1997). Towards the ultimate conservative difference scheme. *Journal of Computational Physics*, 135(2):229–248.

Veritas, N. (2000). *Environmental conditions and environmental loads*. Det Norske Veritas.

Vukčević, V. (2016). *Numerical Modeling of Coupled Potential and Viscous Flow for Marine Applications*. PhD thesis, University of Zagreb.

Wardle, K. E. and Weller, H. G. (2013). Hybrid multiphase cfd solver for coupled dispersed/segregated flows in liquid-liquid extraction. *International Journal of Chemical Engineering*, 2013.

Warming, R. and Beam, R. M. (1976). Upwind second-order difference schemes and applications in aerodynamic flows. *AIAA Journal*, 14(9):1241–1249.

Watanabe, Y., Saeki, H., and Hosking, R. J. (2005). Three-dimensional vortex structures under breaking waves. *Journal of Fluid Mechanics*, 545:291–328.

Weller, H. (2008). A new approach to vof-based interface capturing methods for incompressible and compressible flow. *OpenCFD Ltd., Report TR/HGW/04*.

Weller, H. G., Tabor, G., Jasak, H., and Fureby, C. (1998). A tensorial approach to computational continuum mechanics using object-oriented techniques. *Computers in physics*, 12(6):620–631.

Wheeler, J. et al. (1969). Methods for calculating forces produced by irregular waves. In *Offshore Technology Conference*. Offshore Technology Conference.

Wienke, J. and Oumeraci, H. (2005). Breaking wave impact force on a vertical and inclined slender pile—theoretical and large-scale model investigations. *Coastal Engineering*, 52(5):435–462.

Wroniszewski, P. A., Verschaeve, J. C., and Pedersen, G. K. (2014). Benchmarking of navier–stokes codes for free surface simulations by means of a solitary wave. *Coastal Engineering*, 91:1–17.

Zhang, D., Deen, N., and Kuipers, J. (2006). Numerical simulation of the dynamic flow behavior in a bubble column: a study of closures for turbulence and interface forces. *Chemical Engineering Science*, 61(23):7593–7608.

DTU Mechanical Engineering
Section of Fluid Mechanics, Coastal and Maritime Engineering
Technical University of Denmark

Nils Koppels Allé, Bld. 403
DK-2800 Kgs. Lyngby
Denmark
Phone (+45) 4525 1360
Fax (+45) 4588 4325

www.mek.dtu.dk